ICE DYNAMICS OF THE HAUPAPA/TASMAN GLACIER MEASURED AT HIGH SPATIAL AND TEMPORAL RESOLUTION, AORAKI/MOUNT COOK, NEW ZEALAND

A

THESIS

Presented to the School of Geography, Environment and Earth Sciences

Victoria University of Wellington

In Partial Fulfilment of the Requirements

for the Degree of

MASTERS OF SCIENCE

By

Edmond Anderson Lui, B.Sc., GradDipEnvLaw

Wellington, New Zealand

October, 2016

TABLE OF CONTENTS

LIST OF FIGURES

CHAPTER ONE – LITERATURE REVIEW

CHAPTER TWO – STUDY SITE

CHAPTER THREE - METHODOLOGY

CHAPTER FOUR - RESULTS

CHAPTER FIVE – DISCUSSION

LIST OF TABLES

CHAPTER ONE – LITERATURE REVIEW

No tables

CHAPTER TWO – STUDY SITE

CHAPTER THREE – METHODOLOGY

CHAPTER FOUR – RESULTS

CHAPTER FIVE – DISCUSSION

LIST OF EQUATIONS

CHAPTER ONE – LITERATURE REVIEW

CHAPTER TWO – STUDY SITE

CHAPTER THREE – METHODOLOGY

NO EQUATIONS IN CHAPTERS FOUR AND FIVE

Acknowledgements

This thesis would not have been possible without the advice and assistance of my three supervisors, Dr. Brian Anderson, Dr. Huw Horgan and Dr. Kevin Norton. I want to thank Kevin for his reviews and his ongoing support for the project, Huw for the organisation of field work, his reviews and advice throughout the whole writing process and Brian for guiding me through every step of methodology, developing the algorithms and review and support throughout the whole thesis.

Thank you to Aleks from IT services to making sure the system was up-to-date and for resolving other computer problems. Field work would of course not have been possible with Huw and Brian's input, but also thankyou to Lauren Vargo for assisting with the Trimble GNSS and the measurement of GCPs. To fellow post-graduates, Merjin Thornton and Sam Taylor-Offord, the fieldwork would not have been as fun without you both.

Finally to my partner, Nandini Nair, for your patience and ongoing support from start to completion.

Motivations

Renowned theoretical physicist and one of the founders of modern quantum physics, Richard Feynman once said: "*Science is the belief in the ignorance of experts. I learned very early in the difference between knowing the name of something and knowing something. If you're doing an experiment you should report everything that you think might make it invalid, not only what you think is right about it.*"

If I can live by this opinion of seeking the real truth, not just the truths everyone tells you, then I'd die a happy man.

Acronyms

CCD – Charged-coupled Device
CMOS – Complementary Metal-Oxide Semiconductor
DEM - Digital Elevation Model
EEIC – Eastern Embayment Ice Cliff
GHG – Greenhouse gases
GCP - Ground Control Points
GMSL - Global Mean Sea Level
GPS - Global Position System
MIA – Main Ice Cliff
OpenCV - 'Open Source Computer Vision', an open-source Computer Vision Library
QGIS - short for 'Quantum Geographic Information Systems', a GIS application
TIC – Temporary Ice Cliff
FOV - 'Field of View'
FSF - Flow Scale Factor
PSF - Pixel Scale Factor (a.k.a. Pixel Scale)
SfM - 'Structure from Motion'
SLR - Sea-level Rise

ABSTRACT

Glaciers are among the clearest of signals for anthropogenic climate change and their retreat is considered symptomatic of the observed warming since the start of the 20th century from anthropogenic sources (Mann *et al.*, 2004). New Zealand has 3,100 mountain glaciers, with those in the Southern Alps experiencing losses of 34% since 1977 and a decline in volume of 51 km^3 in 1994 to 41 km^3 in 2010 (NIWA, 2011). The direct impact of increasing atmospheric temperatures on glaciers is well understood (Chinn, 2012) through its effects on the melt and accumulation rates (Kirkbride, 2010; Purdie, 2011; Chinn, 1997; Oerlemans, 2001). However lake calving glaciers such as the Tasman Glacier exhibit different behaviour and are suggested to be at least partially decoupled from climate forcing (Benn *et al.*, 2007).

Here, I present a temporally and spatially complete study of Haupapa/Tasman Glacier, Aoraki/Mt. Cook over three years to investigate the ice dynamics at the terminus. I used oblique photogrammetry at high resolution for data acquisition and adapted computer vision algorithms for correcting this oblique view to a real-world geometry. This technique has been rarely used (Murray *et al.*, 2015; Messerli and Grinsted, 2015; Ahn and Box, 2010; Harrison *et al.*, 1986 and Flotron, 1973) but owing to its cost-effectiveness and high data yields, it is becoming an increasingly powerful methodology favoured by glaciologists.

During the 3 year study period, Tasman Glacier terminus retreat rate U_r was 116 ± 19 m a^{-1} (2013-2014), 83 ± 18 m a^{-1} (2014-2015) and 204 ± 20 (2015-2016). A strong seasonal pattern was evident in the calving events. Three major calving events occurred over the study, one occurring in the summer of 2013 and two in the summer of 2016. The latter two events are responsible for the elevated U_r in 2015-2016. These events were characterised as distinct large-magnitude calving (usually as a large tabular iceberg) which continued to drift and break up in the lake for weeks to months. Three large calving events accounted for 47% of the total surface area loss for the 38 month study period with the remaining surface area loss from 2nd order calving including notching at the waterline and the spalling of lamallae of ice from surface fractures, and ice-cliff melt. During the spring/summer months of 2014 and 2015 there was no large buoyancy driven calving event such as those seen in 2013 and 2016, but there were many smaller-magnitude calving events. Smaller-magnitude events were less frequent in winter months as compared to summer months. Ice flow in winter has been shown to be less than in summer (Horgan *et al*, 2015). While seasonal temperatures and changes to the basal water pressure are linked to these observations, it is also likely that the relatively faster ice flow in summer/autumn could be influencing the rate of 1st and 2nd order calving mechanisms. Overall, the calving rates were calculated as 171 ± 18 m a^{-1} (2013-2014), 136 ± 17 m a^{-1} (2014-2015) and accelerated to 256 ± 20 m a^{-1} in the last year (2015-2016). My results show that almost half of the ice loss at the terminus comes from large, infrequent calving events and that retreat rates for 2015-2016 were high compared to the historic record but the area loss is lower than it has been because of the relatively narrow terminus.

CHAPTER ONE
Literature Review

1.0 Introduction

Glaciers and ice sheets currently cover approximately 10% of Earth's surface (Arendt *et al.,* 2012) and contain 75% of the world's freshwater (NSIDC, 2016). During the last glacial maximum (19-26 ka BP), this ice cover extended to 32% of the total land area (Ehlers and Gibbard, 2004) and global temperatures were estimated to be 4.0 ± 0.8 ° C (95% confidence interval) cooler than present day (Annan and Hargreaves, 2013). In the past 420,000 years, atmospheric carbon dioxide has been strongly linked to the ebb and flow of global temperatures embodied in the cyclical ice ages and short periods of relatively warmer climates during interglacials (Petit *et al.,* 1999). Rapid growth of human populations and industrialisation in the Holocene (10 ka BP) has spurred further increases of greenhouse gases into the atmosphere. There is an unambiguous difference between present day CO_2 concentrations, according to the Mauna Loa Observatory (NOAA, 2016), which has now crossed the 400 parts per million (ppm) threshold, compared to the background oscillation of CO_2 which varied between 200-280 ppm in the past 420,000 years (see Figure 1.0.1).

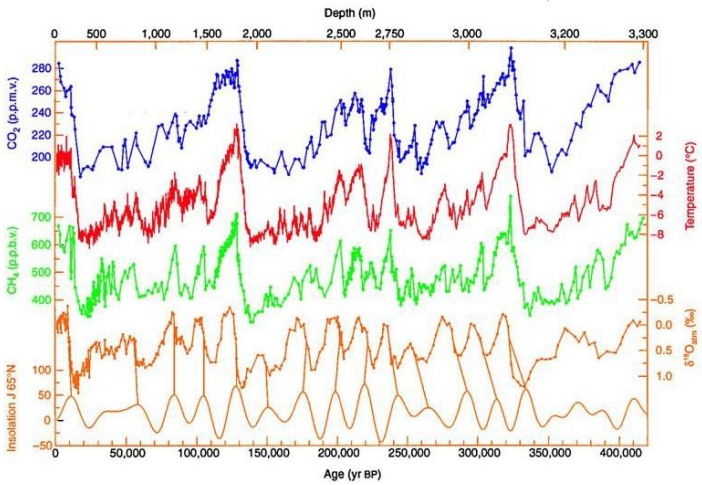

Figure 1.0.1. Vostok Ice Core data from the last 420,000 years showing the correlation between atmospheric CO_2 / CH_4 and temperatures. *Source:* Petit *et al,* 1999

This unequivocal greenhouse forcing from manmade sources has resulted in a combined land and ocean surface temperature warming of 0.85 [0.65 – 1.06] ° C since 1880 AD to 2012 AD (IPCC AR5, 2014). The latest Intergovernmental Panel on Climate Change (IPCC) report

also showed that with climate warming, ice sheets in Greenland in Antarctica have been losing mass between 1992 to 2011 (*high confidence)* and predict that the net ice volume will continue to shrink in the following decades (*high confidence)*. Globally, mean sea levels rose 0.19 [0.17 – 0.21] m for the period over 1901 AD to 2010 AD (IPCC AR5, 2014). Although the historical trends in sea-level rise (SLR) and temperature/CO_2 change are clear, much debate remains on the response of our climate for the next 50 yrs, 100 yrs and even longer timescales. This uncertainty is fundamentally due to the temporal and spatial dynamics occurring in the atmospheric, cryosphere and hydrosphere, which interact with one another in complex ways.

This introduction has been structured to address each of the topics. Firstly in 1.1, a summary of the global trends in ice sheets and mountain glaciers is presented to frame our study. The projected impacts on sea level rise (cryosphere) and subsequent effects of glacial loss on human populations through para-glacial sedimentation (hydrosphere) are also reviewed.

In 1.2, glacial dynamics are explored covering calving mechanisms, the dynamical controls of glaciers and other factors that drive change. This serves as background to further review of the literature that is pertinent to the Tasman Glacier. A further review is presented in Chapter 2.

In 1.3, we analyse an array photogrammetry techniques being used, to date, by other scholars in this field and present the pros and cons of each methodology as a prelude to own methodology in Chapter 3.

In light of the data presented in Chapter 1, objectives for this thesis are presented in 1.4. This serves as a framework for investigation in my methodology.

1.1 Global Trends and Sea-level rise Projections

Evidence of mountain glaciers experiencing rapid decline globally in the last century is robust and abundant (Zemp *et al.*, 2015; Berthier *et al*, 2010; Glasser *et al.*, 2011; Radic and Hock, 2011). In Zemp *et al.*, analysis of 42,000 glacier length changes compiled in the World Glacier Monitoring Service (WGMS) dataset showed a global mean annual glacier mass balance loss of -0.40 m w.e. a^{-1} (1940-60s), -0.20 m w.e. a^{-1} (1970-80s) and -0.47 m w.e. a^{-1} (1990s). According to the IPCC these worldwide glacial changes were estimated to have contributed 0.50 ± 0.18 mm yr^{-1} to sea levels during 1961 – 2003. However direct measurements from tidal gauges evidenced that global mean sea level rose at 1.5 ± 0.2 mm yr^{-1} during 1901 – 1990 and accelerated in the last two decades (1993 – 2010) to 3.2 ± 0.4 mm yr^{-1} (IPCC AR5, 2013).

Similar melting trends have also been assessed in regional studies of glaciers around the world. For example, Alaskan outlet glaciers contributed 0.12 ± 0.02 mm yr^{-1} to sea level rise (previously thought to be 30% of global mean sea level (GMSL) for the years 1962 – 2006) (Berthier *et al.*, 2010) and in the Patagonian icefields at 0.0052 ± 0.0011 mm yr^{-1} (previously thought to account for 10% of GMSL rise).

Source	1901–1990	1971–2010	1993–2010
Observed contributions to global mean sea level (GMSL) rise			
Thermal expansion	–	0.8 [0.5 to 1.1]	1.1 [0.8 to 1.4]
Glaciers except in Greenland and Antarctica[a]	0.54 [0.47 to 0.61]	0.62 [0.25 to 0.99]	0.76 [0.39 to 1.13]
Glaciers in Greenland[b]	0.15 [0.10 to 0.19]	0.06 [0.03 to 0.09]	0.10 [0.07 to 0.13][b]
Greenland ice sheet	–	–	0.33 [0.25 to 0.41]
Antarctic ice sheet	–	–	0.27 [0.16 to 0.38]
Land water storage	–0.11 [–0.16 to –0.06]	0.12 [0.03 to 0.22]	0.38 [0.26 to 0.49]
Total of contributions	–	–	**2.8 [2.3 to 3.4]**
Observed GMSL rise	**1.5 [1.3 to 1.7]**	**2.0 [1.7 to 2.3]**	**3.2 [2.8 to 3.6]**
Modelled contributions to GMSL rise			
Thermal expansion	0.37 [0.06 to 0.67]	0.96 [0.51 to 1.41]	1.49 [0.97 to 2.02]
Glaciers except in Greenland and Antarctica	0.63 [0.37 to 0.89]	0.62 [0.41 to 0.84]	0.78 [0.43 to 1.13]
Glaciers in Greenland	0.07 [–0.02 to 0.16]	0.10 [0.05 to 0.15]	0.14 [0.06 to 0.23]
Total including land water storage	**1.0 [0.5 to 1.4]**	**1.8 [1.3 to 2.3]**	**2.8 [2.1 to 3.5]**
Residual[c]	**0.5 [0.1 to 1.0]**	**0.2 [–0.4 to 0.8]**	**0.4 [–0.4 to 1.2]**

Notes:

[a] Data for all glaciers extend to 2009, not 2010.

[b] This contribution is not included in the total because glaciers in Greenland are included in the observational assessment of the Greenland ice sheet.

[c] Observed GMSL rise – modelled thermal expansion – modelled glaciers – observed land water storage.

Figure 1.1.1. Shows summary of historical sea-level rise (SLR) from varying sources. *Source:* IPCC AR5 Chapter 13 – Sea

It is projected that by the end of this century, glaciers will have contributed 0.124 ± 0.037 m to sea-level rise (Radic and Hock, 2011) with the majority from glaciers in Antarctica, Alaska and Arctic Canada. Based on simulations of 120,000 glaciers worldwide, the authors also concluded that total glacier volume will be reduced by 21 ± 6% globally, with some regions experiencing as high as 75% of their total volume by 2100.

In aggregate, global mean sea-level (GMSL) rise from observational evidence has doubled in speed from in the last decade as compared to rates from 1901 to 1990 (see Figure 1.1.1). The IPCC projects that GMSL will *likely* increase by 0.4 (0.26 to 0.55) m for RCP2.6 and 0.63 (0.45 to 0.82) m for RCP8.5, where RCP represents the Representative Concentration Pathway or the radiative forcing from anthropogenic emissions. Of these projections, thermal expansion is expected to contribute the most, followed by the melting of glaciers and lastly by losses from Greenland and Antarctic ice sheets (see Figure 1.1.2). Our current scientific

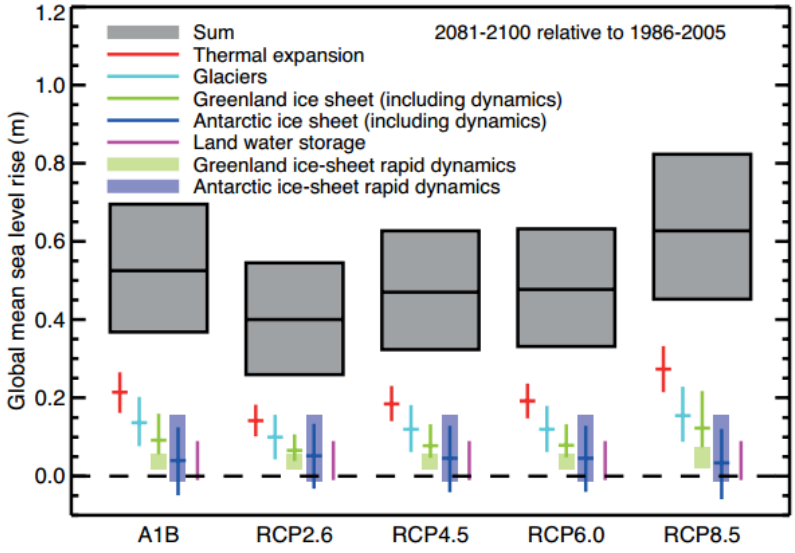

Figure 1.1.2. Projections for sea-level rise (SLR) for 2081-2100. It is expected that glaciers will respond rapidly to anthropogenic radiative forcing and is likely to contribute more than Greenland and Antarctic ice sheets to sea-level rise.
Note: A1 represents the storyline of very rapid economic growth and population growth that peaks mid-century. A1B is a variant of A1 where there is a balanced economy relying on varying sources of energy including fossil-fuels, renewable and other sources. Radiative Concentration Pathways: RCP2.6 represents radiative forcing of + 2.6 W/m^2 relative to pre-industrial values whereas RCP8.5 means + 8.5 W/m^2. *Source:* IPCC AR5 Chapter 13 – Sea Level Change

understanding suggest that if the Greenland Ice Sheet (GIS) disappears, sea levels may rise by 7 m (Houghton *et al.*, 2001). Likewise if the West Antarctic Ice Sheet (WAIS) was to collapse this century, another 3-5 m of sea-level rise will ensue (Cazenave and Llovel, 2010).

Although the rising trend in sea level is clear for this century, the overall IPCC projections are calculated from Atmosphere-Ocean General Circulation Models (AOGCMs) with resolutions of 1 to 2 degrees of latitude or ranging from 50 to 200 km wide (IPCC AR5, 2012). As such, glacial and ice-sheet dynamics occurring over smaller resolutions can influence the accuracy of future projections. Further research into these dynamics is therefore warranted as they fundamentally underpin the accuracy of these AOGCMs; which often ignore the dynamics occurring on local or regional scales particularly for mountain and tidewater glaciers which are subject to limonological/marine dynamics in varying geological conditions.

1.1.1 Sea-level Rise Impacts

The impacts of the projected sea-level rise in this century is likely to drastically affect large populations particularly those residing in low-lying urban centres and floodplains such as Bangladesh. It is estimated for a temperature rise of 4 ° C and resulting SLR of 0.5 – 2 m by 2100, up to 187 million people are to be displaced globally (Nicholls *et al.,* 2010) and 270 million people worldwide will be at risk (Mimura, 2013). In addition, the expected SLR will exacerbate storminess and affect rates of coastal inundation particularly among small Pacific Island nations such as Kiribati. These regional impacts will have stark economic and societal implications for neighbouring countries like New Zealand.

Thus, improving scientific understanding of glaciers and ice sheet dynamics is pertinent, especially since global SLR projections and their consequences on human society rely on robust estimations of the volumetric losses of in our cryosphere.

1.1.2. Glaciers as Repositories of Fresh Water

In addition to the direct impacts of SLR and flooding on human populations are the longer-term repercussions on the water cycle since glaciers act as repositories of fresh water. The declining trend of mountain glaciers in this century is likely to result in flow-on effects in agriculture and human economies, adding further stress to developing countries (Grafton *et al*., 2012). For example, a recent study by Yang, Jian-Ping *et al.* (2015) showed that 92 % of China's 48,571 glaciers experienced light to heavy vulnerability during 1961-2007 and with 41 % classed as under heavy or very heavy vulnerability. These mountain glaciers from the Tibetan Plateau and

Western China constitute as the sources of Asia's ten largest rivers: the Ganges Rivers, Brahmaputra, Indus, Ertix, Ili, Mekong, Salween, Yellow, Tarim, and the Yangtze (Yang *et al.*, 2015) which collectively feed into India, China and other South-East Asian countries. In turn, some 1.3 billion people in this region depend on water provided by ice melt from glaciers (UNEP, 2012).

1.1.3 Para-glacial Sedimentation Impacts

On local spatial scales, discharge from the melting of mountain glaciers will result in a temporary increase in landslide and flood hazards. This is due to the nature of glaciers which buttress their surrounding slopes. Once downwasting occurs, the effective height of ice that held up the rock diminishes, and is followed by the destabilisation of the adjacent mountainside. An enhanced sediment supply to glacial rivers and river basins downstream is another response. Although the volume of sediment supply declines exponentially as the deglaciated slopes stabilise, in the short to medium term of the paraglacial response, such changes may lead to further landslide and flood impacts. At present, these geomorphic impacts remain poorly understood with some authors (Knight and Harrison, 2009) suggesting that we have ignored some crucial metrics in the evaluation of climate change and its effects in such a "sensitive environment". An example would be that current GCMs for long term predictions are rarely used to drive geomorphological evolution models and are thus an incomplete assessment. (Knight and Harrison, 2009).

1.2. Dynamics of calving glaciers

1.2.1 Introduction

Calving glaciers are complex systems that arise from the interaction of multiple processes, from climate, mass balance, stress and strain dynamics to the shape of the underlying bedrock. Iceberg calving is defined as the mechanical loss of ice from a glacial margin and is paramount for predictions of mass balances in many glacial systems globally.
It is a generally accepted idea that the behaviour of calving glaciers are at least somewhat de-coupled from climate, with evidence suggesting that the equilibrium line altitude of such glaciers is an unreliable control of the position and rates of advance or retreat of the calving termini (Nick and Oerlemans, 2006; Benn *et al.*, 2007). Although, in some literature it has been shown that they can experience rapid retreat post an initial climate signal (Meier *et al.*, 1997).

Lake-terminating glaciers are one class of glaciers that exhibit dynamic behaviour as a consequence of many controls including lake levels, precipitation, sub-surface hydrology, and topographic conditions (Haeberli, 1995; Quincey and Glasser, 2009; Hochstein, 1995). Unlike marine-terminating or tidewater glaciers, lake water levels are typically stable diurnally and therefore calving at lacustrine glaciers can be further enhanced by thermal notching or cuts in the ice at the waterline (Diolaiuti *et al.*, 2006).
In general, glaciers typically fall under 3 types: fast, slow-flowing or surging, however the dynamics of how they calve differ from glacier to glacier, presenting endless perturbations from empirical observations around the world (Benn *et al.*, 2007).

1.2.2 Iceberg Calving

Iceberg calving is defined by the mechanical loss of ice from glaciers and ice shelves. This occurs as a result of the ice no longer having the ability to support its own weight and collapsing catastrophically carried by a conversion of its gravitational potential energy into spontaneous kinetic energy (Astrom *et al.*, 2014, Bartholomaus *et al.*, 2012). Fractures in the glacier can exacerbate the rate of calving causing increased stress and strain on exposed ice at the terminus ice cliff. Thermal erosional and subaqueous melt can also undermine the foundations of frontal ice causing them to fall into the sea or lake below. In some cases, entire tabular icebergs can detach from free-floating ice tongues driven by their buoyancy and departure from the grounding line (Bassis and Walker, 2011). Owing to the sporadic nature

and disparate sizes of calving bergs, current deterministic calving laws are unable to explain the diversity of calving regimes seen in nature.

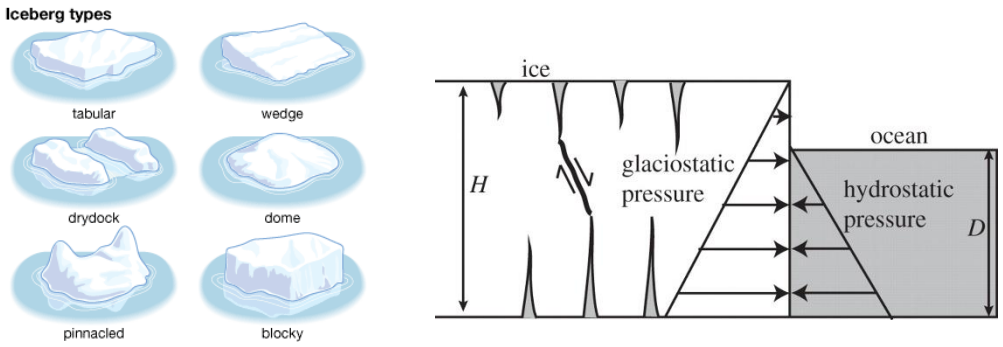

Figure 1.2.2. (LEFT) Shows varying types of icebergs. *Source:* Encyclopedia Britannica, 2008 (RIGHT) Shows a schematic of the exchange of glaciostatic and hydrostatic pressure from fractured ice to a body of water. The depth of the ocean and the height of ice are important controls. *Source:* Bassis and Walker, 2011

Some scholars have attempted to model the dynamic behaviour of glaciers by treating them as an assemblage of granular blocks fused together (i.e. in Bassis and Jacobs (2013)) or in Astrom *et al,* (2014) as self-organising critical system, or a 'system that is fluctuating around a critical point in response to a changing external forcing', (i.e. warming oceans, increase precipitation etc).

It is currently understood that calving plays a dominant role in ice loss around the world. In Greenland it is estimated that one-third to one-half of all ice loss is due to iceberg calving (Murray *et al.*, 2015). Likewise in Antarctica, calving mass balances were estimated to exceed 2,000 gigatonnes per year (Jacobs and Helmer, 1992) as compared to ice-shelf melting of 544 gigatonnes per year. On the contrary, some research is now suggesting that calving is becoming less prevailing mechanism of ice loss, falling behind basal melting which is now accounting for 10 – 90% in the loss of ice shelves in Antarctica (Depoorter *et al.*, 2013). Nonetheless, the total calving flux in this region still accounts for c. 1,321 ± 144 gigatonnes per year based on the recent estimations by Depoorter *et al.*, (2013) and is still a significant contributor to global sea-level rise. Simplistically, the frequency of calving from ice shelves is low, however when they do calve, they do so violently, in large tabular bergs possibly many kilometres wide (Bassis and Jacobs, 2013; Bassis and Walker, 2011; Lazzara *et al.*, 1999; Fricker *et al.*, 2002).

Unlike the floating ice tongues of Greenland and Antarctica, grounded glaciers are those that are still in physical contact with the underlying bedrock and are often termed tidewater

glaciers (if they enter the sea) or lacustrine glaciers (if they enter inland lakes). The behaviour of grounded glaciers vary significantly from calving ice shelves, in that they usually calve smaller and bergs which are less than whole ice thickness may capsize upon detachment (Howat *et al.,* 2007; Bassis and Jacobs, 2015).

Although much work has already been done on calving glaciers, the elusiveness of a unifying theory rests upon their multivariate nature and difficulties in attaining temporal and spatially sensitive data in often challenging environments (Benn *et al.,* 2007). The three key unresolved problems of calving are (1) attaining a feasible method of estimating stresses at the grounding line (a.k.a 'the grounding line problem') (2) quantifying rates of basal movement or glacial slip (a.k.a. 'the unresolved sliding problem') and (3) modelling of ice fracture propagation and the failure of ice.

1.2.3. Controls on the calving process

The longstanding debate in the glaciological community regarding rates of calving is whether it is a direct local response of glacial dynamics that are driving it or whether calving acts more as the 'master' of the system, forcing changes in the terminus position, the velocity and geometry of the glacier (Benn *et al.,* 2007). Van der Veen (1996) argued that the position of where calving occur, rather than the rate of calving is of importance, identifying that H_0 = 50 m, a critical height-above buoyancy, is typically where the calving front will be. H_0, the height-above buoyancy, was initially defined by Sikonia (1982) to be a function of the ice thickness at the terminus (H_T), the densities of the ice (ρ_I) and of the proglacial water (ρ'_W) and the depth of the water (D_W) with an r^2 = 0.82.

(1.1) $$U_C = 1.092 \times 10^6 Q^{0.5689} H_O^{2.175}$$

Q is the discharge at a nearby river (the Knik River which was used as a proxy for subglacial water flux)

(1.2) $$H_O = H_T \frac{\rho'_W}{\rho_I} D_W$$

This supposes that if the glacier thinned, the terminus position would retreat to a position where the height-above buoyancy was equal to some critical height. Although elegant, this model breaks down when the height-above buoyancy tends towards 0, particularly for free-floating ice shelves, the calving rate approaches infinity, which is certainly not the case for

the ice tongues of Greenland and Antarctica (Benn *et al.*, 2007).

Another theory that seeks to model calving is to relate calving rate to the water depth. Several authors have quantified this relationship in the past. For example, Pelto and Warren (1991) showed a relationship of from analysis of 22 Alaskan, Greenland and Svalbard glaciers:

(1.3) $$U_C = 70 + 8.33\ D_W(\ \mathrm{ma}^{\ 1})$$

Likewise, analysis of 21 freshwater glaciers including the Tasman Glacier showed a similar relationship between water-depth and calving rates (Warren and Kirkbride, 2003).

(1.4) $$U_C = 17.4 + 2.3\ D_W(\ \mathrm{ma}^{\ 1})$$

Compiling studies from numerous authors, Haresign (2004) plotted the water-depth to calving relationship from tidewater and freshwater glaciers from different regions of the world. Of note, are the rates from New Zealand which were an order of magnitude less than other freshwater calving glaciers in the world (first evidenced by Funk and Röthlisberger, 1989).

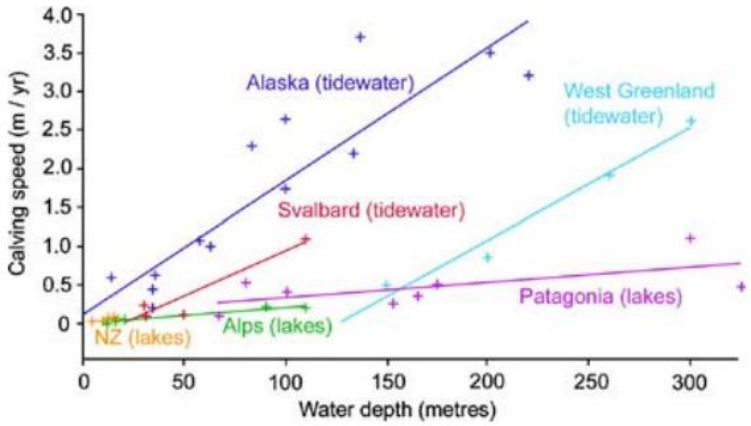

Figure 1.2.3a. Calving speed against water depth from various regions of the world. New Zealand's lake-calving glaciers are on an order of magnitude less than other freshwater glaciers. *Source:* Haresign, 2004

Although these functions relating calving rates to water-depth and calving terminus position can serve as a sort of 'calving law' in modelling, they cannot be applied to every glacier in the world and are mathematical functions that are not fixed in time. In particular, derivations relating calving rates to water depth, particularly for New Zealand, are vastly outdated. For example, Tasman Lake levels were supposedly only 10 m in 1994-1995 whereas lake depth surveys in 2001-2007 by Dykes *et al.*, (2010) showed a maximum lake depth of 240 m.

Calving rates 1994 – 1995 (Warren and Kirkbride, 2004)

Glacier	h_w	t_w	u_i	dL/dt	u_c	$u_c + u_m$
	m	°C	$m\,a^{-1}$	$m\,a^{-1}$	$m\,a^{-1}$	$m\,a^{-1}$
Maud	15	4.3	151	−45	88	106
Grey	12	4.2	52	13	47	65
Godley	17	3.1	5	60	47	65
Ruth	4	3.1	6	30	18	36
Tasman	10	0.5	11	35	28	46
Hooker	20	1.7	28	4	14	32

Figure 1.2.3b. Source of data for New Zealand water-depth v calving rate relationship from New Zealand glaciers 1994-1995, as presented in Haresign's (2004) plot in *Figure 1.2.3a. Source:* Warren and Kirkbride, 2004

1.2.3.1. A hierarchical approach to calving

Benn *et al,* (2007) explains that calving can be categorized into a hierarchical system driven by 1st order, 2nd order and 3rd processes working in conjunction and on overlapping temporal scales.

All calving shares the feature of propagating fractures. The fundamental control on fracture dynamics is the strain rate arising from the spatial variations in velocity (Benn *et al,* 2007). Large fractures can deepen with increasing velocities and enhance the rate of calving whereas, when velocities are slow, surficial fractures are less likely to motivate further calving. As such, the authors argue that this 1st order process is dependent on basal drag, lateral drag and longitudinal stress gradients to resistance, all of which affect the ice flow variably throughout a vertical column of ice.

Underlying this process are 2nd order processes which are defined as (1) stress-strain conditions occurring locally at the terminus which can influence rate of fracture propagation (Benn *et al.,* 2007), (2) as melting and undercutting mechanisms occurring at or below the waterline such as thermo-erosional notch development (Röhl, 2006) and (3) as stress and strain around the grounding line resulting from the buoyancy of ungrounded ice.

Finally, 3rd order processes encompasses subaqueous calving typically from submerged 'ice-feet'.

1.3. Methodology Review

1.3.1 Introduction

Photogrammetry in its simplest sense is defined as the science of making measurements from an image or photograph. This science dates back as far as the 14th-15th century with Leonardo Di Vinci's "*Vitruvian Man"* arguably seen as one of the earliest examples of using an image to present quantifications, namely the dimensions and proportions of the human body.

Today, photogrammetry is one of the foundations of modern data acquisition methodologies particularly ever since the advent of flight whereby photographs of earth's surface can be remotely captured by satellites or aircraft or balloon. Fields that use Geographic Information Systems (GIS) and Remote Sensing (RS) rely heavily on readily available photographs attained from such sources. In the study of glaciers and other features of our cryosphere high-resolution satellite imagery is a desired option for large spatial surveys, especially when surveying land masses such as Antarctica and Greenland (Luthcke *et al.,* 2008; Kjeldsen *et al.,* 2013) and even locally in New Zealand using Advanced Space-borne Thermal Emission and Reflection Radiometer [ASTER] (Redpath *et al.,* 2013; Dykes and Brook, 2010), and aerial photography (Chinn, 1999).

1.3.2. Imaging Geometry

In photogrammetry, an image of a scene is stored as a matrix of pixel values which represent the brightness of a scene, captured within an image plane. Measurements made in the image plane can be used to infer parallel changes in the real-world. However the position of the camera dictates the geometry of the image co-ordinate system relative to the co-ordinate system of the object being captured. In satellite imagery or nadir imaging, where the camera is directly above the object, only the very centre (principal point) of the image plane is physically above the object. Thus, all other pixels are radially distorted, increasingly towards the edge of the image.

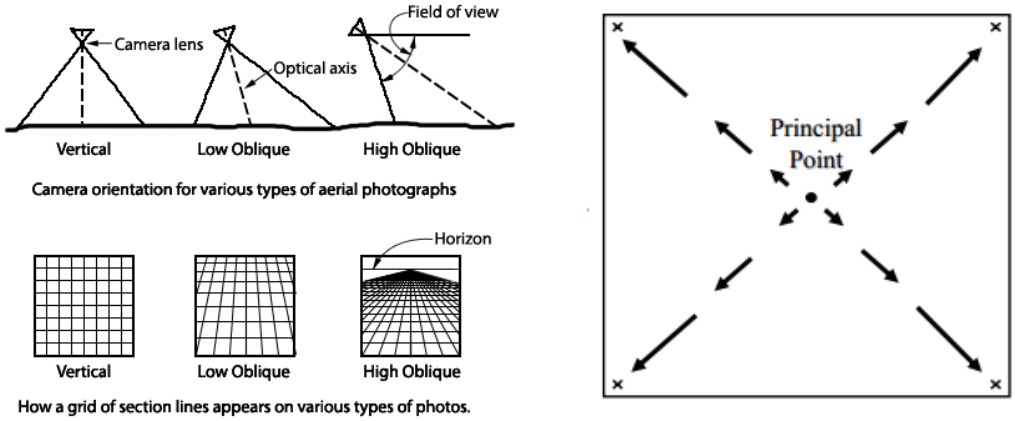

Figure 1.3.2. (LEFT) Shows the differences between nadir imaging and oblique imaging. (RIGHT) Radial distortion increasing away from the principal point of the image. *Source* – (LEFT) Wolf and Dewitt, 2000 (RIGHT) Lyres, 2008

To remediate the radial distortion, the mathematics is explained in Ma *et al* (2001) whereby the corrected image is the addition of the product of the pre-calibrated image coordinate *(u, v)* and a distortion factor, *d(u,v).* In other words this statement holds:

(1.5)
$$u' = u + \delta_u(u, v)$$
$$v' = v + \delta_v(u, v)$$

In order to correct for the radial and tangential distortion, the amount of distortion is given by

(1.6)
$$\delta_{ur} = k_1 u(u^2 + v^2) + O\left[(u, v)^5\right],$$
$$\delta_{vr} = k_1 v(u^2 + v^2) + O\left[(u, v)^5\right].$$

Combining and expanding 1.5 and 1.6, the radial and tangential distortions can therefore be written in the form:

(1.7)
$$u' = u(1 + k_1 r^2 + k_2 r^4 + k_3 r^6) + u_t$$
$$v' = v(1 + k_1 r^2 + k_2 r^4 + k_3 r^6) + v_t$$
$$r^2 = u^2 + v^2$$
$$u_t = 2p_1 uv + p_2(r^2 + 2u^2)$$
$$v_t = p_1(r^2 + 2v^2) + p_2 uv$$

where k_1, k_2, k_3 are the radial distortion coefficients and p_1, p_2 are the tangential distortion coefficients, both attained from the intrinsic camera parameters.

Topographic relief also generates distortions in the aerial image as areas of mountainous terrain will be physically greater in elevation than surrounding valleys and plains. This distortion radiates outwards from the principal point much like the radial lens distortion. The correction of the effects of topography is also known as orthorectification (UCSB, 2011). The following formula simplistically sets out the topographic displacement in a single image:

(1.8) $$d = \frac{r(h)}{H} = \frac{r(h)}{A-E}$$

(1.9) $$h = \frac{d(H)}{r} = \frac{d(A-E)}{r}$$

Where *d* is the radial displacement, *r* is the radial photo distance from the nadir image to the point of displacement (usually the top of the object), *h* is the height of the object or difference in elevation (E) the nadir image and the displaced point and *H* is the height above the base of the object (UCSB, 2011).

In the case of an oblique photo, the principal point (centre) of the image is no longer vertically above the object and therefore no reliable scale can be discerned. Thus, in order to convert what we see on the camera to a real-world quantities a translational technique between the two coordinate systems is employed (a.k.a. image unprojection). Using *Figure 1.3.2.1*, *(x, y, z)* represents the coordinate system of the object being surveyed (i.e. the glacier in the real-world) and *(x_c, y_c, z_c)* represents the coordinate system centred in the camera.

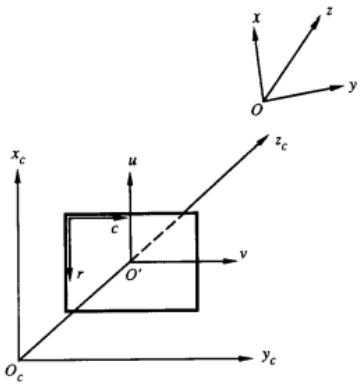

Figure 1.3.2.1. Diagram showing the conversion between the camera coordinate system to the real-world coordinate system.
Source: Weng *et al*, 1992

By assigning z_c to the optical axis and placing the (x_c,y_c) plane on the image sensor plane (as seen in Figure 10) – then the relationship between two coordinate systems is given by:

(1.20) $$\begin{pmatrix} x_c \\ y_c \\ z_c \end{pmatrix} = R \begin{pmatrix} x \\ y \\ z \end{pmatrix} + T$$

Where R = ($r_{i,j}$) is a 3x3 rotation matrix and T = (t_1, t_2, t_3) is a translation vector defining the camera position (Weng *et al.*, 1992). Alternatively, the rotation matrix, *R*, and translation vector, *T*) can also be defined in matrix form using homogenous coordinates (Ma *et al.*, 2001):

$$\lambda \mathbf{x} = APT_{wc}\mathbf{X}$$
$$\mathbf{x} = (u, v, 1)^T$$
$$A = \begin{bmatrix} fs_x & fs_\theta & o_x \\ 0 & fs_y & o_y \\ 0 & 0 & 1 \end{bmatrix}$$
$$P = \begin{bmatrix} 1 & 0 & 0 & 0 \\ 0 & 1 & 0 & 0 \\ 0 & 0 & 1 & 0 \end{bmatrix}$$
$$T_{wc} = \begin{bmatrix} R & T \\ 0 & 1 \end{bmatrix}$$
$$\mathbf{X} = \begin{bmatrix} X_0 \\ Y_0 \\ Z_0 \\ 1 \end{bmatrix}$$

(1.21)

Where λ is the depth or distance between the image centre and the real-world point, *A* is the intrinsic camera matrix containing information such as the focal length and scaling, *f* is the focal length, *P* is the projection matrix, T_{wc} relates the world coordinate system and the camera coordinate system (extrinsic camera matrix) and X are the real-world coordinates in homogenous coordinates.

The undistortion is applied to x = (u,v) after the projection and transformation from real-world to camera coordinates (Ma *et al,* 2001).

It is fundamentally very difficult to unproject pixel coordinates back to the real world for two reasons. Firstly, in general the depth into the image of the object that the pixel represents is generally unknown. Secondly, the equations to correct for distortion cannot be inverted analytically and a numerical scheme is required. To resolve the first problem, triangulation with an independent source of height/scale can be used (e.g. lake level record) and to resolve the second, iterative methods such as OpenCV's *solvepnp* function can be employed.

Also these mathematical technique presumes that the extrinsic camera paramters (i.e. the rotation matrix, $R = (r_{i,j})$ and translation vector, $T = (t_1, t_2, t_3)$) for the camera orientation and the world co-ordinate system are available. As a result, simply having these equations may be inadequate and would require the use of Ground-control Points (GCPs) in the scene to geocorrect or 'ground-truth' the oblique images effectively.

1.3.3. Digital Image Correlation (DIC) Techniques

The fundamental principal behind calculating the movement of features between images is Digital Image Correlation (DIC). Digital image correlation refers to the identification of pixel patterns across a certain domain within one image to an image of another time step for comparison. Historically, this technique's origins date back to the early 20th Century with some of the earliest works by Horough, G., (1919) who built a machine to 'correlate reconnaissance photography to observe changeable ground conditions' (Sutton *et al,* 2009). Today, DIC is used on a multitude of levels ranging from civilian, military to government applications. In more recent decades, DIC has become increasingly popular in

geographical/geological sciences particularly for surveying complex and stochastic interactions between the land, sea and air.

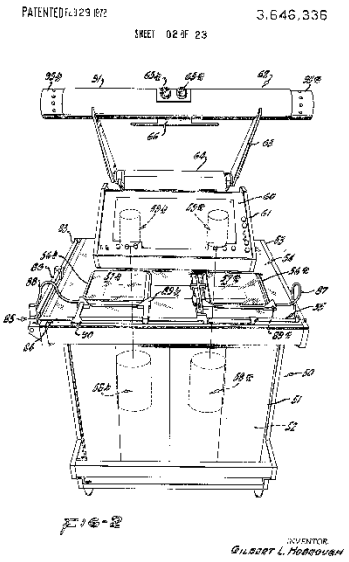

Figure 1.3.3. Shows patented schematic of a digital image correlation machine made in the early 20th century by inventor, Gilbert.L. Hobrough. *Source - https://www.google.ch/patents/US3646336*

For example, it has been used to observe the dynamics of river ice (Bourgault, D., 2006), river-channel morphology (Chandler *et al.*, 2014), volcanism (of Mount St. Helens in Diefenbach *et al.*, 2012) and estuarine geomorphology (Magd and Hillman, 2009).

In glaciology, DIC techniques have been employed primarily through satellite images (i.e. in LANDSAT, SAR, ASTER images) for observing glacier flows (e.g. in Evans, 2000 and Vernier *et al.*, 2011) and more recently by Joughin, I., *et al.*, (2010), Rignot, E., *et al*, (2011) and Fahnestock *et al.* (2015) for mapping flow of ice sheets in Antarctica and Greenland. Of noteworthy mention is the work of Ahn and Howat (2011), who developed a Multi-image/Multi-correlation (MIMC) '*RIFT'* algorithm specifically for feature tracking of glacial surfaces. The RIFT algorithm calculates a range of subsets of the image and then applies cross-correlation for each of those subsets across various permutations of image sets. According to Ahn and Howat (2011), this technique offers a much higher success rate as compared to single-image and single-chip correlation although it also faces similar challenges when coregistering or aligning features in different images, particularly when camera movement is prevalent.

In the case of this thesis, Digital Image Correlation techniques are applied to sets of oblique images to attain flow fields for 2013-2016 at the Tasman Glacier, Mt. Cook, New Zealand.

1.3.3.1. How image subsets are tracked through DIC?

Image correlation can only be applied to images that are non-repetitive, isotropic and presents a high-contrast pattern (Sutton *et al.*, 2009). In mechanical engineering, a speckle pattern is often applied to an object's surface to enhance its contrast. Glaciers with debris layers exhibit a good natural speckle pattern for co-image analysis.

Once images have been pre-processed, a subset is chosen of a defined subset size (i.e. a 5 x 5 pixel subset). Pixel patterns within the reference subset is then matched against another 5 x 5 subset found in the deformed image and given a score based on their exactness (also known as a 'similarity score'). A point (P or Q in Figure 3.3.8a) on the initial image is deemed as correlated when the subset of neighbouring pixels best matches a similarly-sized subset in the target image (Sutton *et al,* 2009).

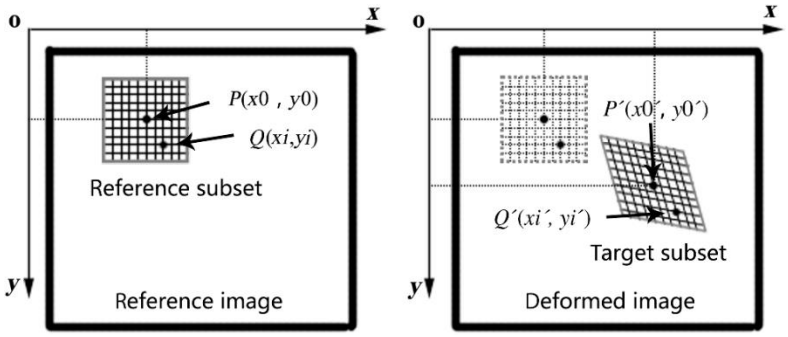

Figure 1.3.3.1. Digital Image Correlation (DIC) example. Shows a reference subset in the first image where points P and Q are identified. In the deformed image, corresponding locations of P and Q are used to extrapolate a target subset. *Image Source:* Liang *et al,* 2013

1.3.4. Why oblique photogrammetry?

Methodologically, many of the studies on both the Tasman Glacier and on glaciers in general have largely been based around remote sensing techniques (which have low temporal resolution) (Purdie *et al.,* 2011), climate analysis (Lorrey *et al.,* 2014) or field-based instruments such as gravity sensors, ground-penetrating radar or GPS (Hochstein, 1995; Quincey and Glasser, 2009; Kirkbride, 1995, 2010, 2013). The potential offered by the use of high temporal resolution oblique time-lapse photography may be the ideal data acquisition method for attaining further understanding of the ice and sub-glacial morphological processes which are occurring over a much shorter timescale, are spatially complex and often occurring in difficult terrains unsuitable for long-term habitation. This relatively novel technique has yet to be proven effective in resolving some of the above-mentioned gaps in our knowledge. However, were it successful, it would not only enhance our understanding, it would may inspire similar applications for glacier monitoring in the global inventory as well. To date authors such as Murray *et al.,* 2015; Messerli and Grinsted, 2015; Ahn and Box, 2010; Harrison *et al.,* 1986 and Flotron, 1973 have shown the immense datasets that can be attained from oblique terrestrial photogrammetry and their applicability in glaciology. Moreover, a technique such as this is non-selective and would even capture the geomorphic evolution of

hillslopes adjacent to glaciers and measure/predict the incidence of rock avalanches and other hazards which pose a direct threat to the human populace.

As opposed to conventional aerial imaging and photography, terrestrial oblique photogrammetry proposes a low-cost alternative with a significantly higher temporal resolution able of capturing images at every second, minute, hour or day. While there are restrictions in spatial breadth compared to satellite imagery (i.e. the LANDSAT and ASTER programs acquires spatial data for the entirety of the Tasman Glacier at a 30 m resolution), terrestrial photogrammetry can offer superior spatial resolution of up to sub-metre resolution which is comparable to high-resolution but expensive satellite imagery for a fraction of the cost.

In addition, satellite images can occasionally produce cloudy outputs and aerial flights are subject to weather and flight conditions whereas terrestrial photogrammetry allows a much higher frequency of image samples which can be used to navigate around poor-quality or cloudy imaging.

1.4. Thesis Objectives

Considering the urgency to better understand the dynamics of glaciers and their role to play in the sensitivity of the climate system, quantitative observations have to be increasingly more comprehensive on spatial and temporal levels. Oblique photogrammetry is therefore the optimal choice for this investigation. The following objectives creates a wider framework for this thesis and sets out the direction of my investigation.

(A) Can quantitative information on glacier terminus and dynamics be extracted from oblique photographs? Test and validate.
(B) What are the factors which control the style and magnitude of calving at the Tasman Glacier?
(C) What is the rate at which the Tasman Glacier is calving compared to other records in the past to attain a better understanding on what drives these calving processes?

CHAPTER TWO
Literature Review of the Study Site

2.0 Introduction

Haupapa/Tasman Glacier is the largest glacier in New Zealand (NZ) and is ~ 23km long (as of 2010) and 2km wide (at terminus) flowing from the main divide of the Southern Alps towards Tasman Lake (Dykes *et al.,* 2010; Kirkbride, 2010; Purdie, 1999; Hochstein, 1995). In the last century much research has focussed on estimating the mass balance and rates of retreat (Chinn, 1969; Anderton, 1975;Kirkbride, 1995; Hochstein, 1995), and in more recent years by researchers on calving process at the terminus (Röhl, 2006; Dykes, 2010; 2011), the effect of El Nino and regional climatic variations like the Southern Annular Mode (SAM) on the Tasman (Lorrey *et al.,* 2014; Purdie *et al.,* 2011; Chinn *et al.,* 2006) as well as studies on snow accumulation variations (Purdie *et al.,* 2011). Much like many other glaciers in the Southern Alps, Tasman has been retreating from its Little Ice Age (LIA) maximum extent since the period A.D. 1750-1890 (Chinn, 1995). During the 1910-1970, faster retreat from the LIA glacial extent occurred during a warm phase in the New Zealand climate (Chinn *et al.,* 2006). However in the last three decades, a period of retreat and advance fluctuations at many NZ glaciers took hold and has spurred some renewed interest in the response times of glaciers to climatic perturbations as well as research into the underlying process and feedbacks that drive such responses.

2.0.1 The role of glacial debris

The role debris plays in the ablation process is one key area of interest. Chinn (1995) showed that the rate of ablation varied spatially and is not homogenous across the entire glacial mass. Most notably, he identified the differences in ablation and melting processes at the terminus of the Tasman glacier where the ice sits under a layer of debris which serves to insulate or enhance ablation depending on its thickness. Kirkbride and Dugmore (2003) supported this observation and gave estimates that a debris cover of 15-30 mm would warm the underlying ice enough to enhance melting whereas any more than 30 mm would insulate the ice from the surface energy balance via albedo feedback, thereby slowing its melt rate (Østrem, 1959). Although the theory is solid, the complexity of estimating the thickness of the debris layer is great and remains largely unresolved – particularly when debris is capable of developing

within the glacier in the sub-strata or in the form of en-glacial debris bands (Pellicciotti *et al.*, 2015; Kirkbride and Deline, 2013).

2.0.2. Lake Surveys to date

Several lake-depth surveys (Hochstein, 1995; Watson, 1995; Röhl, 2005; Dykes *et al.*, 2011; Purdie *et al.*, 2015) have been conducted on the Tasman Lake using sonar and other tools. Although these studies provided insights into the depth of the glacier and the pro-glacial lake, many questions regarding whether lake depth serves as an important control on calving rates are still largely unresolved.

2.0.3. Gaps in the literature

It is also crucial to note that in all the literature reviewed, none of the methodologies provided a spatial and temporally sequence to observe ice dynamics considering that the majority of the research has been focussed on the long-term, inter-decadal or centennial response of the Tasman Glacier (Chinn, 1995; Kirkbride, 2010; Purdie, 2011; Lorrey, 2014; etc.) rather than the short-term, annual or monthly time scale where a lacustrine/upstream signal is likely to be found (i.e. in varying rainfall patterns that may speed up or slow down glacial movement or variations in lake level), with the exception seen in Horgan *et al*, 2015 and Redpath *et al.*, 2013.

Such short term glacial dynamism is perhaps best epitomised in recent years (1990-2007) when the Tasman glacier underwent some dramatic changes and receded a total of ~ 3.7 km. The 1990 terminus was replaced by the expanding pro-glacial lake which amounted to ~ 5.96 km^2 and at an approximate lake depth of 240m (Dykes, 2010; Quincey and Glasser, 2009; Purdie *et al.*, 2015), doubling in size from 2000-2008. With the lake's size increasing, it is likely to accelerate calving (Dykes, 2010) however the mechanisms that drive calving events are complex and still not fully understood.

2.0.4. Calving Processes

The ongoing debate between whether calving is a response to upstream and local processes ('slave') or if it embodies the so-called 'master' of glacial dynamics is at large, unresolved (Benn *et al.*, 2007). Many factors including the rate of down wasting, sub-glacial water flux, fracture dynamics and propagation, and even morpho-limnological conditions such as the height of the terminal ice cliff above buoyancy can have an important role to play in controlling the calving rate (Haresign, 2004). An example of the dynamic impacts of lake

waters on ice is seen in Röhl (2006) where the average calving rate from thermo-erosional notch formation was estimated to be 34 m a^{-1}. This process occurs when lake levels remain relatively stable for months, particularly during winter when the lake freezes over, and results in a horizontal cut of the ice at the waterline and thus creating high strains that result in additional calving. Yet the rate of notch formation is not homogenous across and between glacier termini, with the author emphasising the complexities that control this behaviour such as debris supply, lake level, lake temperature and cliff shape (Röhl, 2006).

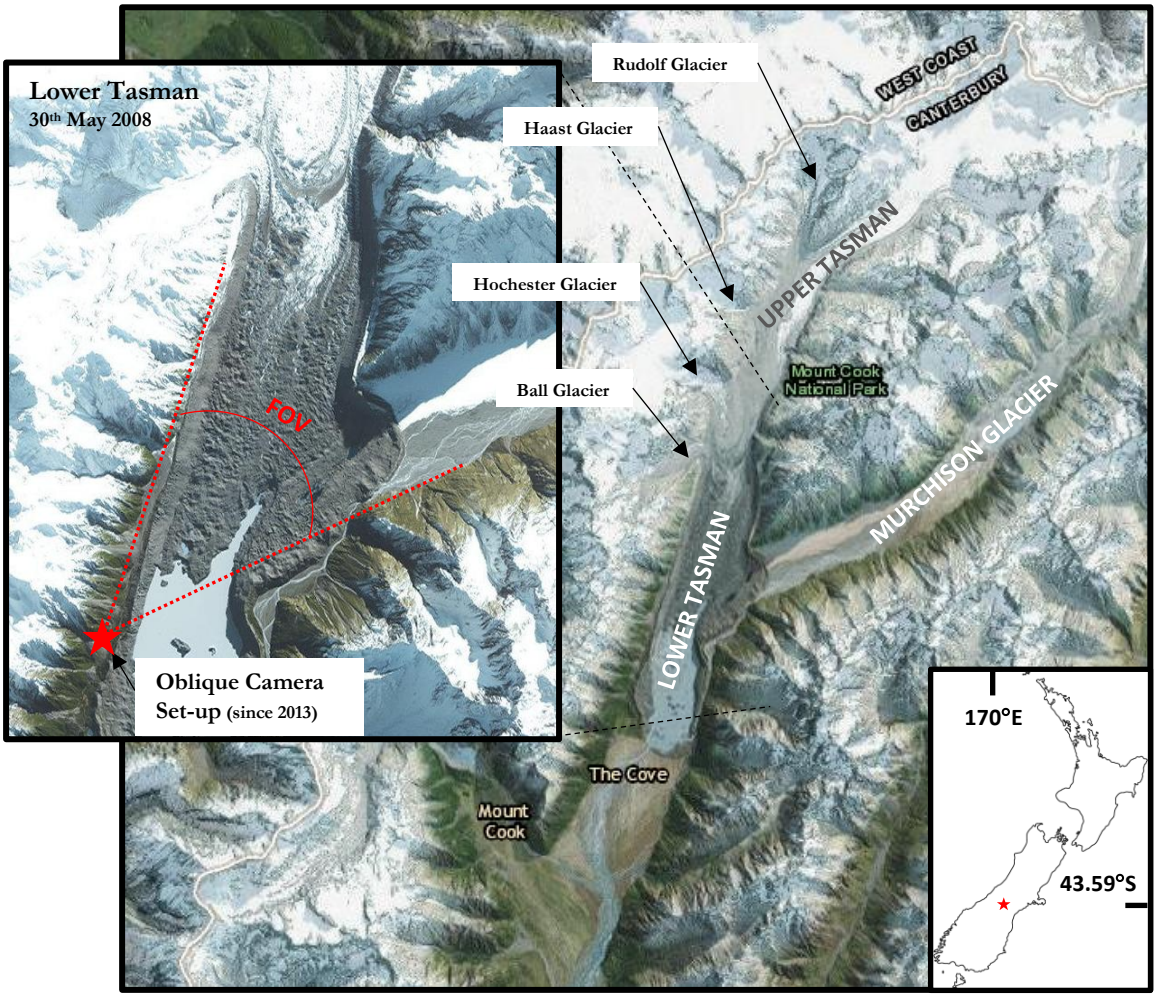

Figure 2.0.1. Shows the Tasman Glacier fed by the Ball, Hochester, Haast and Rudolf Glaciers in the upper regions. Towards the terminus, the meltwaters from the Murchison Glacier feed into the Tasman Lake. *Source:* USGS Landsat Look Viewer's "World-Imagery" base map with highest resolution of 0.3m. Original base-map source: ESRI and others from *http://services.arcgisonline.com/arcgis/rest/services/World_Imagery/Mapserver*

Furthermore, the impacts of accelerated calving and increased destabilisation on surrounding morphologies such as on neighbouring moraines or buttressed mountain sides presents many interesting and unanswered questions. The stability of such slopes and the possible threat of glacially-driven rock avalanches/debris slips pose concerning safety threats to tourists and the

neighbouring settlements such as the Mt. Cook village and tourists commuting on the lake itself. None of these topics have yet to be investigated but are certainly warranted in the near future although the hazards posed by glaciers have been documented around the world (Evans and Clague, 1994; Haeberli, 2013 and Iribarren Anacona *et al.*, 2015).

In Chapter Two, I summarise the key findings in the literature regarding the Tasman Glacier's evolution in the 20th and 21st century and identify some gaps in our current understanding of the Tasman Glacier. *2.1* details the changing geometry of the Tasman Glacier as it thins and retreats. *2.2* outlines the observed melting and downwasting trends. *2.3* is on the contemporary changes to the Tasman Lake and the recaps the varying calving mechanisms that may be occurring at the terminus. This is followed by a review of the relevant measurements of the Tasman Glacier which include rates of terminus retreat (U_r) in *2.4*, ice velocity (U_i) in *2.5*, and calving rates (U_c) in *2.6.* In *2.7,* I summarise how the ice dynamics fundamentally fit in within the climate system and discuss observations made in this topic. Finally in *2.8,* a refined set of scientific questions are presented which serve as a key points of enquiry for the thesis.

2.1. Geometry of the Tasman Glacier

The Tasman Glacier flows between the main divide and the Malte Brun Range, collecting ice from a number of tributaries until contacting the Tasman Lake at ~ 715 m (NZ Topo Maps, 2016). The lower glacier is impounded by post-LGM outwash gravels and is situated beside many LIA and older late Holocene glacial moraines (Winkler, 2004; Schaefer *et al*, 2009).

In the last two centuries, historical records of the Tasman's shape, extent and geometry have been well documented from disparate sources. Some of the earliest work were made by von Haast who surveyed and photographed the glacier in 1862 and 1869 respectively (Kirkbride and Warren, 1999). Later work from Brodrick in 1891 (Kirkbride and Warren, 1999) developed the first record of the Tasman's lengthwise concavity using surface elevation measurements at 2 and 10 km from the terminus. Following Brodrick, Broadbent (1973) and Anderton (1975) determined ice thicknesses at the same 2 and 10 km transects to extrapolate a profile of the Tasman Glacier as well as determined thinning rates since 1890. Furthermore, Hochstein *et al.,* (1995) and Kirkbride and Warren, (1999) advanced on our understanding making similar surveys by the end of the last century. In 1986, the longitudinal surface shape of the glacier had predominantly changed from one that was previously convex (AD 1890-

1986) to a concave profile (Kirkbride and Warren, 1995). Additionally, the longitudinal shape had also become steeper over the previous century, with the gradient increasing from 3.3 x 10^{-2} to 4.0 x 10^{-2} (see Figure 2.1.1) from AD 1890 to 1986.

Following the 1986 surveys by Kirkbride (1995a), the Tasman underwent some dramatic changes which resulted rapid retreat of the terminus and the creation of a pro-glacial lake now known as the Tasman Lake (Purdie and Fitzharris, 1999). In coincidence with the retreat, glacial surface surveys by Röhl (2005) revealed a dramatic steepening of the glacial profile and may explain the flow velocity increases observed by Quincey and Glasser (2006) after January 2006. As of 2001 to 2003, the terminus ice cliff height was measured as approximately 10-15 m high (mean) and maximum 35 m high (Röhl, 2005).

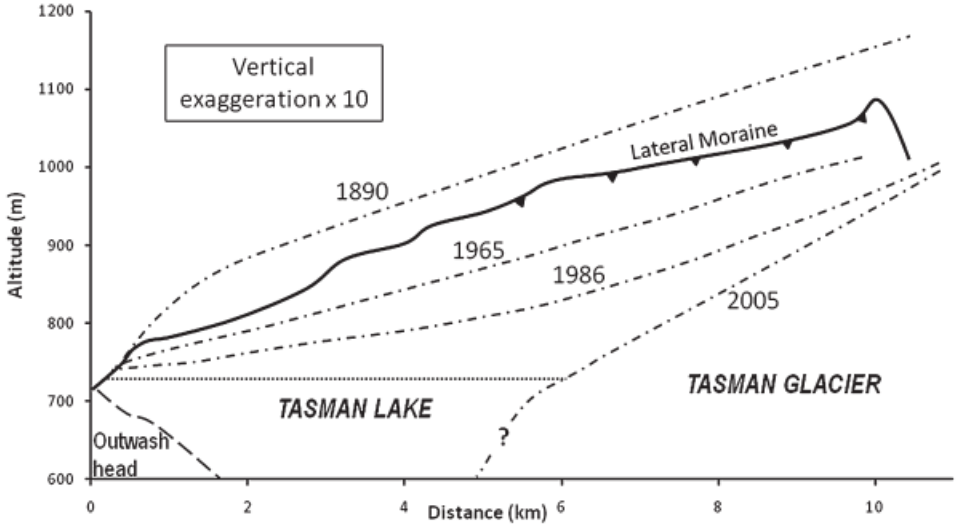

Figure 2.1.1. Presents historical glacier profile changes since 1890. The most recent measurement by Röhl (2005), shows a dramatic retreat of the terminus from ~29km to ~23km long and a steepening of its longitudinal profile possibly accelerating ice flow. *Source:* Kirkbride and Warren (1999) original image adapted by Dykes *et al.,* 2010

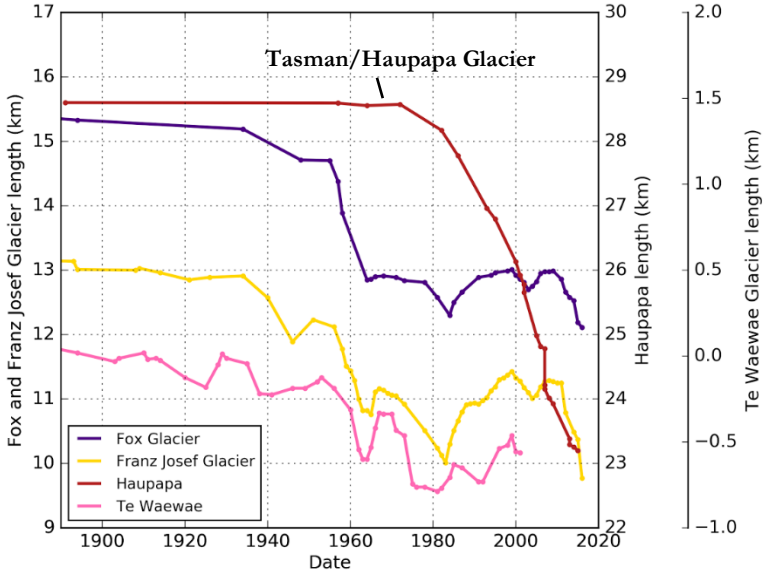

Figure 2.1.2. Glacier length change at Fox, Franz Josef, Tasman/Haupapa and Stocking/Te Waewae glaciers. . Data for Fox and Franz Josef Glaciers are from (Purdie et al., 2014); for Tasman Glacier from (Dykes *et al.*, (2010) references therein, and more recent satellite imagery; for Stocking/Te Waewae Glacier are from Burrows (2005). Note that the Te Waewae Glacier length is on a different scale (right) compared to the other glaciers. *Source:* Dr. Brian Anderson

Despite its slower response time, the Haupapa/Tasman Glacier has retreated consistently in the last three decades, losing a length of ~ 5 km (since mid-1980s) compared to ~ 3 km at Fox Glacier and ~ 3.2 km at Franz Josef (both since mid-1940s)(*see Figure 2.2)*.

2.2. Melting and down-wasting (thinning) of the Tasman Glacier

The glacier has been decreasing in mass for the majority of the 20th century through thinning, rather than terminus retreat (Skinner, 1964). A vertical loss of 82 m of ice at Ball Hut was documented for the first half of the last century which equated to a thinning rate of 0.3 – 1.2 m a^{-1} (Hochstein *et al.*, 1995). Following decades of downwasting, a proglacial lake formed in the 1980s (Kirkbride, 1993; Hochstein *et al.*, 1995). Following this, the Tasman Glacier began to be dominated by a calving regime at the lake interface. According to Purdie and Fitzharris (1999), the calving process at the lower Tasman terminus region accounted for 73% of the total ice loss with the remaining ~ 27% from melt occurring beneath the debris cover and from supraglacial loss. A total of 21 million m^3 a^{-1} of water was estimated to be lost in the lowest 4 km^2 of the glacier. However if considering ice loss from the entire ablation zone (~ 11-12 km upstream from LIA extent), calving only accounts for 4% of the total, with 80% of ice loss from the melting of exposed ice (Purdie and Fitzharris, 1999).
The rate of melting also varied with space and time. A maximum ablation rate was measured at 117 mm day^{-1} or roughly 17 m a^{-1} on exposed ice during summer at Ball Hut by Kirkbride (1989). In contrast, ice melt occurring beneath the debris covered regions during the 1980s was only 0.6 – 1.3 m a^{-1}. Surface lowering in the 21st century has however increased almost four fold in the debris covered regions.

Quincey and Glasser (2009), estimated down-wasting rates were as high as 4.2 ± 1.4 m a^{-1} in areas adjacent to the lateral moraine edges for the period 1986-2007. Nonetheless the average thinning rate for the same period across the ablation zone was 1.9 ± 1.4 m a^{-1} and conforms to the estimated rate in the 20th century by Hochstein *et al,* 1995. In summary, the majority of the 20th century saw the Tasman glacier thinning at an estimated rate of 0.3 to 1.2 m a^{-1} (Hochstein *et al.*, 1995) with minor changes to the terminus position. In the 1990s, the formation of a 2.5 km^2 lake at the terminus instigated a gradual decoupling of the terminus from climatic forcing (Chinn, 1996; Purdie and Fitzharris, 1999; Dykes *et al.*, 2010). However, in terms of total volumetric ice loss, ablation occurring over exposed ice still

accounts for 108 million m^3 a^{-1} (as approximated from Ball Hut to the terminus or the lower 10 km of the glacier), roughly 5 times that of water loss in the lower 4 km^2 of the Tasman (Purdie and Fitzharris, 1999). This suggests that although calving is now the dominant ice loss regime at the terminus (~ 75% accountable), across the entire ablation zone the melting regime is remains the principal cause of net ice loss (~ 80%). However it is likely to see this ratio between calving and melting losses increase as the lake expands at a rate of 0.34 km^2 a^{-1} as measured for years 2000 to 2008 (Dykes *et al*, 2010) and through the processes of thermo-erosional notch formation (Röhl, 2006; Kerr and Owens, 2008).

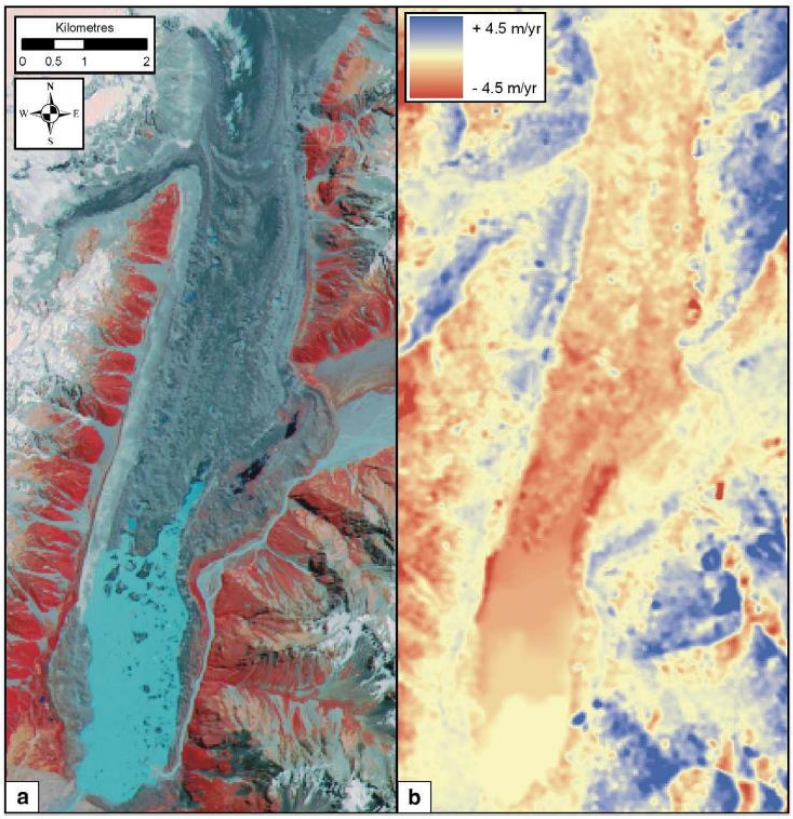

Figure 2.2.1. [A] Shows ASTER image in 2007 [B] Rate of surface ablation of the Tasman Glacier calculated by subtracting two DEMs – (1) LINZ data (1986) (2) ASTER Data (2007).While the elevation changes are clearly not correct on the steep slopes surrounding the glacier due to the misalignment of the DEMs, the thinning rates on the glacier are probably correct. *Source:* Quincey and Glasser (2009)

2.2.1. Debris cover and rates of ablation

Of particular note is the role debris plays in affecting the overall mass balance on the Tasman Glacier. Already mentioned was the role debris played in affecting the rates of ablation and how they varied spatially across the glacier. In areas of exposed ice, the melt rate was measured to be at least 13-28 x that which was occurring beneath

debris cover (Kirkbride, 1989). As such, the lower 4 km^2 of the Tasman which is predominantly debris covered will have a dramatic impact on the annual rate of retreat and net ice budget (Dykes *et al.,* 2010). However the impact of debris is not homogenous spatially and varies with vertical depth. Debris accelerates melt when its thickness is below 3 cm creating a thin blanket over the ice and increases total heat flux. Any depth above 3 cm will act in the opposite direction and instead insulate the ice, up to a depth of 2 m (Mattson *et al.,* 1993). This critical thickness however, does vary from glacier to glacier. For example, an experimental study by Reznichenko *et al.,* (2010), found a critical thickness of 5 cm. Likewise, in another study of another Himalayan glacier by Kayastha *et al.,* (2000), the critical thickness was also found to be 5 cm with the maximum enhancement to ablation occurring at 3 cm. Therefore an inverse relationship between ablation rates of debris-covered ice and the depth of debris is evident (Pratap *et al.,* 2015) however the exact critical threshold for our study site is unknown and will depend on the debris grain size and composition.

For the Tasman Glacier, an average debris thickness was estimated to range from 0 to 3 m thick (Kirkbride, 1989). Although data on spatial distributions of melt occurring beneath the debris are currently unavailable, Purdie and Fitzharris (1999) deduced that debris on the Tasman Glacier is likely to serve as an insulator rather than enhance ablation as calculated in their study which assumed the average debris depth was 1.1 m across the lower 4 km^2 of the Tasman. Overall, my assessment of the literature shows that debris plays an important role in the glacial dynamics and is certainly a primary cause for lower melt rates occurring in the lower Tasman as compared to upstream where ice is bare. This corroborates with recent observations of calving processes becoming the dominant regime in the debris-clad terminus region (Dykes *et al.,* 2010) superseding the rate of melting.

2.3. Contemporary lake formation and calving

The formation of the pro-glacial lake in the 1990s and the continued expansion of the lake in the 21st century is a driver of iceberg calving through thermo-erosional notch formation and thermal undercutting. Observations from Dykes *et al.,* (2010) indicated that the lake expanded at a rate of 0.34 $km^2\ a^{-1}$ for the years 2000 to 2008. In May 2008, total surface area of the lake was 5.96 km^2 and the maximum lake depth had risen to ~ 240m. Since 1995, the

lake volume has doubled in size to ~ 510 x 10^6 m^3 in 2008 (Dykes *et al.*, 2010).
Of particular note is the method by which the lacustrine environment interacts with the terminus ice. Röhl (2006) argued that when the waterline remains unchanged for many months (i.e. suggested to occur during winter when the lake freezes over), it enhances ice loss by creating horizontal cuts in the ice cliff. These cuts, known as thermo-erosional notches, are responsible for increased shear and tensile stresses which can result in mechanical failures in the form of calving (Röhl, 2006). Notch formation rates were estimated for the Tasman ice cliff at 10 to 30 cm d^{-1} with a maximum of 65 cm d^{-1} and an annual average calving rate approximated to be 34 m a^{-1} during 2001 to 2003. If compared to the annual mean terminus retreat rates (U_r) of 54 m a^{-1} for 2000 to 2006 (Dykes *et al.*, 2010), it would suggest that thermo-erosional notch formation is the primary driver of calving. Feedback loops may also persist as increased calving results in an expansion of the lake area/depth and may accelerate or decelerate notch development (and other forms of iceberg calving such as buoyancy-driven). Nonetheless, the rate of notch formation is highly complex and is influenced by other factors such as debris, variations in lake height and cliff shape (Röhl, 2006). As such, meaningful predictions of these glacio-limnological interactions will require further spatial and temporal understanding of the ice velocity and glacier geometry as well as lake parameters such as temperature, lake level variation and ice cliff shape.

2.3.1. Buoyancy-driven Calving

Buoyancy-driven calving is defined by calving occurring as a result of buoyant forces that hinge around pre-existing weaknesses in the glacier ice. These weakness can arise from basal crevasses which allow for buoyant forces to exceed the mechanical strength of the glacier to hold it below its critical flotation height thereby resulting in calving. In some cases, these crevasses can also propagate the full ice thickness of the ice (i.e. joining up with surface crevasses) and simply result in detachment. A critical threshold whereby a glacier can no longer maintain in its grounded state (Van der Veen, 2002) and where basal shear stress approaches zero is defined by, h_f, or the flotation thickness of the glacier.

$$h_f = \frac{\rho_w}{\rho_i} h_w \qquad (2.1)$$

where ρ_w is the density of water (1000 kg m^{-3}), ρ_i is the density of the glacier ice (917 kg m^{-3})(Shumskiy, 1959) and h_w is height of the waterbody.

A simplification of the flotation thickness can therefore be written as:

$$h_f = 1.09 h_w \qquad (2.2)$$

This implies that as the glacier is pushed into deeper water or if the lake depth increases, the critical point where flotation is likely to occur also recedes back (i.e. if h_w increase, h_f also increases, which means the corresponding terminus position for flotation equilibrium will be further back than when $\triangle h_f = 0$) (Van der Veen, 2010).

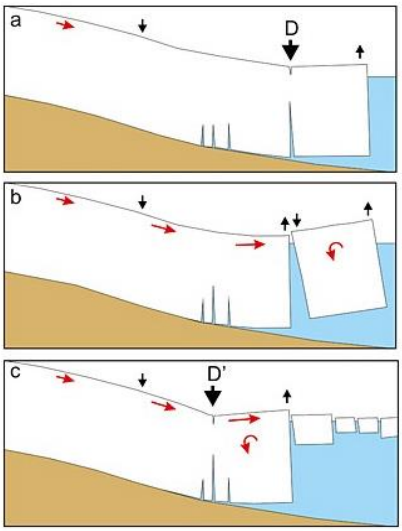

Figure 2.3.1. Shows a qualitative model for the evolution of buoyancy-driven calving. **D** demarks the flexion zone. (a) Initially a basal crevasse causes a flexure zone in the glacier. This results in the greatest moment occurring at the terminus. (b) Calving occurs at the initial flexure zone. (c) a new flexure zone is created as the glacier continues to flow into the lake. *Source:* Murray *et al.,* 2015

Of the literature reviewed, no study provided empirical observations of buoyancy-driven calving occurring at the Tasman Glacier. One study did attribute changes observed at the terminus in 2006-2008 whereby the growth of supraglacial ponds and lake depth was surmised to have influenced the stress regime at the terminus and thereby resulted in the observed accelerations in terminus retreat (Dykes *et al.,* 2010). In this paper, the authors argued that a relatively constant ice cliff height of 10-15 m coupled with increasing lake depth (c. 200 m) in 2006-2008 led to increased torque at the terminus and contributed to its rapid disintegration over this period. Retreat rates for 2007-2008 were ~ 144 m a^{-1} as compared to ~ 54 m a^{-1} in the five years prior (Dykes *et al.,* 2010).

Buoyant flexure driven by basal crevassing has however been observed in other

calving glaciers around the world (Boyce *et al.*, 2007; James *et al.*, 2014; Murray *et al.*, 2015; Wagner *et al.*, 2016). This recent evidence suggests that this mechanism may be more important than previously thought and could be a crucial 1st order control on calving.

2.3.2. Other forms of calving

Other forms of iceberg calving include (1) the spalling of thin lamallae of ice from the subaerial ice cliff resulting from crevices and fissures at the immediate vicinity of the terminus (Warren and Kirkbride, 1997) (2) the collapse of subaerial seracs (or columnar blocks of ice) from the ice cliff often due to cuts at the waterline (Röhl, 2006) (3) subaqueous calving of submarine ice and (4) the detachment of tabular bergs typically where transverse crevasses have extended through the ice thickness commonly seen in ice sheets in Antarctica and Greenland (Bassis and Walker, 2011; Lazzara *et al.*, 1999; Fricker *et al.*, 2002). Based on Benn *et al.*, (2007)'s classification of 1st order, 2nd order and 3rd order processes influencing calving, (1), (2) and (4) fall under 2nd order processes and (3) falls under 3rd order processes, the latter of which typically occurs at slower timescales compared to the former.

These are summarised in *Figure 2.3.2.*

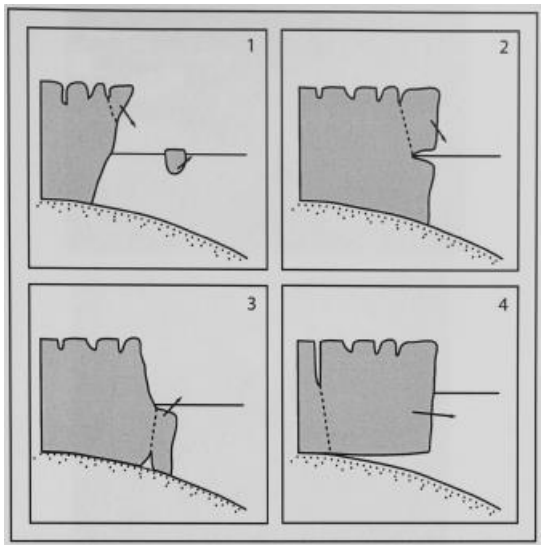

Figure 2.3.2. Shows four categories of calving at the terminus. (1) Calving of lamallae of ice (2) Collapse of seracs from cuts at the waterline (3) Subaqueous calving (4) Detachment of ice arising from deep crevasses that approach terminus ice thickness. *Source:* Haresign, 2004 adapted from Benn and Evans, 1998

2.4. Historic Terminus Retreat Rates (U_r)

Prior to the 1990s, the Tasman Glacier primarily experienced thinning and a gradual steepening of its longitudinal profile. Concurrent to the lake's formation, the terminus began retreating for the first time since 1980 and had receded ~ 3.5 km by 2007 compared to the 1986 terminus position (Quincey and Glasser, 2009). Dykes *et al.,* (2010) using satellite imagery similarly reported a retreat of ~ 3.7 km during their study period for 2000 to 2008. Using Quincey and Glasser's (2009) terminus measurements, the average U_r was ~ 166 m a^{-1} for years 1987 to 2007. In comparison, the higher temporal resolution study from Dykes *et al.,* (2010) showed that retreat rates varied with time especially during years 2000 to 2006 where U_r = ~ 54 m a^{-1} which then accelerated to a mean of ~ 144 m a^{-1} for 2007 to 2008. In summary, Dykes *et al.,* (2010) noted that sudden retreats in terminus positions were being driven by large buoyancy-calving events and indicates the presence of other controlling mechanisms aside from thermo-erosional notch development. Further investigation into this dynamic behaviour is therefore warranted.

The overall length of the Tasman/Haupapa Glacier is now just over 23 km as compared to 1980 levels (~ 28.6 km) (*see Figure 2.2)*. Continued retreat may be expected with a warmer climate but a projected rate is not known.

2.5. Surface ice velocity (U_i)

Surface ice velocities can vary with time and space. The flow of ice can slow when compressed against topographic features beneath the ice but it can also speed up when the topography steepens (Paterson, 1994). Consequently, this dynamic behaviour of flowing ice can impact on the rate of ice loss at the terminus, particularly for marine and lacustrine terminating glaciers (Howat *et al.*, 2005; 2010; Joughin *et al.*, 2008).
Historical ice velocity of the Tasman dates back to Brodrick (1894) who first reported a surface velocity of 167 m a^{-1} at Ball Hut (~ 10 km upstream from terminus). Following this, no observations were made for eight decades till Anderton (1975)'s work who observed a deceleration to 88 m a^{-1} also in the same location.

Kirkbride (1995a) derived ice velocities using photogrammetry tracking thermo-karst sink holes in the lower 2.5 km^2 of the glacier and provided further evidence of the Tasman slowing down up until the 90s prior to formation of the pro-glacial lake i.e. a deceleration from 1957 (~ 13 m a^{-1}) to 1986 (~ 8 m a^{-1}).

A reversal of this long-term (>100 year) slowing trend occurred at the onset of ice-lake dynamics in the 1990s. Field observations using six markers by Kirkbride (1995b) revealed an annual velocity of 11 to 24 m a^{-1} at the terminus; which was a ~ 4 – 8 fold increase from the 3.3 m a^{-1} measured in 1986 at roughly the same location (Kirkbride and Warren, 1999). The authors surmised that the acceleration from 1986 to 1995 had resulted from ice-front dynamics (i.e. the lake formation) and is a precursor to faster calving rates at the terminus in the long run. Without this ice acceleration, calving would only incur from waterline melting as quantified in following years by Röhl (2005) to attribute roughly 34 m a^{-1} to calving (Kirkbride and Warren, 1997).

Measurements of ice velocity on the lower tongue of Tasman Glacier. By 1995, the terminus had retreated to the location of the former '2.0-km transect'

Year	Distance above terminus (km)	Measurement interval (days)	Maximum velocity (m yr^{-1})	Reference
1890	7.75	32	103	Brodrick (1891)
1890	10.0	32	167	Brodrick (1891)
1971–1972	10.6	229	88	Anderton (1975)
1972–1973	10.0	407	61	Anderton (1975)
1986	2.07	210	3.3	Kirkbride (1995a)
1986	10.0	211	98	Kirkbride (1995a)
1995	2.0	16	24	Kirkbride and Warren (1999)

Table 2.5.1. Shows a table summarising the historical (20th century) ice velocities up to 1995 from Kirkbride and Warren (1999). *Source:* Kirkbride and Warren, 1999

In more recent years, Röhl (2006) calculated ice velocities at two regions of the terminus, the main-ice cliff (MIC) and the slower eastern embayment ice cliff (EEIC). Respectively these velocities were 2.5 m a^{-1} and 8.5 m a^{-1}. This corroborated with Quincey and Glasser (2009) which showed an almost linear velocity gradient from the Hochstetter icefall down to the calving face into a region of 0 – 20 m a^{-1} for the study period of 2002 to 2007. In this same study, the highest velocities were 200 m a^{-1} in the upper Tasman catchment and 150 m a^{-1} at the base of the Hochester icefall (Quincey and Glasser, 2009). Although a spatial pattern in ice flow was evidenced (see Figure 2.5.1.), one of the main criticism of their work was that it did not capture any temporal variability (annual nor seasonal) owing to their limited dataset which only used ASTER images from the 2002 to 2003 period to be compared it to the 2006 to 2007 period (Redpath *et al.*, 2013).

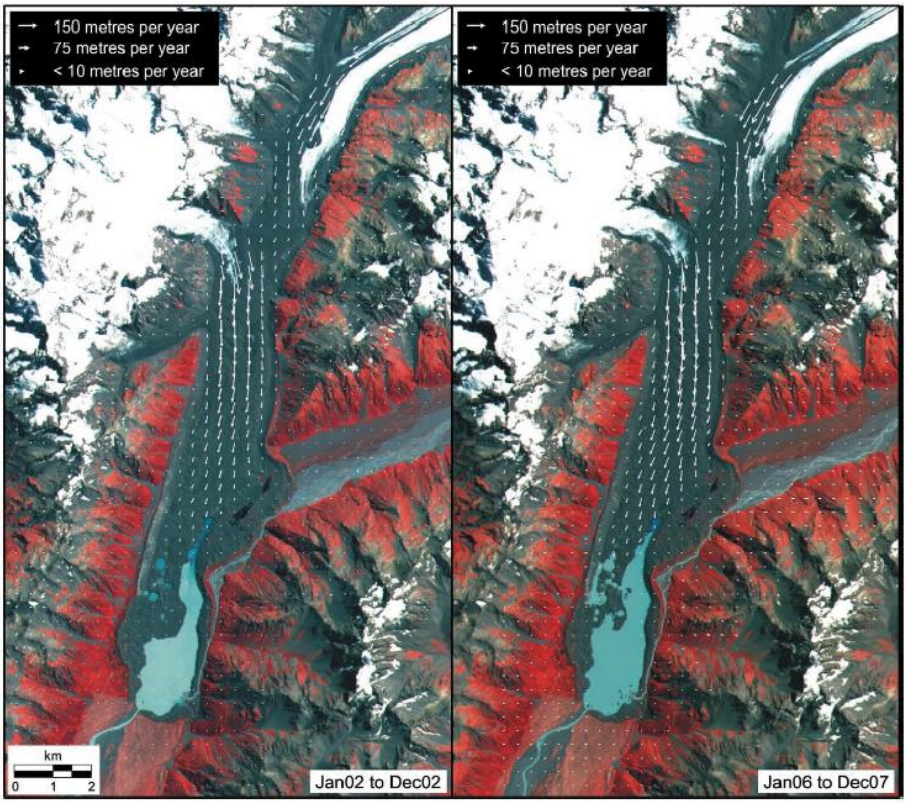

Figure 2.5.1. Glacier velocity fields (2002 – 2007) calculated using COSI-Corr plugin to ENVI on ASTER (Band 3N) imagery and orthorectified using Ground-Control Points (GCPs). The error related to this velocity field quantification was ~ 15 m. No temporal behaviour was concluded due to limitations in the study. *Source:* Quincey and Glasser, 2009

As such, Redpath *et al.*, (2013) also created flow fields of the Tasman for the periods 2009 to 2010 and 2010 to 2011 using Digital Image Correlation (DIC) orthorectified by matching 10-16 ground control point (GCP) markers across the four (ten-to-one) resampled ASTER images (following resampling methods in Scherler *et al.*, 2008). A grid spacing of 150 m was created for the DIC component and a search window size (i.e. subset size) of 600 x 600 pixels was allocated for the correlation (Redpath *et al.*, 2013). This allowed for movements between the annually-spaced satellite image pairs of 450 m in x and y directions.

In summary, their data presented similar flow-field structure echoed by earlier works of Kääb (2002) and Quincey and Glasser (2009) showing a velocity disconnect between the upper and lower Tasman (see Figure 2.5.2.). Ice flow at the base of the Hochstetter Icefall peaked at 300 m a^{-1} with average 150 m a^{-1} decreasing steadily to below 50 m a^{-1} at the terminus (Redpath *et al*, 2013); with relative uncertainties of ~ 34 %.

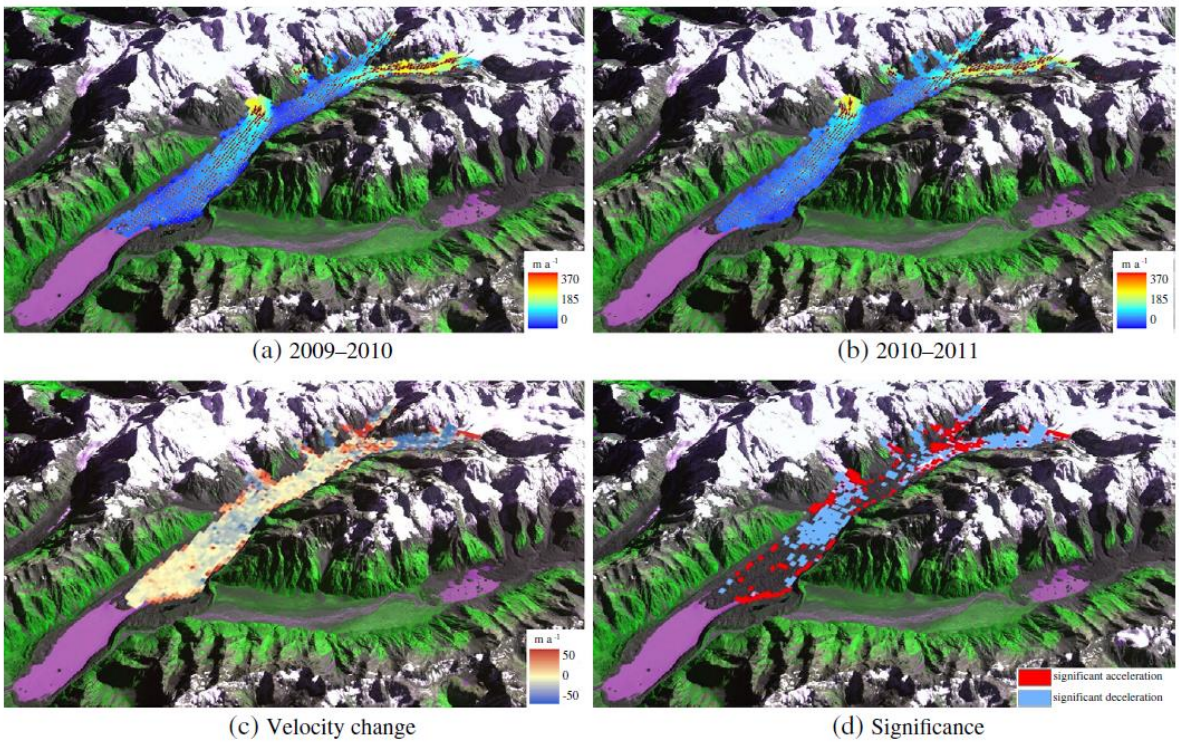

Figure 2.5.2. [A] Glacier velocity fields (2009-2011) [B] Glacier velocity fields (2010-2011) [C] Velocity changes [D] Significance of the change. **N.B.** Two sources of ice flow from the Hochstetter Icefall and further upstream flowing from the Tasman accumulation zone illustrate the spatial dynamism of the Tasman Glacier. *Source:* Redpath *et al.,* 2013

Of particular note was the temporal variability illustrated in *(c) Velocity change*, whereby a accelerations/decelerations of ice were observed from the flow-field below the Hochstetter Icefall and the upper Tasman region of ± 50 m a^{-2} between the two years. The authors also distinguished no apparent ice velocity changes in the terminus region and would suggest that only a more comprehensive temporal (e.g. a multi-year, weekly resolution) study could reveal dynamics on this spatial level.

One such study, conducted by Horgan *et al,* (2015) from February 2013 to November 2014 using three GPS stations situated on the Tasman debris surface aptly revealed an example of how velocity varied quite spontaneously with time. A strikingly large acceleration of up to 36 times the background speed was observed to coincide with periods of high precipitation (> 20 mm hr^{-1}) when horizontal and vertical displacements at the GPS stations were calculated over 3-hour intervals (Horgan *et al.*, 2015). This result proposes that the terminus region is susceptible to velocity changes occurring over weekly or seasonal timescales and can contribute to 11-14% of the annual displacement as concluded by the authors.

However no study of the Tasman to date has provided a high spatial and temporal resolution velocity field thus far owing to two main reasons (1) studies using satellite imagery (i.e. ASTER, LANDSAT) are limited temporally due to limitations caused by cloud cover, frequency of images captured or chosen and lack of ground-control points (i.e. Kääb, 2002; Quincey and Glasser, 2009; Redpath *et al*, 2013) (2) studies using point-sources may be temporally complete but lack the spatial understanding to fully quantify dynamics occurring across the 3-dimensional entity that is the Tasman glacier (i.e. Brodick, 1894; Anderton, 1975; Kirkbride; 1995; Horgan *et al.*, 2015).

It is therefore one of the aims of this thesis to make velocity field observations with a fine temporal resolution across only the terminus region using terrestrial photogrammetry. Future studies of the Tasman can adopt a similar approach (detailed in *Chapter 3: Methodology*) at sections in overlapping fields-of-view of the initial setup; and incrementally spaced upstream, to be assimilated in a spatial and temporally-complete map of ice-flow dynamics occurring across the entire 23 km length of the glacier. Although more labour intensive, this approach will be significantly cheaper than high-frequency (daily/weekly) and high resolution (< 2 m) satellite or aerial imaging.

2.6. Calving Rates (U_c)

The annual calving rate of any glacier is important because it is indicative of the net ice loss crucial to global sea-level rise projections (Luckman *et al.*, 2015) and can be used as a standard for comparing with other glaciers around the world. Although calving mechanisms are comprised of both sub-aerial calving processes such as thermo-erosional notch development and submarine melt and calving, the calving rate (U_c) can usually be estimated from mass continuity equations without quantification of these mentioned contributions (Paterson, 1994; Motyka *et al*, 2002; Amundson and Truffer, 2010).

Following from Benn *et al.* (2007), Dykes *et al.* (2010) estimated the calving rate using the ice velocity at the terminus (U_i) and the observed retreat rates for 2000 to 2008 ($\frac{\partial L}{\partial t}$).

$$U_c = U_i - \frac{\partial L}{\partial t}. \qquad (2.3)$$

Their results revealed similar disparities to retreat rates between the 2002 to 2005 and 2006 to 2008 time periods where the full-width calving rate (U_c) ranged from 32 m a^{-1} to 501 m a^{-1} across the entire study area (Dykes *et al.*, 2010). Constrained study of regions situated at the terminus also revealed similar temporal patterns with the Main Ice Cliff (MIC) averaging 78 m a^{-1} in 2002 to 2005 enhanced to 227 m a^{-1} in 2006 to 2008. However, the Eastern Embayment Ice Cliff (EEIC) saw significantly less acceleration in the calving rate with U_c averaging 24 m a^{-1} in 2002 to 2005 and only 30 m a^{-1} in 2006 to 2008. This may suggest that the terminus is divided by two separate calving regimes. These results suggests that the EEIC may only be subject to melting at the waterline and basal processes as the lake contact had retreated to the mouth of the Murchison valley even in 2000 whereas the MIC is subject to all of the above as well as large buoyancy driven calving events due to its 'protrusion' into the lake and the associated stresses caused by water depth increase to 240 m (Dykes *et al.*, 2010) responsible for the observed retreat rates and elevation in calving rates elapsing 2002 to 2008.

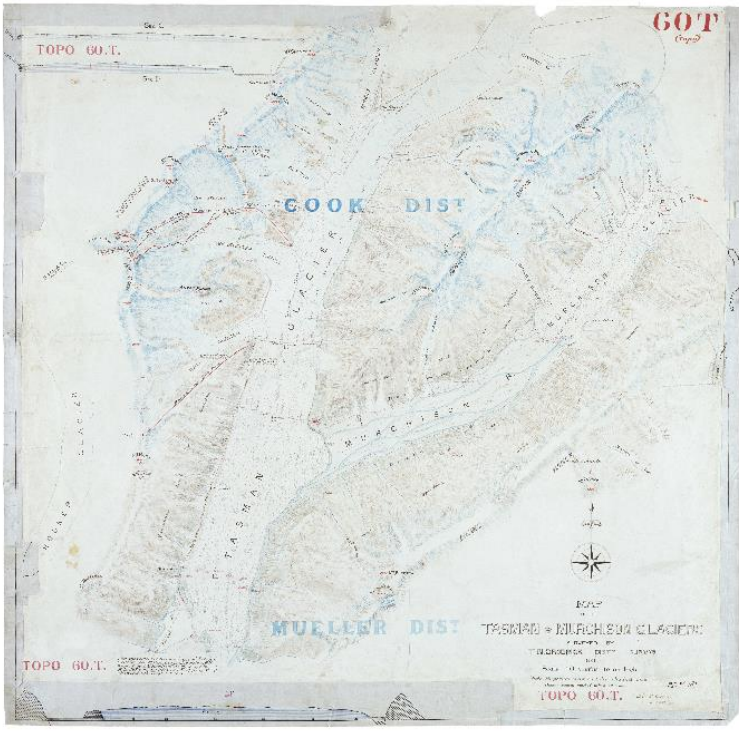

Figure 2.6.1. Shows Brodrick's (1891) original map of the Haupapa/Tasman Glacier. *Source:* Brodrick, 1891

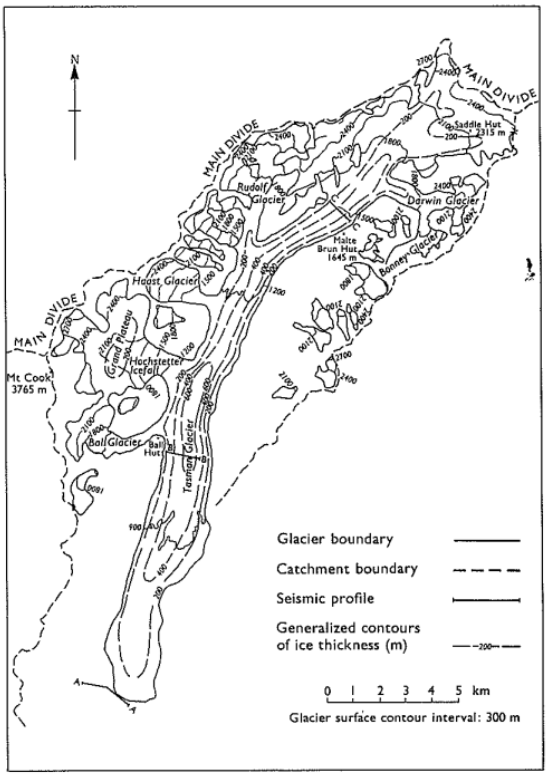

FIG. 3 — The Tasman Glacier system, showing generalized contours of ice thickness.

Figure 2.6.2. Generalised contours of Tasman Glacier bed elevation from seismic surveys. *Source:* Anderton, 1975

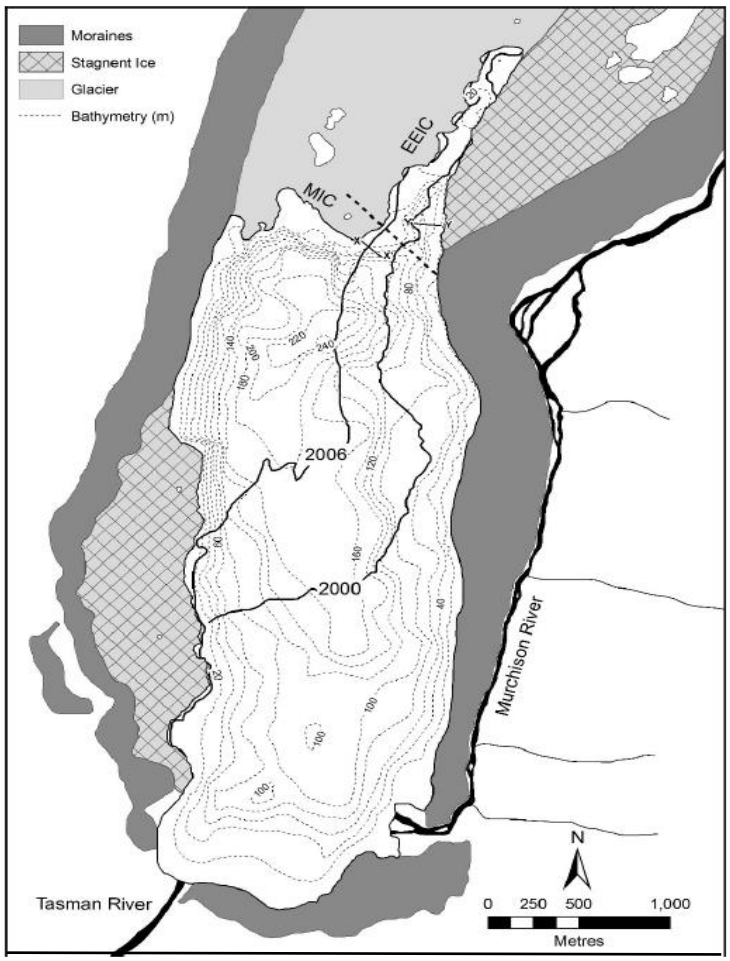

Figure 2.6.3. Bathymetry map of the Tasman Glacier from data collected in April 2008 using echolocation. Also demarked are the location of the Main Ice Cliff (MIC) and the Eastern Embayment Ice Cliff (EEIC) termed by the authors. A maximum lake water depth of 240 m is located just ahead of the MIC in 2008. *Source:* Dykes *et al.,* 2010

2.7. Regional climate: Net mass balances from meteorological changes

Glacier fluctuations are among the clearest of signals of anthropogenic climate change providing symptomatic responses to changes in our global energy balance (Haeberli, 1994; Chinn, 1996). However, the response time of glaciers to climate shifts vary from glacier to glacier and the magnitude of their response is also not homogenous. The Tasman Glacier is a large valley glacier that prior to the 1990s saw only 9% of its surface area lost from its Little Ice Age maximum extent (Chinn, 1996). This mass loss is contrasted by the much faster responding glaciers such as the Richardson glacier (~ 40% area loss), McKerrow glacier (~ 43% area loss) and the nearby Murchison glacier at ~ 26% area loss since AD 1750 – 1890 (Chinn, 1996). Thus, in order to understand response times and the magnitude of changes from climatic forcing at the Tasman glacier it is paramount to closely examine regional climates and the seasonal variations in precipitation which control the Tasman's annual snow/ice budget as well as glacial dynamics such as ice speed and calving rates.

2.7.1. Regional circulation and precipitation trends

Regional circulation patterns at the Tasman Glacier are largely dominated by south-westerly air passing over the Southern Alps of New Zealand. Owing to the orographic uplift of air flow, precipitation on the western front experiences the highest levels of precipitation of ~ 15,000 mm a^{-1} (Chinn *et al.*, 2006; DOC, 2009). In the Tasman Glacier region which sits on the eastern margin of the main divide, precipitation is highest at ~ 7000 mm a^{-1} and diminishes to 3000 to 5000 mm a^{-1} at the terminus (Anderton, 1975). At the terminus however, the direction of air flow becomes much more chaotic and no longer follows the general south-southwest trajectory (Röhl, 2006).

Evidence supporting the importance of regional climates can be found in the Tasman's history. In the last century (20^{th}), glaciers throughout New Zealand experienced large mass losses which climaxed in the 1950s. Steeper cirque and alpine glaciers such as the Franz Josef glacier lost roughly 50% of their LIA extent throughout this period, whereas longer, and lower-gradient valley glaciers (i.e. the Tasman) saw only 25% of mass lost (Chinn, 2006). In the 1980s to 2000 however, New Zealand glaciers underwent a reversal in this trend with Franz Josef advancing ~

1420 m, the Fox glacier by ~ 710 m (Chinn *et al.*, 2006; Purdie *et al.*, 2014). Cumulatively, glaciers in the Southern Alps experienced advances in terminus positions which their average peaking at ~ 780 m in 1996-1997 (see Figure 2.7.1). Overall, these changes were argued to be linked to regional climate systems such as events from the El Niño -Southern Oscillation (ENSO) and a reversal in the Interdecadal Pacific Oscillation (IPO). For instance, ENSO with an average periodicity of 2 to 8 years was in its El Niño phase for the majority of the years spanning 1980 to 2000 which would have enhanced the westerly circulation during summer producing greater precipitation during the ablative months (Chinn *et al,* 2006). In addition, the IPO was predominantly in a positive phase during the glacial re-advance, resulting in an even stronger westerly circulation over the Alps (see Figure 2.7.3). As such the effects of ENSO/IPO during the 1980s – 2000 may explain the observed glacial advances by Chinn *et al.*, (2006).

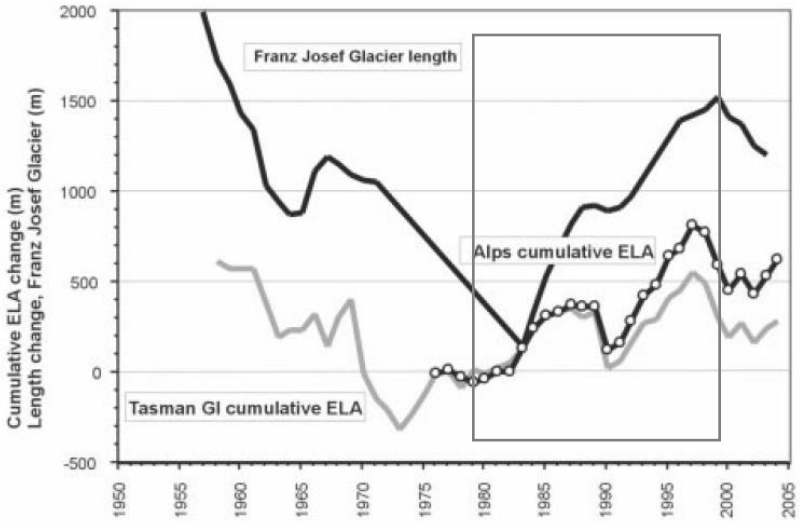

Figure 2.7.1. Shows cumulative plot of annual average length changes of the two NZ glaciers and the aggregate from glaciers in the Southern Alps, NZ. Data was obtained from Equilibrium Line Altitude (ELA) surveys by Chinn, T. The advance appears to have initiated in the early 1980s, peaking in 1995-1999 and ends in 2007/08. *Source:* Chinn *et al,* (2006)

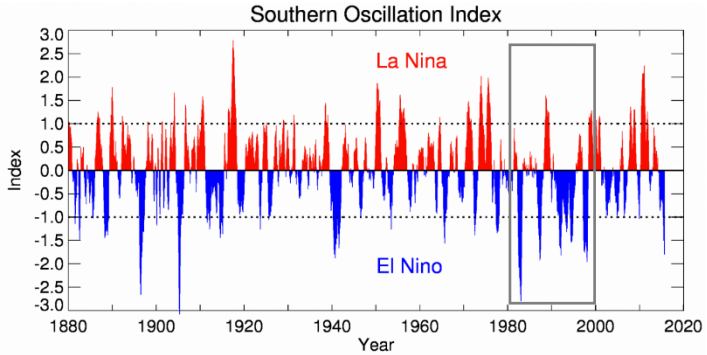

Figure 2.7.2. The phases of ENSO from 1880 to present day. Marked in box is the period 1980 to 2000 whereby NZ glaciers experienced recent advances. *Source:* NIWA, 2016

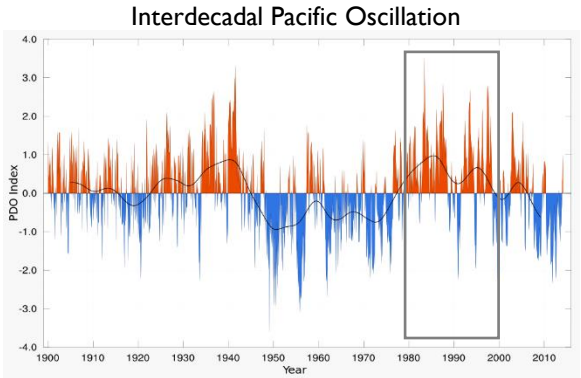

Figure 2.7.3. Shows the historical positive and negative phases of the Interdecadal Pacific Oscillation observed from 1900 to 2014. *Source:* Deser *et al,* 2004; Dong and Dai, (2015)

Although it is clear that the direction and strength of the westerlies have an impact on rates of snow accumulation at the Tasman Glacier (Chinn *et al.,* 2006; Kerr and Owens; 2008), whether they are linearly correlated to regional climate variability such as ENSO and IPO has still not been established empirically.

2.7.2. Temperature sensitivity and future projections

Aside from regional variations in precipitation, Anderson and Mackintosh (2012) indicated that the mass balance of glaciers in the Central Alps were also susceptible to temperature variations at a mean rate of ~ 1.9 m w.e. a^{-1} K^{-1} (- 1.1 m w.e. a^{-1} K^{-1} to – 4.4 m w.e. a^{-1} K^{-1}). This sensitivity appears to conform to previous estimations that ranged between 1.3 and 2.0 m w.e. a^{-1} K^{-1} for the Alps (Oerlermans, 1997; Anderson *et al.,* 2006) and is considered high by global standards (Braithwaithe *et al.,* 2003; De Woul and Hock, 2005). For the Southern Alps, an equivalent increase of 82% in precipitation is therefore required to offset 1 K of warming and with global temperature projections of > 2 ° C (best estimate) by 2099 (IPCC, 2013), it is undeniable that NZ will experience rapid loss of its glaciated environment over this century. Temperature predictions therefore have a crucial role to play in estimating the cumulative ice mass balance of the Tasman Glacier in the coming decades. However, it is likely that temperature perturbations from regional and global climate trends will impact the Tasman glacier significantly less as compared to other glaciers such as the Franz Josef and Fox, which have faster response times. The surface area, volume and topography of the Tasman all contribute to this delayed response. Furthermore, the debris cover on the lower 8km of the Tasman glacier also dampens the effects of climatic variations by reducing overall ablation (Anderson and Mackintosh, 2012). Overall, due to the decoupling of calving glaciers from climate, a mass balance projection for 2100 is therefore inconclusive.

According to Dykes *et al* (2010), speculations that the Tasman could retreat by a further 8-10 km of its Little-ice Age (LIA) position was made by interpolating the depth of the glacier bed which sits at 350 m below the Tasman Lake's surface as compared to 20 km upstream where the depth is 950 m. The present height of the lake is 240 m (Dykes *et al.,* 2010). This estimation makes wide assumptions about the behaviour of the Tasman Glacier as it recedes further up valley and sees the glacier

retreating at higher rates in the future. It is not fully known what will happen to the Tasman Glacier in coming decades owing to the complexity of ice dynamics in an evolving landscape and climate.

Although, this study may only suggest future changes, it may provide insights into the Tasman's unique response to climatic forcing while providing spatially and temporally sensitive observations of its rate of retreat, and flow patterns across a three year study period.

2.8. Investigation aims

Below I've set out some of the more specific questions that will be answered by thesis underlying the key objectives mentioned in Chapter One.

- What is the Tasman's rate of retreat (U_r) from February 2013 to March 2016? And how does that compare to the background rate?
- Furthermore, to what extent are position and surface area changes attributed to calving events and what are the drivers of these events? Thermal undercutting? Or something else?
- What is the Tasman's velocity at the terminus? What spatial distributions - are some regions faster than others and why? Did any accelerations occur?
- What is the Tasman's calving rate (U_c) for the same period?
- Are there climatic or limonological drivers of retreat, calving and velocity variations? And does it reveal behaviour consistent with the literature?

It is thus the general aim of this thesis to provide further insights into the Tasman's unique behaviour by studying its morphology across a fine spatial and temporal resolution. This is paramount to improving mass balance models which are crucial to sea-level rise predictions and future climate scenarios.

CHAPTER THREE
Methodology

3.0 Introduction

Low-cost and long term monitoring techniques are desirable for studying glacier flow and calving. In previous studies, satellite imaging, airborne remote imaging as well as other high-spatial resolution photogrammetry techniques were used for observing annual and inter-annual ice fluxes (Kääb, 2002; Quincey and Glasser, 2009; Redpath *et al.,* 2013). However, these methods are often expensive to conduct, labour and technologically intensive and do not provide the required temporal resolution (i.e time between images) to answer relevant questions regarding processes occurring over weekly and monthly timescales. In this thesis, an oblique time-lapse camera anchored to bedrock overlooking the terminus region of the Tasman Glacier was used to quantify the retreat rate and ice flow for the 37 months between February 2013 to March 2016. The methodologies for these two measurements had slightly different processing requirements although they both used the same images attained in the field.

Since February 2013 our camera installation accumulated over nine thousand (9659) full resolution images of the Tasman Valley. The images were taken at a frequency of one per hour during daylight hours which amounted to eight to fourteen full sized (16.2 megapixel) images per day (*see 3.1 Phase One: Data Acquisition* for full details*).* There were periods where images were not taken due to environmental conditions and technical difficulties. Temporal data coverage will be outlined in more detail in sub-chapters 3.2 and 3.3. Overall, data acquisition covered 88% of the 3-year time series at a sub-daily temporal resolution. The camera continues to operate with 6 monthly maintenance checks and nearby remote downloading through a wireless connection.

Following the initial data-acquisition process, in *3.2. Phase Two: Image Selection* the images are put through several phases of image selection and correction which recognizes and accounts for camera movement, camera lens distortion, and weather anomalies, the latter of which results in images under different lighting conditions and cloud cover that obscures the terminus region. This series of image corrections is of critical importance as it underpins the accuracy and precision of our results.

Once the images had been corrected and selected (described in *3.3. Phase Three: Post Processing*), they were post-processed either through a digital image correlation algorithm and/or manual digitisations to calculate the terminus displacements and velocities. Briefly, the digital image correlation is a common photogrammetry technique that identifies shared features among images and calculates their pixel displacement in *x* and *y* directions. For our investigation, we used Elizabeth Jones's (2015) *Advanced Digital Image Correlation (DIC)* script on Matlab to attain *x* and *y* displacements as well as the direction of movement for each and every pixel (and sub-pixel) of every subsequent chosen image (Jones, 2015).

The second post-processing step was a digitisation of the terminus-lake interface. This boundary was only vectorised on the visible face of the terminus owing to our oblique camera position. Unfortunately, circumstances did not allow for a second camera to be installed on the opposing mountain face which would have contributed significantly to resolving the issue of camera depth and remove parallax errors from obliquity. Extrinsic camera parameters were calculated using 20 Ground-Control Points (GCPs) captured in the field in the Autumn of 2016 to allow real-world positions to be transformed into pixel coordinates and vice versa.

Finally, in *3.4. Phase Four: Results, comparisons and correlations* provides an explanation of the meteorological and lake-level records used to understand the controls on glacier behaviour and elaborates on how we calculated the calving rate at the terminus.

3.1 Phase One: Data Acquisition

Terminus position was determined by the position of the lake-ice interface visible in images acquired using an oblique camera setup which provided a time-series record of the glacial retreat between February 2013 and March 2016. The next section will explore in detail the conditions that were considered for the setup in order to achieve our goals and explain the equipment used.

3.1.1 Equipment setup

The Tasman camera was set up in early 2013 to meet the demands of an effective monitoring system operating in harsh conditions. The camera setup had to satisfy conditions such as:

- Operate ceaselessly in an exposed elevated position
- Operate according to an allocated time frame (daylight hours) as images taken at night would serve no purpose to the investigation
- Operate by taking images hourly for at least 6 months to a year without maintenance.
- Have an independent off-grid power source to run the internal computer system and camera.
- Have an independent source of time to ensure camera system turns on as programmed.
- Have a digital storage drive to store images until wirelessly extracted.
- Is fixed strongly into bedrock as to ensure minimal camera movement from winds that can exceed 115km/hour or 60 knots at camera altitude[1] (MetService, 2016). Even slight movements in the position of the camera will result in a different perspective which will prove problematic for digital image correlation and other measurements.
- Has a protective casing surrounding the entire setup to mitigate damage of vital components.
- Additionally have a protective lens cover to reduce damage of the camera lens and minimise glare from the sun and reflection.
- Have wireless transmission of images to a receiver below the camera setup to eliminate the need of manually extracting images.

[1] Wind speed inferred from daily maximum wind speed from Tasman saddle hut (2316m) through the New Zealand Meteorological Service. A wind speed of 115km/hour or roughly 60knots is classed as winds from a '*Violent Storm*' and is ranked 11th out of 12 classifications on the Beaufort Wind Force Scale. The most extreme on the Beaufort Scale is '*Hurricane Winds*' for anything above 64 knots (Stewart, 1997).

Images continued to be captured for five months until unknown technical difficulties rendered a cease to the automated camera operation on the 7th of June 2013. During fieldwork in July, replacement of the camera (from the Nikon d5100 to the Nikon d3200) took place and further improvements were carried out. The first five months of data exhibited a large amount of camera movement. To address this, an aluminium plate was bolted to reinforce the base of the camera module. It was noted that while changing the camera and lens, the field of view (FOV) also changed. This change to the FOV meant that post-processing had to be first divided into two separate batches, the first being from the camera perspective of the first five months and the second for images ensuing this alteration.

Figure 3.1.1. [LEFT] Image taken on the 23rd February 2013 following a major calving event. This is one of many images taken in the first 6 months and also captures much of the surrounding geomorphic features. [RIGHT] Shows a typical image (25th February 2014) in the second camera batch with greater focus on the terminus. This field of view is common to the majority of images used for our results.

In July 2014, during the second annual field maintenance, images stored on the SD card were manually extracted and the hard-drive was cleaned. Key components required to meet our engineering conditions documented during this trip are presented in *Table 3.1* and *Figure 3.1.2.*

Table 3.1. Conditions required for the project and respective equipment. Details in courtesy of Dr. Brian Anderson.

Project Conditions	**Equipment and Solution**	**Specifications of equipment/remarks**
Camera and data acquisition	Nikon camera capturing at 16.2 million pixels (MP) and hard-drive	Nikon D5100 and D3200 with 28mm and 35mm lens 32/64 GB SD card
Independent source of time	GPS Unit	This tells the Raspberry Pi when to turn on the entire system
Ascertaining images in allotted time frame (daylight hours)	Raspberry Pi control system	Programmable system to capture and store image when activated
Reliable power source and storage of power	60 W Solar Panel Battery	
Mitigation of camera movement and wobble	External mounting components made from galvanised steel for strength. Internal components are aluminium bolts, plates and brackets.	Internal components are lighter than steel, strong enough to withstand 115km/hr winds. Does not rust. Perfect for outdoor use. Melting point 660°C (Marggraf, 1746 cited in Britannica Encyclopaedia).
Protection from environmental hazards and wind	Hard plastic outer casing and lens hood	The case is not fixed to any of the vital components within the module. It is merely a protective shell so as to avoid wind shear.
Module safety and protection from electrical malfunction	Solar controller	SunSaver-6L Solar controller SS-6L-12V
Remote access to images and camera setup	Wireless transmitter and receiver	Antenna required
In-situ capture of GCPs for geo-referencing images	System	Trimble G6 GNSS with fixed Base Station and roaming Rover module. 440 channels. UHF radio transmission. Highly accurate measurements.

Figure 3.1.2. [LEFT] Shows the internal processor that communicates with the camera and specifies when to capture an image. [MIDDLE] The Tasman camera module is bolted into the bedrock as seen to mitigate camera movement. A 60W solar panel is used to power the entire setup. [RIGHT] Manual download of the images is time-consuming and only conducted when doing our 6 monthly maintenance check.

3.2 Phase Two: Image Selection

Image selection underpins both the accuracy and precision of our observations and is a fundamental step of our methodology. In the 41-month record captured from February 2013 to March 2016 the Tasman camera took nine-thousand-six-hundred and fifty-nine (9659) 16.2 MP images amounting to over 250 GB of raw images. However upon close review of the images, many of the images contained obscurities from clouds, shadows and disparities in contrast which will prove problematic in post-processing when pixel patterns are identified and tracked (see Figure 3.3. for examples). Consequently, a criteria for selecting images was warranted and inspired the development of a three part selection process – (1) Image stabilisation (2) Automated time sorting and (3) Manual image selection.

3.2.1 Image Stabilisation

Firstly all images were stabilised for camera movement as small changes in the camera perspective can result in large readings in pixel displacements or terminus positions. This technique was primarily used for the first batch of photos (first 6 months) prior to the camera rebolting made in July 2013. To achieve this, Hugin's open-source *Align Image Stack* and *Cpfind* functions were used to remap all images in the first batch (as seen in LeBlanc, B., *et al.*, 2013 and Hugin, 2003b). Hugin's *Cpfind* function is an image by image one-step detector that determines digital control points common within a batch of images (Hugin, 2003a). Hugin uses image pairs by correlating pixel subsets (the basis of digital image correlation algorithms). Control points between images are then presented in each respective image (*see Figure 3.2.1a).* The control points were all situated on the stationary features in the image such as stable boulders on hillslopes and adjacent moraine which meant the application was robust. Feature identification and matching functionality on Hugin can similarly be found in other Structure from Motion (SfM) software including Agisoft's *Photoscan* and Microsoft's *Photosynth* (Westoby, 2012).

As a corollary to the stabilisation, images that had too much cloud cover or ambiguous image features such as shade or snow-cover did not result in many common control points for Hugin's alignment function. We therefore noted images that were too ambiguous for Hugin to detect during this phase and culled them before Hugin's control point detection was run. A secondary, more detailed culling was conducted post-stabilisation which would thoroughly remove images that had even minor levels of cloud cover, shade or variances in lighting and contrast. This is outlined in *3.2.3. Manual Image Selection Criteria*.

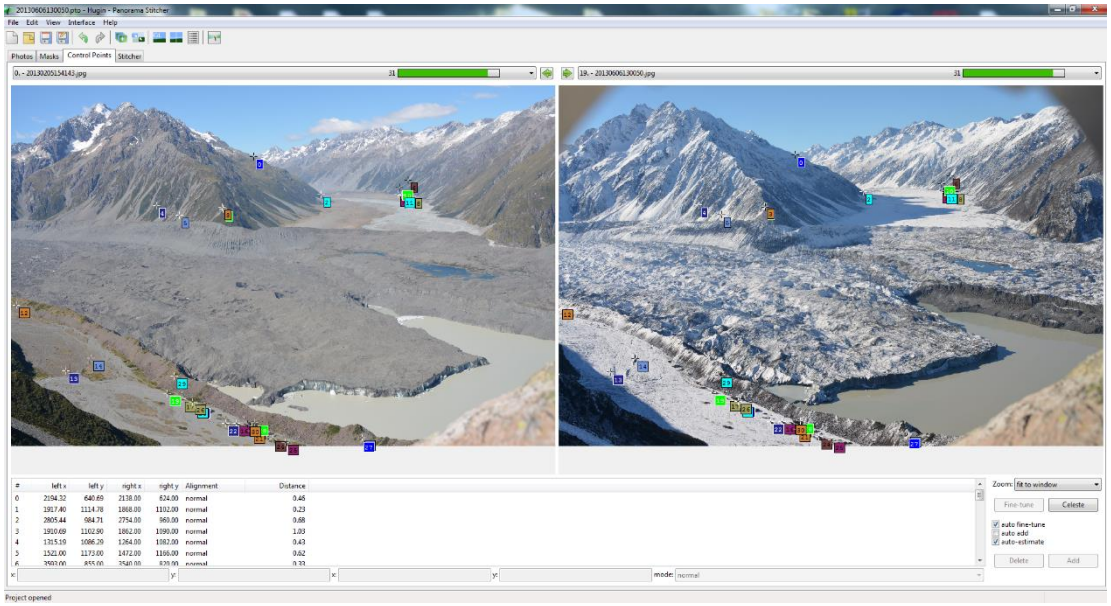

Figure 3.2.1a. Shows typical output from Hugin's *Cpfind* function that correlates and identifies common points amongst photos for stabilisation. The two images shown here are 5 months apart and although the glacier looks completely different it is still able to identify control points from the stationary features in the landscape. Control points on the glacier were not presented as correlations in those regions would have been sparse.

Images captured following the camera rebolting in July 2013 contained significantly less camera wobble and did not require stabilisation via Hugin as potential movements were on a sub-pixel scale. Yet we recognised the need to have a safeguard step before post-processing the second batch of images. As such, OpenCV's *solvepnp* function embedded within the ground control point (GCP) algorithms were used to further stabilize and correct images accordingly. More details regarding this step is explored in *3.4. Phase Four*: *Resolving Parallax and the Issue of Depth.*

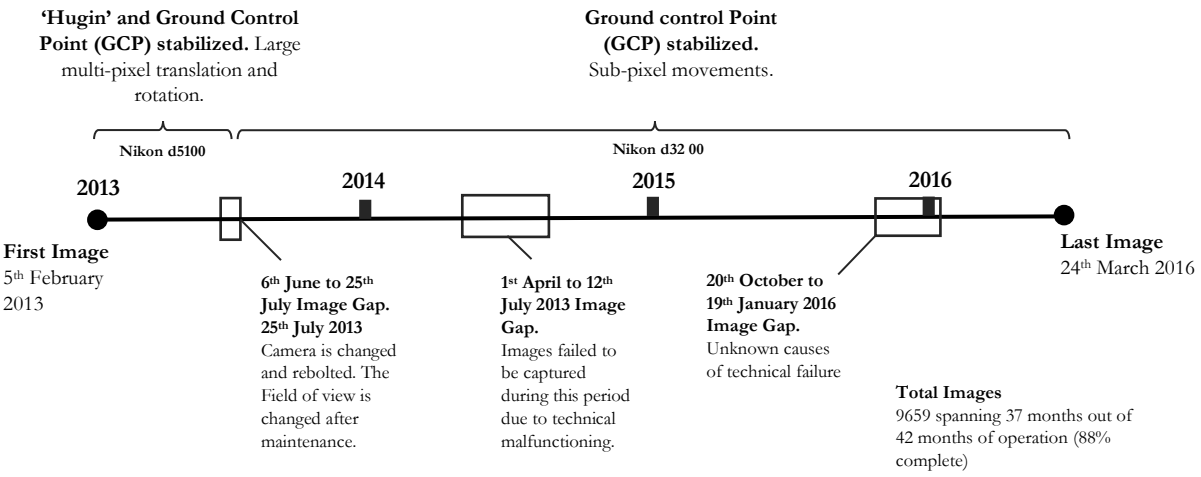

Figure 3.2.1b. Illustrates a timeline of images captured for this study and the respective images that used Hugin for image alignment due to significant camera movement.

3.2.2 Temporal selection of images

To specifically address variances in lighting and contrast, images were automatically sorted using their metadata into their time allotments and were grouped with a deviation of ± 5 minutes from their mean assigned time (i.e. the hourly photo taken at midday could be taken at 11.57pm, 12.02pm, 12.05pm etc. which accounts for technical delay during data acquisition). By doing this, differences in lighting between images chosen daily is optimized. However, the variation in solar angle and thus lighting of the glacier seasonally would persist across images throughout the year. Since image correlations were conducted between image pairs on a sub-weekly timescale, the fluctuations in seasonal lighting have no discernible effect on our post-processing where the terminus-lake boundaries are digitized. Additionally, pixel patterns were identified with images with similar histograms and were captured at approximately the same time in the day (see *3.3. Phase Three: Post Processing).* Furthermore, subsequent images in each batch are hand-picked based on the criteria set out in the next sub-chapter. Examples of the variation in contrast taken at different times of the day are shown here.

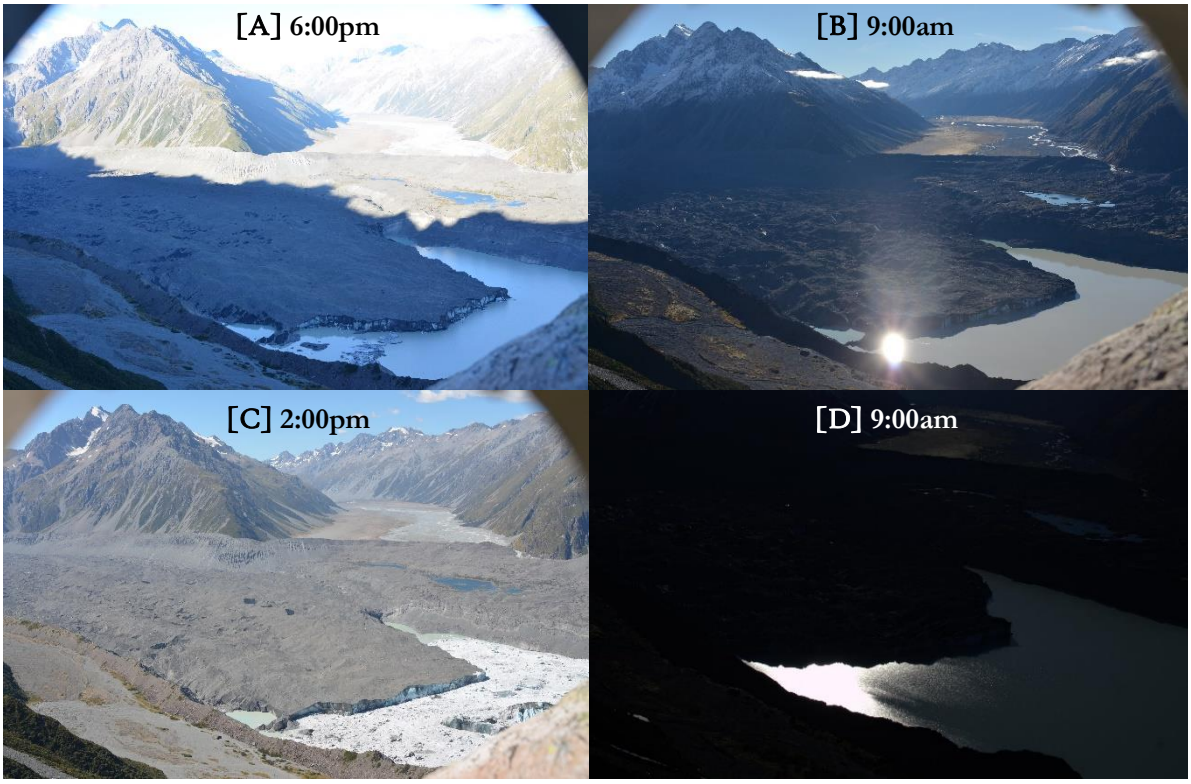

Figure 3.2.2. It's clear that from comparing images B and D, that even with temporal sorting, you can capture completely different photos of the Tasman. [A] Image with shadow cast by the adjacent mountain face at **6:00pm** on the 22nd February 2013. [B] Image captured at **9:00am** on the 6th April 2013 shows a vastly different contrast with the rising sun reflecting off the lake. [C] An ideal image captured at **2:00pm** on the 23rd February 2013 following the major calve event of 2013. [D] Imperfect image taken at **9:00am** on 30th August 2015 in winter where the glacier outline is barely visible.

Once images have been stabilised and sorted into their respective timeframe, they are manually selected using a stringent criteria. This step is critically important and relies on close examination of each image in their respective time allotments. Automated image selection was considered for the project however the tested programs did not provide the consistency and accuracy required for it to be feasible (i.e. a small shadow projected from a single cloud above the Tasman will fail to be culled by the automated image filters, yet can be easily identified by the human eye). We expected the use of a mask of the glacier would resolve some of these issues, however the output resulted in a less than desirable amount of images due to small variations in illumination and contrast. Until image recognition and computer vision algorithms advance further, manual selection remains the most rigorous solution for a stringent image selection process although it is undoubtedly more labour intensive. Once the best images of each time allotment had been chosen, a library of the best photos was collated with a temporal leniency of ± 2 hours of the preceding image (i.e. if the first image time is 1:00pm, then the second image can be selected from the 11:00am to 3:00pm time periods). This was to ensure an allowable consistency in illumination for the images chosen for the study.

The **criteria** we sought for our image selection is shown in the following:

- Images are already **stabilised** in the previous steps
- Images need to have **unobscured view of the entire glacial tongue**. A clear day preferably. No cloud cover directly over terminus region (manual).
- Images have a **similar histogram distributions** to base comparison image (automated).
- Images must have **no shadows** projected from adjacent features or clouds over terminus and glacier regions (manual).
- Images should have **similar contrasts of terminus features** to base comparison image. Ideally taken at the same hour of the day with a leniency of ± 2 hours (manual).
- Finally, only for the digital image correlation post-processing component, images **cannot contain snow cover** on its debris-laden surface as pixel features will fail to track effectively (manual or automated).

Here, we present sample images and respective time **before** the manual image selection:

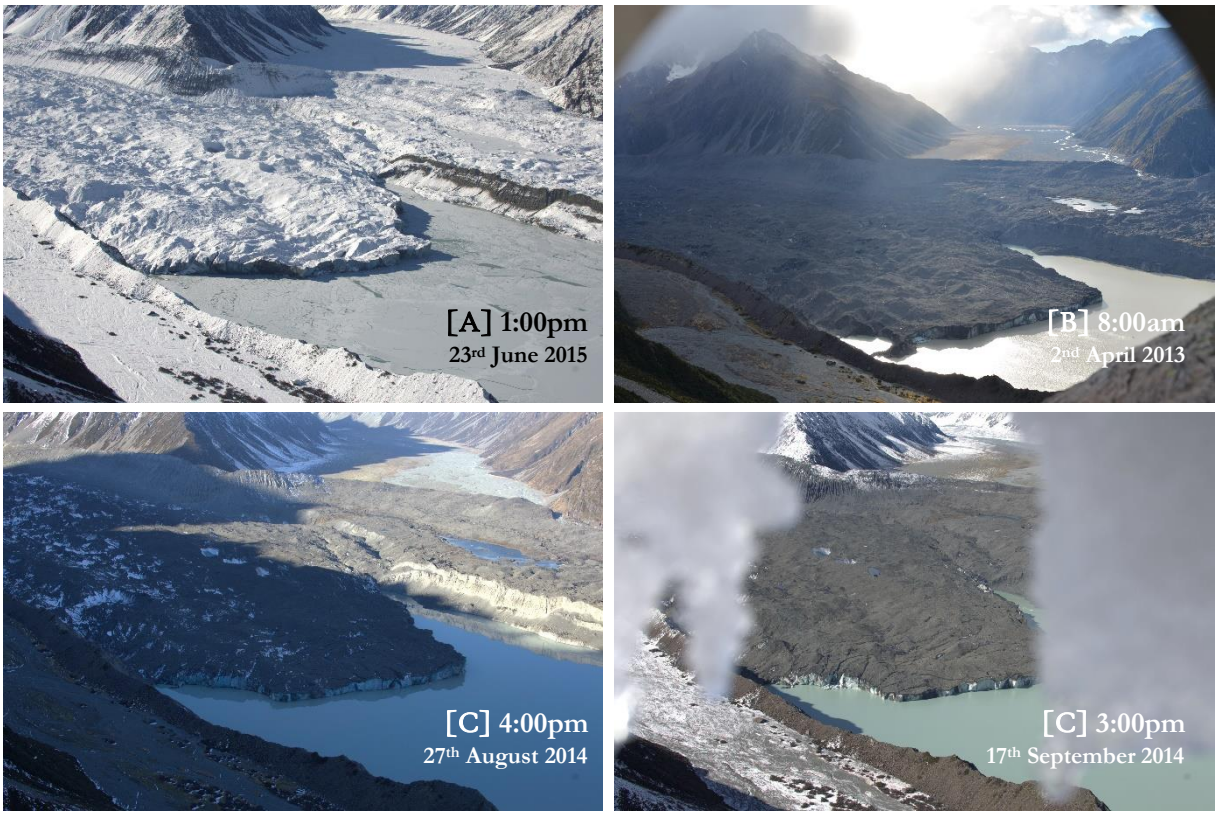

Figure 3.2.2a. [A] Snow cover on Tasman debris will prove difficult during image tracking. Extended periods of complete or partial snow cover had to be eliminated before correlating. [B] A typical image capturing morning dew hovering over the valley. [C] Shadows in the afternoon cast by the northward face of Mt.Cook range. [D] A sub-perfect image aside from ice frozen over the lens casing. Surprisingly this image passed our initial histogram filters.

Here, we present sample images **after** manual and automated image selection processes:

Figure cont. on following page

Figure 3.2.2b. Shows four ideal images after all selection phases captured at 3:00pm across 2013-2015. Although captured at the same hour of the day, small variations in lighting remain. Our digitisation of the terminus is unaffected by such disparities as long as we can clearly see the lake-ice boundary. As for the digital image correlation component of this study, images are compared across a high resolution sub-pixel subset of 51 pixels in grayscale thereby minimising the potential of errors caused by lighting discrepancies. Furthermore images are correlated in sequential order so that variations in solar angle are minimised significantly between images.

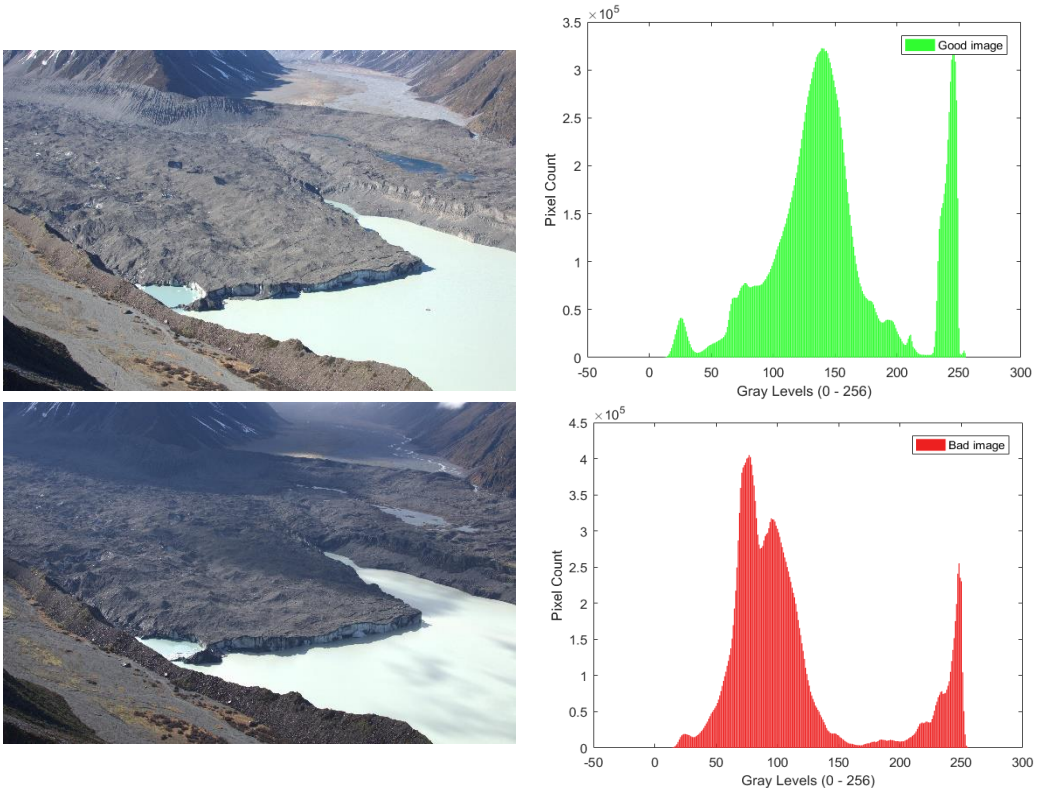

Figure 3.2.3c. Corresponding image histograms of an ideal image and non-ideal image. The ideal histogram is centred on the 145 level and share similar distributions. Images are converted to grayscale with bins 0-256 prior to histogram analysis.

3.2.3 Summary of Phase Two: Image Selection

In all, of the 9659 images captured in our study period which spanned just over 1200 days, 182 images were selected for correlation to produce a temporally-sensitive spatial distribution of the Tasman glacier. For the terminus position step, 152 images at an approximate weekly interval (7 ± 4 days) were sampled.

3.3 Phase Three: Post Processing and Results

3.3.1 Introduction and framework

Here I present my post-processing methodology to attain velocity and displacement of the Tasman terminus using oblique photogrammetry. To date, the majority of remote sensing observations have been from satellite or airborne imagery with the few exceptions seen in Murray *et al.*, (2015), Messerli and Grinsted (2015), Ahn and Box, (2010), and older works by Harrison *et al.*, (1986) and Flotron (1973). In order to attain an accurate quantitative representation of the glacial dynamics, the time series of images spanning the period February 2013 to March 2016 was post-processed for two main measurements, velocity and position.

A variety of tools were used in the process of attaining these measurements from the raw image data. These included the Matlab calibration toolbox for estimating intrinsic parameters, OpenCV for image geometry, and Quantum GIS (QGIS) for processing terminus vectors and mapping. In the post processing step, results were quantified and plotted using Matlab (*scripts are attached in appendix)* and QGIS for a final interpolation of the flow map. iPython and Agisoft's Photoscan was also used in the process to attain the Flow-Scale Factor (FSF) and the Pixel-Scale Factors (PSF) vital for image geometry. Finally, back-projection of the lake-ice interface was done in conjunction with lake level data (or elevation) attained from a lake sensor on the Tasman Lake.

In summary, velocity was attained by a pixel-tracking, digital image correlation (DIC) algorithm conducted in Matlab adapted from Jones, E., (2015). A selection of sampling points were chosen for comparisons with rainfall and other drivers of glacial movement. The raw velocities are then undistorted into real-world velocities with OpenCV equations using Flow Scale Factors (FSF) at 119 digitally generated (100 m) sample points.

For the terminus positions, manual vectorisation of the lake-ice boundary (where the bottom of the visible ice contacts the lake) was conducted in QGIS at a sub-monthly (~ 5-10 day per sample, with a mean of 7 days) timescale. The pixel-space coordinates are then converted from the camera co-ordinate system to a real-world co-ordinate system, the NZ Transverse Mercator (NZTM), using the same projection algorithms which adapts OpenCV's image geometry functions. After replotting the output in QGIS, initial area measurements and rates

of terminus retreat were ascertained for error checking.

Real-world digitally generated transects are further plotted to find their intersection with our sets of post-processed termini to attain a time series of position. Moreover, glacial area loss was estimated in Matlab for large calving events which were visually identified through time-lapse footage. Our area loss and positions were only indicative of a portion of the entire glacial tongue (a minimum for area and spatially incomplete for positions) as some of the terminus boundary was not visible in the majority of images. A meticulous exploration of each rung of our post-processing methodology is provided in the following subheadings.

3.3.2. Intrinsic Camera Parameters

The intrinsic camera parameters (herein known as 'intrinsic parameters' or 'intrinsics') vary from camera to camera, lens to lens and in essence, represents the geometry by which light from an external source hits the charged-coupled device (CCD) or CMOS sensor within the camera to be stored as a pixel of visual information.

The intrinsic parameters of any 'ideal' pinhole camera is comprised of the focal length (f_x, f_y) and the principal point also known as the optical centre (c_x, c_y). However in the real-world, simply quantifying the intrinsics is inadequate because in a real-world camera, there exists radial and tangential lens distortions (Weng *et al.*, 1992). These distortions are typically quantified as k_1, k_2 and k_3 for radial distortion and p_1, p_2 for tangential distortion (Zhang, 2000; Weng *et al.*, 1992). In order to attain these intrinsic parameters, camera calibration is conducted with the cameras used for our study. Moreover, the parameters can also be attained from any Structure-from-motion (SfM) software with reasonable accuracy (~<2.5 pixels) depending on the number of image perspectives captured for the digital elevation model (DEM) (Caroti, 2015).

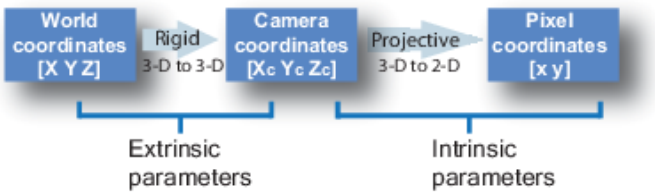

Figure 3.3.2. Shows the difference between extrinsic camera parameters and intrinsic camera parameters. The intrinsic parameters dictate how a three-dimensional object in the real world is represented in two-dimensions in a photo. *Source: http://au.mathworks.com/help/vision/ug/camera-calibration.html*

Calibration of the camera was required in the initial stages of the post-processing phase to attain the intrinsic camera properties for the two cameras used for data acquisition (Nikon d5100 and Nikon d3200). Our first camera, the Nikon d5100, captured 5 months of photos spanning February to June 2013 and the remainder captured using the Nikon d3200 till the last image date.

For the first camera, calibration photos were taken prior to field installation and processed using Caltech's *Calibration Toolbox* in Matlab. Results from our camera calibration using a checkerboard are shown in *Figure 3.3.1.1*.

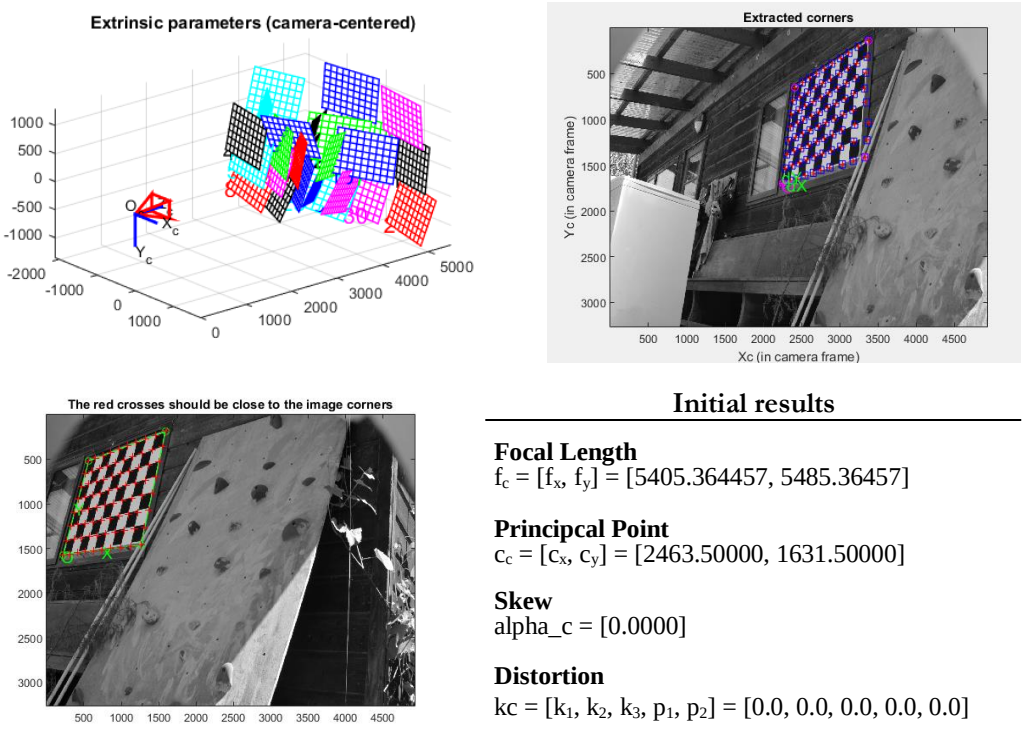

Figure 3.3.2.1 Camera calibration of 33 camera angles of a 9x7 checkboard taken by the Nikon d5100 and the intrinsic parameters produced. The Camera calibration toolbox used for this step was produced by Computational Vision Labs, Caltech. *Source code: http://www.vision.caltech.edu/bouguetj/calib_doc/*

As for the images taken post July 2013 using the newly installed camera; the Nikon d3200, no manual camera calibration was conducted prior to its installation. Thus we were compelled to rely on intrinsic parameters created from SfM. Notwithstanding the fact that there was a high uncertainty associated with our results while using our initial calibration from the checkerboard, which was significantly reduced after using intrinsic parameters from our SfM reconstruction. No further correction was deemed

necessary for the new camera as the SfM intrinsic parameters were 3-4x better than with the checkerboard.

3.3.1.2 Intrinsic Parameters attained from Structure from Motion (using Agisoft's *Photoscan*)

Our principal technique of attaining intrinsic camera parameters for the cameras was by using two DEMs created from Agisoft's *Photoscan* in 2013 and 2014. The 2013 SfM was created using the Nikon D5100 which is the same camera used to capture our time-lapse images from 5th February 2013 to 6th June 201. Below the final intrinsic camera parameters used for the camera calibration step of our post-processing methodology are presented.

Table 3.3.1. Shows **Final Intrinsic Camera Parameters** used for this study.

Camera	Batch Numbers	Focal Length (f_c)		Principal Point (c_c)		Radial Distortion	Tangential Distortion	Pixel Error
		f_x	f_y	c_x	c_y	k_1, k_2, k_3	p_1, p_2	
Nikon d5100	1	6015.38	6015.38	2363.47	1374.66	-0.00716, -0.375, 1.88	-0.00012, 0.00398	2.25
Nikon d3200	2,3,4	9407.66	9407.66	3221.05	1848.22	-0.0472, 2.824, -8.557	-0.007378, 0.000954	1.095

3.3.3. Extrinsic Camera Parameters

In an oblique image, the principal point is not vertically above the object as opposed to nadir imagery from satellites and planes. Thus, in order to convert the camera coordinate system back to the real-world coordinate system, a set of transforming parameters must be employed. These parameters known as the Extrinsic Camera Parameters (herein known as the "Extrinsics") are comprised of a rotational matrix and translation vector which accounts for the oblique angle by which a real-world object is viewed from our slanted perspective.

First, the relationship between the two coordinate systems are given by equation (1). (x, y, z) represents the coordinates in the camera coordinate system (i.e. our camera capturing the terminus of the glacier) and (x_c, y_c, z_c) represents the real-world coordinates in order to make quantifications of retreat rates and position.

$$\begin{pmatrix} x_c \\ y_c \\ z_c \end{pmatrix} = R \begin{pmatrix} x \\ y \\ z \end{pmatrix} + T \qquad (3.1)$$

$$R = \begin{bmatrix} R_{11} & R_{12} & R_{13} \\ R_{21} & R_{22} & R_{23} \\ R_{31} & R_{32} & R_{33} \end{bmatrix} \quad (3.2)$$

$$T = \begin{bmatrix} t_1 \\ t_2 \\ t_3 \end{bmatrix} \quad (3.3)$$

where R represents ($r_{i,j}$), a 3x3 rotational matrix and T is a (t_1, t_2, t_3), translational vector defining the Extrinsics (Weng *et al*, 1992).

An extrapolated version which includes the focal length and principal point (the Intrinsic Camera Parameters) of the camera is given by combining 3.4 with 3.1, 3.2 and 3.3.

$$\begin{aligned} r - r_0 &= s_u u \\ c - c_0 &= s_v v \end{aligned} \quad (3.4)$$

where (r, c) is the position of a corresponding pixel in a digitized image

$$\begin{aligned} \frac{u}{f} &= \frac{r - r_0}{f_u} = \frac{r_{1,1}x + r_{1,2}y + r_{1,3}z + t_1}{r_{3,1}x + r_{3,2}y + r_{3,3}z + t_3} \stackrel{\text{def}}{=} \dot{u} \\ \frac{v}{f} &= \frac{c - c_0}{f_v} = \frac{r_{2,1}x + r_{2,2}y + r_{2,3}z + t_2}{r_{3,1}x + r_{3,2}y + r_{3,3}z + t_3} \stackrel{\text{def}}{=} \dot{v} \end{aligned} \quad (3.5)$$

where *f* is the effective focal length of the camera, $\mathbf{r_0}$ and $\mathbf{c_0}$ denotes the pixel position of the principal point O' and $f_u = s_u f$ and $fv = s_v f$ defines the row focal length and column focal length respectively (Weng *et al*, 1992).

However this mathematical technique presumes that we have some idea of the rotation matrix, $R = (r_{i,j})$ and translation vector, $T = (t_1, t_2, t_3)$. between the camera position and the real world dimension. As a result, simply having this conversion equation is inadequate and requires the use of ground-control points (GCPs) in order to reconcile the images effectively. This outlines the mathematics behind the image geometry solution from OpenCV's *solvepnp* function.

3.3.4. Ground-Control Points (GCPs)

Twenty GCPs situated along the vicinity of the Tasman Glacier terminus and within view of our oblique camera setup were attained to resolve this issue. Prior to our fieldwork, potential GCPs were visually identified. We initially chose large boulders and other prominent features on Ball Hutt Road on the true-left of the Tasman valley and several distinguishable features on the moraine plateau at the intersection of the Murchison and Tasman valleys (see *Figure 3.3.4.2.*).

On the 20th of March 2016, the real-world positions of our GCPs were attained using the Trimble G6 GNSS system with a base station set up within 2-3km of our GPS rover. Each

location was sampled roughly 600-1000 times and was then averaged to produce longitude, latitude and elevation data for each of our GCP sites. While traversing the Tasman surface, the rover was left on auto-sample. Upon reaching our GCP feature, the rover was held stationary for 10-15 minutes for continuous sampling. Owing to time constraints only 7 GCPs were captured on the opposite side, as opposed to 13 from the left-flank of the valley, along Ball Hut Road.

3.3.4.1 GCP Equipment

The Trimble R6 GNSS System is a 220 channel, high precision GPS device designed to perform exceptionally well in remote environments. It specifies a horizontal accuracy of ± 0.25 m + 1ppm RMS and vertical accuracy of ± 0.5 m + 1ppm RMS. We operated the Trimble R6 over two days in the autumn of 2016 to attain our Ground Control Points.

Figure 3.3.4.1. Shows the Trimble R6 GNSS system. (A) The Rover and Base station in its protective casing (B) The controller (C) Base Station

Our base station was set up on an elevated position (i.e. the top of a moraine wall) and was expected to communicate with our rover station as we roamed to each GCP site. We were mindful not to roam beyond 2-3km radius from the Rover to ensure accurate recording of our GPS data.

3.3.4.2. GCP Sites

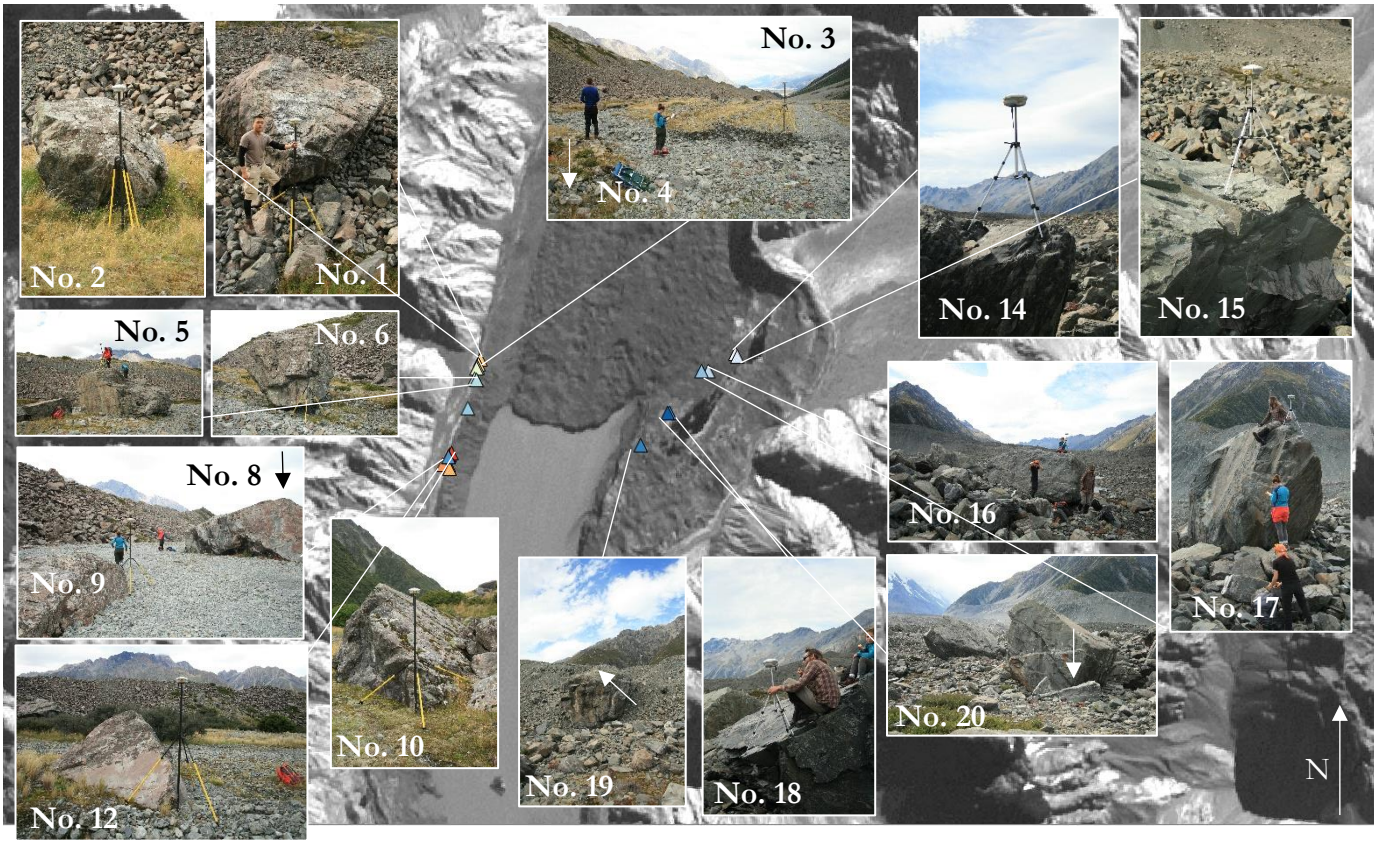

Figure 3.3.4.2a. Location of Ground Control Point sites with 13 on the western margin and 7 on the eastern margin at the mouth of the Murchison valley. Base is a 15 m resolution ASTER image captured on the 9th April 2016. Not displayed are GCP Numbers 7, 11 and 13. *Source:* MADAS (METI AIST Data Archive System)

Table 3.3.4.2a. Shows recorded GPS data with errors from each Ground Control Point (GCP) listed in order of collection.

GCP Site (#)	Description	Latitude x	Longitude y	Elevation z	RMS x_{error}	RMS y_{error}	RMS z_{errrr}
1	First Boulder	1372582.632	5162670.403	965.84	0.0217	0.1202	0.0621
2	Boulder on tussock	1372570.439	5162628.642	964.368	0.1092	0.2440	0.3574
3	Visible corner	1372553.932	5162594.975	963.523	0.1472	0.2645	0.3565
4	Other corner	1372548.438	5162590.365	963.315	0.2127	0.3311	0.5401
5	Next big Boulder	1372527.809	5162477.173	960.015	0.1657	0.2596	0.3678
6	Big boulder	1372547.942	5162474.831	955.461	0.1700	0.2934	0.6370
7	Another big boulder	1372459.407	5162195.843	938.118	0.1217	0.2757	0.3896
8	Massive boulder	1372269.324	5161719.956	907.198	0.1118	0.5090	0.3325
9	Small rock near 8	1372278.366	5161738.571	904.554	0.2070	0.3336	1.5192
10	Other boulder behind 9	1372298.913	5161751.332	903.790	0.1846	0.3523	0.4930
11	Large boulder after massive boulder	1372268.368	5161639.982	898.979	0.2076	0.3357	0.9428
12	Pinnacle-like rock	1372217.128	5161639.460	898.892	0.2179	0.2179	0.7623
13	Outcrop on Moraine Wall	1372283.306	5161599.058	913.371	0.0557	0.0557	0.1361
Other Side of Tasman							
14	First large boulder found	1375110.798	5162729.827	825.761	0.0811	0.2986	0.2134
15	White boulder near 14	1375127.447	5162704.766	827.831	0.0863	0.3568	0.2036
16	Boulder near small pond	1374843.503	5162560.983	820.023	0.1930	0.4885	0.6756
17	Large vertical outcrop	1374778.912	5162559.550	820.008	0.1360	0.3073	0.2618
18	Corner of black boulder	1374456.711	5162150.326	810.187	0.1365	0.2102	0.2511
19	Tip of massive boulder	1374174.214	5161831.962	811.846	0.0511	0.1184	0.1738
20	White boulder, at the base	1374439.494	5162149.597	808.197	0.0911	0.4190	0.1856

As a corollary of our methodology thus far, any changes to the pixel position of our GCPs will result in a distorted set of extrinsic camera parameters which in turn will produce faulty results. Such changes can occur when there are significant levels of camera wobble or when the camera is changed altogether to a different lens and therefore captures a different resolution.

In application, our camera change in July 2013 and other wobble events thus warranted the creation of four distinct post-processing batches (1-4) and consequently we had to re-identify pixel positions of the corresponding GCPs in each of those batches. To achieve this we first plotted our set of GCPs against batch one (images from our widest FOV captured by the Nikon d5100) in Matlab. An image from each other batch was then plotted beside it. Pixel coordinates of our GCPs were then visually identified in our new batches in a process of manual translation (see Figure 3.3.4.2b below for examples). Owing to changes in the image sensor and camera lens, the resolution were remarkably different particularly when translating GCPs from batch one to batch two, and less so for batches three to four. In *Table 3.3.4.2b.*, GCP's and their respective pixel positions from each Batch after this translation process are presented.

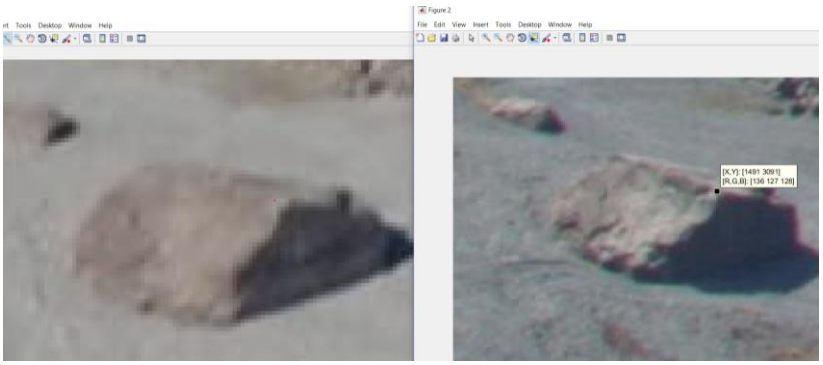

Figure 3.3.4.2b. (A) The Massive Boulder GCP. Pixel co-ordinates were transcribed visually between Batches. Human errors are at most on the scale of 1-2 pixels.

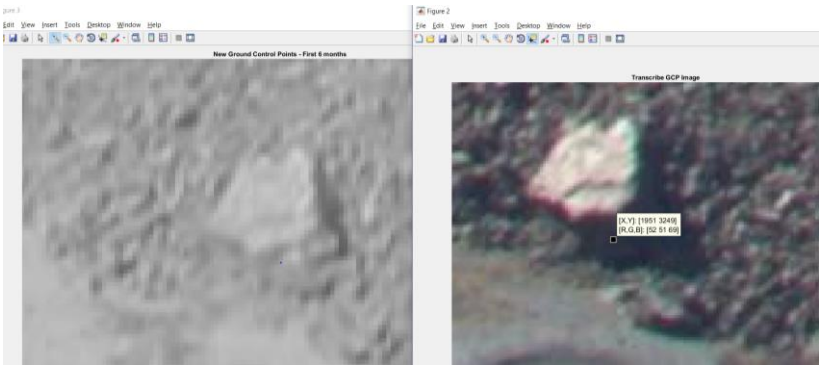

Figure 3.3.4.2c. (B) The Large Boulder near Massive Boulder GCP. Pixel co-ordinates were transcribed visually between Batches. Human errors are at most on a scale of 1-2 pixels.

Table 3.3.4.2b. Comparison table of new GCP locations in each respective Batch after our translation process.

GCP Site	**Description**	**Batch 1** (Feb-June 2013)		**Batch 2** (July-Nov 2013)		**Batch 3** (Nov 2013 - August 2013)		**Batch 4** (August 2015 - March 2016)	
(#)		x	y	x	y	x	y	x	y
1	First Boulder	82	2013	OOFOV	OOFOV	OOFOV	OOFOV	OOFOV	OOFOV
2	Boulder on tussock	132	2035	OOFOV	OOFOV	OOFOV	OOFOV	OOFOV	OOFOV
3	Visible corner	146	2056	OOFOV	OOFOV	OOFOV	OOFOV	OOFOV	OOFOV
4	Other corner	149	2059	OOFOV	OOFOV	OOFOV	OOFOV	OOFOV	OOFOV
5	Next big Boulder	325	2110	OOFOV	OOFOV	OOFOV	OOFOV	OOFOV	OOFOV
6	Big boulder	382	2108	OOFOV	OOFOV	OOFOV	OOFOV	OOFOV	OOFOV
7	Another big boulder	787	2259	OOFOV	OOFOV	OOFOV	OOFOV	OOFOV	OOFOV
8	Massive boulder	1722	2873	1438	3053	1455	3081	1467	3083
9	Small rock near 8	1682	2862	1374	3034	1386	3062	1401	3063
10	Other boulder behind 9	1695	2820	1402	2972	1416	3000	1432	3003
11	Large boulder after massive boulder	2039	2956	1914	3220	1930	3246	1951	3249
12	Pinnacle-like rock	1889	3054	1677	3347	1689	3377	1702	3379
13	Outcrop on Moraine Wall	2231	2890	2217	3137	2231	3166	MISSING	MISSING
Other Side of Tasman									
14	First large boulder found	3089	1488	3715	1057	3735	1091	3750	1094
15	White boulder near 14	3131	1482	3782	1054	3804	1092	3819	1091
16	Boulder near small pond	3151	1552	3803	1165	3824	1204	3839	1204
17	Large vertical outcrop	3109	1566	3738	1181	3758	1219	3770	1218
18	Corner of black boulder	3555	1674	4422	1397	4435	1443	4457	1446
19	Tip of massive boulder	3943	1779	4993	1608	5015	1656	5026	1652
20	White boulder, at the base	3530	1685	4375	1417	4394	1459	4408	1459

KEY:
OOFOV = "Out of Field of View"
MISSING = Feature no longer present in images

As seen in the above table, seven of the initial twenty captured during fieldwork in 2016 failed to be identified in batches 2-4 due to being beyond the FOV of the camera. To account for any potential discrepancies in the production of our Extrinsic Parameters, 7 secondary GCPs ascertained in 2013 by Dr. Brian Anderson were used instead. These secondary GCPs are presented below:

Table 3.3.4.2c. Secondary GCPs for Batches 2-4 to account for the lack of newer Ground Control Points. These GCPs were attained by Dr. Brian Anderson in 2013. Also listed are the corresponding pixel positions for these secondary GCPs.

GCP Site	**Description**	**GPS Co-ordinates**			**Batch 2** (July-Nov 2013)		**Batch 3** (Nov 2013 - August 2015)		**Batch 4** (August 2015 - March 2016)	
(#)		Lat (x)	Long (y)	Elevation (z)	x	y	x	y	x	y
	SECONDARY GCPs									
1	Massive Boulder	1372268.486	5161714.007	905.300	1460	3062	1474	3090	1491	3091
2	Small Rock near 1	1372286.057	5161794.102	904.513	1106	2929	1120	2955	1136	2956
3	Corner Rock	1372456.944	5162195.542	933.982	31	2098	863	2336	64	2119
4	Other corner	1372525.641	5162472.526	954.221	2638	3536	401	2142	328	2118
5	Next big Boulder	1372547.59	5162474.312	953.044	398	2134	454	2129	380	2105
6	Big boulder	1372240.838	5161508.845	893.175	2644	3564	2649	3567	2662	3569
7	Another big boulder	1374548.141	5162153.163	810.793	4515	1384	4485	1410	4500	1408

In summary, 27 GCPs and matching intrinsic parameters were used to calculate the extrinsic camera parameters for each corresponding batch of images using an adaptation of OpenCV's *solvepnp* function. The final GCP x_{error} was quantified as < 0.21m, y_{error} < 0.5m and z_{error} < 0.94 m.

Further details on how the GCPs and intrinsic camera parameters were used to estimate the extrinsic camera parameters (i.e. the Rotational 3x3 Matrix and Translation 3x1 Vector) are presented in the next subchapter, *3.3.6.*

3.3.5. Summary of Batch Allocation

Although our camera is fixed to one location, minor camera movement caused by wind and other natural/man-induced sources can alter the pixel location of the objects quantified in the image. During our image stabilisation stage, major camera movements were recorded and utilised to divide our entire dataset into time allotments, which we termed an image batch. In aggregate, four main image batches were created. The first image batch had to be separated simply due to a change in camera and lens to the Nikon d3100 in July 2013, while the remaining three batches resulted from significant camera movements and thus deviated the location of our GCP features. In retrospection, a comparison of the pixel movements between the batches is used to provide quantitative evidence for the creation of the four post-processing batches (shown in the Table below).

Table 3.3.5. Shows a summary comparing GCP positions from batches 1-4. These mean deviations are based off our reference GCPs against the same GCP feature in a different batch. Significant pixel errors between the batches justifies their initial creation. The largest variation existed from batch 1 to 2 when the camera was replaced by the Nikon d3200 and also resulted in a smaller Field of View (FOV) thereby altering pixel positions significantly. Failure to account for pixel movements from varying batches would have produced incorrect image geometries.

Comparison (Batch vs Batch)	**Average variation in Pixel Co-ordinates of GCPs (x,y)**		**Standard Deviation (σ)**	
	x	y	x	y
1-2	314.15	-79.98	519.92	297.68
2-3	17.08	34.92	3.80	7.43
3-4	13.92	1.77	5.28	2.25

Figure 3.3.5 summarises the periods of the dataset where images were lacking and the

allotment of four batches based on our analysis of image stability presented in the previous subchapter, *Table 3.3.5.*

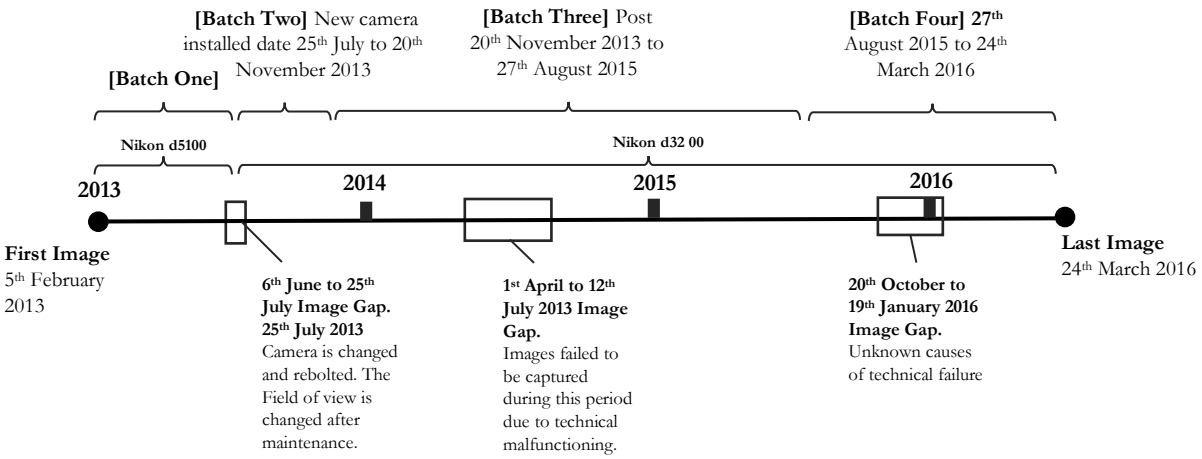

Figure 3.3.5. Shows the periods by which the batches were allocated based on large pixel displacements caused by camera movement (from both natural and man-made sources i.e. by new camera installation or maintenance)

3.3.6. Estimating extrinsic parameters using GCPs

Figure 3.3.6. Parallax and issues of depth is depicted when comparing [1] A recent LANDSAT-8 satellite image of the Tasman terminus captured on 13th February 2016 [2] An oblique image from our camera setup taken on the 13th of February 201. Resolving parallax is of paramount importance in order to extrapolate accurate real-world results from the study.

Resolving image parallax is the pivotal step in oblique photogrammetry applications as it allows us to make real-world measurements from a distorted plane of reference and serves as the foundation for this study. Below, I outline how the extrinsic camera parameters were calculated using the GCPs and the OpenCV's *solvePnP* function.

3.3.6.1. SolvePnP

Once the GCPs for each respective batch were post-processed, the *cam_extrinsic_gcp.py* script was used generate sets of extrinsic camera parameters.

The OpenCV s*olvePnP* function actually stands for 'solving the perspective-n-point (PnP) problem'. This PnP problem is in fact a common mathematical problem in computer vision to ascertain the position and orientation of a camera lens given its intrinsic camera parameters (Lepetit *et al.*, 2008). Although three differing methodologies were provided in the *solvePnP* algorithm, we used an iterative method based off Levenberg-Marquardt optimisation which seeks to minimise the reprojection error (RMS error) between the image points (pixel coordinate space) and the projected points (real world coordinate space). The outputs of this function were presented previously in *Table 3.3.7.* as a 3x3 rotation matrix and 3x1 translation vector for each image batch. Alternative methods to resolve the PnP problem which performs faster than iterative methods could have been used (i.e. using Lepetit *et al*'s (2008) 'Efficient Perspective-n-point Camera Pose estimation') however accuracy of the Extrinsic Camera Parameters was prioritised for this study.

3.3.6.2. Optimisation of GCPs

Initially, the extrinsic results had substantial RMS errors as high as 120m from where the GCP was initially identified. However after a process of optimisation; where individual GCPs were culled due to their inaccuracies and the extrinsics reprocessed, the average error was reduced to < 10-12m across all batches. It's important to note that this maximum error was not homogenous across the entire image plane with the GCPs furthest from the camera being also those that contained the highest RMS reprojection errors. We supposed this observation arose from the compounding effects of small pixel errors in the identification of the ground control point's particularly from features furthest away from our camera (i.e. at the intersection of the Tasman and Murchison valleys). For example a boulder on the furthest side of Tasman may be represented by 10 pixels whereas a similarly sized boulder closer to the camera may be represented by 50 pixels, thus representing the resolution issue arising from the camera's obliquity and consequently affects the identification of GCPs within and between batches.

Based on this rationale, this maximum RMS error < 10-12m for our extrinsic camera parameters was accepted as it accounts for the spatial inhomogeneity in errors arising from an obliquity of our camera and the embedded camera geometry errors associated to every pixel (a.k.a the Flow-Scale Factor and the Pixel-Scale Factor).

In summary, a smaller selection of GCPs were used to optimize the Extrinsic Parameters and to produce a lower RMS error. The results from this optimisation process are shown in *Table 3.3.6.1*.

Table 3.3.6.1. Shows our GCP optimisation results. Mean RMS error was reduced from < 110m to < 10-12 m across all batches.

Batch Number	**Total Number of GCPs prior to optimisation**	**Number of GCPs chosen for optimisation**	**Mean RMS Error before optimisation**	**Mean RMS Error after optimisation**
1	27	18	28.04 m	10.25 m
2	23	20	92.09 m	8.44 m
3	20	13	75.88 m	8.39 m
4	20	19	224.08 m	12.084 m

3.3.6.3. Limitations and discussion of our GCP methodology

Although thirty potential GCP features were identified from our photos prior to the fieldwork, only 20 GCPs were distinguished due to field difficulties in identification. Compounded by time constraints on the second day, only 7 GCPS were captured on the moraine plateau at the junction of the Tasman and Murchison valley. In addition to this, another 7 GCPs captured on the proximal side (to camera position) failed to be identified in the FOV of batches 2-4. This miscalculation meant that secondary GCPs attained in previous years had to be employed to bolster our GCPs to a minimum of twelve GCPs (that is, after optimisation) as compared to 27 total GCPs prior to optimisation. Had we managed to capture thirty GCPs in total during our fieldwork in 2016, we would have expected a much lower extrinsic RMS error after optimisation. The justification behind having at least twelve GCPs is because the extrinsics are comprised of 12 unknowns (i.e. a 3x3 rotational matrix and a 3x1 translation vector). Additional GCPs over this minimum allows a least-squares estimate of the extrinsic camera parameters.

3.3.7. Summary of Extrinsic Camera Parameters

Following the attainment of the intrinsic camera parameters and 'ground-truthing' with GCPs to attain the extrinsic camera parameters, a conversion of real-world positions to camera pixels can ensue. Below, the final extrinsic camera parameters produced by OpenCV's *solvepnp* function for batches 1-4 are presented.

Table 3.3.7. Final summary of extrinsic camera parameters estimated from our intrinsic parameters and ground control points. Photos from batch 1 were captured by the Nikon d5100 as opposed to the Nikon d3200 for the remaining batches. The Rotational and Translation vectors from batches 2-4 are very similar due to the camera being fixed (unchanging in position nor camera lens/technology) post-July 2013. This observation verifies their accuracy.

Batch Number	Rotational Matrix (Rmat = [3x3])			Translation Vector (Tvec = [3x1])
1	$5.268703263766565392e-01$ $-1.235012491032658755e-01$ $8.409251456899644595e-01$	$-8.479690442977535492e-01$ $-8.942091740987367920e-03$ $5.299703188934734577e-01$	$-5.793236657093742137e-02$ $-9.923041270020136473e-01$ $-1.094365589657392002e-01$	$3.653892485834579915e+06$ $2.168200361245413369e+05$ $-3.888199078206335660e+06$
2	$4.762973074145767649e-01$ $-1.648094606707988796e-01$ $8.637005943167026523e-01$	$-8.787277438834268928e-01$ $-1.241624101523292056e-01$ $4.608917964497826203e-01$	$3.127981903987681056e-02$ $-9.784791962931892462e-01$ $-2.039608671835540232e-01$	$3.881868242148630787e+06$ $8.681039388580626110e+05$ $-3.562789552718312945e+06$
3	$4.799094285684389338e-01$ $-1.631833808821324117e-01$ $8.620081928699933060e-01$	$-8.769296643180777284e-01$ $-1.184574801786891785e-01$ $4.657920021089879681e-01$	$2.610180472876300062e-02$ $-9.79458528776789e-01$ $-1.999492090414691781e-01$	$3.867635424062634353e+06$ $8.364325678245576564e+05$ $-3.585753475134216249e+06$
4	$4.779634729803913795e-01$ $-1.618768574082357636e-01$ $8.633346984409674407e-01$	$-8.777408223123600584e-01$ $-1.255004047884578644e-01$ $4.624075012846948218e-01$	$3.349578097230143658e-02$ $-9.787980033865857354e-01$ $-2.020705352679818545e-01$	$3.874490450892680325e+06$ $8.709906690686068032e+05$ $-3.570114168317223433e+06$

3.3.8. *Framework for Measurement One* – Estimating displacement and velocity across glacier at various sample points

Camera Parameters: For each specific batch of photos, intrinsic camera parameters are attained independently using Agisoft's *Photoscan*.

SFM with *Photoscan*: Sample images from many camera angles are used to create a digital-elevation model (DEM) of the Tasman Glacier.

Ground Control Points (GCPs): Measurements made in-situ on the 18th of March 2016 using Trimble GNSS.

Pixel World Displacements at chosen points are calculated. The output is a time series of x and y displacements, and correlation coefficients. This is achieved using Imcorr or Elizabeth Jone's Digital Image Correlation (DIC) algorithm.

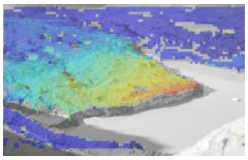

Orthophoto import to QGIS: **Select digital sample points.** (*displacement_points.py)*

Extrinsic Camera Parameters: Rotation and translational matrix is accounted for in *cam_extrinsic_gcp.py*

$$\begin{pmatrix} x_c \\ y_c \\ z_c \end{pmatrix} = R\begin{pmatrix} x \\ y \\ z \end{pmatrix} + T$$

Identify new **Projected Points** using digital points and real-world GCPs on each subsequent image in batch. (*cam_project_point.py* and *project_displacement_points.py)*

Direction of Flow: GPS data provided by Horgan *et al,* (2015) to attain a direction of flow used to calculate the Flow Scale Factor (FSF) which resolves image geometry errors.

Flow Scale Factor (FSF): Is ascertained using (*cam_points_scale.py).*

Real World Displacements are calculated using the Flow Scale Factor (FSF) and Pixel Scale Factor (PSF) in the following formula: Real World Displacement = Pixel World Displacements * FSF * PSF (*cam_plot_imcorr.py)*

Post-processing 119 real-world evenly spaced (100 m) grid is plotted on top of the glacier in QGIS. FSF and Pixels Scales are calculated beforehand at these locations. Examination of results are also done in QGIS.

Post-processing Conducted in Matlab, where grid positions from the DIC and the grid positions from 119 sample points plotted in QGIS are matched. The results are then translated and plotted against time. (*DirectionOfFlowAttain.m* and *VelocityConversionFinal.m*)

Figure 3.3.8

3.3.8.1 Measuring Pixel-world Velocities and Direction of Flow

In parallel to the GCP post-processing, displacement and velocity as well as the pixel-space direction of flow were calculated. This sub-section will elaborate on the steps used to quantify the first of our two main measurements, velocity.

In the case of our methodology, we adopted the more simplistic[2] single-image, single-chip DIC algorithm to solve for ice flow. Following Jeong and Howat (2015), we corrected images for movement using image stabilisation software and the extrinsic camera parameters ascertained in previous steps. Moreover, the accuracy of their correlation results was mapped using a 'Matching Ratio' which represents the ratio of successful pixel matches (ranged 0-1, where the higher the better the match). We produced a correlation coefficient map which is analogous to the 'matching ratio' of Jeong and Howat (2015).

In the following sections, we present our DIC methodology in a stepwise manner from the conversion to grayscale to our final outputs using an adaptation of Elizabeth Jones's *Improved Digital Image Correlation Algorithm* in Matlab and an assemblage of QGIS/Matlab/iPython tools.

3.3.8.2. Grayscale Conversion

As opposed to conventional aerial photography whereby flights would only operate on clear, sunny days, oblique photogrammetry techniques implies that a large number of images will be unusable due to the indiscriminate capture of visual data across all weather conditions.

In Vernier *et al* (2011), this problem was solved by selecting two images of similar lighting conditions, and converted the images into grayscale via the following formula:

$$I_{gray} = 0.30 \times I_{jpeg}(\text{Red}) + 0.59 \times I_{jpeg}(\text{Green}) + 0.11 \times I_{jpeg}(\text{Blue}). \qquad (3.6)$$

Likewise, stabilised, post-processed images were converted into grayscale to improve the quality of the feature identification and tracking process.

[2] Compared to Ahn and Howat's (2011) Multi-image/Multi-correlation (MIMC) 'RIFT' Algorithm, our methodology only used a single set of correlation parameters among many images.

3.3.8.3. DIC in Matlab

Following each batch's conversion to grayscale, the *Improved Digital Image Correlation* algorithm was utilised (Jones, 2015). Jones' (2015) algorithm was initially designed for engineering applications to measure strain and deformation using speckle-patterns on an object. The benefit of her DIC algorithm was that it allowed images to be processed in sequential order across a user-specified grid spacing and subset size (see Figure 3.3.8.2.). The subset size fundamentally affects the reference subset used for cross-correlation with the subsequent image and underpins the accuracy of the correlation (Pan, B *et al.,* 2008). A larger subset size will account for larger movements and produce more unique outcomes however at the expense processing time.

To attain the optimal subset size, we tested correlations between images spaced a month apart across different subset sizes and found the optimal subset size to be 51 pixels for all batches. This produced an average matching coefficient of ~0.88 for images spaced a month apart which was adequate.

We then applied the same settings across a variation of grid spacing. The lower the grid spacing, the more grid points are produced and likewise, is inversely proportional to processing time. After experimentation, we found that a grid spacing of 20 pixels would yield a fine enough result without compromising processing time significantly. This meant that for images in our first batch, it amounted to 8816 grid points, and for batches 2-4, 9480 grid points were used for correlation.

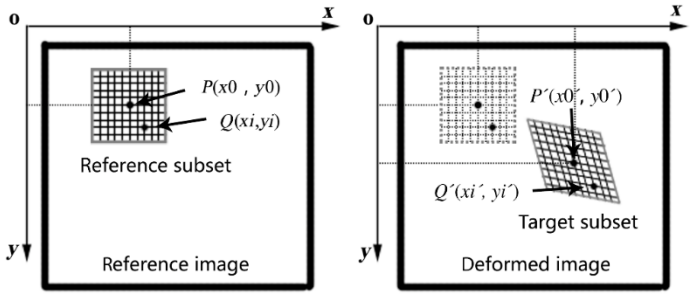

Figure 3.3.8.3. Illustrates the basis of Digital Image Correlation (DIC) using a reference subset which is then identified in the deformed image to approximate direction and magnitude of flow. *Source:* Liang, Z *et al,* (2013)

Once the correlation parameters were optimized, each batch was processed at a monthly timescale using a subset of 51 pixels, and grid spacing of 20 pixels. The results are then presented in terms of horizontal displacement, vertical displacement, magnitude of displacement, the correlation coefficients and finally a quiver plot showing direction of pixel-space flow. Only the total magnitude of displacement, quiver plots and correlation coefficient plots are shown in the results due to the amount of data produced in this

process.

3.3.8.4. Pixel Flow into Real-world Flow

A conversion from pixel velocities to real-world velocities requires an understanding of the camera's position from the object and is represented by the Extrinsic Camera Parameters. Using those attained from our GCPs in the field, and a velocity field of the Tasman Glacier, a factor known as the Flow Scale Factor ('FSF' or S_f) and the Pixel Scale Factor ('PSF' or S_p) is then calculated for each specific sample point. The magnitude of displacement in the real-world is therefore a multiplication of the pixel-space magnitude by this FSF and the PSF. For below, X_{pixel} is the pixel movement between images and X_{real} is the equivalent displacement in the real world.

$$\mathrm{X_{real}} = S_f S_p X_{pixel} \qquad (3.7)$$

$$v = \frac{dX_{real}}{dt} \text{ - Velocity} \qquad (3.8)$$

Individual sample points (119 samples in total, spaced 100 m) were chosen with their own respective FSF to estimate glacier velocity over time. For batch one the FSF was uniformly 1.07139 which implies that 7% of the real-world movement for every pixel could not be observed due to the camera obliquity. Each sample point however has a unique pixel scale factor which additionally encapsulates the apparent parallax. Likewise, batch two had a FSF of 1.12029 (+ 12 %), batch three a FSF of 1.11696 (+ 11 %) and batch four a FSF of 1.12129 (+ 12 %). These are markedly different owing to a different camera and lens setup post-July 2013.

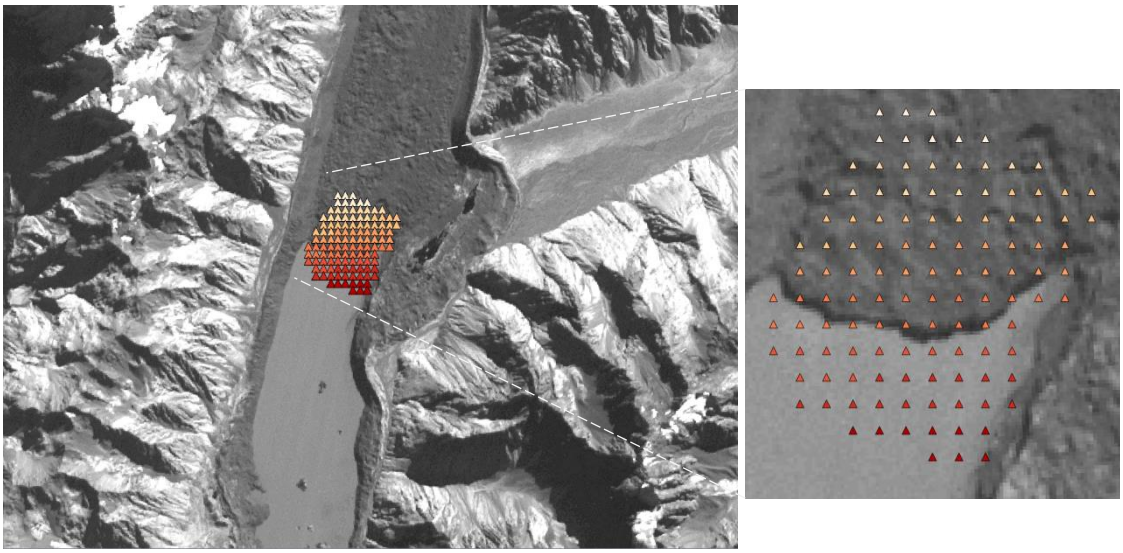

Figure 3.3.8.4. Shows 119 sample points created from an equidistant grid over the Tasman terminus region. Velocity will be calculated at each of these sample points if available. Distance between sample points is 100 m. Rear image – ASTER captured on 9th April, 2016.

3.3.9. *Framework* for *Measurement Two* – Digitizing Terminus Position relative to Lake Level for Retreat Rate (U_r) and Planform Area Flux ($\frac{dA}{dt}$)

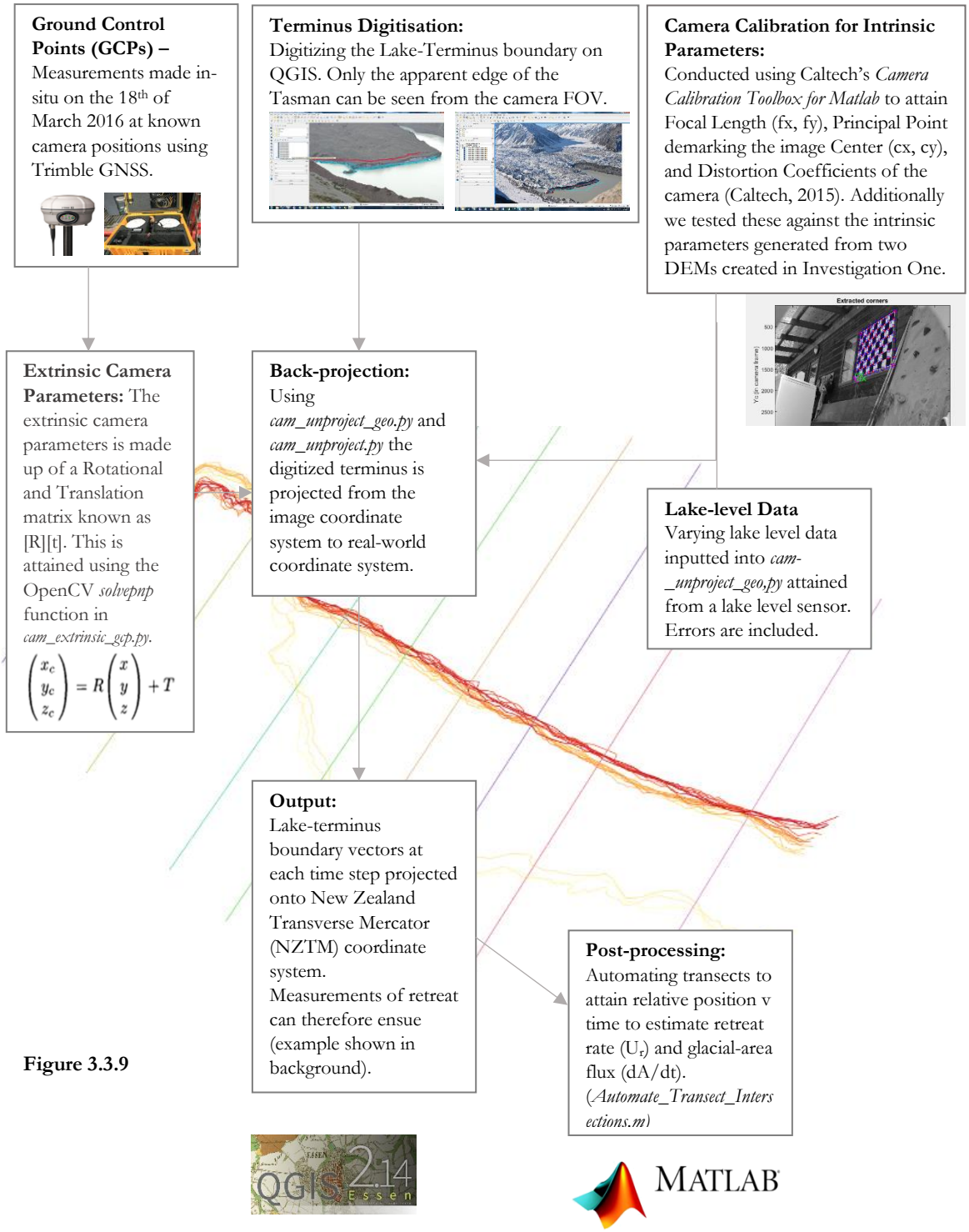

Figure 3.3.9

3.3.9.1. Measuring Terminus Position

Terminus positions from our oblique images was quantified by digitizing the lake-ice boundary where the waterline contacted the terminating ice cliff. Initially, consideration of automated detection software such as the *edge* function in Matlab was attempted, however it proved more difficult than expected due to the dynamic nature of this boundary. In contrast, by manually digitizing the terminus meant we could account for the irregular morphologies as well as differences in contrast or lighting presented in the images. Examples of the irregular types of ice cliff features we had to digitize across are shown here in QGIS.

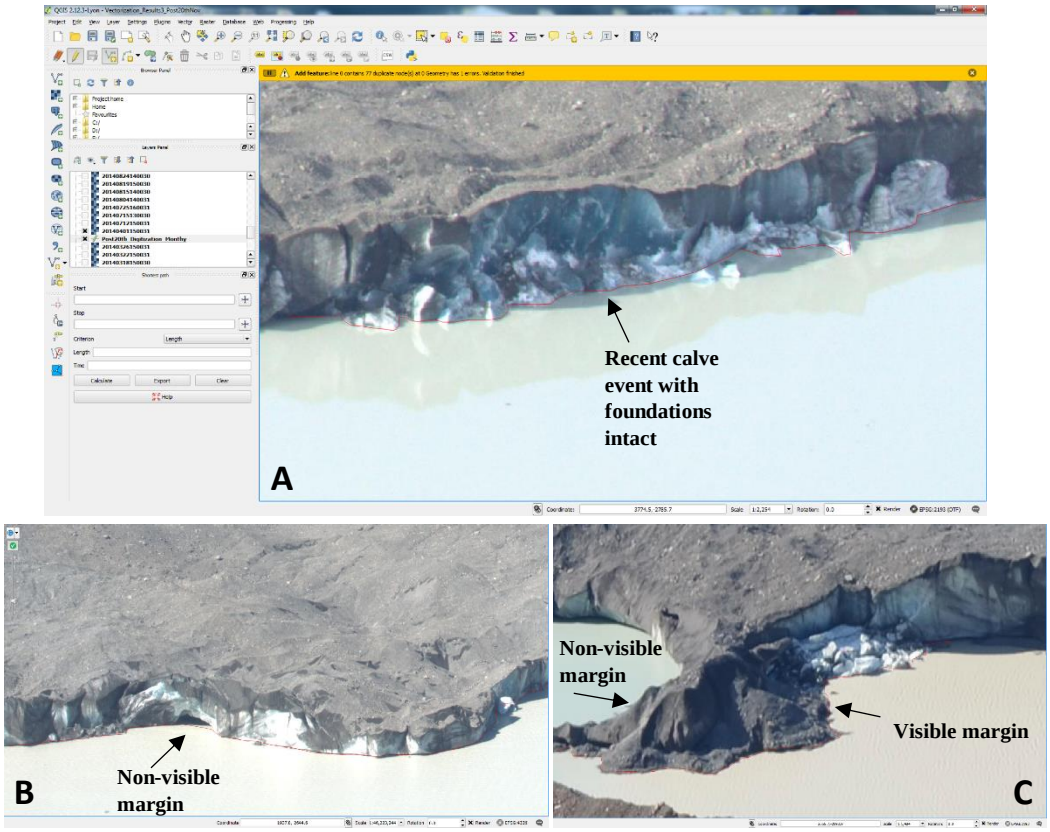

Figure 3.3.9.1a. Shows various irregularities in the lake-ice boundary during manual digitisation. (A) A recent calving event has left a fresh scar. The lake-ice boundary we defined as the apparent edge even if the event has left ice at the base of the ice cliff. (B) Shows a cavity burrowed in the ice cliff. We assumed the smallest distance to the other side of the cavity rather than digitize into the cavity. (C) A portion of ice that covers vision of the lake-ice boundary. Here, we ended our digitisation at the closest visible vertex of the ice.

Due to the diverse ice-cliff morphologies, the following rules for the digitisation process were established to minimise the associated human errors.

- **Cavities in ice cliff**: Digitize across cavity with the shortest distance between the start and end of cavity.
- **Non-visible margins**: End the digitisation if the lake-ice boundary cannot be seen or if there is a break in the boundary.
- **Supra-glacial debris slip**: If debris has come off the glacier and a fan now sits over the lake-ice boundary, digitize around the fan and assume it is part of the ice.
- **Shadows cast by ice cliff**: Visually delineate between the boundary and shadow. Zoom for increased accuracy.
- **Recent calving event with foundation intact:** Digitize the lake-ice boundary as visually depicted.

Following the manual digitisation process for each Batch of images, unprojection from the pixel-world to real world positions took place. This was achieved using the *cam_unproject_geo.py* script which utilises the rotational matrix and translation vector matched with the corresponding elevation to unproject each of the digitized points.

Using the ideal camera model from equation 1.21 (*see Chapter One)*, lambda (depth) needs to be attained in order to do a back-projection (or unprojection) from (*u,v*) pixel coordinates to (*Xo,Yo,Zo*) real-world coordinates. The steps are as follows:

(1) Find gradient of line between camera and real-world ice/water interface by doing a forward projection using equation 1.21 for two different values of lambda
(2) Use the gradient, camera elevation, and lake level, to find *lambda_ice* - the depth between the camera and the ice/water interface
(3) Rearrange equation 1.21 to get equation 3.9:

$$R_{wc}^{-1}(A^{-1}\lambda\mathbf{x_u} - t_{wc}) = \mathbf{X} \qquad (3.9)$$

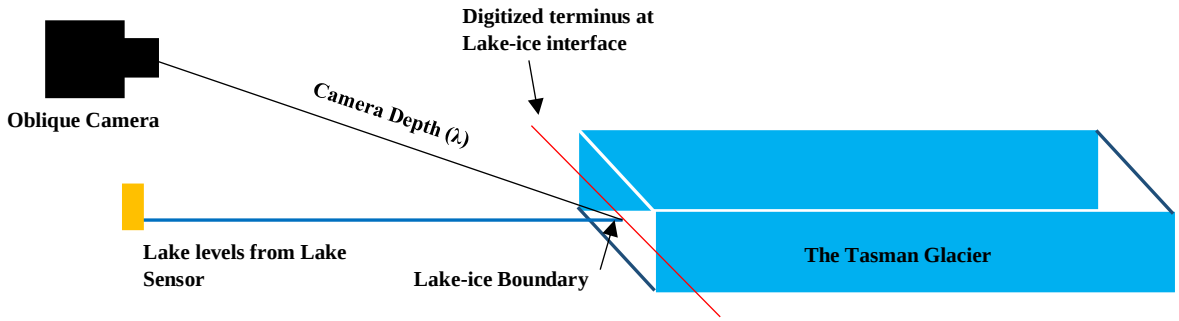

Figure 3.3.9.1b. Shows a simplistic model on how the camera depth was attained by estimating various slopes towards the digitized terminus. The lake-level was used to intersect the many digitized termini to calculate the camera depth for every image and every batch. Vectors are converted from the image plane to the real-world plane using this technique. *Source:* Dr. Brian Anderson

Elevation was attained by inputting lake level data captured hourly using a lake-level sensor situated on fringe of the lake. Data from the lake sensor are those used in Horgan *et al.*, (2015). The output is a collection of 152 lines across the four batches in the New Zealand Transverse Mercator (NZTM) projection system which represent real-world terminus positions.

3.3.9.2. Automating Transects for measuring relative termini positions

A caveat to most remote sensing of position is that it relies on a scale by which measurements can be inferred from. The irregular shapes of our digitized termini reinforces this point because depending on where our measurements are made, one particular calving event can be appear larger or smaller than its true value. Furthermore, to quantify the surface area of the terminus region, changes in planform area would have to be calculated relative to a scale (or rectangle). Outline of these post-processing techniques are shown in the following subheadings.

Firstly, transects of even length was drawn onto our existing termini data to serve as a reference for distance. Further, intersections of these transects with our digitized termini was then used estimate the average retreat rate (U_r) for the Tasman Glacier for 2013-2016 at sub-weekly time steps.

An initial reference transect was first digitally drawn using the *ginput* command in Matlab to intersect our 152 unprojected termini vectors. The two endpoints (x_1, y_1; x_2, y_2) were saved and then translated by stepping 100 m in the x direction and 5 m in the y direction to construct twenty equal length transects in uniform direction across the glacier front.

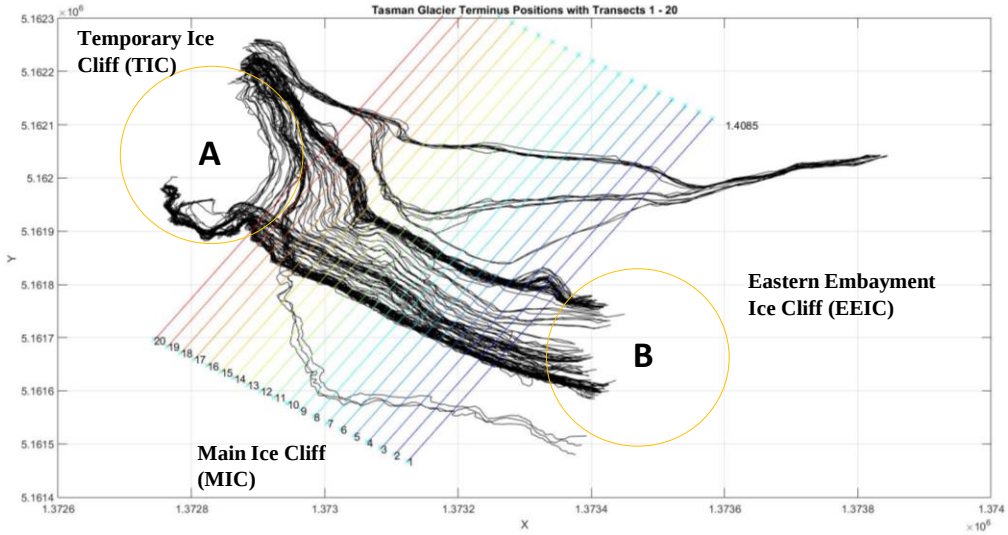

Figure 3.3.9.2. Shows real-world termini vectors with 20 transects automated across in an assumed direction of flow drawn perpendicular to the termini of 2014-2015.

Transect projections across the regions A and B (see Figure 3.3.9.1.) were not implemented because the former (Temporary Ice Cliff) contained a region where earlier digitisations ended abruptly due to the unseen lake-ice margin and similarly in the latter (Eastern Embayment Ice Cliff), for the bulk of our digitisations, with the exception of those post-Jan 2016 when the glacier had receded far back enough for the margin to be visible.

3.3.9.3. Calculating intersections with transects

Once the all the transect endpoints have been stored in Matlab, they are then converted to vectors using the *linspace* function and evenly-spaced the vector size of each digitised termini in two *for* loops. Transects were required to have the same number of vectors because the *intersection.m* script we used creates rectangular search zones for each vector point to attain robust intersections between two curves/lines (Schwartz, 2006). The *automate_intersections.m* script outputted x and y coordinates of every intersection and the scalar position of the intersections as measured on our twenty transect rulers from left to right, bottom to top (see Figure 3.3.9.3.). In total 3080 intersections were calculated and plotted. All intersections were measured off a 789m digitally drawn transect.

3.3.9.4. Estimating relative Area Changes

Conceptually, estimations of planform area between the undistorted digitized points would have been a simple task if the points were computer generated and thereby smoothed (i.e. in modelling) or if our results were forced to fit a polynomial. In order to solve this spatial problem, I used boundary areas created to surround all termini positions and constrained by transects 1 and 20.

By doing this, ice-area was approximated from first principles using a methodology to create a polygons encapsulating each terminus position. Specifically, a horizontal boundary line in front of the terminus (see Figure 3.3.9.3) was used as a baseline to form a polygon. Following this, intersections with each termini and transects 1 (right-hand margin) and 20 (left-hand margin) were calculated. By way of using *linspace* and the *polyarea* functions in Matlab, surface area flux from each time step was therefore attained.

One must note that because the *polyarea* function estimates between the boundary line and the terminus, the output is actually representative of the lake-area changes. To attain changes glacier area, we simply subtracted the lake-area change from the cumulative area of the most recently captured terminus position (i.e. from our final image 22nd March 2016).

This concludes the post-processing component of our images to attain the real-world position of the terminus and surface area change using oblique photogrammetry techniques.

3.4 Phase Four: Results and comparisons

Once terminus retreat rates (U_r) and vertically-averaged flow speeds (U_t) are calculated, it is then possible to attain a calving rate for the Tasman Glacier.

3.4.1. Calculations for the Calving Rate

Changes in the terminus position is given by the sum of three varying rates of change (1) The rate of at which the glacier moves down valley, given by a vertically-averaged ice velocity (U_t), (2) by the rate of calving (U_c) which acts in the opposite direction (3) and lastly by the rate of melt ($\dot{m}$) which thins the glacier front but occurs on slower timescales compared to calving (Amundson and Truffer, 2010).

$$\frac{dX}{dt} = u_t - u_c - \dot{m}, \qquad (3.9a)$$

Following Dykes *et al.*, (2010) the calving rate was simplified by assuming melt rate is negligible. Therefore U_c calculated by the subtraction of the rate of retreat (U_r or dX/dt) from the vertically-averaged ice velocity (U_t) (Benn *et al.*, 2007).

$$U_c = U_t - U_r \qquad (3.9b)$$

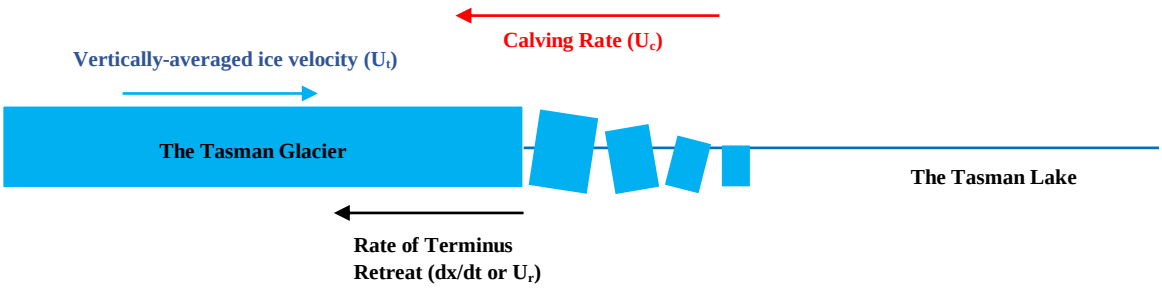

Figure 3.4.1. Shows a qualitative model explaining the rate of terminus retreat comprised of the rate of calving and the vertically averaged ice velocity. This model ignores the melt rate of the glacier.

CHAPTER FOUR
Results

4.0 Introduction

In this chapter, I present this study's findings for the Tasman Glacier for 2013-2016. Results are comprised of two sub-chapters for each of our measurements shown in our methodology. In *4.1.*, I present position measurements attained via manual digitisation in QGIS and further analysis in MATLAB to approximate surface area loss and rates of retreat and in *4.2.* I disclose pixel displacement distributions across the glacier attained using digital image correlation (DIC) methods

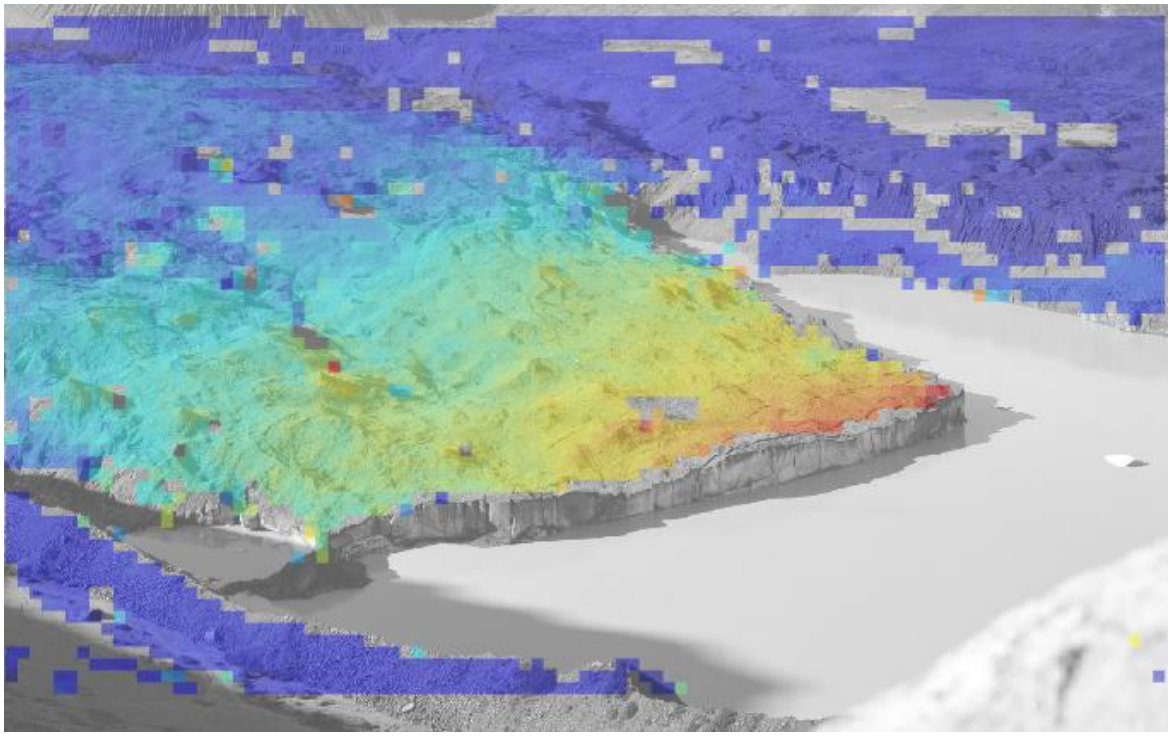

Figure 4.0.1. An example of the output from the Digital Image Correlation (DIC) phase used to attain position changes on the glacier and annual velocities. Correlations are conducted on a block by block level with a fixed search zone of 51 pixels and a gridpoint spacing of 40 pixels.

Batch One - 19 Digitisations

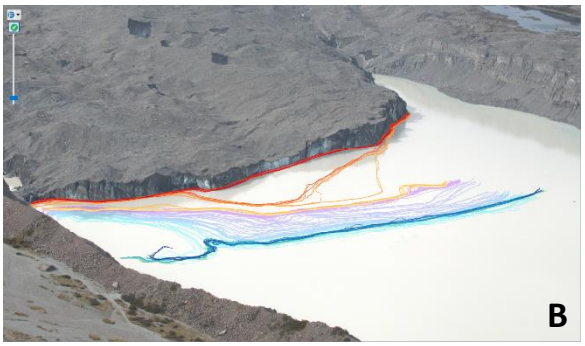

Batches Two to Four – 133 Digitisations

Figure 4.0.2. Presents digitized shapefiles in QGIS for Batch 1 (A) and Batches 2-4 (B).

4.1. Observed terminus position changes (2013-2016)

In the study period from the 5th of February 2013 to 22nd March 2016, the Tasman Glacier experienced three major calving events from the Main Ice Cliff (MIC). The first event occurred on the 22nd of February 2013, 17 days after the first camera installation. The latter two events occurred in the summer of 2016 and were within weeks of each other. No position observations were made of the Eastern Embayment Ice Cliff (EEIC) as the terminus-to-lake interface was not visible from our oblique camera perspective.

Reprojected terminus positions were plotted against an independent record of lake boundaries acquired from disparate sources. This record was comprised of a combination of LANDSAT, ASTER, NZ Topomap and terrestrial Structure from motion (SFMs) outlines. The reprojected terminus positions aligned with the lake boundaries in our independent records (*see Figure 4.1 below*) and confirms the validity of our results.

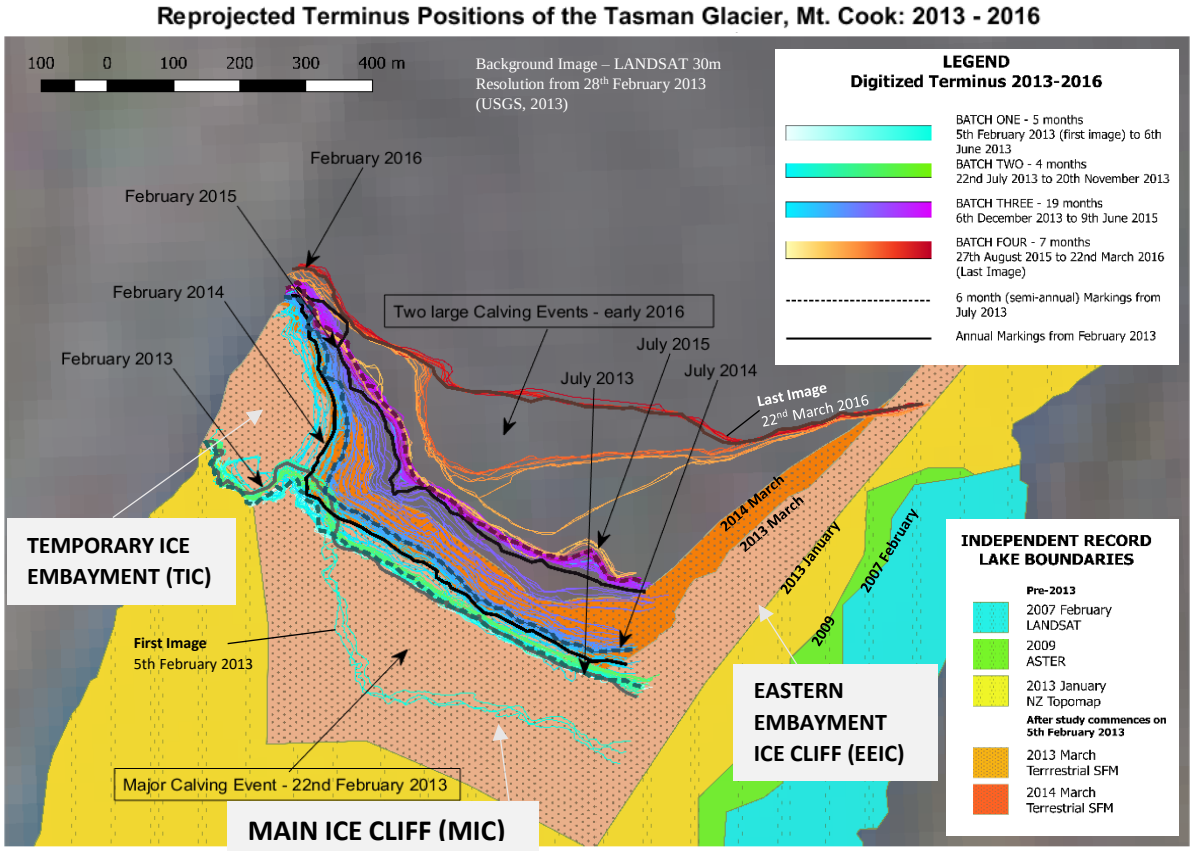

Figure 4.1. Presents the final unprojected termini digitisations in NZTM 2000 compared against an independent record of lake boundaries. The undistorted lines align well with the independent record and validates our methodology. *Base image source:* 30m resolution LANDSAT image from 28th February 2013. *Source of Terrestrial SFM:* Dr Anderson, Brian

4.1.1. Rates of retreat (U_r) from Batches 1-4

Spatial patterns of terminus retreat was ascertained using 20 transects evenly spaced along the ice front. The record is broken into batches 1-4 due to variations in image geometry posed by camera movement and camera change. The transect azimuth (*dx/dy*) is 0.71 or 215 degrees (SW) from grid north.

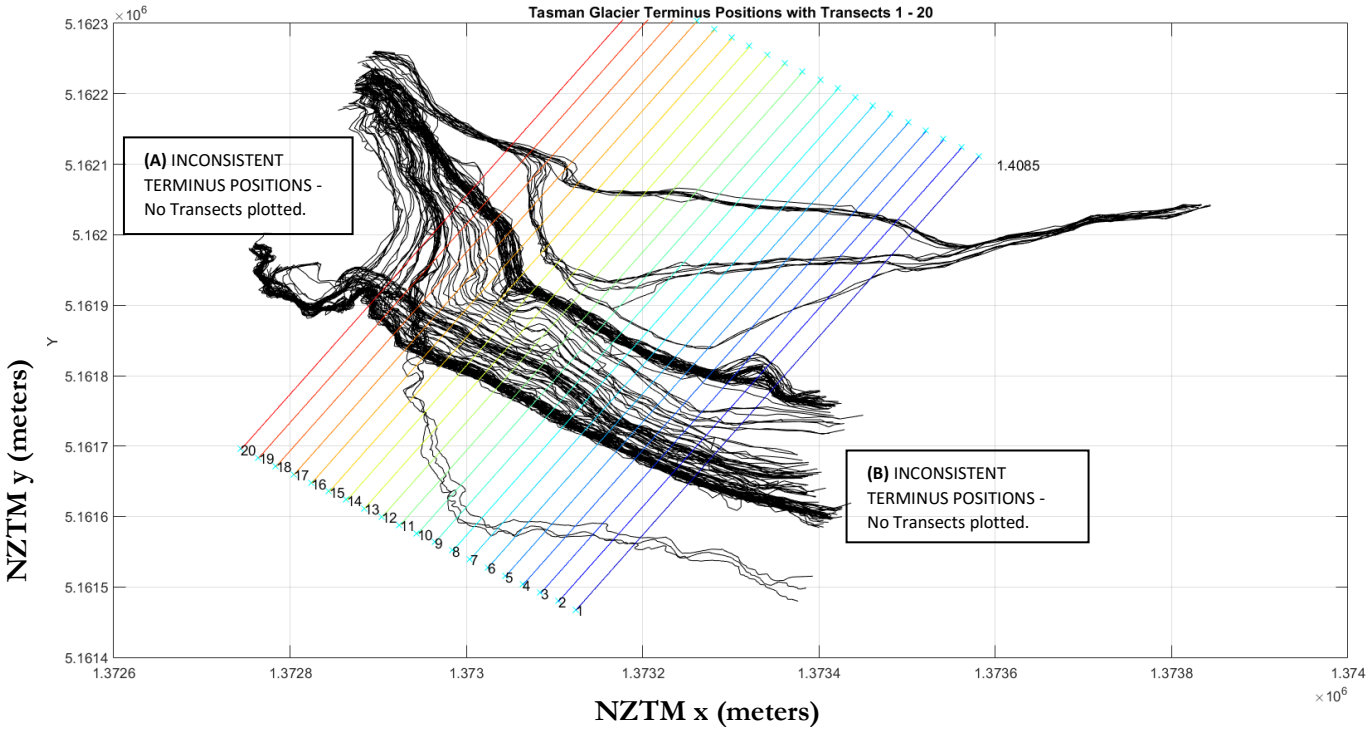

Figure 4.1.1.1. Shows the initial 20 transects plotted against reprojected terminus positions for February 2013 to March 2016. Regions A and B contain no transects due to irregularities in terminus positions (i.e. a recess in region A and non-visible margin at region B).

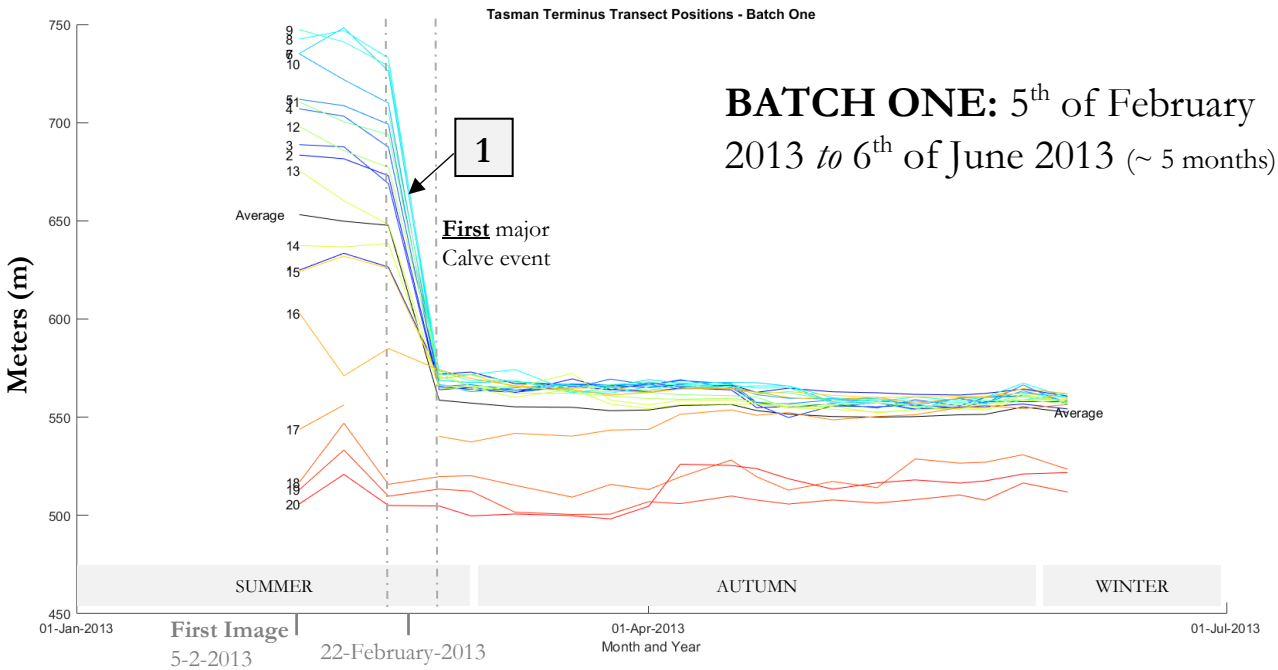

Figure 4.1.1.2. Batch one results of terminus position change at each transect over time.

For dates between 5th February and 6th June 2013, terminus positions from the MIC retreated a maximum of 185 m from a single calving event. The average rate of retreat (U_r) for this period was ~ 301 ± 93 m a^{-1} with a range of minimum - 47 m a^{-1} to maximum 703 m a^{-1} or ~ 0.825 ± 0.25 m day^{-1}. Standard error of the mean was 15.78 m. Measurements from transects 18, 19 and 20 indicated a minor advance in the glacial position of roughly 7 ± 23 m. The major calving event (22nd February 2013), averaged across all transects was a sudden retreat of the terminus by ~ 89 m.

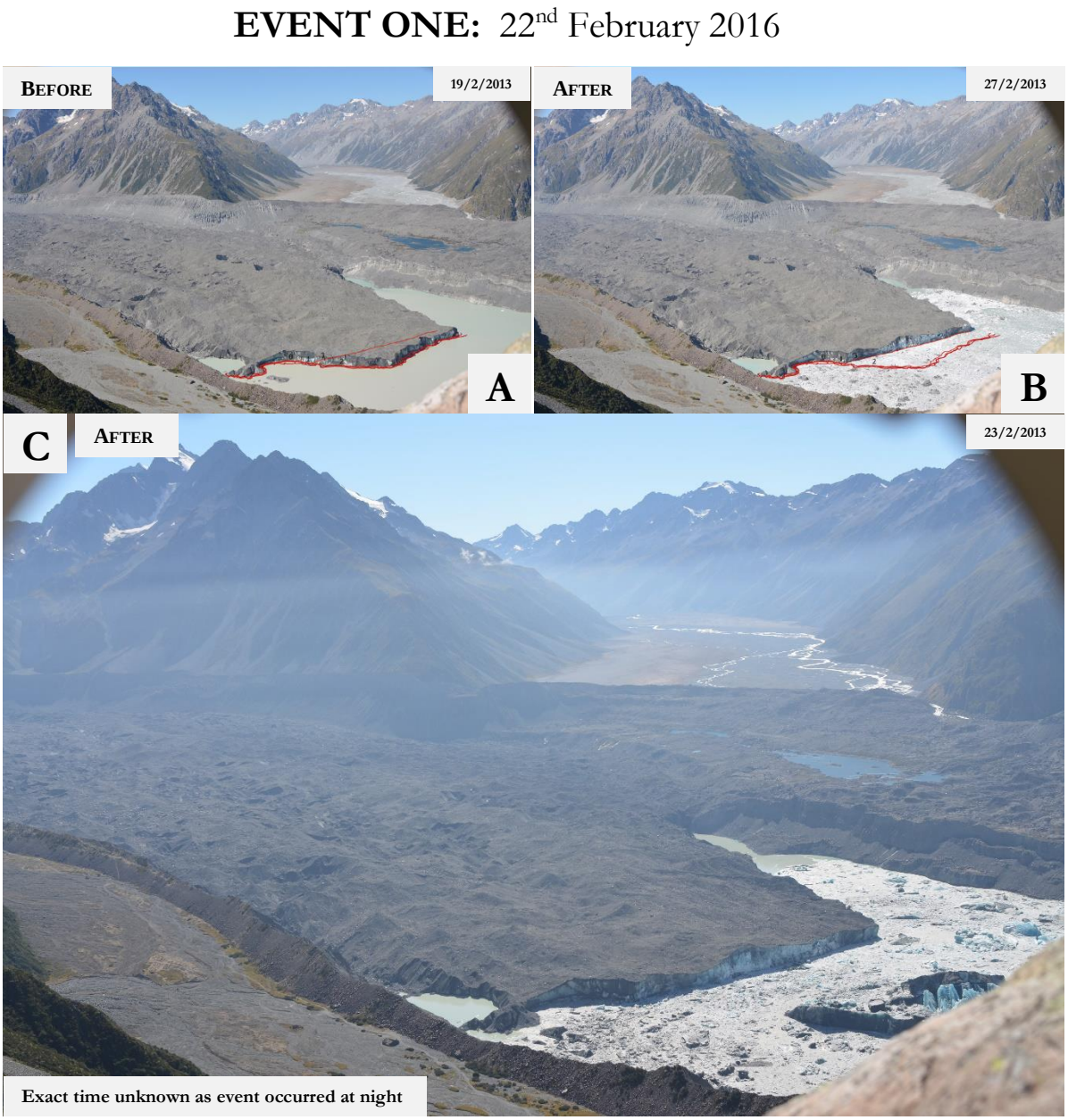

Figure 4.1.1.3. (A) Stabilised image from 19th February 2013. Three days before major calving event. **(B)** Stabilised image from 27th of February 2013. Five days after major calving event. **(C)** Several hours after event on the 23rd February 2013 10:00am. This image was not stabilised and not pre-processed due to hue variations and thus was not included as an image sample.

BATCH TWO:

22nd of July 2013 *to* 20th November 2013 (~ 4 months)

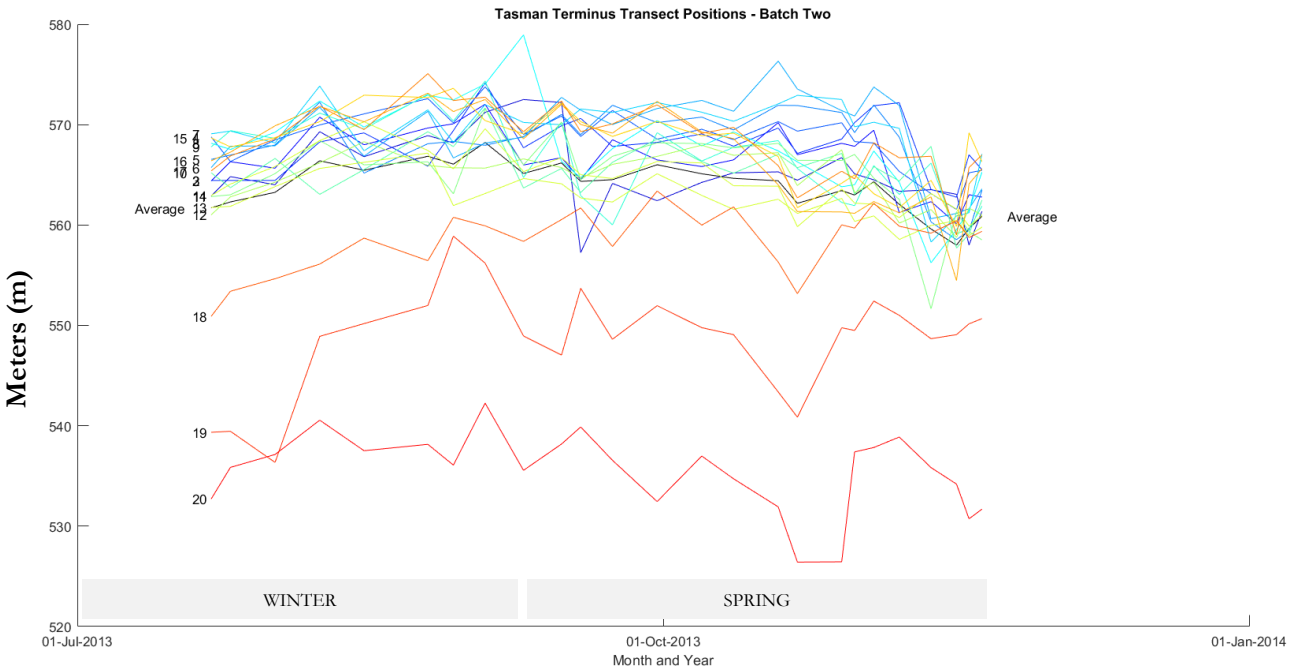

Figure 4.1.1.4. Batch Two results of terminus position change at each transect over time.

Batch two captured another 4 months of terminus positions. Transects 1-17 revealed relative stability of the terminus position (mean position = 563.74 m with max 568.23 m and min 557.99 m). The mean rate of retreat (U_r) during this period was 0.0023 ± 0.11 m day^{-1} or when extrapolated annually at ~ 2.57 ± 39 m a^{-1} (including data acquisition and standard errors). The observed U_r was significantly less than its respective mean error of ± 12.05 m for each termini (see *4.2.3 Errors for U_r*). Overall, measurements from all transects in batch two did not exceed more than 20 m advance or retreat at each time step. An advance trend is evident in all transects which peak towards the end of winter.

Batch three was by far the longest continuous record of terminus positions spanning 21 months or 639 days with no abrupt changes to the camera perspective. Average U_r was 82.33 ± 10.01 m a^{-1} or 0.23 ± 0.0274 m day^{-1} for this period. Loss of ice related to seasonality can be distinguished clearly by periods of progressive retreat and periods of relative stagnation or minor advance[3]. The maximum retreat was measured from transect 20 occurring in the summer/autumn of 2014. However, upon examination of image pairs, this change in glacier position resulted from the permanent detachment of an adjoining ice embayment on the

[3] Note that retreat rates are a function of surface velocities and calving rates. Therefore this seasonality in retreat rate indicates corresponding disparities in these variables.

western margin of the Main Ice Cliff (MIC) thereby relocating the transect intersection to a pre-existing position of the calving front.

BATCH THREE:

6th of December 2013 *to* 6th September 2015 (~ 1 year 9 months)

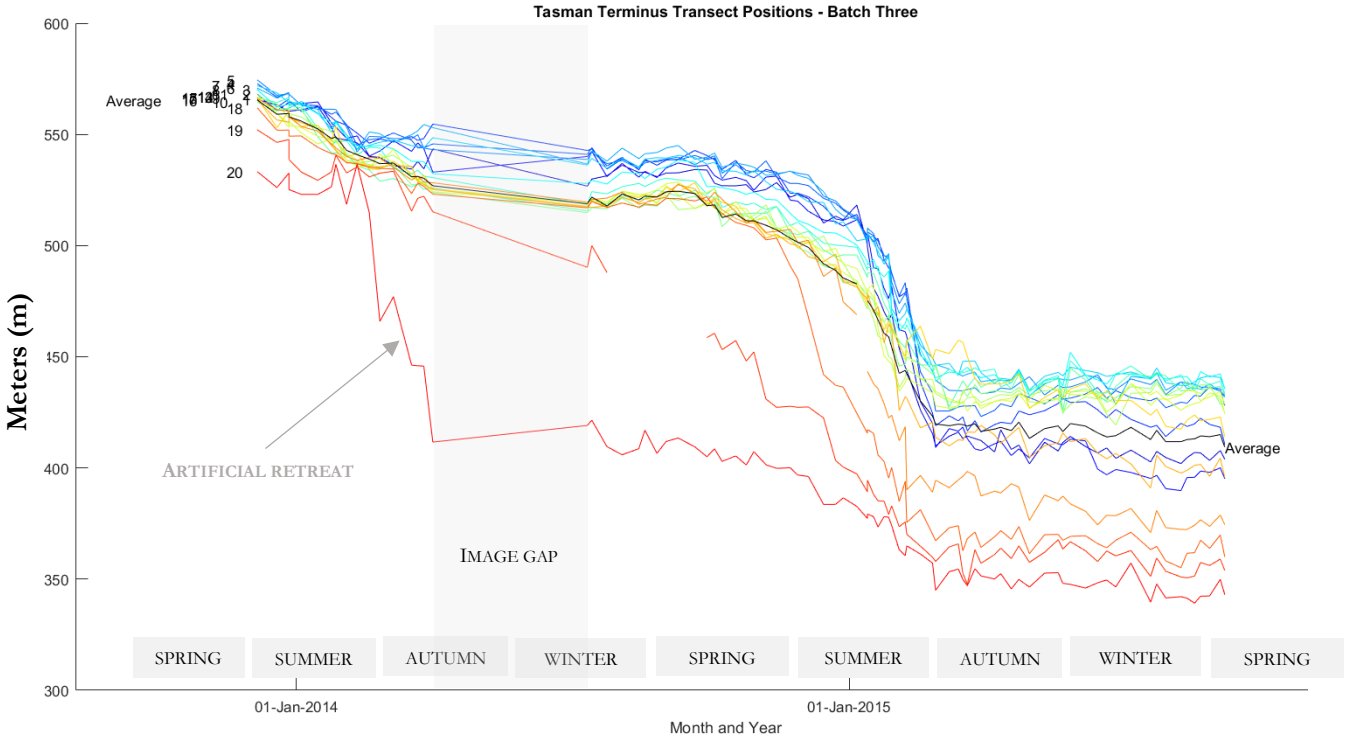

Figure 4.1.1.5. Batch Three results of terminus position change at each transect over time.

Observations from the final batch of images, Batch four, supported the accelerated calving trend during the final months of summer with two large calving events responsible for ~ 68% of the total terminus retreat in the entire 6-7 month period. Similar to the first major calving event recorded in February 2013, photographic evidence points towards calving of this magnitude occurring within hours of an image capturing no apparent signs of activity (see Figure 4.1.1.6a. and 4.1.1.6b.).

EVENT TWO: 20th January 2016

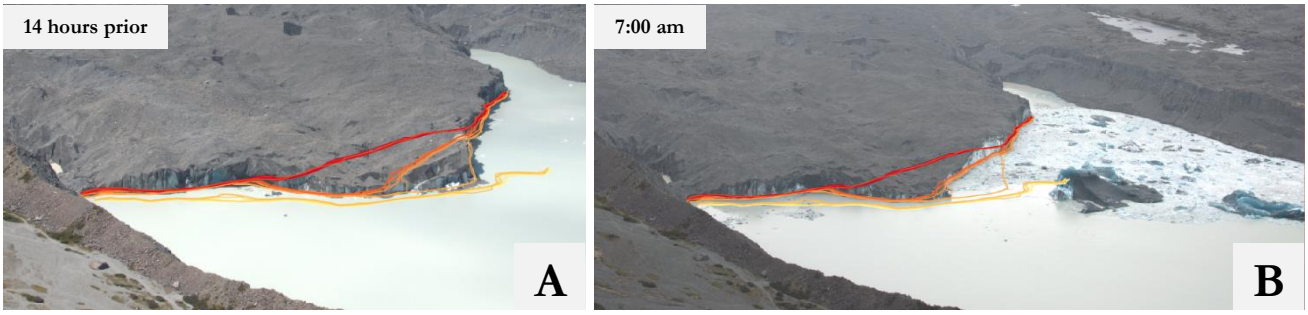

Figure 4.1.1.6a. Major calving event Two - (A) Image captured on 20th January 2016 at 3:00 pm, the afternoon before the calving event. (B) Post calving seen on the 21st January 2016 at 7:00 am.

EVENT THREE: 18th February 2016

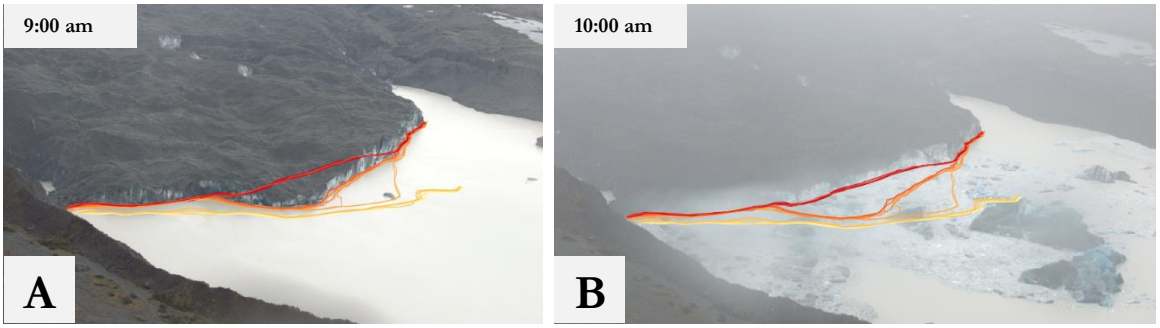

Figure 4.1.1.6b. Major calving event Three - (A) Image captured on 18th February 2016 at 9:00 am, an hour before the event. **(B)** Post calving seen on the 18th February 2016 at 10:00 am.

While there was a large data gap spanning ~ 3 months (*Figure 4.1.1.7)*, our results still show the average change over the period between 20 October 2015 and 19 January 2016. U_r over the entire batch period was 0.88 ± 0.148 m day^{-1} or equivalent to an annual retreat rate of 321 ± 54 m a^{-1}. A noticeable acceleration of the retreat rate (change in slope of transect lines) was observed in the late spring leading up to a climax with the two calving events in the summer of 2016, and followed by a deceleration of U_r in autumn across all 20 transects. Transect 4 recorded the maximum U_r of 459 m a^{-1}.

The overall U_r for the years 2013-2014, 2014-2015 and 2015-2016 are presented in the following section which will provide annually averaged rates of retreat for the Tasman Glacier for inter-annual comparison.

BATCH FOUR:

6th September 2015 *to* 22nd March 2016 (~ 6 months 24 days non-continuous)

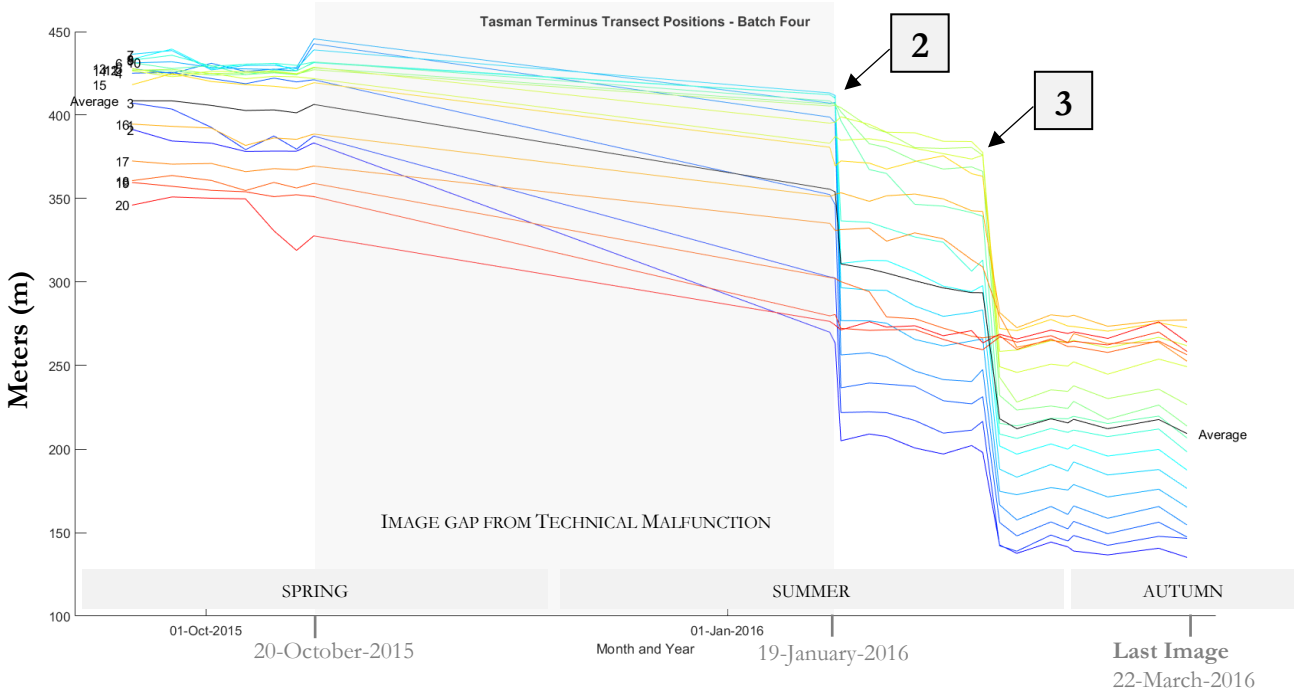

Figure 4.1.1.7. Batch Four results of terminus position change at each transect over time. Events 2 and 3 are marked.

Yearly averaged rates of retreat (U_r) have been widely used as a standard for comparing with rates from the past to indicate an acceleration or deceleration from year to year (Quincey and Glasser, 2009; Dykes *et al*, 2010). For this thesis, annual U_r is calculated commencing from the first image on the 5th February 2013 and concluding on the 22nd of March 2016 (equating to an extra month and 17 days for the 2015-2016 period and 1 year durations for the 2013-2014 and 2014-2015 rates). For the period 2013-2014, average U_r was ~ 116.32 ± 18.9 m a^{-1}. This diminished in 2014-2015 to ~ 82.48 ± 17.7 m a^{-1} and in 2015-2016, U_r experienced almost a three-fold increase to ~ 203.89 ± 20 m a^{-1}. In the three year study period, the Tasman glacier's Main Ice Cliff (MIC) receded an average of 443 m (minimum of 241 m and a maximum retreat 569 m) controlled by a relatively small number of events.

4.1.2 Summary of rates of retreat (U_r)

The findings for U_r are summarised in the table below for the relative positions of the Tasman Glacier terminus.

Table 4.1.2. Tasman Glacier rates of retreat (U_r): 2013-2016 Summary of results table.

Batch Number/Duration	Duration	Daily Mean U_r (m day^{-1})	Annual Mean Ur (m a^{-1})	Max Ur	Min Ur	Max Data Acquisition Error (m)*	Standard Deviation (σ)	Standard Error ($\sigma_{\bar{x}}$)
1 5th February 2013 to 6th of June 2013	4 months (121 days)	0.825 ± 0.254	**301 ± 92.68**	703.25	-47.11	15.2	70.61	15.78
2 22nd July 2013 to 20th of November 2013	4 months (121 days)	0.0023 ± 0.110	**2.57 ± 39.81**	9.26	-34.15	12.3	4.04	0.90
3 6th December 2013 to 6th of September 2015	1 year, 9 months (639 days)	0.23 ± 0.0274	**82.33 ± 10.01**	102.61	72.87	12.5	23.42	5.23
4 6th September 2015 to 22nd March 2016	6 months 24 days (208 days)	0.88 ± 0.148	**321 ± 54**	459.34	115.92	16.04	66.74	14.92
2013-2014	1 year	0.32 ± 0.052	**116.32 ± 18.85**	-	-	15.2	16.34	3.65
2014-2015	1 year	0.23 ± 0.049	**82.48 ± 17.74**	-	-	12.5	23.41	5.24
2015 - 2016	1 year	0.55 ± 0.055	**203.89 ± 20.11**			16.04	22.53	4.07
2015 - end of study	1 year and 47 days	0.67 ± 0.058	**348.59 ± 21.08**	-	-	16.04	22.53	5.04
All	3 years 47 days (1141 days)	1.21 ± 0.05	**141.99 ± 18.97**	-	-	16.04	13.09	2.93

*** For details on how errors were calculated for each data acquisition stage, see *4.2.4 Errors for U_r*.**

ALL BATCHES: 5th of February 2013 *to* 22nd March 2016 (~ 3 year 1 months 17 days or 1141 days)

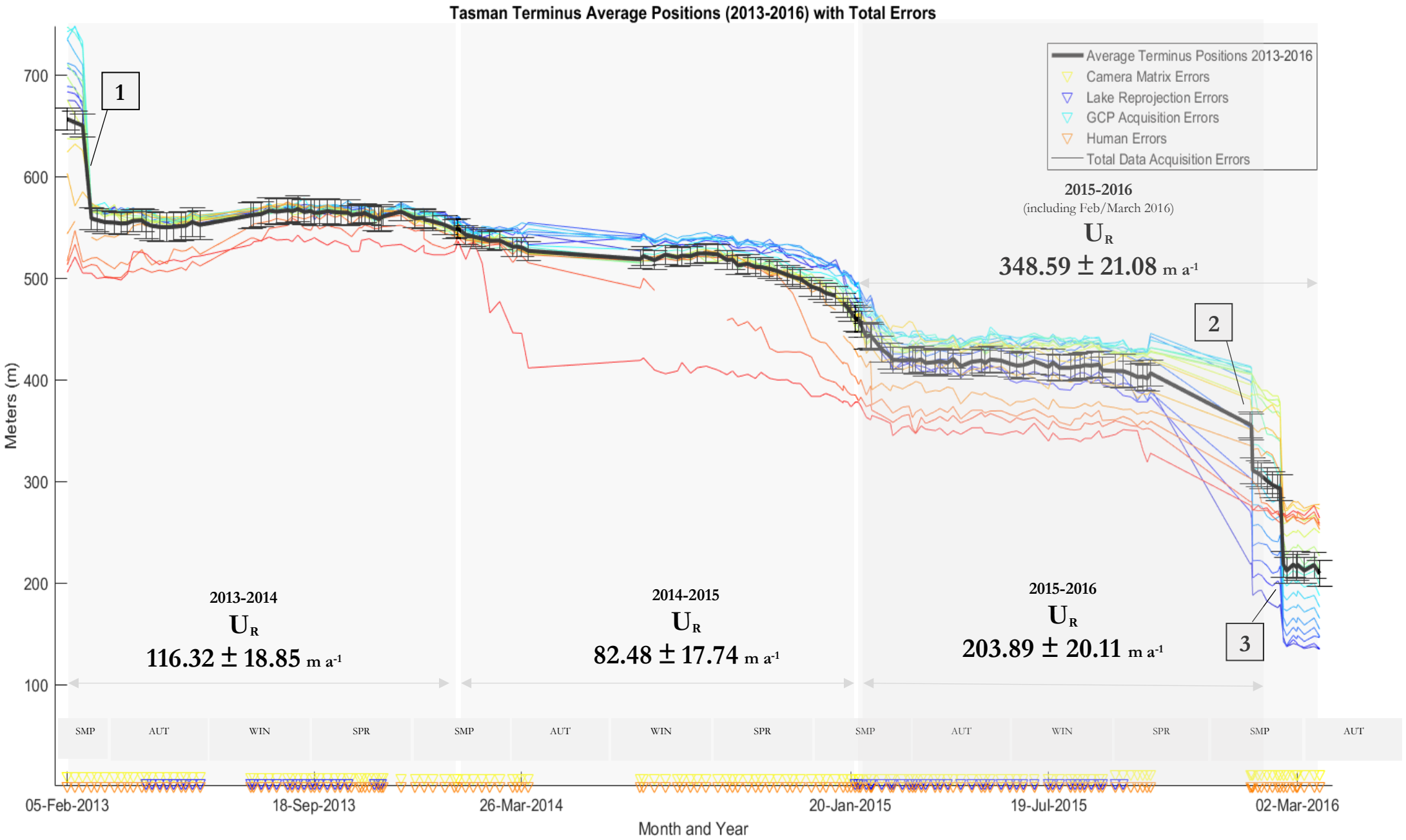

Figure 4.1.2. Positions from transects 1-20 for all four batches. For seasons: SMP = Summer, AUT = Autumn, WIN = Winter, and SPR = Spring. Gaps in the image series are represented by gaps in the error bars. Gray background markings are only visually indicative of annual blocks (i.e. 2013 to 2014), no temporal gaps were actually incorporated in the calculation of annual rates.

4.1.3. Errors for U_r

The estimated errors for the U_r calculations consist of four data acquisition errors (1) Camera Matrix Errors which are the errors associated with reprojecting the GCPs back onto the image using the camera model. The output of this process are our Extrinsic Camera Parameters with RMS errors in meters. (2) the Lake reprojection errors those that arise from errors in the lake levels (3) The Ground Control Point acquisition errors resulted from our Trimble GNSS R6 measurements in the field and (4) from human errors during the digitisation process of the terminus-lake boundary. Of the four errors, the Camera Matrix Errors and Lake Reprojection Errors were by far the greatest with deviations as high as ± 12.084 m and ± 3.67 m respectively of all image Batches. A breakdown of these errors are shown in Figure 4.1.4.2.

Optimisation of camera parameters using ground control points reduced reprojection errors significantly. This optimisation was presented in our methodology chapter where each batch of images has different reprojection errors. Errors from our field attained GCPs were close to the error specification of the Trimble GNSS (± 0.25 m) at ± 0.3157 m. Position errors from lake level are generally small (< 0.25 m) but much higher during data gaps where lake levels were estimated from rainfall records. In terms of human errors, pixel-level examination of terminus vectors revealed inaccuracies of up to ± 2 pixels. By multiplying the pixel scale (variable depending on position in image), a generous estimation of ± 0.5 m error in the real world was attributed to human errors.

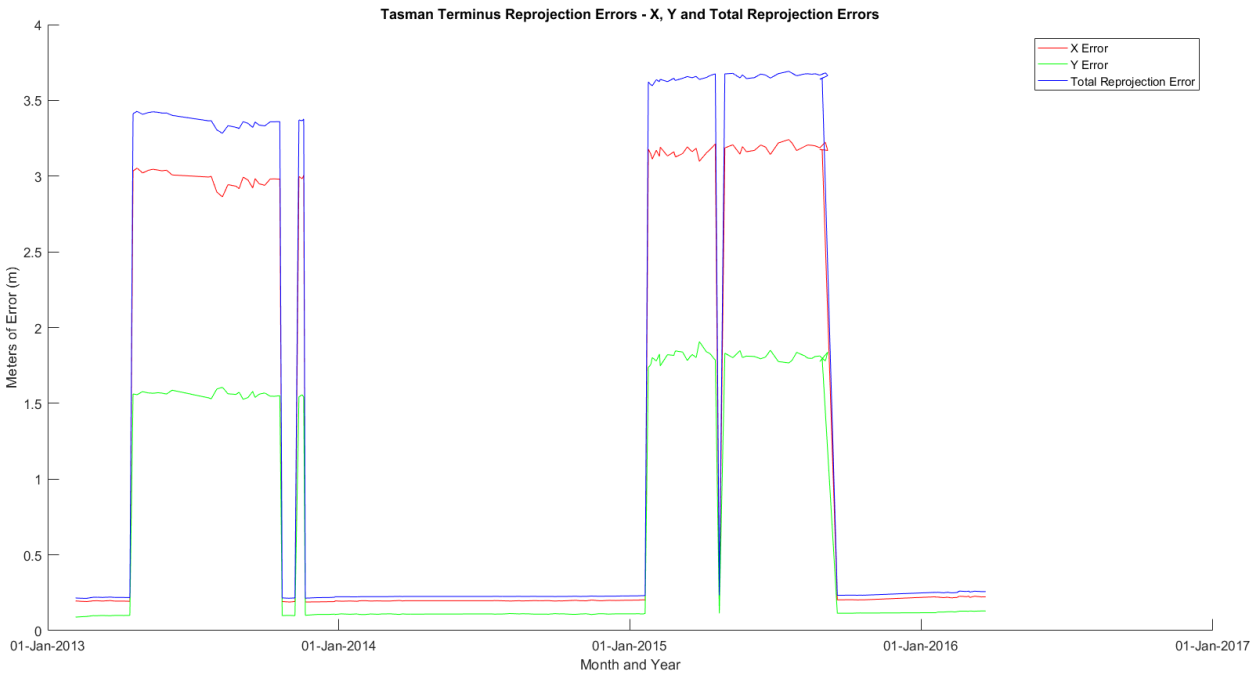

Figure 4.1.3.1 – Lake Reprojection Errors: Breakdown of reprojection errors in x and y directions. The maximum error is the superimposed value of x and y errors combined.

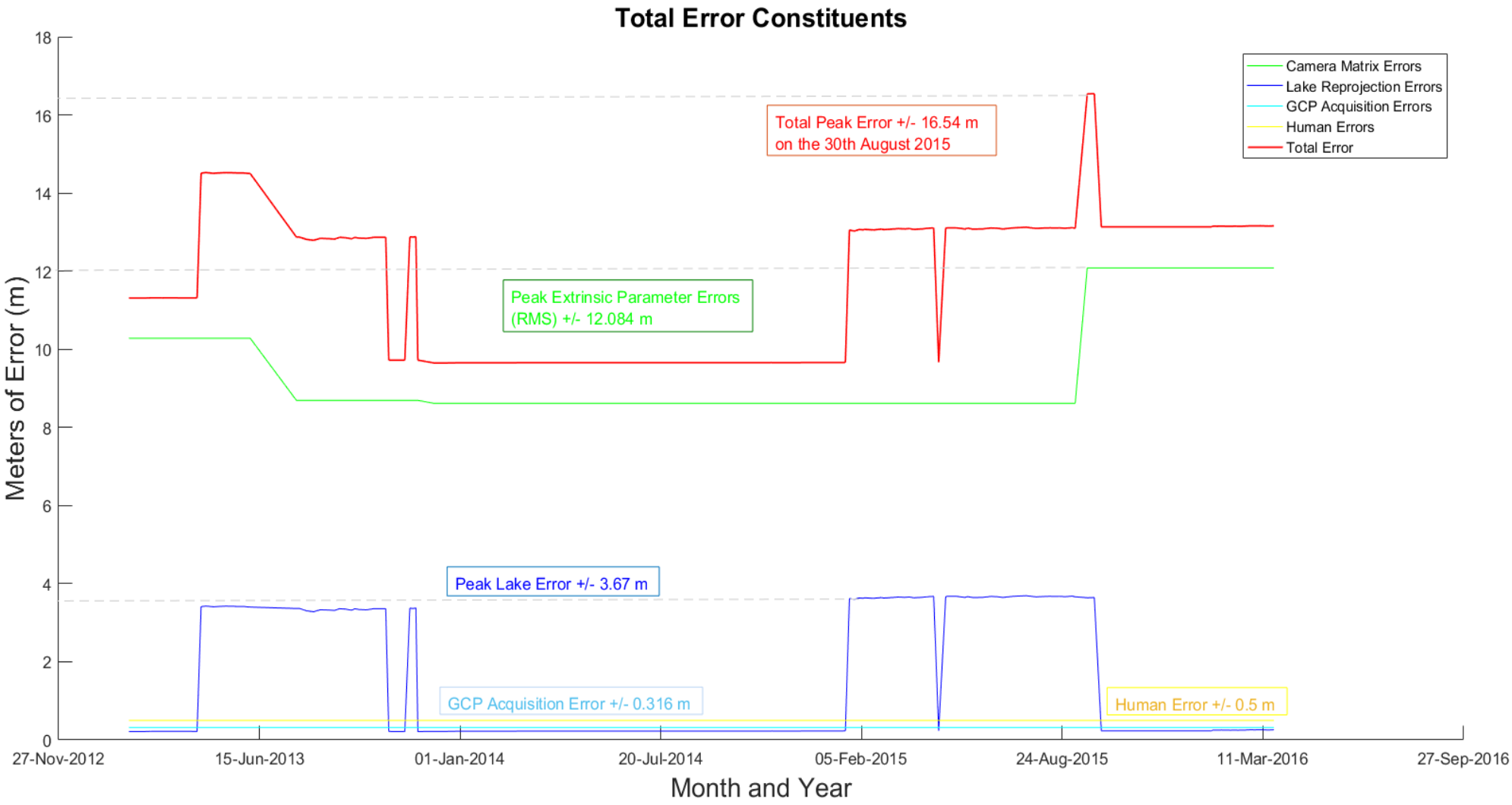

Figure 4.1.3.2 – Cumulative data acquisition errors: Breakdown of errors from our methodology. The peak error is ± 16.04 m. The total error is calculated by superposition of all errors in our study at each and every time step.

4.1.4. Surface area change (2013-2016)

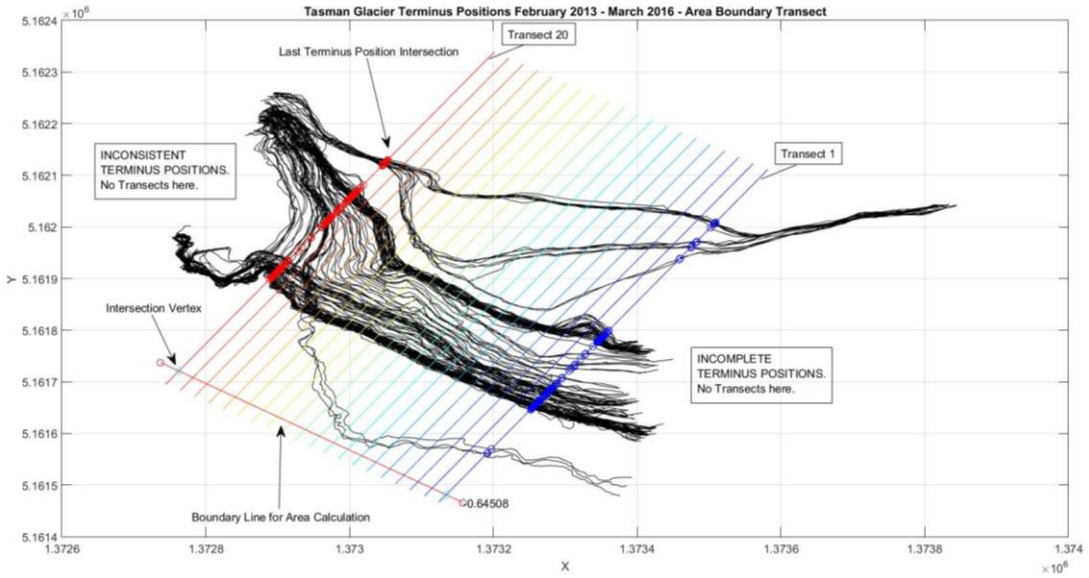

Figure 4.1.4. Presents digitized termini intersections with transect 1 (blue) and 20 (red). A lower boundary line was generated with slope - 0.64508 to intersect all transects at the front of the glacier. Area calculated using *polyarea* would produce a negative of the real-world glacier-area, therefore the result is subtracted from the net area calculated from the last terminus position on the 22nd March 2016. Our surface area change is only representative of the minimum change persisting 2013-2016.

In total, the Tasman Glacier lost a minimum of 203,430 m^2 (0.2034 km^2, 20.34 ha) from the 5th February 2013 to 22nd March 2016. The annually averaged minimum rate of loss is therefore ~ 65,076 $m^2\ a^{-1}$ or 0.065 $km^2\ a^{-1}$ (~ 6.5 ha a^{-1}). Intra-annual surface area variations revealed minor increases in ice area during the winter months and significant losses in three large calving events occurring at the end of the summer months in 2013 and 2016. In total, these three discrete large-magnitude events (events 1, 2 and 3 in *Figure 4.2.1.9*) amounted to a surface area loss of 95,641 m^2 or ~ 0.096 km^2 (9.5 ha) and responsible for ~ 47% of the total surface area loss for the entire 3 year study.

Unlike the losses seen from these large magnitude calving events, the summer of 2015 saw sustained loss from many smaller magnitude calving events. This period from December 2014 (start of summer) to February 2015 (end of summer) resulted in a minimum loss of ~ 36,832 m^2 (0.0368 km^2). In comparison to the larger magnitude calving events, this three month period of continuous small-magnitude calving accounted for ~ 18 % of the entire observed surface area loss. Event One was ~ 19.8 %, Event Two was ~ 9.4 % and Event Three ~ 17.7 % of the total. These results indicate that single large magnitude events may exceed the cumulative ice loss of an entire calving season.

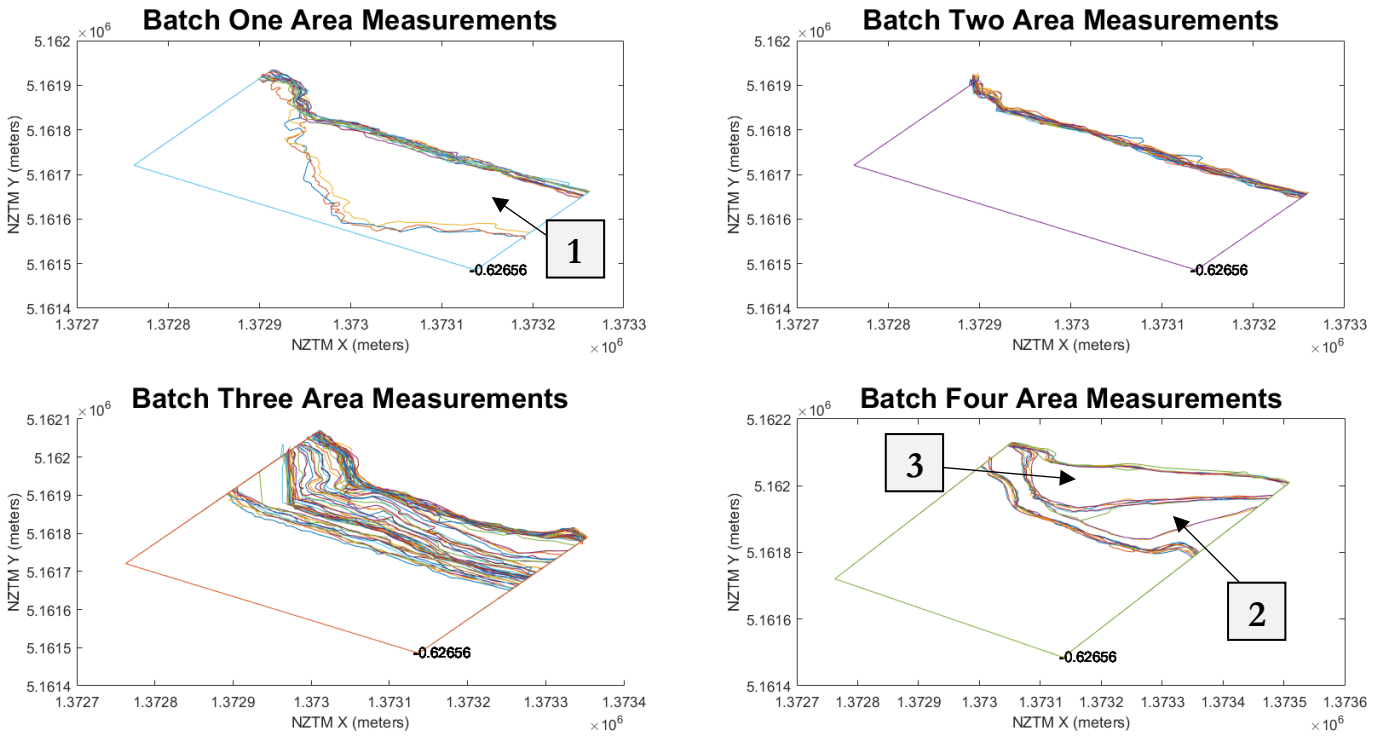

Figure 4.1.4a. Displays area measurements from each batch. In every terminus position, the boundary formed by Transect 20, Transect 1 and the lower transverse boundary line are consistent to ensure reliability in our surface area results. A minor issue is apparent in batch three where 1-2 of the terminus vectors exceeded the transect boundary. The area was therefore calculated at its intersection with the transect 20 and the larger of the two areas was selected for our results.

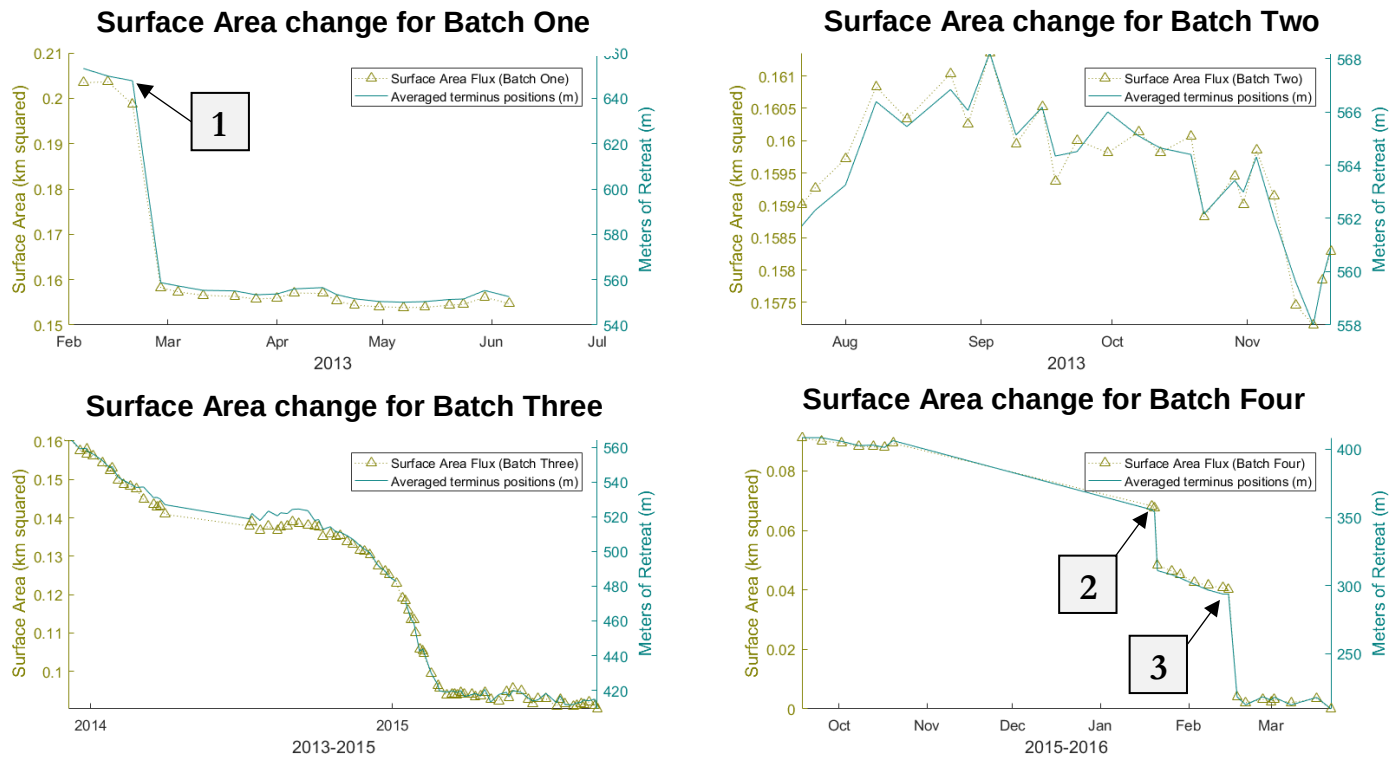

Figure 4.1.4b. Surface area change results from each batch. Similar seasonal patterns can be seen between the surface area change and retreat rate. This makes sense as our averaged terminus positions are a 1-dimensional record and our surface area change is a measure in 2-dimensions of the same region.

Minor surface area increases were observed during the winter and spring months. This amounted to only ~ + 2 % of surface area change in Batch One, ~ + 60 % in Batch Two, ~ + 14 % in Batch Three and ~ + 5 % in Batch Four. In all, 25 surface area increase/advance events were recorded amongst the 154 time sample.

Annual rates of surface area change depict a similar ascending trend compared to annual terminus retreat rates. For 2013-2014, the Tasman Glacier MIC region lost ~ - 55,991 m^2 a^{-1} in surface area. This dropped to - 41,742 m^2 a^{-1} for 2014-2015 but doubled to -105,693 m^2 a^{-1} in 2015-2016b [including all of February 2016, otherwise - 69,467 m^2 a^{-1} for 2015-2016] (*see Figure 4.1.5b*). Although these depreciations are significant, the results here are not representative of the entire terminus because of our approach was constrained within a bounded area (i.e. between Transects 1 and 20 and excluded the Eastern Embayment Ice Cliff (EEIC) and Temporary Ice Cliff (TIC) regions). Thus these absolute quantifications represent the minimum ice surface area loss at the terminus for this study period. Nonetheless monthly and inter-annual patterns are evident.

4.1.4.1. Surface Area Change: Background Small-Magnitude Calving Events vs Discrete Large-Magnitude Calving Events

Three large-magnitude calving events were identified in our study, previously termed Event One, Event Two, and Event Three. Excluding these events, the background rate of surface area loss from small-magnitude calving events were calculated to be - 15,568 m^2 a^{-1} for 2013-2014, - 41,742 m^2 a^{-1} for 2014-2015 (no change, because no Events occurred from 2014-2015) and – 60,893 m^2 a^{-1} for 2015-2016. In percentage of the total area loss, the larger-magnitude events were 27%, 0%, and 88% respectively.

In summary, area calculations did not account for the motion of the glacier. In fact, the surface area results presented here are reduced by the additional input from upstream ice flow, which has a seasonal signal.

Figure 4.1.4c. Surface area change for entire study period. For seasons: SMP = Summer, AUT = Autumn, WIN = Winter, and SPR = Spring.

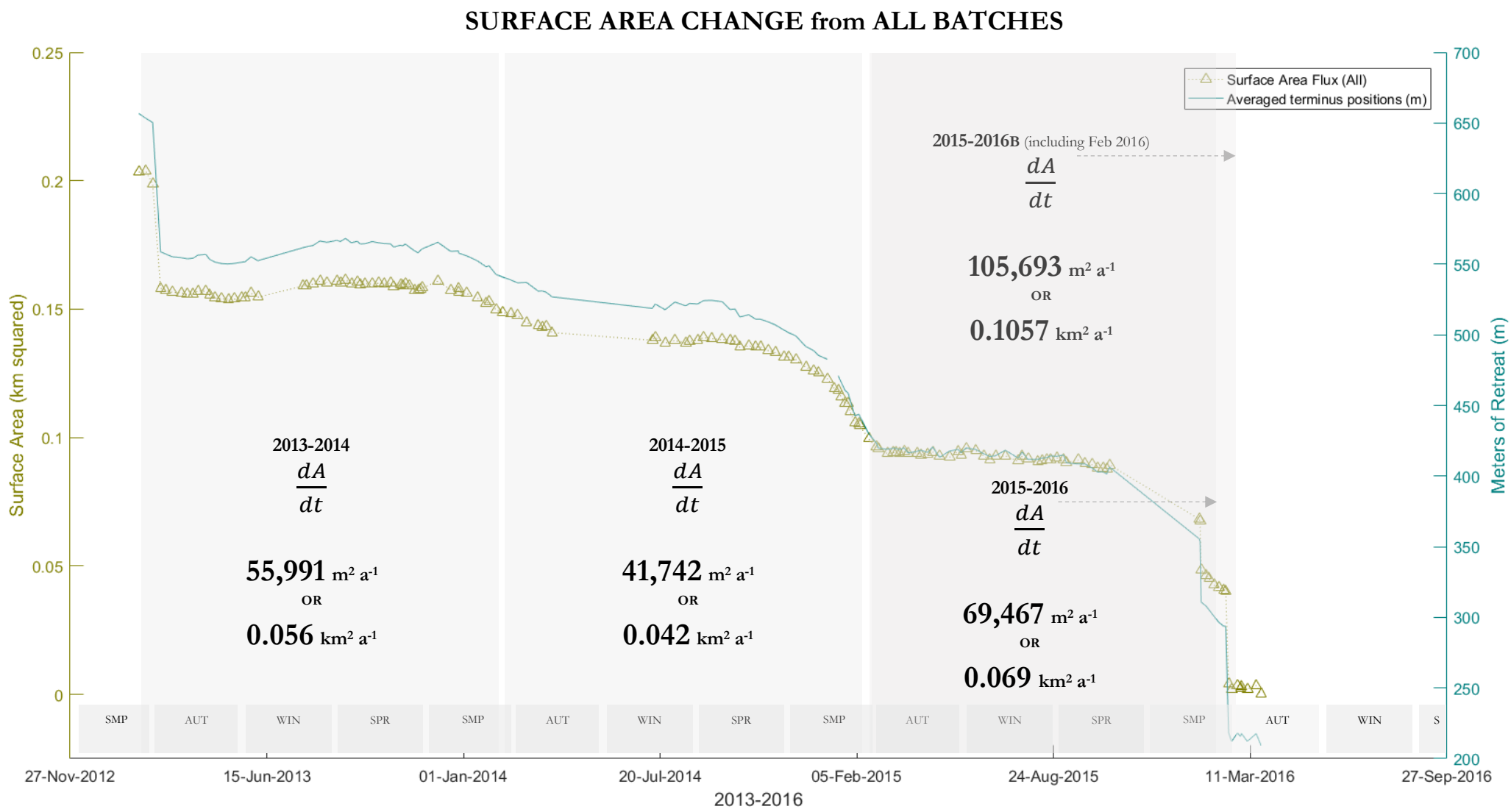

4.2. Initial Pixel Displacement Estimations (2013-2016)

By adopting Jones (2016)'s algorithm for digital image correlation, I attained image correlations starting from the 5th February 2013 to the 24th March 2016. The output of the algorithm also contained direction of movement (or quiver plots) and a scale to measure the accuracy of the correlation known as the correlation coefficient. These are shown in this section. These preliminary measurements are intended to demonstrate the process by which the final results can be attained and are suitable for inter-comparison but do not contain quantified estimates of flow speed in real-world coordinates (*see Summary in 4.2.6)*. These pixel-flow images are the basis by which further velocities were calculated.

The real-world surface velocities are not presented in the results because of difficulties in dealing with invalid pixel correlation results, while maintaining the integrity of the displacement time series. However, the datasets and initial real-world displacement results can be found in the Appendix. These initial velocity result show that, while valid velocities can be obtained using the techniques detailed in Chapter 3, that post-processing is complex and independent velocity dataset are required for validation.

4.2.1 Pixel Displacements from Batch One: 5th Feb 2013 – 6th June 2013 (1 sub-batch)

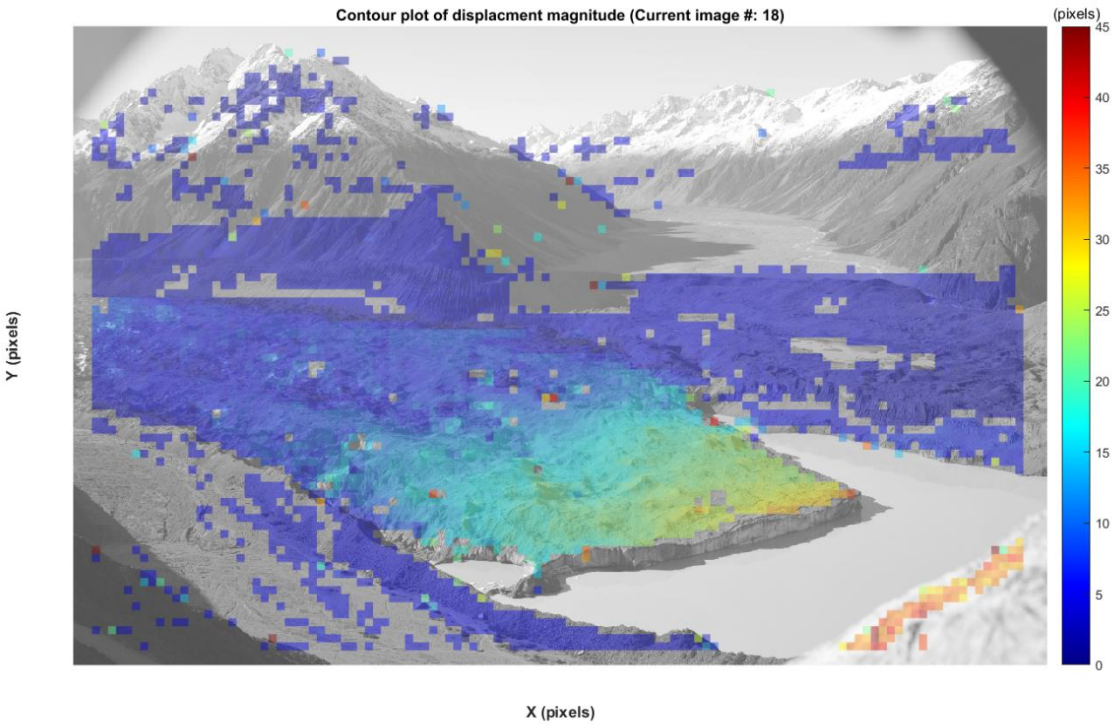

Figure 4.2.1a. Displacement magnitude for batch one. One sub-batch was used across 18 images. Note scale is 0-45 pixels.

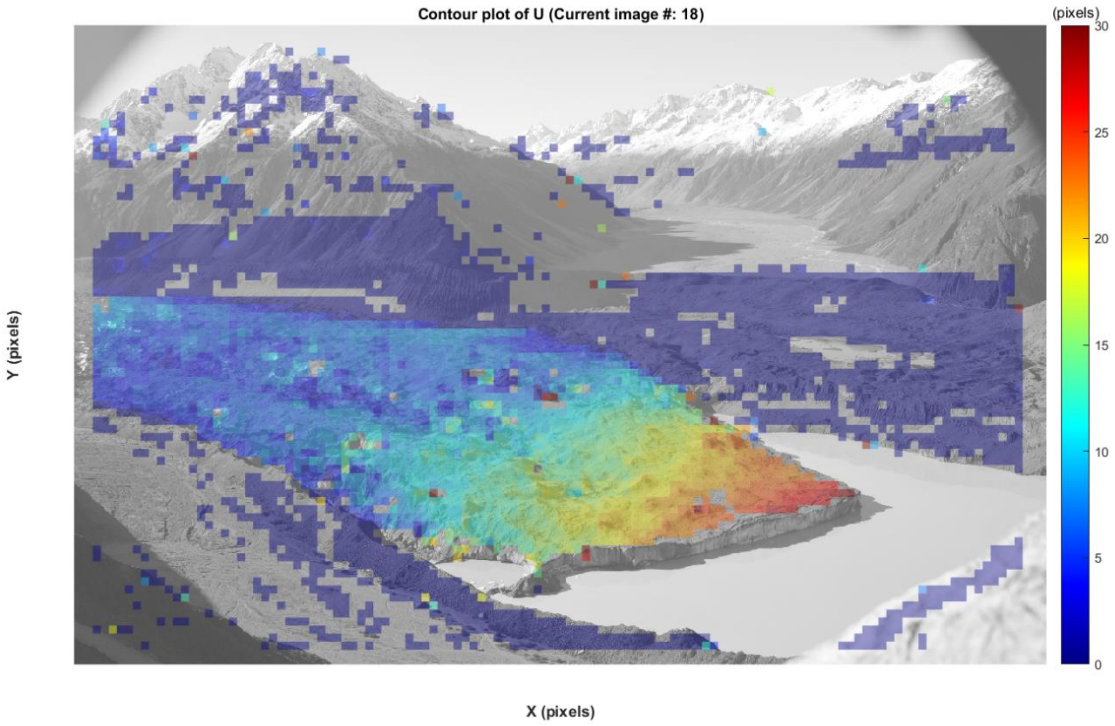

Figure 4.2.1b. X-direction (horizontal) displacement for batch one. One sub-batch was used across 18 images.

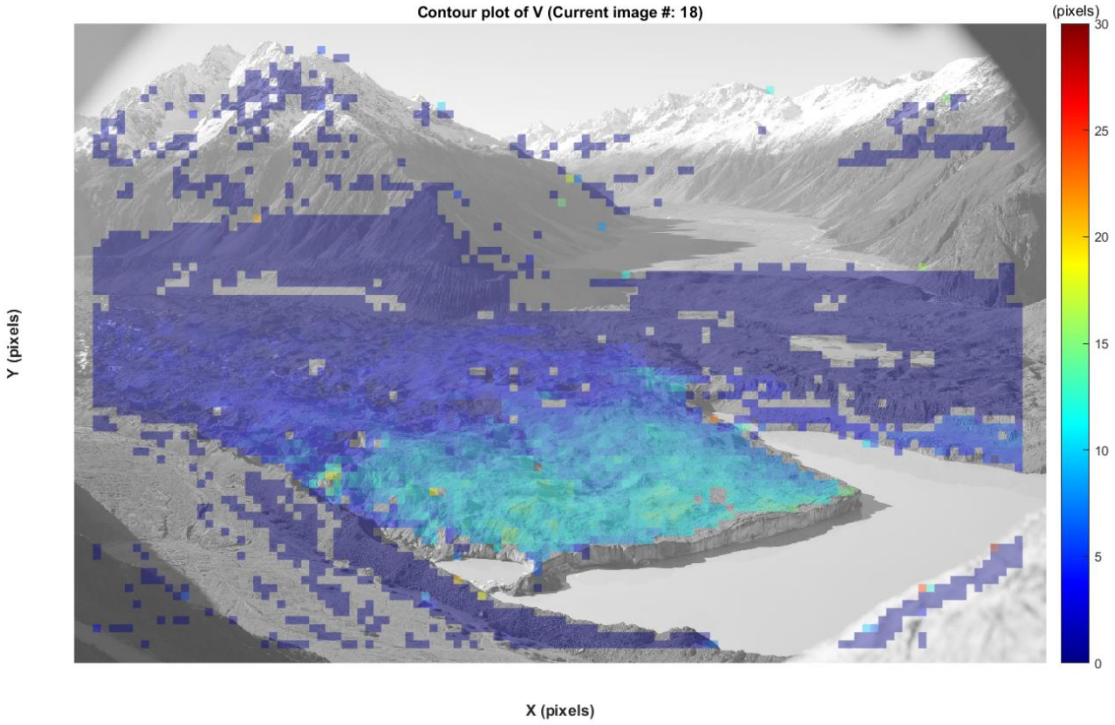

Figure 4.2.1c. Y-direction (vertical) displacement for batch one. One sub-batch was used across 18 images.

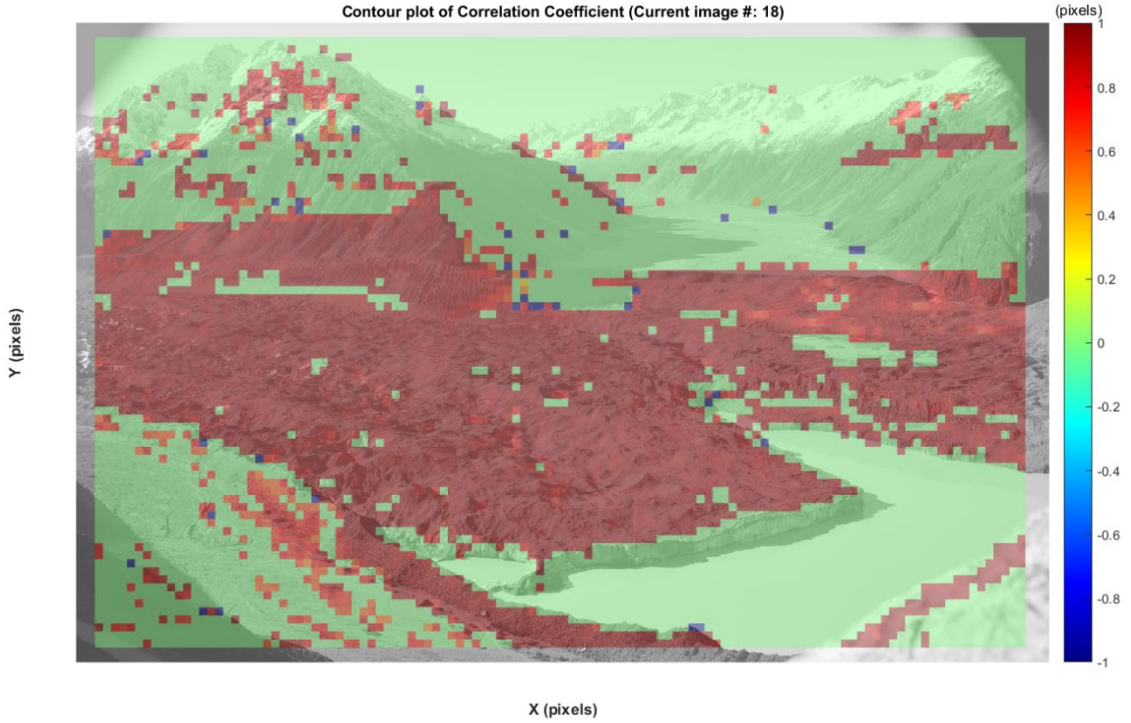

Figure 4.2.1d. Batch one: Image correlation coefficient ranges between -1 and 1. Where 1 represents the best correlations and 0 represents no correlation.

4.2.2 Pixel Displacements from Batch Two: 22nd July 2013 – 20th Nov 2013

(3 sub-batches, only the last sub-batch is presented)

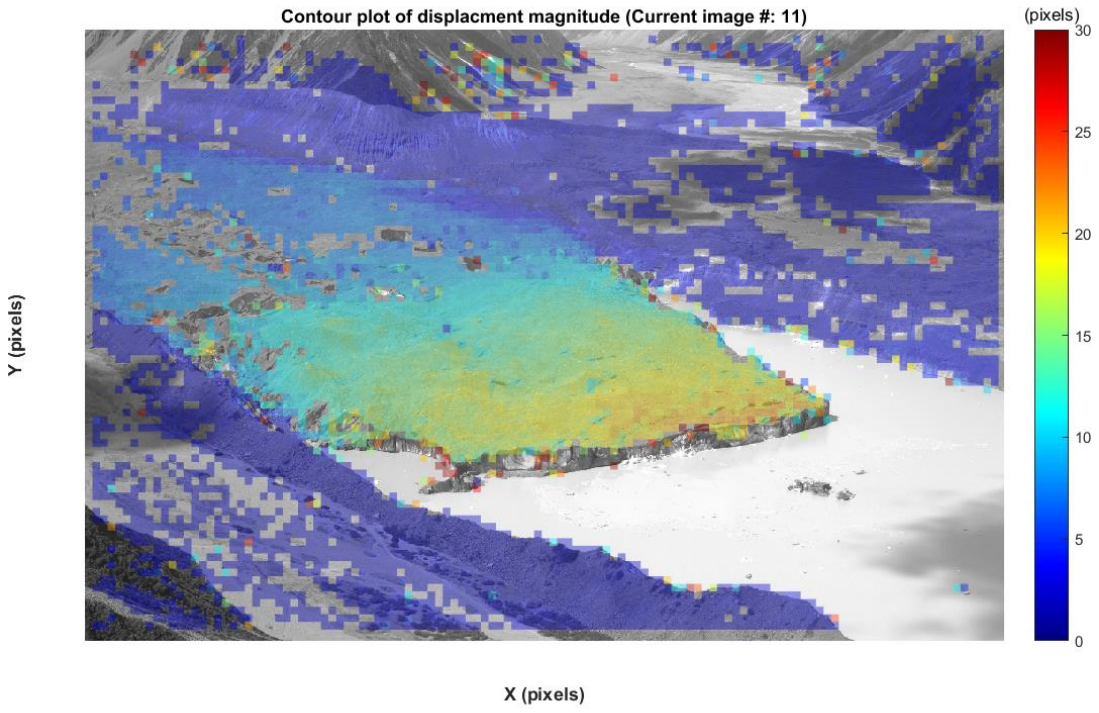

Figure 4.2.2a. Displacement magnitude for batch two. Three sub-batches were used across 28 images.

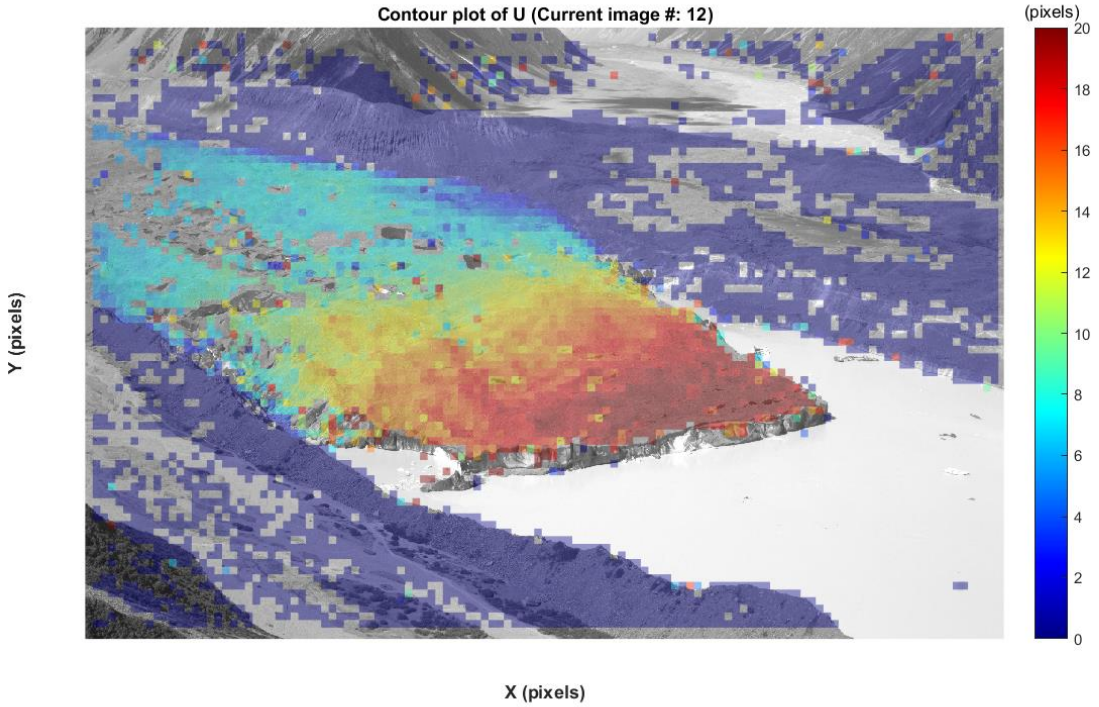

Figure 4.2.2b. X-direction (horizontal) displacement for batch two. Three sub-batches were used across 28 images. Note: scale is 0-20 pixels.

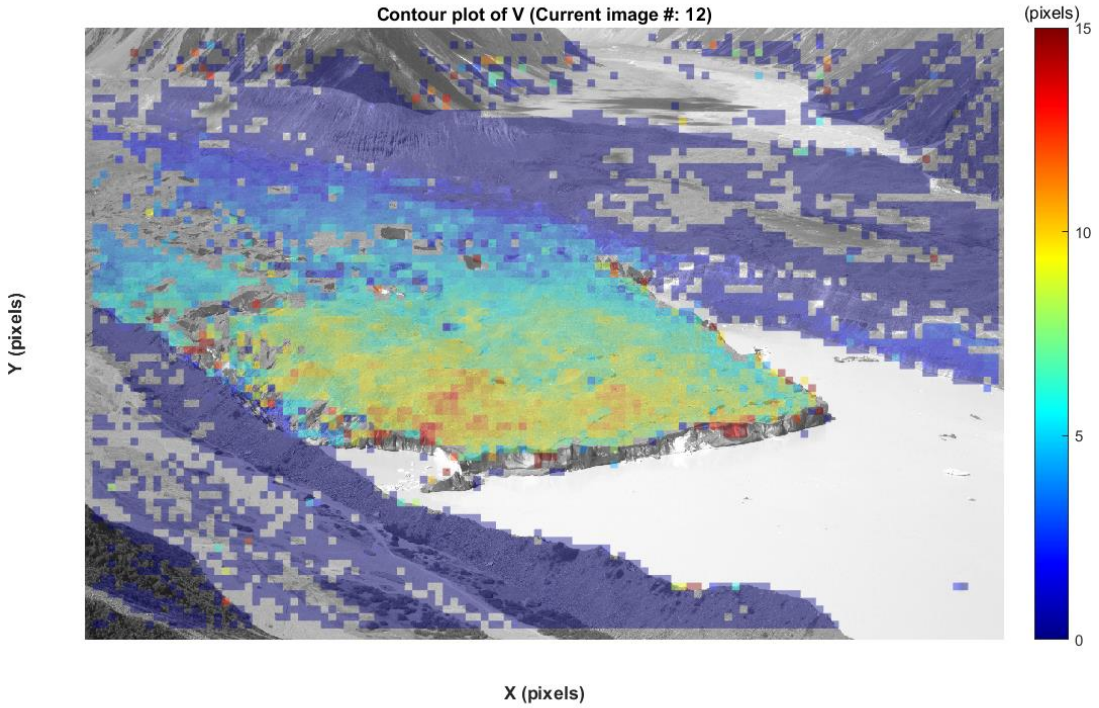

Figure 4.2.2c. Y-direction (vertical) displacement for batch two. Three sub-batches were used across 28 images. Note: scale is 0-15 pixels.

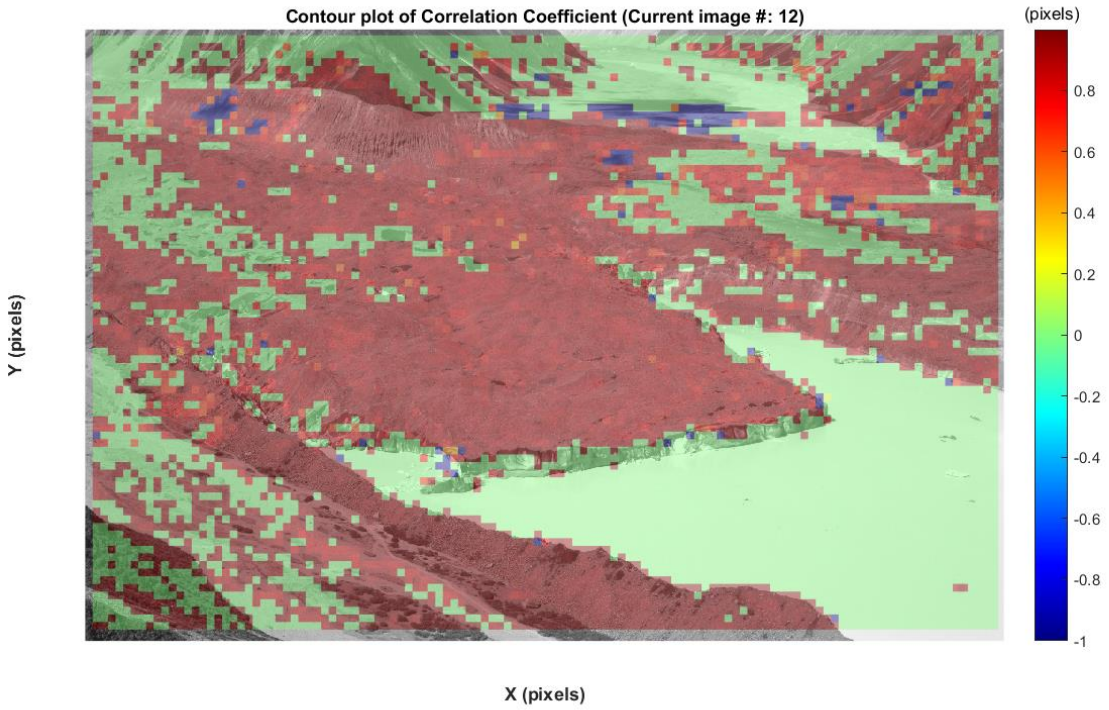

Figure 4.2.2d. Batch two: Image correlation coefficient ranges between -1 and 1. Where 1 represents the best correlations and 0 represents no correlation.

4.2.3 Pixel Displacements from Batch Three: 9th Dec 2013 – 14th Feb 2014 (1 sub-batch)

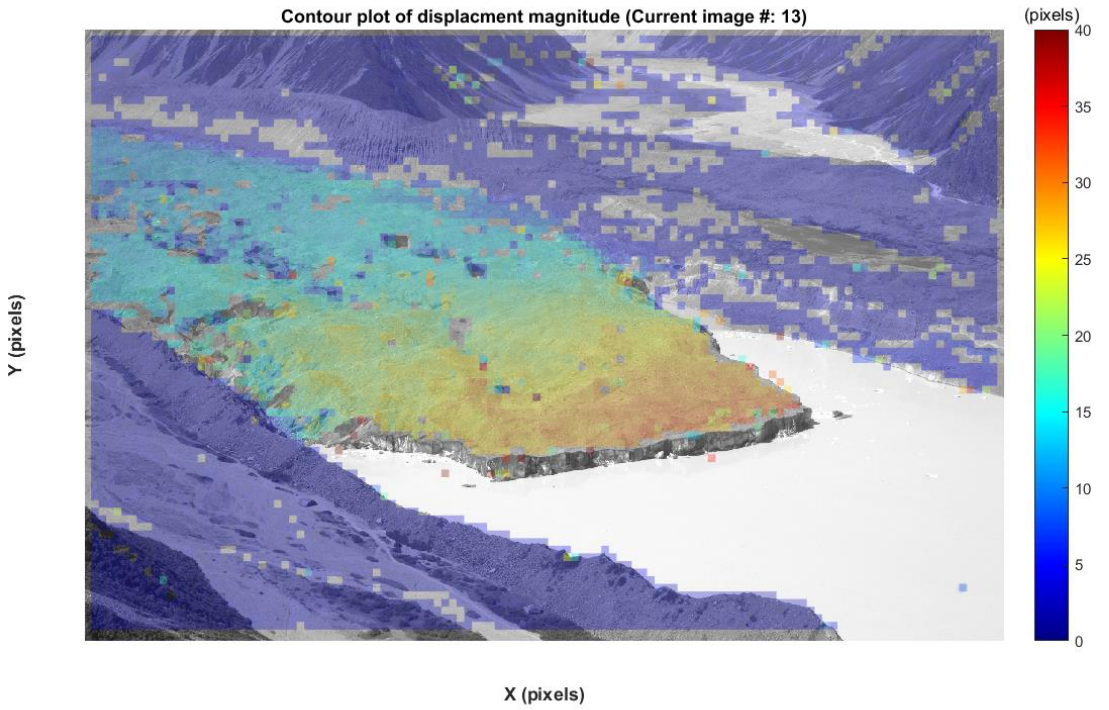

Figure 4.2.3a. Displacement magnitude for batch three. 1 sub-batch was used across 13 images.

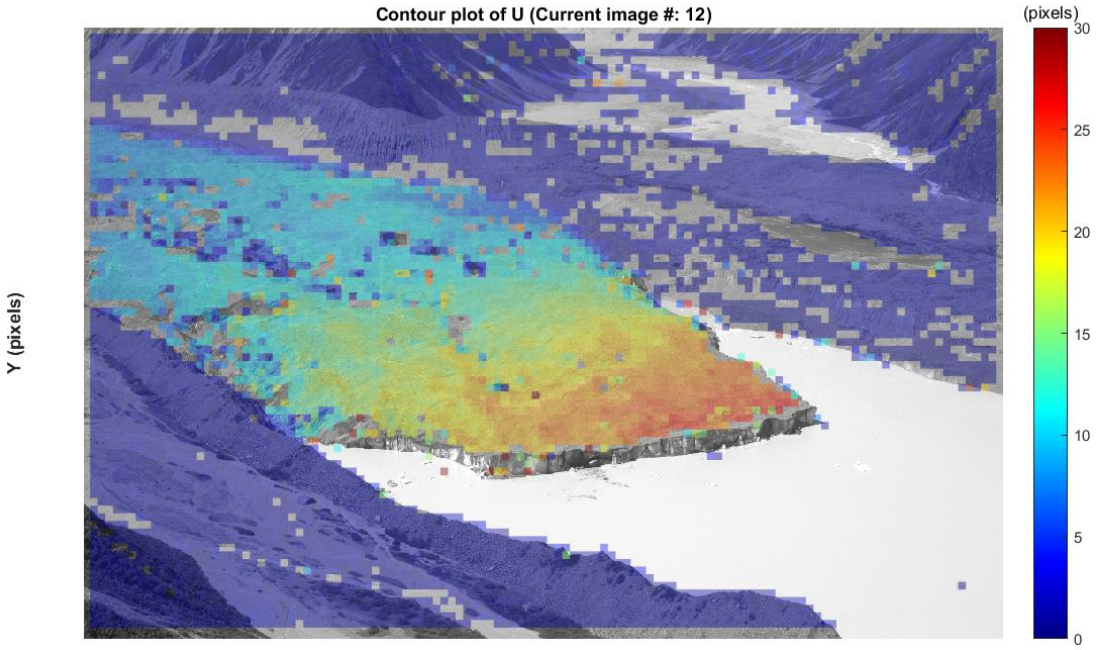

Figure 4.2.3b. X-direction (horizontal) magnitude for batch three. 1 sub-batch was used across 13 images.

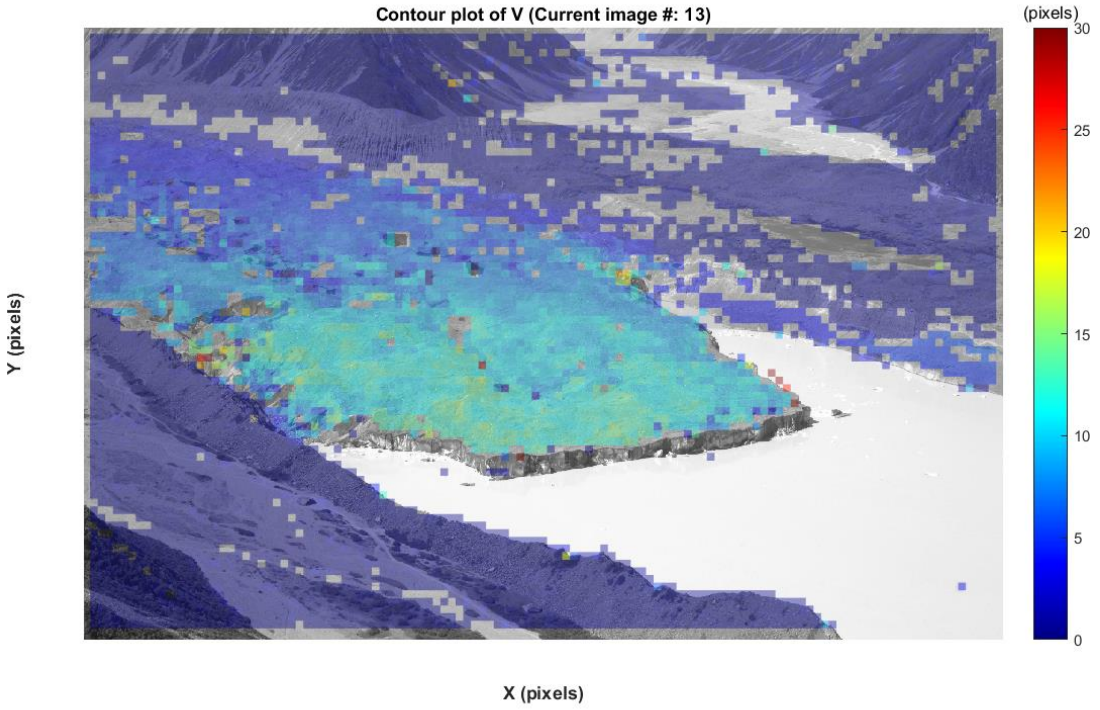

Figure 4.2.3c. Y-direction (vertical) displacement for batch three. 1 sub-batch was used across 13 images.

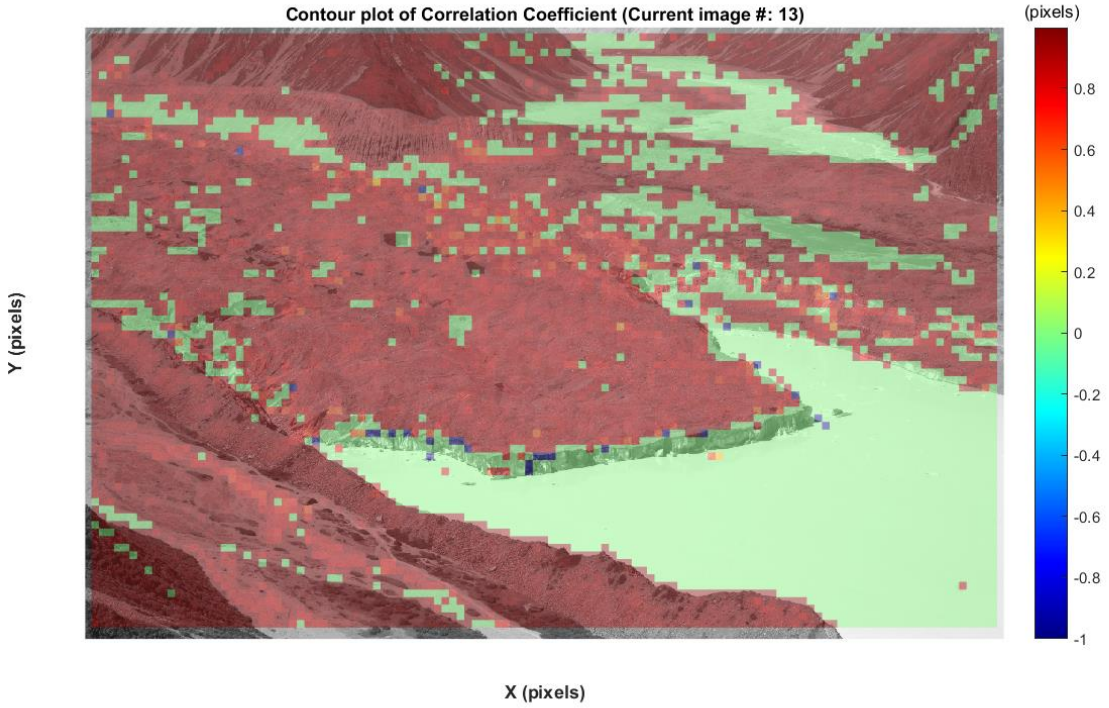

Figure 4.2.3d. Batch three: Image correlation coefficient ranges between -1 and 1. Where 1 represents the best correlations and 0 represents no correlation.

4.2.4 Pixel Displacements from Batch Four: 18th Feb 2014 – 6th Sep 2015

(8 sub-batches across 100 images, only the last sub-batch is shown)

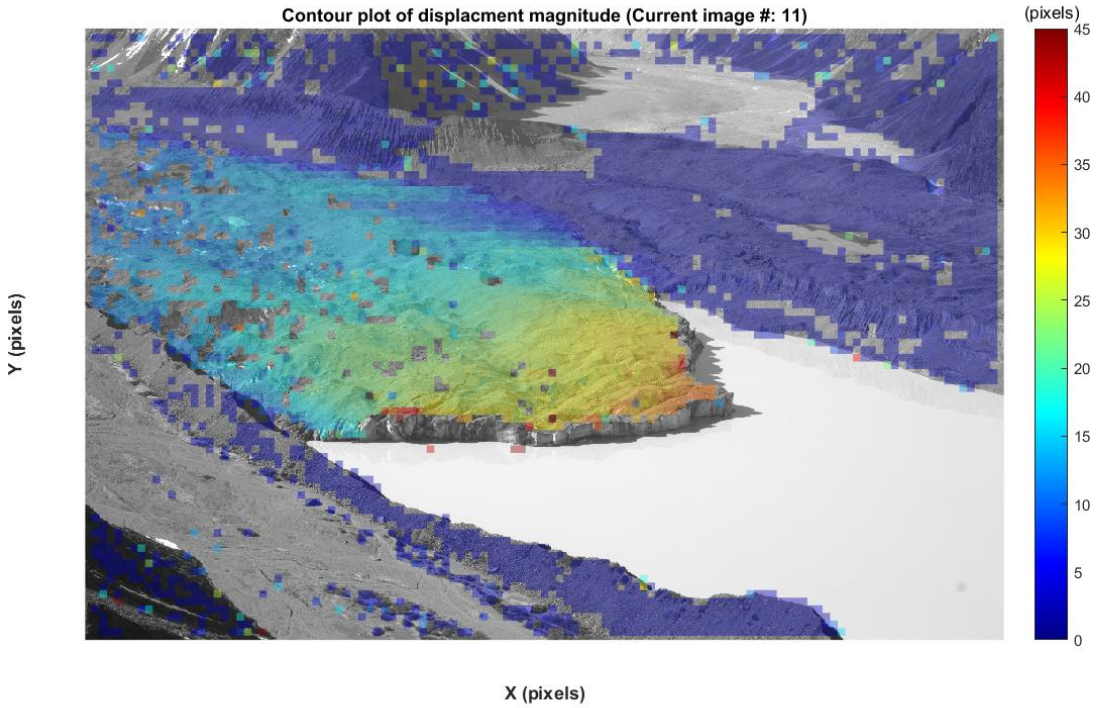

Figure 4.2.4a. Displacement magnitude for batch four. 8 sub-batches were used across 100 images. Only last sub-batch is shown here.

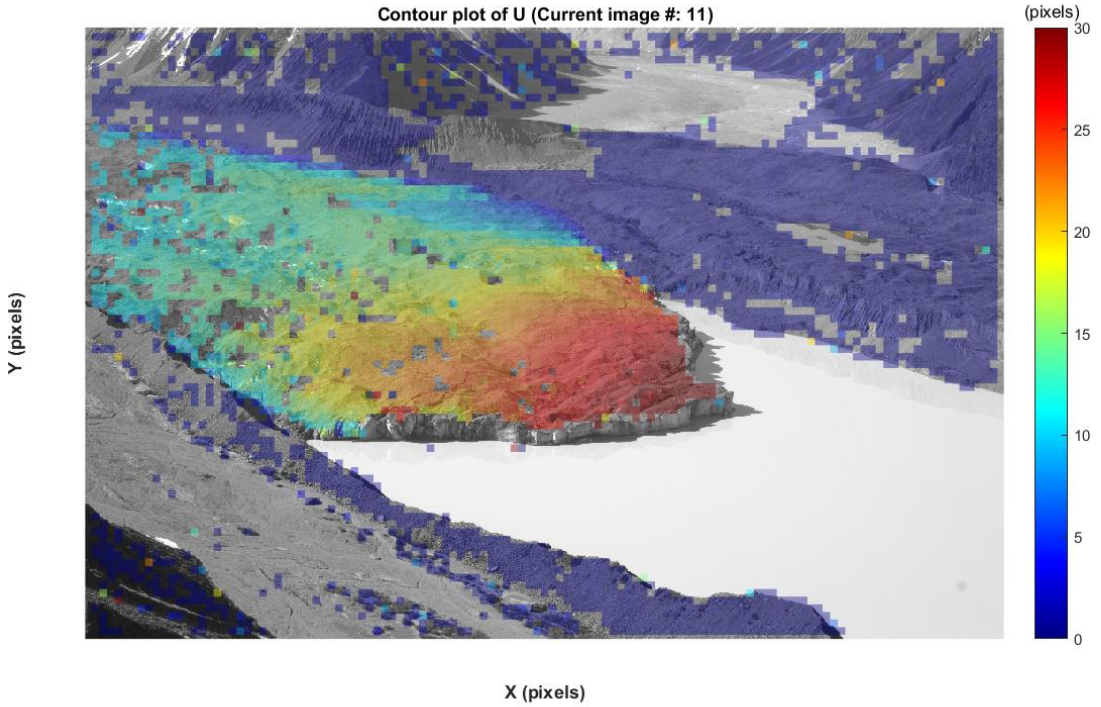

Figure 4.2.4b. X-direction (horizontal) magnitude for batch four. 8 sub-batches were used across 100 images. Only last sub-batch is shown here.

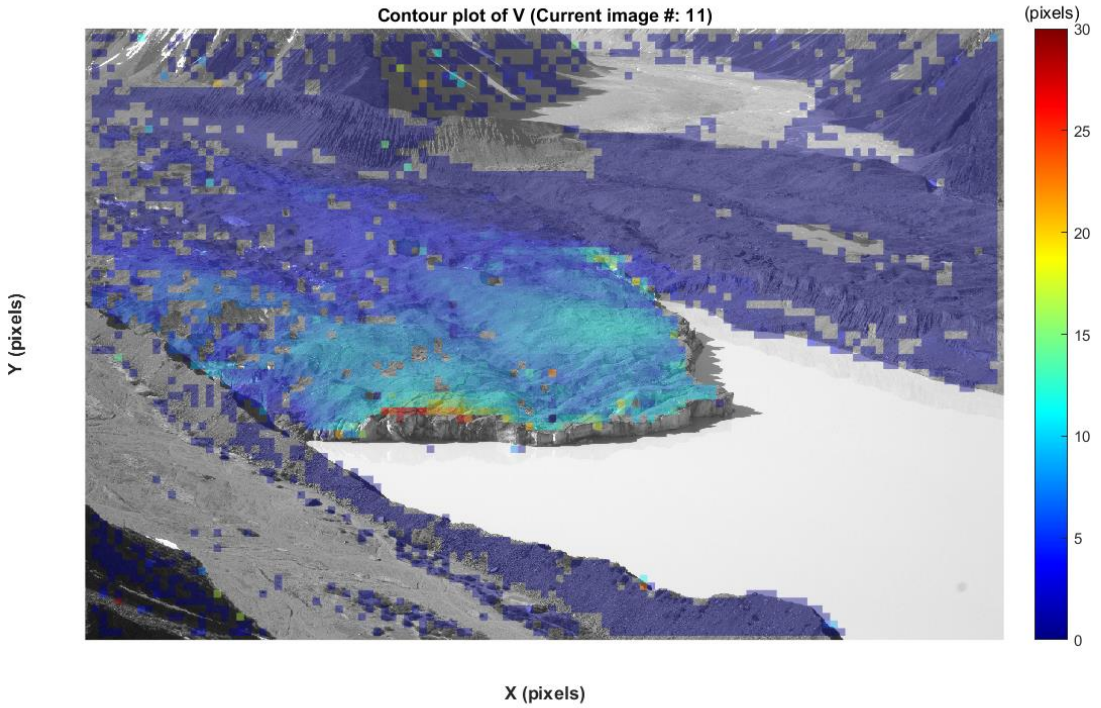

Figure 4.2.4c. Y-direction (vertical) displacement for batch four. 8 sub-batches were used across 100 images. Only last sub-batch is shown here.

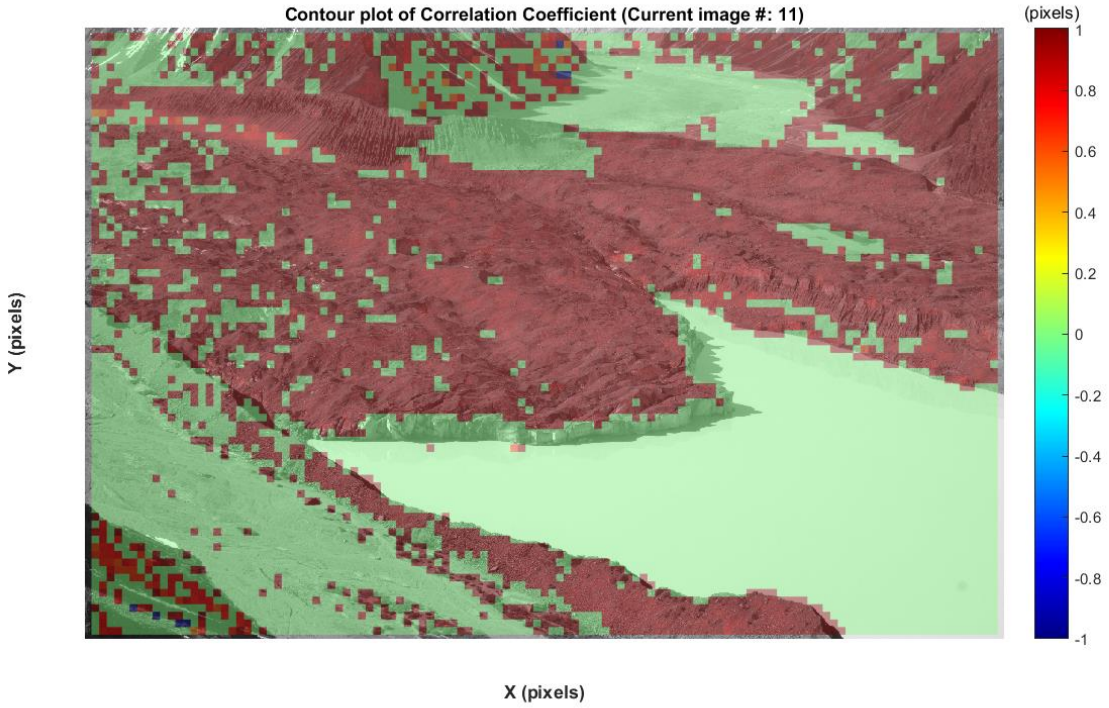

Figure 4.2.4d. Batch four: Image correlation coefficient ranges between -1 and 1. Where 1 represents the best correlations and 0 represents no correlation.

4.2.5 Pixel Displacements from Batch Five: 27th Aug 2015 – 22nd March 2016

(3 sub-batches, only last sub-batch is shown)

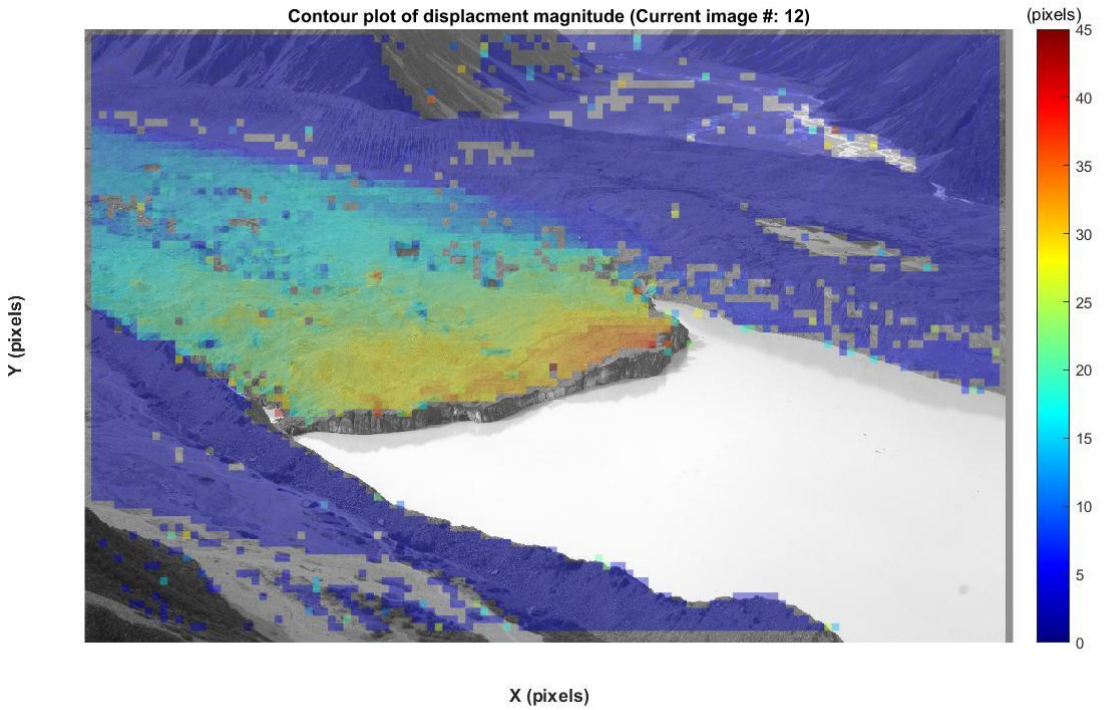

Figure 4.2.5a. Displacement magnitude for batch five. 3 sub-batches were used across 24 images. Only last sub-batch is shown here.

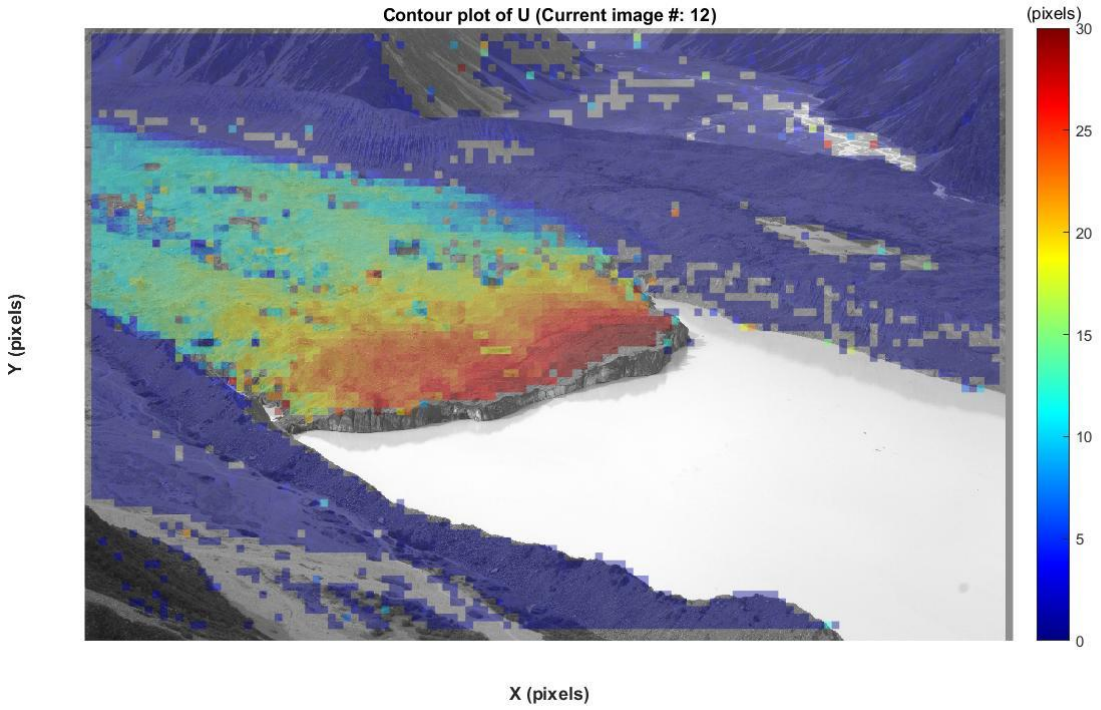

Figure 4.2.5b. X-direction (horizontal) magnitude for batch five. 3 sub-batches were used across 24 images. Only last sub-batch is shown here.

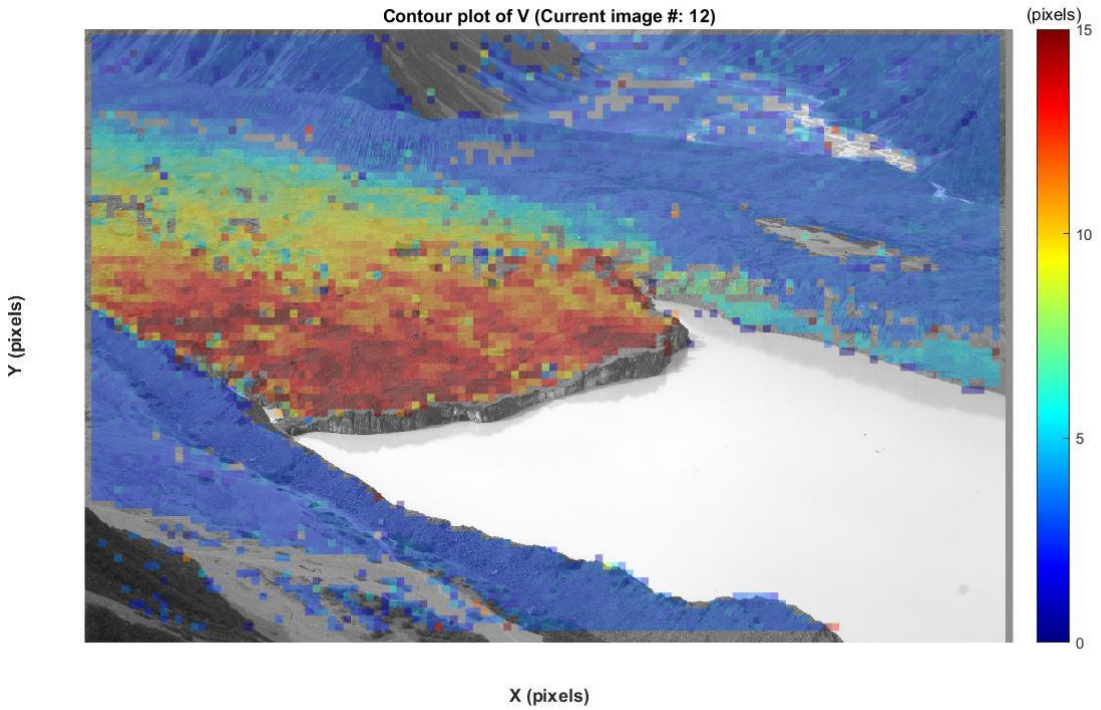

Figure 4.2.5c. Y-direction (vertical) magnitude for batch five. 3 sub-batches were used across 24 images. Only last sub-batch is shown here. Potential issues with the image selection may also be evident here where the background is seen to increase vertically by 5 pixels.

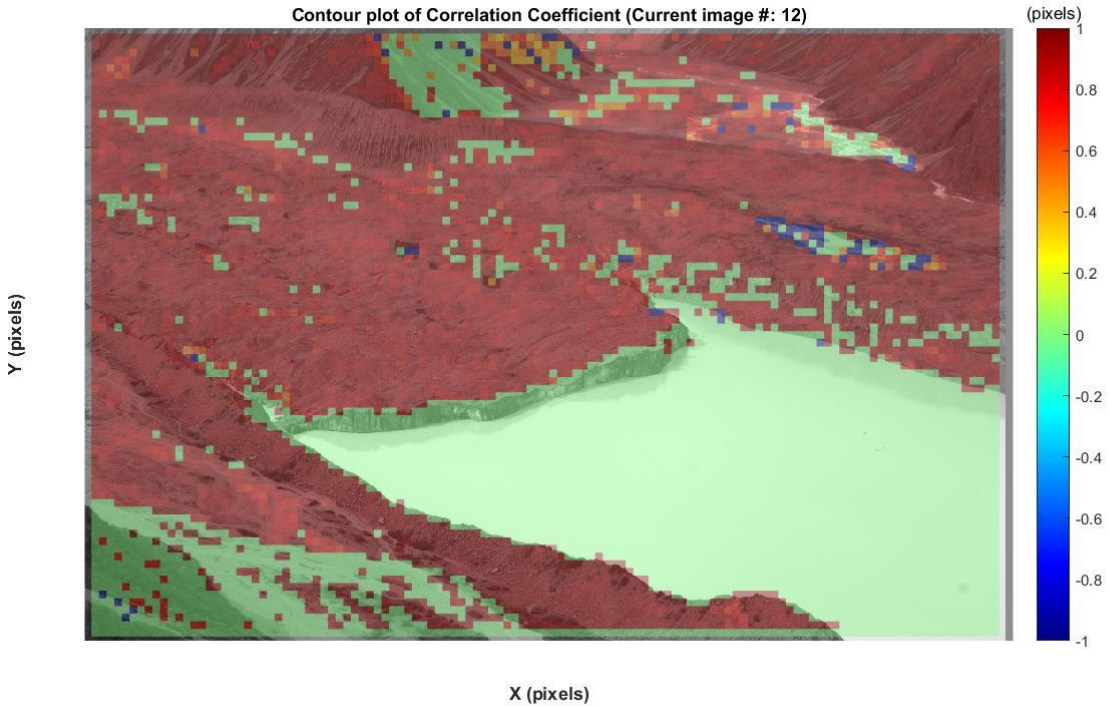

Figure 4.2.5d. Batch five: Image correlation coefficient ranges between -1 and 1. Where 1 represents the best correlations and 0 represents no correlation.

4.2.6 Summary of Pixel Displacements (*estimates from arbitrary sample A*)

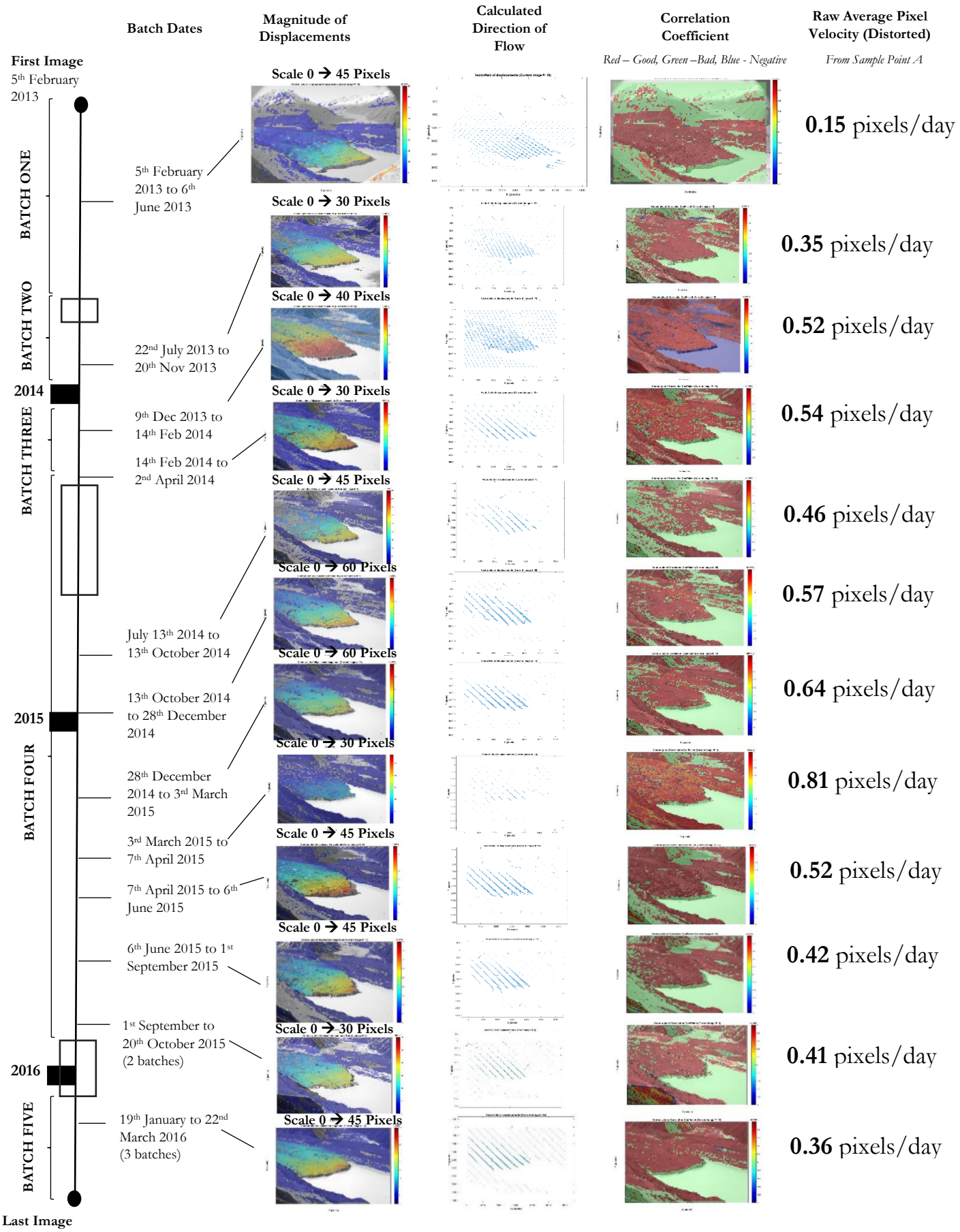

Figure 4.2.6. Presents the initial DIC results conducted over 16 different batches to attain pixel displacements in x and y directions, direction of movement (middle plot) and correlation coefficients (last plot, where red indicates a strong correlation [~ 1] and green, a poor correlation [< 0.5].

CHAPTER FIVE

DISCUSSION

5.0 Introduction

This high spatial and temporal resolution study of the Tasman Glacier using high-frequency oblique photogrammetry revealed detailed observations of the glacier dynamics on unprecedented scales. Calving processes were observed to fall under two categories: (1) smaller-magnitude calving events (by the spalling of lamallae of ice and by the undercutting of seracs at the waterline) that are punctuated by (2) orders-of-magnitude larger events which are driven by buoyancy or by dislocation from the parent ice resulting from deep crevasses that approach the ice thickness.

The terminus position observations suggest that larger-magnitude events serve as a 1st order control on calving dynamics at the Tasman Glacier. This is akin to observations made at Helheim Glacier in Greenland where calving was dominated by 1 km^3 events resulting from buoyant flexure and basal crevassing (James *et al,* 2014). Although it is not clear whether a similar process by buoyant flexure is also occurring at the Tasman, the events observed were of significantly larger than the background rate of calving and resulted in surface area losses of ~ 40,423 m^2 from Event One, ~ 19,208 m^2 from Event Two and ~ 36,832 m^2 from Event Three. In total, these events accounted for ~ 96, 463 m^2 of the ~ 203,426 m^2 loss of ice over the three year study, ~ 47% of the observed change.
Temporally averaged ice velocities (U_t) are known to increase in the summer/autumn months and decrease in the winter/spring months (Horgan *et al,* 2015). The maximum background horizontal surface velocity was used to estimate calving rates (U_c) for 2013-2016.

This discussion has been structured to explore some of the above-mentioned topics. *5.1* will summarise and analyse the observations in length changes (U_r), comparing to previously established rates of retreat and surface area change. *5.2* will synthesize velocity measurements since the 20th century and discuss how our initial results fit in with the current understanding of ice flow at the Tasman Glacier. *5.3* is a discussion on the mechanisms behind the dynamic calving behaviour observed and *5.4* will identify the limitations of this study and finally in *5.5.* a summary of all findings with recommendations for future study is presented.

5.1. Retreat rates and surface area change

Modern length changes of the Tasman Glacier were first documented in the 1980s. Three field surveys carried out by Hochstein (1995) estimated the glacier had retreated 1.3-1.6 km between 1971 and 1993, equating to an annual U_r of 59 – 72 m a^{-1}. Satellite image correlation using remote-sensed data between years 1990 to 2007 showed further retreat in the 1990s and early 2000s of 3.5 km (Quincey and Glasser, 2009), or an equivalent annually-averaged U_r of 206 m a^{-1}.

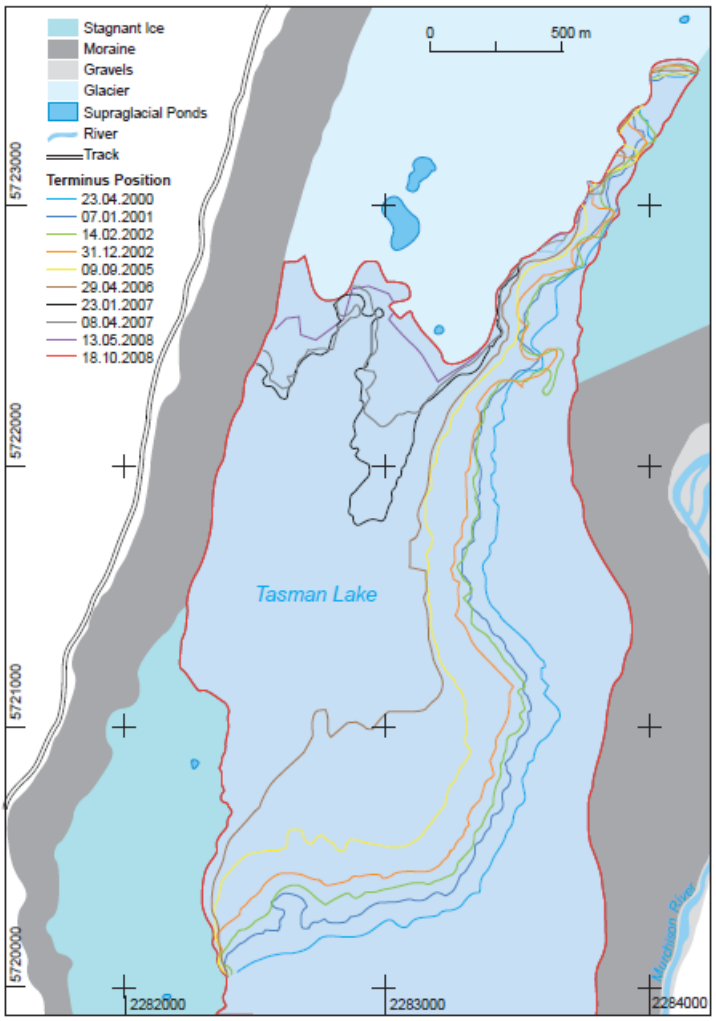

Figure 5.1.1. Shows terminus positions of the Tasman Glacier from 23/04/2000 to 18/10/2008 from satellite imagery. The authors note that on the true-right side of the Tasman Glacier, retreat is slower than at the main ice cliff. *Source:* Dykes *et al.,* 2009

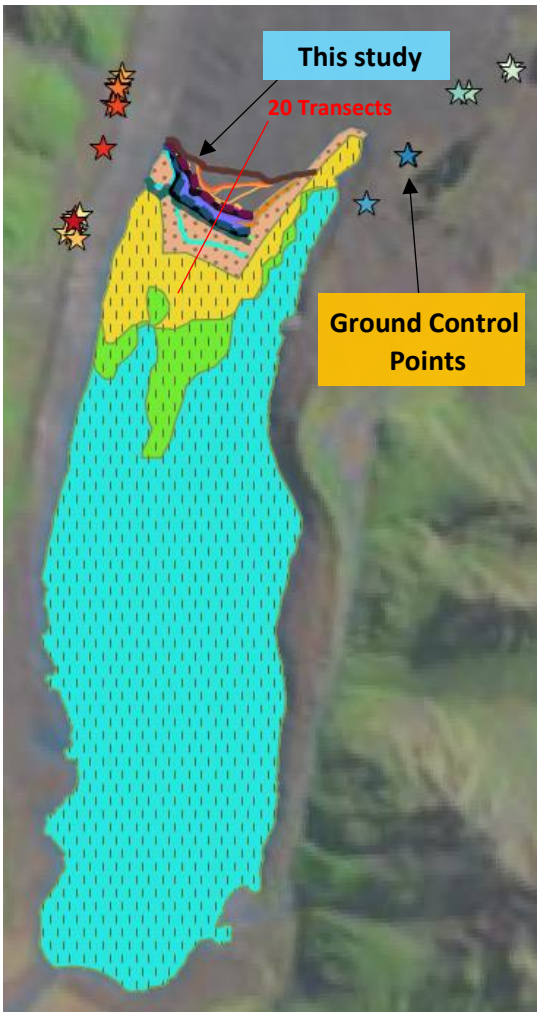

Figure 5.1.2. Shows terminus positions of the Tasman Glacier from 5/02/2013 to 22/03/2016 from oblique photogrammetry. See *Figure 4.2* for more details on shaded rasters. *Source:* This study

Here I show the Tasman Glacier retreated a minimum of 0.24 km and maximum of 0.57 km from 2013 to 2016 depending on the location of measurement. Inter-annual disparities in the rate of retreat were also evident within our results. 2014-2015 positions retreated the least of the three years (82.48 ± 17 m a^{-1}) but even so, exceeded 1971-1993 U_r (59 – 72 m a^{-1}) and the 2000-2006 U_r (54 m a^{-1}) from Hochstein (1995) and Dykes *et al,* (2009) respectively.

The greatest changes in U_r coincided with the three major calving events. Event one (22nd February 2013) resulted in an instantaneous retreat of 91.5 m (average) of the terminus position. This amounts to ~ 70 – 94% of the annual retreat 2013-2014. In 2014-2015, no major calving events were observed and the majority of calving occurred in small-areas predominantly occurring during spring and summer, and ice cliff melt.

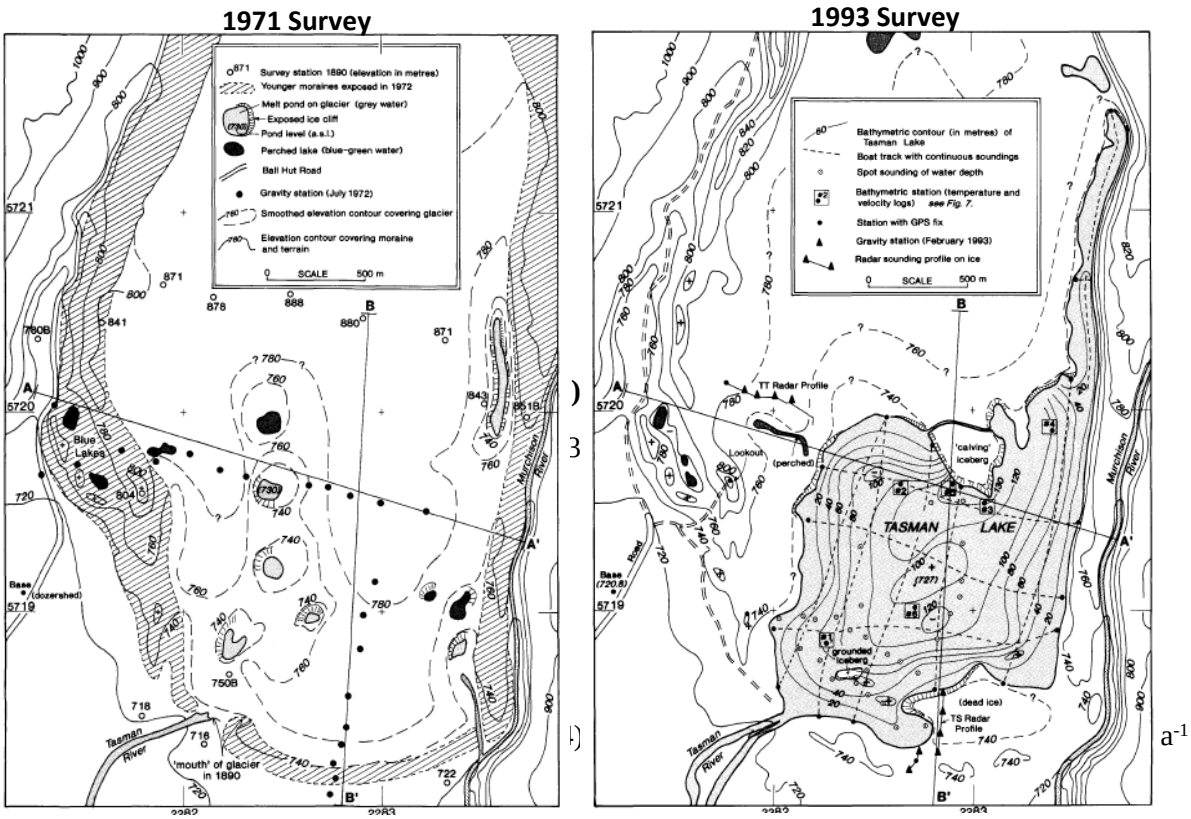

Figure 5.1.3. Shows terminus positions, topography and bathymetry of the Tasman Glacier from 1971 (left) to 1993 (right) from field surveys and aerial photography. **Note**: Terminus retreat rates were measured along transect B-B. *Source:* Hochstein, 1995

Table 5.1a. Shows terminus position changes from observations since 1971 to 2016. No published observations were made between 2008 and 2013. *Sources:* Seen in table.

Dates	Averaged Length Change	Annual U_r	No. of Major Calving Events	Reference
1971 to 1993	1.3 – 1.6 km	59 – 72 m a^{-1}	N/A	Hochstein *et al.*, (1995)
1990 to 2007	3.5 km	206 m a^{-1}	N/A	Quincey and Glasser, (2009)
2000 to 2006	215 m	54 m a^{-1}	N/A	Dykes *et al.*, (2010)
2006 to 2008	357 m	144 m a^{-1}	N/A	Dykes *et al.*, (2010)
5/2/2013 (start) – 5/2/2014	116 ± 18 m	116.32 ± 18 m a^{-1}	1	This study
5/2/2014 to 5/2/2015	82 ± 17 m	82.48 ± 17 m a^{-1}	0	This study
5/2/2015 to 5/2/2016	204 ± 20 m	204 ± 20 m a^{-1}	1	This study
5/2/2015 to 22/3/2016 (end of study)	349 ± 21 m	349 ± 21 m a^{-1}	2	This study

An acceleration in terminus retreat rates occurred from 2015-2016 with one major calving event (Event Two causing an average retreat of 43 m) occurring on the 21st of January 2016. If we included position data from both February and March of 2016 into the calculations, U_r increased to 349 ± 21 m a^{-1} due to the ~ averaged 75 m caused by another large-magnitude calve event, Event Three, occurring on the 18th February 2016.

5.1.1. Surface Area Changes

Table 5.1.1a. Shows surface area change from observations since 1978 to 2016. A limited number of published sources are available. The dA/dt values from Dykes *et al,* (2010) are from lake expansion rates for 2000-2008. I make the assumption that lake expansion rate equates to an equivalent loss in surface ice for the sake of comparison. *Sources:* Seen in table.

Dates	Tasman Net Surface Area	dA/dt (from study area)	No. of Major Calving Events	Reference
Pre-1978	99.35 km^2	N/A	N/A	Chinn *et al.*, (1996)
2000 to 2008	Lake area 5.96 km^2	0.34 km^2 a^{-1} (lake growth)	N/A	Dykes *et al.*, (2010)
5/2/2013 (start) – 5/2/2014	N/A	0.056 km^2 a^{-1} (min)	1	*This study*
5/2/2014 to 5/2/2015	N/A	0.042 km2 a^{-1} (min)	0	*This study*
5/2/2015 to 5/2/2016	N/A	0.069 km^2 a^{-1} (min)	1	*This study*
5/2/2015 to 22/3/2016 (end of study)	N/A	0.1057 km^2 a^{-1} (min)	2	*This study*
Total Surface Area Change 2013-2016	N/A	203, 426 m^2 / 0.20 km^2 (min)	3	*This study*

Surface area changes (*dA/dt*) in 2013-2016 are significantly slower compared to the 2000-2008 lake expansion rates from Dykes *et al.*, (2010) which are an order of magnitude larger than 2013-2016 rates. The results calculated from this study are representative of only a portion of the total surface area loss, and in reality the total change will be a factor of measured values. Factoring this in, it still does not account for the dramatic differences when comparing these results. It is likely that surface area ice loss have slowed since the rapid retreat of 2000-2008. However the average retreat rates presented in *Table 5.1a* are not reflective of such changes because even the lowest rate of retreat (82 m a^{-1} in 2014-2015) measured by our study exceeds the average 54 m a^{-1} (2000-2006). This inconsistency may be attributed to differing methodologies in quantifying the terminus retreat between previous studies and this study. No details of precisely how measurements were made in Dykes *et al*, (2010) to calculate their average retreat rates at the MIC and for the full-width of the glacier. However, the authors did present their measured results. Position changes occurring at the Main Ice Cliff (MIC) in 2006 were substantially greater than those occurring on the true-right margin or the Eastern Embayment Ice Cliff (EEIC) and that U_r at the MIC peaked at 592 m a^{-1} in 2007. This confirms the observation that 2000-2008 *dA/dt* was significantly larger than that of 2013-2016 by accounting for the discretized retreat rates at the MIC and the EEIC (refer to *Figure 5.1.4)*.

		Full width			MIC			EEIC		
Survey interval	Time interval (t) in days	∂L_{mean} (m)	U_r (m a^{-1})	U_c (m a^{-1})	∂L_{mean} (m)	U_r (m a^{-1})	U_c (m a^{-1})	∂L_{mean} (m)	U_r (m a^{-1})	U_c (m a^{-1})
29/04/00–07/04/01	344	66 ± 29	70	75	74 ± 26	79	87	40 ± 24	42	45
07/04/01–14/02/02	313	24 ± 28	28	32	32 ± 25	37	46	7 ± 27	8	11
14/02/02–31/12/02	321	37 ± 18	53	58	42 ± 18	48	56	26 ± 16	30	32
31/12/02–09/09/05	984	88 ± 59	33	37	115 ± 38	43	51	23 ± 52	9	11
09/09/05–29/04/06	233	108 ± 144	226	230	149 ± 163	255	264	30 ± 13	47	49
29/04/06–23/01/07	269	190 ± 366	497	501	291 ± 436	592	600	25 ± 13	34	36
23/01/07–08/04/07	75	46 ± 76	224	228	63 ± 86	307	315	8 ± 20	39	41
08/04/07–13/05/08	401	73 ± 77	66	71	107 ± 88	97	106	29 ± 14	26	29
13/05/08–18/10/08	159	48 ± 66	110	115	80 ± 63	184	192	5 ± 36	11	14
2000–2006	2195	323	54	59	412	69	78	126	21	24
2006–2008	904	357	144	149	541	218	227	67	27	30

Figure 5.1.4. Full-width, MIC and EEIC retreat rates, calving rates and mean retreat. *Source:* Dykes *et al,* 2010

Due to the irregular shape of the terminus front, how one ultimately measures the terminus retreat is of importance. For this study, 20 transects parallel with the flow direction were used as a scale to measure changes occurring over the ~ three years from February 2013 to March 2016. Dykes *et al.*, (2010) obtained terminus retreat rates using perpendicular lines drawn at

various regions. The exact positions of where these measurements were made are not known, but from review of their results, terminus positions evolved in non-linear and incongruous ways from 2000-2007 (*see Figure 5.1.1)* reflecting the very irregular shape of the glacier, and reinforcing the importance for a common scale of reference. Future studies of retreat rates at the Tasman Glacier should therefore use similar scalar measures in order to attain comparable rates of retreat, otherwise the continuity of results is disrupted.

5.1.2. Simple projections assuming *ceteris paribus*

According to Chinn (1996), the Tasman Glacier had a surface area of 99.35 km^2 before it began forming a proglacial lake and calving. The current surface area of the Tasman Glacier is not known however a subtraction of the lake-surface area gives an approximation of 93.39 km^2 (Dykes *et al.*, 2010). At the maximum observed surface area rate of change (2015-2016) of 0.069 $km^2\ a^{-1}$ it will still take 1350 years for it to disappear and even at the higher rates of surface area change, such as 0.34 $km^2\ a^{-1}$ from 2000-2008, 274 years. These loose calculations are only to demonstrate the rate at which calving at the terminus is affecting the Tasman Glacier on the whole. They do not, of course, account for the melting of bare ice upstream from the terminus, nor do they factor in changes in the calving rate/retreat rates or changes in the rates of snow accumulation in the upper Tasman Glacier. Future variations in precipitation and the strength of the westerlies are likely affect any simple projections based on the current observations (Kerr and Owens, 2008).

5.2. Surface ice velocity

Numerous works have sought to quantify the ice flow in various regions on the Tasman Glacier however the majority were measurements from 10 km above the terminus or near the vicinity of Ball Hut (Brodrick, 1891; Anderton, 1975; Kirkbride, 1995). Additionally, due to the changing terminus position since the 1980s, the distance scale used by some of the earlier studies is only relevant when the exact location can be pinpointed. Measurements in 1986 showed that ice velocity was relatively low at 3.3 m a^{-1} at ~ 2 km from the then terminus (Kirkbride, 1995). Following this, another survey calculated from the 1995 terminus showed that velocities had doubled to 24 m a^{-1} at 2 km from the onset of calving (Kirkbride and Warren, 1999). Post-1995, comparisons with sources are more difficult due to the before mentioned reason. A series of image correlation studies using satellite imagery (ASTER primarily) were conducted in the early 2000s to 2013. A summary of the velocities measured by these sources are presented in *Table 5.2.1*.

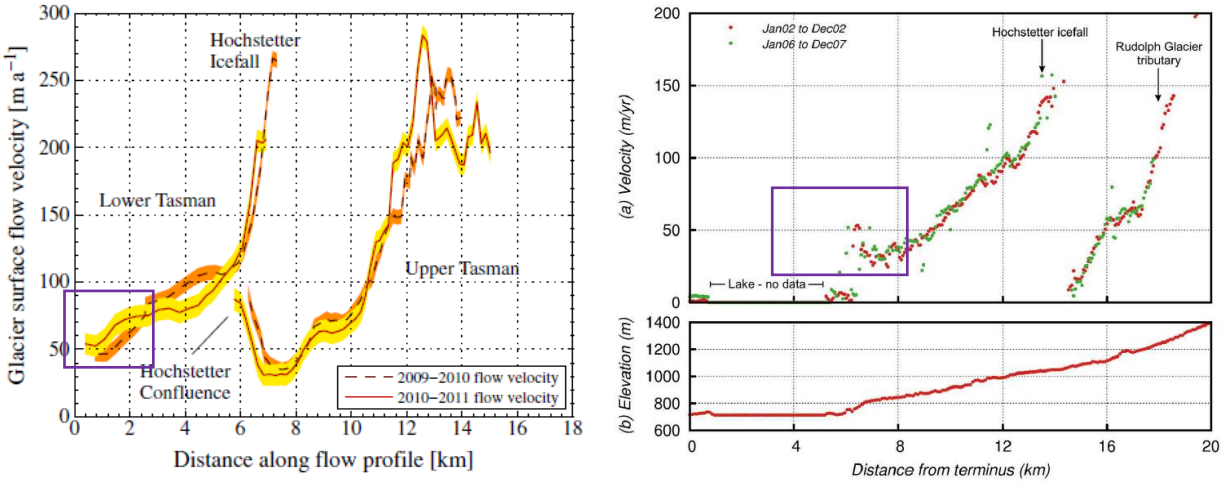

Figure 5.2.1. (RIGHT) Comparison of maximum and mean velocity for 2008-2011. *Source:* Redpath *et al.,* 2013. **(LEFT)** Comparison of maximum and mean velocity between 2002 and 2006-2007. *Source:* Quincey and Glasser, 2009. Marked in purple indicates the scope of our study (i.e. the distance from terminus). These averages are used for comparison with our data in *Table 5.2.1*.

5.2.1. Spatial Variations in Ice Velocity

Spatial variations in surface ice velocity are visible in the ice flow maps as shown in *Chapter Two* and the recent work of Horgan *et al.,* 2015. Below is a summary of velocity measurements from various sources.

Table 5.2.1. Compares maximum velocity (U_t) estimated by previous studies from varying distances above the terminus. Since the terminus began receding in the 1980s, the relative distance can only be used when comparing ice flow from the same location. *Sources:* References therein.

Years	Distance above terminus 1890 (km) and others	Measurement interval (days)	Maximum Velocity (U_t *max*) (m a^{-1})	Mean Velocity (m a^{-1})	Reference
1890	7.75	32	103	N/A	Brodrick (1891)
1890	10.0	32	167	N/A	Brodrick (1891)
1971-1972	10.6	229	88	N/A	Anderton (1975)
1972-1973	10.0	407	61	N/A	Anderton (1975)
1986	2.07	210	3.3	N/A	Kirkbride (1995)
1986	10.0	211	98	N/A	Kirkbride (1995)
1995	2.0 (from 1995 terminus)	16	24	N/A	Kirkbride and Warren (1999)
2000-2001 (ice flow map)	2.0 -3.0 (from 2000 terminus)	Annually averaged*	50	N/A	Kääb (2002)
2001–2003 (GPS)	Ice cliff	1-12 months	8.5	2.5	Röhl (2006)
1.1.2002 to 1.12. 2002 (ice flow map)	8 (from 2002 terminus)	Annually averaged*	51	33	Quincey and Glasser (2009)
1.1.2006 to 1.12. 2007 (ice flow map)	8 (from 2002 terminus)	Annually averaged*	53	36	Quincey and Glasser (2009)
2009 to 2010 (ice flow map)	1.5 (from 2009 terminus)	Annually averaged*	50	N/A	Redpath *et al.,* (2013)
2010 to 2011 (ice flow map)	1.5 (from 2009 terminus)	Annually averaged*	70	N/A	Redpath *et al.,* (2013)
2013 to 2015	0.5 (from 2013 terminus)	790	730	45.5 (36.5 – 54.75)	Horgan *et al.,* (2015)

The mean velocity measured in the lower 2-3 km of the 2000 terminus was ~ 50 m a^{-1}, compared to a mean velocity of ~ 45.5 m a^{-1} calculated by Horgan *et al.,* (2015) at 0.5 km from the 2013 terminus. If velocities were unchanged since Kääb's (2002) 2000-2001 analysis, present day maximum flow should exceed 150 m a^{-1} at the current terminus margin. Indeed, later work by Quincey and Glasser (2009) and Redpath *et al* (2013) showed that ice velocities in the location of the present-day terminus did not exceed 50 – 70 m a^{-1} and ice velocity at the ice cliff varied between 2.5 – 8.5 m a^{-1} (Röhl, 2006).

This evidence might suggest that ice flow may be linearly dependent on the distance-from-terminus at the Tasman Glacier (see linear progression of ice velocity from *Figure 5.2.1* at distances approaching the Hochstetter Icefall*).*

5.2.2. Seasonal Variations in Ice Velocity

In the past, several authors have alluded that velocity dynamics occurring at Tasman are due to the variation of ice flow on local scales or from seasonal deviations (Kääb, 2002; Redpath *et al.,* 2009). This was suggested in our pixel displacement data where ice surface was noted to change dynamically on local spatial scales while varying significantly between

summer/autumn and winter/spring. In Horgan *et al.*, (2015) the seasonal variability at the Tasman Glacier was estimated to be as high as 10.27 ± 0.13 m a^{-1} from 3 GPS stations set up at 0.5 km (2 station) and 4.7 km (1 station) from the terminus. Similar seasonal patterns have been observed at tidewater/marine-terminating glaciers such as the Rink Isbræ, Greenland (Howat *et al.*, 2010), Jakobshavn Isbræ, Greenland (Luckman and Murray, 2005), and at the Shirase Glacier (Nakamura *et al.*, 2007) and Polar Record Glacier (Zhou *et al.*, 2014) in East Antarctica. Although the processes responsible for velocity variability suggested by all these cases differ from glacier to glacier, insights into what may be occurring at the lake-terminating margin of the Tasman Glacier may be garnered. For example, in Zhou *et al.* (2014), the estimated 19% slowdown of the Polar Record Glacier in winter was attributed to the freezing of sea ice in winter which created increased resistance to the ice flow. Such changes could be occurring at the Tasman Lake, which is also known to freeze over in winter although the number of days where this occurs is not being monitored as of present. Seasonal velocity is due to variations in the water supply and sub-glacial hydrology evolution which result in reduced basal lubrication and thereby slower surface ice speeds (Paterson, 1994; Horgan *et al.*, 2015).

Similar observations were made at the Fox Glacier which is also situated at the Southern Alps of New Zealand. The slowing down of ice velocity during the winter of 2005 were similarly attributed to changes in the basal water supply and it was suggested to coincide with the growth of water storage cavities, thereby creating restrictions on the basal water pressure crucial for glacial sliding (Purdie, 2004). Time lags (as much as 24 hours) between precipitation events and surface velocity change were also noted in the authors study. Overall, a 26% reduction in surface velocity was observed to occur in winter compared to summer at the Fox Glacier.

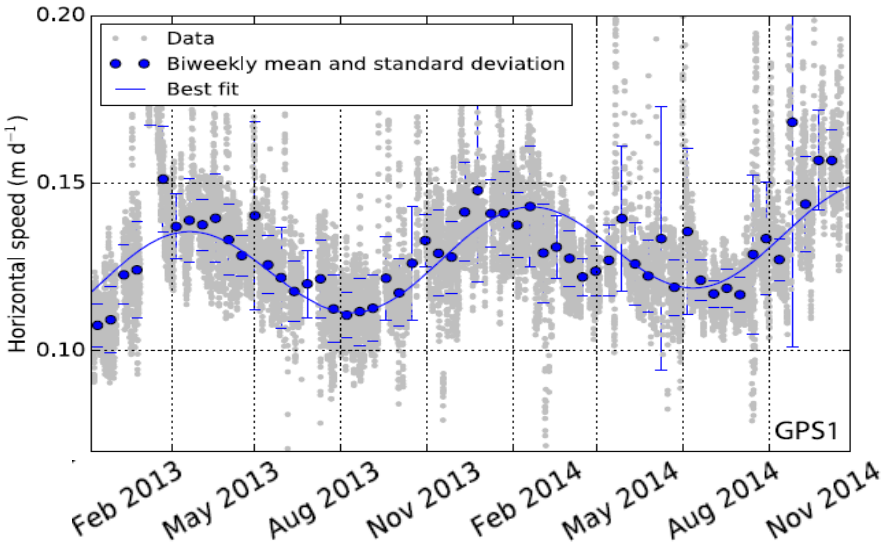

Figure 5.2.2. Horizontal speed variation from GPS 1 (0.5 km from 2013 terminus). A maximum background horizontal surface velocity of 0.15 m d^{-1} was used to calculate the calving rates in this study. *Source:* Horgan *et al.*, 2015

5.3. Calving Rates (U_c) and dynamic calving behaviour

Following Benn *et al.,* (2007) the calving rate is defined by the addition of the absolute values of retreat rate (U_r) and the rate of surface ice velocity at the terminus (dL/dt). I used the maximum background surface velocity by Horgan *et al.,* (2015) and the annual retreat rates to calculate the following calving rates.

Table 5.3. Calving rates of the Tasman Glacier. Ice velocities used by *Dykes et al,* (2010) were attained from Röhl, 2006. *Sources:* References therein.

Dates	**Ice velocity (U_i) (m a^{-1})**	**Annual Calving Rate (U_c) for Main Ice Cliff (m a^{-1})**	**No. of Major Calving Events**	**Reference**
2000 to 2006	8.5	78	N/A	Dykes *et al.,* 2010
2006 to 2008	8.5	227	N/A	Dykes *et al.,* 2010
5/2/2013 (start) to 5/2/2014	54.75	171 ± 18	1	*This study*
5/2/2014 to 5/2/2015	54.75	136 ± 17	0	*This study*
5/2/2015 to 5/2/2016	54.75	256 ± 20	1	*This study*
5/2/2015 to 22/3/2016 (end)	54.75	403 ± 21	2	*This study*

The annual calving rates (U_c) demonstrate the inter-annual calving dynamics occurring at the Tasman Glacier. The rates for 2013-2016 which are higher than those from 2000-2006 (Dykes *et al.,* 2010) suggest an acceleration in the background calving rate. This is epitomised by 2014-2015 calving rates (136 ± 17 m a^{-1}) compared to those in 2000-2006 (78 m a^{-1}). No large-magnitude events occurred in the year 2014-2015 and similarly, no significant changes to the planform shape of the Tasman Glacier was evident from 2000-2006 (*as seen in Figure 5.3a)*. Overall, too few large calving events have been documented to accurately assess seasonality, however all 3 main events have occurred in the summer season.

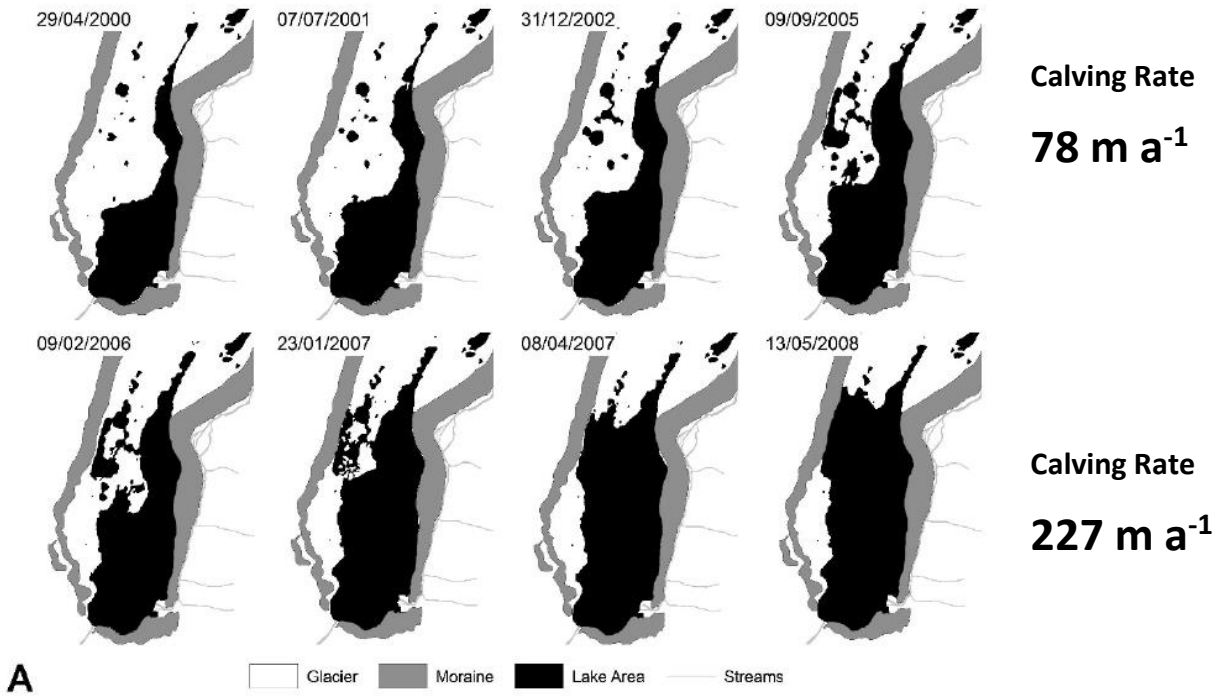

Figure 5.3a. Shows the planform shape of the Tasman Glacier in 2000-2006, which retreated relatively slowly compared to 2006-2008 when rapid retreat took place. *Source:* Dykes *et al,* 2010

Post 09/02/2006, a sudden retreat of ice resulted from the continued growth of supra-glacial ponds that had rapidly disconnected the tongue from the main ice trunk till the glacier had retreated to its 2008 position. The acceleration of calving rates in 2015-2016 to 229 ± 20 m a^{-1} relative to the first two years our study is reminiscent of changes that occurred in 2000 to 2008 (possibly due to similar glacier profiles). However, no supra-glacial ponds were identified in the terminus region which implies that changes occurring post summer-of-2015 are of a different nature. The frequency of large-magnitude events should also be noted, with one occurring at the start of our study in 2013 and two at the start of 2016. These events are linked to the glacial dynamics and alludes to buoyancy-driven mechanisms possibly from the ice tongue extending into the lake during summer at faster rates compared to winter (Horgan *et al*, 2015).

5.3.1. Large-magnitude vs small-magnitude calving

The idea that glacial dynamics (i.e. ice flow) can contribute as a 1st order control on calving process is evidenced with roughly ~ 47 % of net surface area loss of the Tasman Glacier for 2013-2016 attributed to these large-magnitude events. Smaller-magnitude ('background') calving events which behaved like 2nd order calving accounted for the remainder of the calving losses but had increased from year to year (*Figure 5.3b)*.

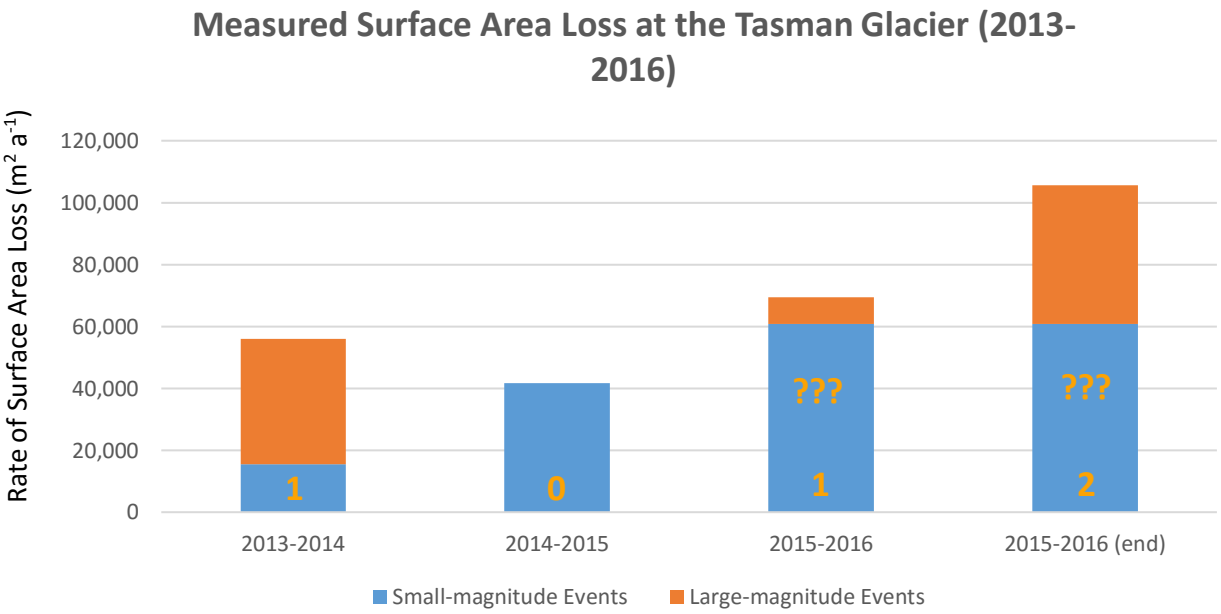

Figure 5.3b. Compares the rate of surface area loss at the Tasman Glacier (2013-2016) from small-magnitude ('background') events and discrete large-magnitude events. Numbers in orange indicate the number of major calving events. Question marks indicate an assumption where position changes were assumed to be from smaller magnitude events due to the lack of image data.

A major gap in the summertime of 2015-2016 meant that the observed change in terminus position was assumed to be from smaller-events rather than an unobserved large-magnitude event. This assumption questions the validity of the acceleration in the background rate of calving (or small-magnitude events) to – 60,893 $m^2 a^{-1}$. Without sufficient data between batch 3 and batch 4 of the terminus measurement (i.e. 20th October 2015 to 19th January 2016), this question cannot be fully resolved.

Nonetheless, an acceleration did occur in the background rate surface area loss between 2013-2014 and 2014-2015. However no subsequent evidence from historical studies mean it is difficult to explain the fundamental processes driving the diversity of calving behaviour witnessed here. It is possible that the smaller-magnitude events occurring at varying rates at every point of the terminus could be driving the morphological and geometry changes of the

terminus tongue which precondition to a major calving event. This is evident from the planform perspective whereby the ice tongue is protruding into the lake prior to the incidence of a large-magnitude event in this study and in Dykes *et al.*, (2010). At some critical stress state, this tongue can no longer maintain its structural integrity while continuing to slide further into the lake at higher lake levels as observed in summertime (Röhl, 2006). The height-above buoyancy of the ice cliff begins decreasing until a critical height where the buoyant forces exceeds the internal strength of the glacier and thereby results in the observed large-magnitude events (Van der Veen, 1996; 2010). Pre-existing weaknesses such as deep fractures or crevasses in the ice serve as the hinge points for these events (Benn *et al.*, 2007; James *et al.*, 2014; Murray *et al.*, 2015).

Perhaps in the case that smaller-magnitude events do not precondition for a structurally-weaker extension of the ice tongue, it presumes the glacier will consistently retreat at relatively the same rate across the full-width of the glacier. In such cases, small-magnitude calving events occurring at the waterline and sub-aerially will continue to dominate. This was observed in 2014-2015 where the overall 'shape' of the terminus remained relatively unchanged at the MIC whilst coinciding with no major calving events (*see Figure 4.1 in Results).*In 2015-2016, observed increases in small-magnitude calving on the true-right (EEIC) margin 'sharpened' the ice-tongue and resulted in two large magnitude events in the summer of 2015-2016.
Overall, the ice tongue may also be enhanced during surface velocity speed ups in summer/autumn but it will depend on the underlying shape of the valley and the presence of moraine shoals beneath the glacier which can act as front brakes on the glacier. Once the glacier has calved beyond the moraine shoal, the water depth beneath the terminus increases once again and allows the formation of a protruding ice tongue that may no longer be grounded (*as seen in Figure 2.3.1.)* to develop into a 1st order calving event.

The dual nature of our terminus position results indicate that the calving dynamics are inherently linked to processes occurring in the basal hydrology (Röhl, 2006; Benn *et al.*, 2007; Dykes *et al.*, 2010; Purdie *et al.*, 2010; Horgan *et al.*, 2015) speeding up the glacier in summer/autumn and constrained by the local bathymetry at the lake-terminus boundary. Similar seasonal variations in the calving was documented at the terminus by Röhl, (2006) of ~ 30 m a^{-1} in winter and ~ 80 m a^{-1} in summer.

The presence of sub-aqueous ice ramps, in some instances 60 m below the waterline, may also have a contributing factor to accelerated calving rates post-2015 (Purdie *et al.*, 2015). These ice ramps were observed to extend 100-200 m from the visible sub-aerial terminus but disintegrated within a month of the initial survey in 2015. It's possible that the ice foot is a bi-product of 1st order and 2nd calving occurring above or at the waterline.

Although no lake depth was measured for this thesis, a retrospective bathymetrical study of the present-day lake may reveal that calving is dominated by small-magnitude events (2nd order calving) at varying rates across the terminus (Röhl, 2006) until lake-depth increases and a reduction of basal resistance occurs (by loss of an ice foot or retreat from moraine shoals). This results in a terminus planform morphology and glacier geometry that is conducive to large-magnitude calving (1st order) which may quicken due to ice surface accelerations and further lake level increases associated with the summer/autumn seasons.

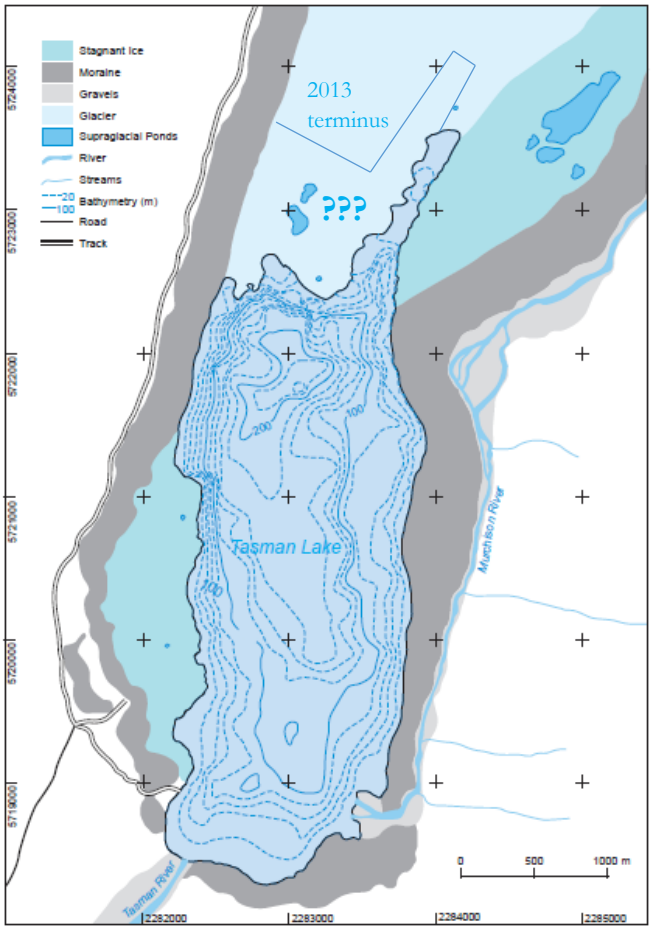

Figure 5.3c. Tasman Lake bathymetry relative to 717 m a.s.l. In blue is the approximate location of the 2013 terminus. No published bathymetry results exist in region highlighted by question marks (???). *Source:* Dykes *et al.*, 2009

5.4. Limitations of this study

5.4.1. Limitations in pixel displacements and surface velocity observations

(*see Appendix for velocity work*)

Measurements of ice flow were difficult in practice and more time-consuming to attain compared to terminus positions. This was owing to the multi-step processing required in order to resolve image geometry, correlate pixel movements, translate pixel movements to real world movements, and finally quantifying the results whilst dealing with image gaps and other limitations through every step. A summary of these limitations are provided here:

- The first and most prominent issue was our incomplete image time series as explained in *Chapter 3.* Three breaks in the time series occurred in the course of the study period amounting to 196 days of the 1141 day study period or 17 % of the total. This meant that surface displacements occurring during these periods are not captured in our final results. As such, our velocities may be on the low-end of estimations which explains why our annually-averaged maximum ice flow were ~ 20 m a^{-1} different to those measured at 2 km from the terminus (Kirkbride and Warren, 1999; Quincey and Glasser, 2009; Redpath *et al.*, 2013; Horgan *et al.*, 2015).
- Although images were captured on a daily basis, not every image could be used due to variability in cloud cover, shadows and hue/colour. These changes can significantly affect the image-correlation results therefore the best images were chosen on a sub-weekly basis. This means that the ice flow results presented in this study does not account for the daily or hourly changes. Our results only reflect ice flow variability on weekly, monthly or annual temporal scales. Despite this fact, this study is the second high-temporal resolution study of the Tasman Glacier, after the first in Horgan *et al,* (2015).
- In order to compute the spatial variations occurring on the surface, cross-correlation was conducted initially in the image space. This presented interesting spatial patterns but in the oblique perspective. For translating displacements form the image plane to the real-world plane, specific grid points had to be adopted as processing every pixel would be too intensive for the scope of the project. As such, a 100 m grid (119 sample points in total) was used to convert displacements. A finer resolution was not attained in this study.

- Due to having limited number of sample points (119), many correlations between image pairs at various time steps had failed. Failed correlations were saved as NaN in Matlab, and could not be further processed to attain a cumulative displacement that represented the overall change without resampling. Therefore only 20 of the initial 119 sample points were chosen because they satisfied a continuous record of the surface positions with exceptions being SP94 and SP89 which ended after batch two post-calving. Having a reduced number of sample points was not ideal and would have affected the spatial distribution we presented at the end. In some respects, our methodology reflected one that was not the best temporally, nor the best spatially but a good hybrid of temporal and spatial data acquisition.

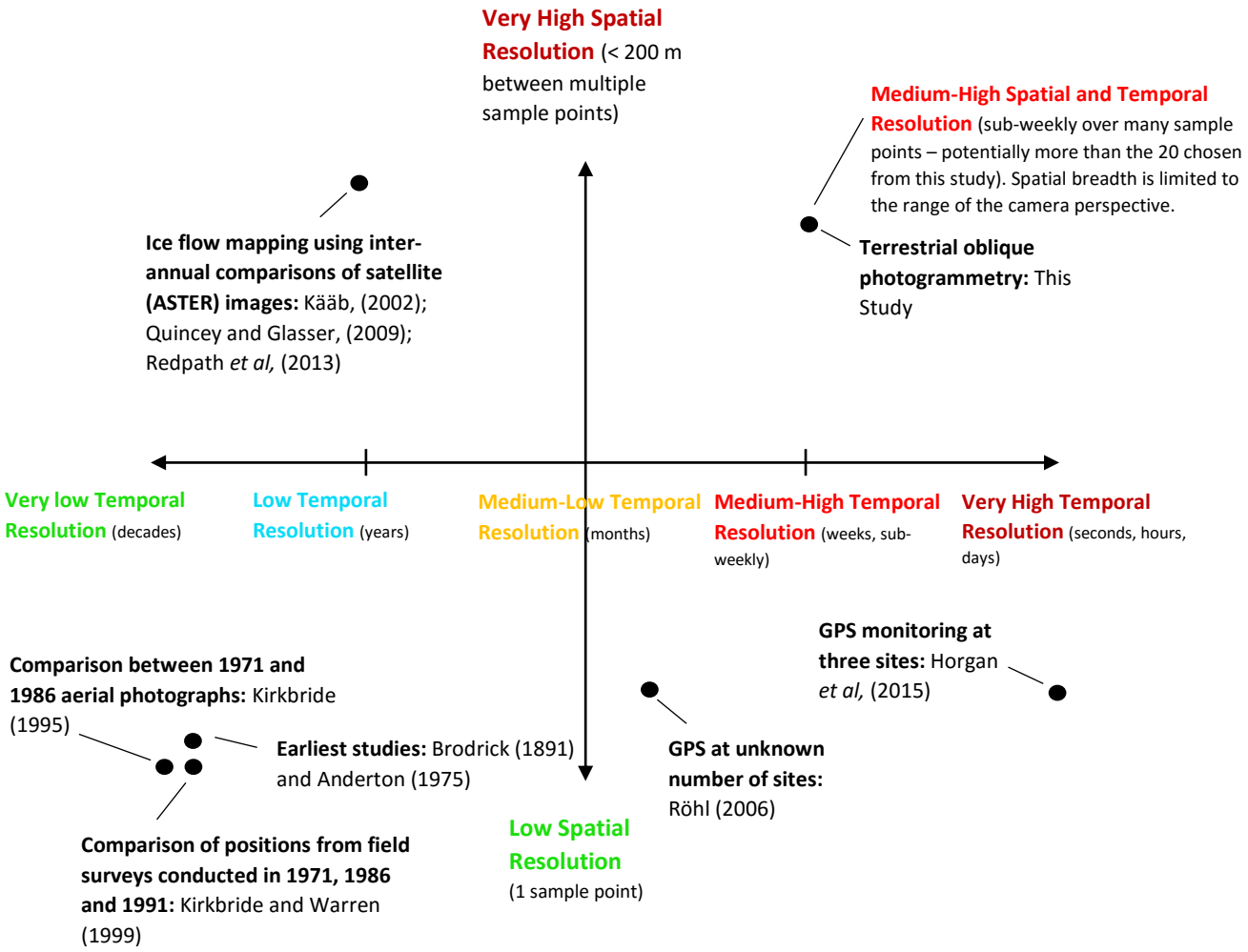

Figure 5.4.1. Summarises the spatial and temporal scope of surface velocity observations made prior to this study.

5.4.2. Limitations in terminus position and surface area change observations

Terminus positions were relatively easier to attain as it relied upon the accurate digitisation of positions. The results were limited spatially due to our methodology and there were errors associated with the image projection/correction phase which were outlined in *Chapter 4.1.3.* A summary of limitations are as follows:

- The transience of terminus positions were calculated using 20 evenly spaced digital transects perpendicular to a direction of retreat. The transects did not encompass the Temporary Ice Cliff (TIC) region due to its irregular morphology as well as parts on the true-right of the glacier including the Eastern Embayment Ice Cliff (EEIC). Therefore the changes in retreat rates averaged across all transects only represent those mainly occurring at the Main Ice Cliff (MIC).

- Likewise, surface area measurements were calculated between transects 1 and 20 used for measuring terminus positions. Thus, the surface area is not indicative of the net surface area loss experienced at the Tasman Glacier for 2013-2016. Rather it captures part of the wider picture of terminus mass balance/surface area loss and reveals intriguing intricacies about the nature of its calving dynamics. As such, the ratio between major calving events and background calving (currently ~ 47% from major calving events and 53% from background smaller-magnitude calving events) will be altered if the data included the gaps posed by the TIC and the EEIC, however presumably not by significant magnitudes as terminus retreat was predominantly occurring at the MIC.

- Overall, three image gaps were present in our terminus position measurements. These image gaps did not alter any of the net terminus positions as each terminus vector drawn represented a cumulative change. The image gaps do however mask the temporal dynamics occurring on sub-weekly timescales and although this study proposes a technique to monitor glacial at high-temporal resolution relative to other remotely-sensed studies (10 year temporal frequency in Hochstein (1995), 1-3 year frequency in Quincey and Glasser, (2009) and annual/sub-annual frequency in Dykes *et al,* (2009)), the results would have been further enhanced by an uninterrupted record.

5.5. Conclusions and recommendations for future studies

It is projected that continued warming in the 21st century will result in the dramatic loss of ice particularly ice stored in mountain glaciers. Such changes to may add further stress to human populations in the form of short-term flooding (Haeberli, 1984; Clague and O'Connor, 2015) and other longer-term climate impacts. Furthermore, the retreat of mountain glaciers is a direct contributor sea-level rise as well as a catalyst of geopolitical strife by impacting human populations through changes in the water cycle (Grafton *et al.,* 2012; Yang *et al.,* 2015). To date, many estimations of global ice balances have made in the literature but are critiqued for their over-simplification of glacier dynamics (Clarke *et al.,* 2015). This study has shown that finer temporal and spatial resolution studies of glaciers can be achieved using low-cost oblique terrestrial photogrammetry and may be the key to better understand the characteristics of mountain glaciers.

- The observed changes in surface area and rates of terminus positions change were highly variable as were those in previous studies and this study showed that they may be linked to seasonality and the associated variations in mean temperatures. Calving rates were shown to be much higher in summer/autumn compared to winter/spring. Large-magnitude calving behaviour accounted for 47 % of the total surface area change in the study period. The average retreat rates (U_r) were 116 ± 18 m a^{-1} (2013-2014), 82 ± 17 m a^{-1} (2014-2015) and speeding up to 204 ± 20 m a^{-1} in 2015-2016.

- Finally, the calving rates of the Tasman were estimated to be 171 ± 18 m a^{-1} (2013-2014), 136 ± 17 m a^{-1} (2014-2015) and accelerated to 256 ± 20 m a^{-1} (2015-2016). By including the third large-magnitude calving event in February 2016, the calving rate was 403 ± 21 m a^{-1} (2015-2016[end]). Our results suggest this dynamic behaviour governing 1st order buoyancy-driven calving events is linked with subglacial hydrology, basal crevassing and the planform morphology/glacial geometry of the ice tongue. Continued monitoring is highly recommended as rates of calving have increased progressively up to 2016.

A summary of objectives for this thesis and recommendations for future studies are presented in the following:

Objective 1: Develop and test methods to extract quantitative information on glacier terminus and dynamics using oblique photographs

(1) Oblique terrestrial photogrammetry is a cost-effective but manually intensive technique that can be used to cheaply attain vast amounts of spatial and temporal data. From this thesis, it has been shown that measurements of retreat rates (U_r) and surface area change (dA/dt) can be readily attained from timelapse photography. Surface ice velocities (U_t) can also be attained however requires further post-processing in order to make sense of the data. In all steps, image capture, selection and pre-processing therefore play a key part in ensuring the accuracy of measurements. The ideal photogrammetry dataset would be one with no image gaps and contain perfectly stabilised imagery from the moment of capture.

(2) It has been shown that irregular ice cliff morphologies make length-wise quantifications difficult to attain. Although the majority of terminus records account for length-changes, a better representation is found by looking at surface-area. Using digitisation and post-processing techniques, surface-area changes (dA/dt) can be attained. Using a single camera setup may conceal regions of the lake-ice interface that are used for digitisation. Therefore future studies should at least use two or more camera angles for monitoring. This will also be beneficial to calculating the image depth and the extrinsic camera parameters used for resolving the image geometry.

Objective 2: Understand the factors which control the style and magnitude of calving at the Tasman Glacier
Objective 3: Compare the rate at which the Tasman Glacier is calving to other records in the past to attain a better understanding on what drives these calving processes.

(1) Through this study it has been shown that large-magnitude calving events were individually larger than smaller-magnitude calving events with the three large-magnitude events accounting for ~ 47 % of the net surface area change between 2013-2016. They behaved like 1st order buoyancy calving causing large tabular slabs of ice to hinge off structural weaknesses such as basal crevasses. These events also occurred in the summer of 2013 and 2016, and although it is not clear whether they can only occur in summer months, the results suggest they are linked to water supply,

and subglacial hydrological evolution. Further research should investigate the dualism observed in the mode and frequency of these calving events.

(2) The rate of calving shown to increase from year to year throughout our study. The 2015-2016 calving rate of 256 ± 20 m a^{-1} exceeded previous records in 2006-2008 by Dykes *et al.,* 2010, and represents the highest calving rate observed at the Tasman Glacier. These calving rates were however calculated using a maximum averaged horizontal surface velocity from 2013-2015 (Horgan *et al.,* 2015). Surface velocities estimated in this study were not used as their validity is questioned (*see Appendix)*. The calving rates presented here also suggest that calving is controlled by glacier geometry and planform morphology. The shape of the ice tongue, the levels of water within/beneath the glacier and the lake level all play an important role in governing calving, particularly the large-magnitude events.

(3) A bathymetrical study in the future may provide more insights into the glacial processes responsible for the calving behaviour occurring at the *Haupapa*/Tasman Glacier, Mt. Cook (*Aoraki*), New Zealand.

REFERENCES

A

Alley, R.B., Clark, P.U., Huybrechts, P., and Joughin, I., (2005) – 'Ice Sheet and Sea-Level changes', *Science,* 310(5747), 456-460

Ahn, Y., and Howat, I.M., (2011) – "Efficient automated Glacier Surface Velocity Measurement from repeat images using multi-image/multichip and Null exclusion Feature Tracking" *IEEE Transactions on Geoscience and Remote Sensing, Vol. 49, No.8 August 2011*

Anderson, B. M., W. J. Lawson, I. F. Owens, and B. Goodsell., (2006) – 'Past and future mass balance of "Ka Roimata o Hine Hukatere" Franz Josef Glacier, New Zealand', *J. Glaciol.,* 52, 597–607, doi:10.3189/172756506781828449.

Anderson, B., and Mackintosh, A., (2012) – 'Controls on mass balance sensitivity of maritime glaciers in the Southern Alps, New Zealand: The Role of Debris Cover', *Journal of Geophysical Research, Earth Surface,* VOL. 117, F01003

Anderton, P. W., (1975) – 'Tasman Glacier 1971–73.' *Hydrological Research Annual Report 33, Wellington.*

Annan, J.D., and Hargreaves, J.C., (2013) – 'A new global reconstruction of temperature changes at the Last Glacial Maximum', *Climate Past,* 9, 367-376, 2013

Amundson, J.M., and Truffer, M., (2010) – 'A unifying framework for iceberg calving models', *Journal of Glaciology,* Vol.56, No. 199, 2010

Arendt, A.A., Echelmeyer, K.A., Harrison, W.D., Lingle, C.S., and Valentine, V.B., (2002) – 'Rapid wastage of Alaskan glaciers and their contribution to rising sea level', *Science,* 297(5580), 382-386

Arendt, A. and *7 others.,* (2006) – 'Updated estimates of glacier volume changes in the western Chugach Mountains, Alaska, and a comparison of the reginal extrapolation methods', *Journal of Geophysical Resources,* 111, F03019, doi:10.1029/2005JF000436

Arendt, A.A., Luthcke, S., and Hock, R., (In press) – 'Glacier changes in Alaska: can mass-balance models explain GRACE mascon trends', *Annual Glaciology,* 50

Åström, J.A., Vallot, D., Schäfer3, M., Welty, E.Z., O'Neel, E.Z., Bartholomaus, T.C., Liu, Y., Riikilä, T.I., Zwinger, T., Timonen, J., and Moore, J.C., (2014) – 'Termini of calving as self-organizing critical systems', *Nature Geoscience,* Vol.7, December 2014, DOI: 10.1038/NGEO2290

Asdwanden, A., Fahnestock, M.A., and Truffer, M., (2015) - 'Complex Greenland outlet flow captured', *Nature Communications,* 7:10524 | DOI: 10.1038/ncomms10524

B

Bartholomaus, T.C., Larsen, C.F., O'Neel, S., and West, M.E., (2012) – 'Calving seismicity from iceberg-sea surface interactions', *Journal of Geophysical Research,* Vol.117, December 2012

Barthomolomaus, T.C., (2013) [PHD DISSERTATION] – 'Seismicity, Seawater and Seasonality: New Insights into Iceberg Calving from Yahtse Glacier, Alaska', *Proquest Publishing,* University of Alaska Fairbanks, December 2013

Bassis, J.N., and Walker, C.C., (2011) – 'Upper and lower limits on the stability of calving glaciers from the yield strength envelope of ice', *Proceedings of the Royal Society A, Mathemtical, Physical and Engineering Sciences,* 23 Nov 2011

Bassis, J.N., and Jacobs, S., (2013) – 'Diverse calving patterns linked to glacier geometry', *Nature Geoscience,* Vol.6, October 2013, 833-836

Benn, D.I., Warren, C.R., and Mottram, R.H., (2007) – 'Calving processes and the dynamics of calving glaciers', *Earth-Science Reviews,* Vol.82, 143-179

Berthier, E., Schiefer, E., Clarke, G.K.C., Menounos, B., and Remy, F., (2010) – 'Contribution of Alaskan glaciers to sea-level rise derived from satellite imagery', *Nature Geoscience,* Vol.3, February 2010

Birchfield, S., and Tomasi, C., (1998) – 'A pixel dissimilarity measure that is insensitive to image sampling', *IEEE Transactions on Pattern Analysis and Machine Intelligence, 1998*

Bourgault, D., (2008) – "Shore-based photogrammetry of river ice", *Canadian Journal of Civil Engineering,* 35: 80-86, 2008

Boyce, E.S., Motyka, R.J., and Truffer, M., (2007) – 'Flotation and the retreat of a lake-calving terminus, Mendenhall Glacier, southeast Alaska, USA', *Journal of Glaciology,* Vol.53, No.181, 2007

Braithwaite, R. J., Y. Zhang, and S. C. B. Raper., (2003) – 'Temperature sensitivity of the mass balance of mountain glaciers and ice caps as a climatological characteristic', *Z. Gletscherkd. Glazialgeol.*, 38(1), 35–61.

Broadbent, M., (1974) – 'Seismic and gravity surveys on the Tasman Glacier 1971–72.' *Wellington, New Zealand: Geophysics Division report 91*, Department of Industrial Research, 43 pp.

Brown, J.D., (2006) – "Photogrammetry's digital revolution", *Quality Digest, Geodetic Systems Incs., Accessed online at: http://www.qualitydigest.com/sept04/articles/03_article.shtml*

C

Caltech., (2015) – 'Camera Calibration Toolbox for Matlab', *Accessed online at: http://www.vision.caltech.edu/bouguetj/calib_doc/ , Last updated by: Jean-Yves Bouguet, October 14th, 2015*

Cazenave, A., (2006) – 'How fast are the ice sheets melting?', *Science,* 314(5803), 1250-1252

Caroti,G., Zaragoza, M.E., and Piemonte, A., (2015) – 'Accuracy Assessment in Structure From Motion 3D Reconstruction from UAV-Born Images: The Influence of the Data Processing Method', *International Archives of the Photogrammetry, Remote Sensing and Spatial Information Sciences, Vol. XL-1,* International Conference on Unmanned Aerial Vehicles in Geomatics, Toronto Canada

Clague, J.J., and O'Connor, J.E., (2015) – 'Chapter 14 - Glacier-Related Outburst Floods, In Snow and Ice-Related Hazards, Risks and Disasters, Academic Press, Boston', 2015, Pages 487-519, ISBN 9780123948496, http://dx.doi.org/10.1016/B978-0-12-394849-6.00014-7

Clarke, P.U., Shakun, J.D., Marcott, S.A., Mix, A.C., Eby, M., Kulp, S., Levermann, A., Milne, G.A., Pfister, P.L., Santer, B.D., Schrag, D.P., Solomon, S., Stocker, T.F., Strauss, B.H., Weaver, A.J., Winkelmann, R., Archer, D., Bard, E., Goldner, A., Lambeck, K., Pierrehumbert, R.T., and Plattner, G.K., (2016) - 'Consequences of twenty-first-century policy for multi-millenial climate and sea level change', *Nature Climate Change,* doi:10.1038/nclimate2923

Chandler, J., Ashmore, P., Paola, C., Gooch, M., and Varkaris, F., (2014) – "Monitoring River-Channel Change using Terrestrial Oblique Digital Imagery and Automated Digital Photogrammetry" *Annals from the Association of America Geographers, 92(4), 2002, pp. 631- 644*

Chandler, J., Ashmore, P., Paola, C., Gooch, M., and Varkaris, F., (2014) – "Monitoring River-Channel Change using Terrestrial Oblique Digital Imagery and Automated Digital Photogrammetry" *Annals from the Association of America Geographers, 92(4), 2002, pp. 631- 644*

Chinn, T., Winker, S., Salinger, M.J., and Haakensen, N., (2006) – 'Recent glacier advances in Norway and New Zealand: A comparison of their glaciological and meteorological causes', *Geographical Annals,* 87 A (1), 141-157

Corne, S., Murray, T., Openshaw, S., See, L., and Turton, I., (1999) – 'Using computational intelligence techniques to model subglacial water systems', *Journal of Geophysical Systems,* 1, 37-60

D

Dandois, J.P., and Ellis, E.C., (2013) – 'High spatial resolution three-dimensional mapping of vegetation spectral dynamics using computer vision', *Remote Sensing of Environment,* Vol. 136, September 2013

Deser, Clara; Phillips, Adam S.; Hurrell, James W., (2004) – 'Pacific Interdecadal Climate Variability: Linkages between the Tropics and the North Pacific during Boreal Winter since 1900'.*Journal of Climate* **17** (15): 3109–3124.

De Woul, M., and Hock, R., (2005) – 'Static mass-balance sensitivity of Arctic glaciers and ice caps using a degree-day approach', *Annals of Glaciology, 42,* 217-224

Diefenbach, A.K., Crider, J.G., Schilling, S.P., and Dzurisin, D., (2012) – "Rapid, low-cost photogrammetry, to monitor volcanic eruptions: An example from Mount St. Helens Washington, USA" *Bull Volcanol, (2012), 74:579- 587*

Diolaiuti, G., Citterio, M., Carnielli, T., Agata, C.D., Kirkbride, M., and Smiraglia, C., (2006) – 'Rates, processes and morphology of freshwater calving at Miege Glacier (Italian Alps)', *Hydrological Processes,* 20, 2233-2244

DOC., (2009) – 'Aoraki/Mount Cook National Park', *Department of Conservation,* Accessed online at: http://www.doc.govt.nz/documents/getting-involved/students-and-teachers/field-trips-by-region/canterbury/aoraki/aoraki-mt-cook-education-resource-colour.pdf

Dolling, O.R., and Varas, E.A., (2003) – 'Artificial Neural Networks for streamflow prediction', *Journal of Hydraulic Research,* Vol. 40, 2002, No.5

Dong, B., and Dai, A., (2015) – 'The influence of the Interdecadal Pacific Oscillation on Temperature and Precipitation over the Globe', *National Centre for Atmospheric Resaerch, Climate and Global Dynamics,* Accessed online at: http://www.cgd.ucar.edu/cas/adai/papers/DongDai-CD2015-IPO.pdf

Dykes, R.C., and Brooks, M.S., (2010) – "Terminus recession, proglacial lake expansion, and 21st century calving retreat of Tasman Glacier New Zealand", *New Zealand Geographer, Vol. 66, 203-217*

Dykes, R.C., Brook, M.S., Robertson, C.M., and Fuller, I.C., (2011) – "Twenty-first century calving retreat of Tasman Glacier, Southern Alps, New Zealand", *Arctic, Antarctic, and Alpine Research, Vol. 43, No. 1, 2011, pp. 1-10*

Dyurgerov, M., and McCabe, G.J., (2006) – 'Associations between accelerated glacier mass wastage and increased summer temperature in coastal regions', *Arctic, Antarctic and Alpine Research,* 38(2), 190-197

E

Ehlers, J., and Gibbard, P.L., (2004) – 'Quaternary Glaciations – Extent and Chronology', *Elsevier,* ISBN 978-0-444-51471-4.

Evans, S.G., and Clague, J.J., (1994) – 'Recent climatic change and catastrophic geomorphic processes in mountain environments', *Geomorphology,* 10:107-108

Evans, A.N., (2000) – "Glacier surface Motion Computation from Digital Image Sequences" *IEEE Transactions on Geoscience and Remote Sensing, Vol. 38, No.2 March 2000*

F

Fahnestock, M., Scambos, T., Moon, T., Gardner, A., Haran, T., and Klinger, M., (2015) – 'Rapid Large-area mapping of ice flow using Landsat 8', *Remote Sensing of Environment,* November 2015

Farinotti, D., Longuevergne, L., Moholdt, G., Duethmann, D., Molg, T., Bolch, T., Vorogushyn, S., and Guntner, A., (2015) - 'Substantial glacier mass loss in the Tien Shan over the past 50 years', *Nature Geoscience,* 8, 716-722, 2015

Flotron, A., (1973) – 'Photogrammetirsche Messungen von Gletscherbewegunen mit automatischer Kamera', Schweiz. Z. Vermess. Photogramm. Kult. Tech., 71, 1–73, 1973.

G

Ghosh, S.K., (1970) – "History of Photogrammetry – Chapter 6: Analytical Methods" *ISPRS Proceedings, Found online at: http://www.isprs.org/proceedings/XXIX/congress/part6/311_XXIX-part6.pdf*

Glasser, N.F., Harrison, S., Jansson, K.N., Anderson, K., and Cowley, A., (2011) – 'Global sea-level contribution from Patagonian Icefields since the Little Ice Age maximum', *Nature Geoscience,* Vol.4, May 2011

Glowacki, O., Deane, G.B., Moskalik, M., Blondel, Ph., Tegowski, J., and Blaszcyk, M., (2015) – 'Underwater Acoustic signatures of glacier calving', *Geophysical Research Letters,* 42, 804-817, doi:10.1002/2014GL062859

Grafton, R.Q., Pittock, J., Davis, R., Williams, J., Fu, G., Warburton, M., Udall, B., McKenzie, R., Yu, X., Che, N., Connell, D., Jiang, Q., Kompas, T., Lynch, A., Norris, R., Possingham, H., and Quiggin, J., (2012) – 'Global insights into water resources, climate change and governance', *Nature Climate Change,* Vol.3, April 2013

H

Haeberli, W., (1983) – 'Frequency and characteristics of glacier floods in the Swiss Alps', *Annals of Glaciology,* 4, 85-90

Haeberli, W., (1994) – 'Accelerated glacier and permafrost changes in the Alps. In: Beniston, M. ed. Mountain environments in changing climates.' London and New York, Routledge. Pp. 91-107.

Haeberli, W., (1995) - "Glacier fluctuations and climate change detection— operational elements of a worldwide monitoring strategy". *World Meteorological Organisation Bulletin 44, 23–31.*

Haeberli, W., (2013) – 'Mountain permafrost – research frontiers and a special long-term challenge', *Cold Regions Science and Technology,* 96: 71-76.

Harrison, W. D., Raymond, C. F., and MacKeith, P., (1986) – 'Short period motion events on Variegated Glacier as observed by automatic photography and seismic methods', Ann. Glaciol., 8, 82– 89, 1989

Hartley, R.I., (1999) – 'Theory and Practice of Projective Rectification', *International Journal of Computer Vision,* 35, 2, pp 115-127

Heikkilä, J., and Silvén, O., (1997) – 'A Four-step Camera Calibration Procedure with Implicit Image Correction', *Infotech Oulu and Department of Electrical Engineering University of Oulu* FIN-90570 Oulu, Finland, accessed online at: http://www.vision.caltech.edu/bouguetj/calib_doc/papers/heikkila97.pdf

Heng, P.B.C., and Chandler, J.H., (2010) – "Applying close-range digital photogrammetry in soil erosion studies" *The Photogrammetric record, 25 (131): 240-256*

Herman, F., Anderson, B., and Leprince, S., (2011) – 'Mountain glacier velocity during a retreat/advance cycle quantified using sub-pixel analysis of ASTER images', *Journal of Glaciology, Vol.57, No.202, 2011*

Hobrough, G.L., (1968) – 'Patent US3646336 - Correlation unit', US Patent, *Accessed online at: https://www.google.ch/patents/US3646336*

Hochstein, M.P., Claridge, D., Henrys, S.A., Pyne, A., Nobes, D.C., Leary, S.F., (1995) - "Downwasting of the Tasman Glacier, South Island, New Zealand: changes in the terminus region between 1971 and 1993", *New Zealand Journal of Geology and Geophysics, 1995, Vol.38: 1-16*

Hoffman, M.J., (2011) – 'Spatial and Temporal Variability of Glacier Melt in the McMurdo Dry Valleys, Antarctica', *Portland State University,* 2011

Horgan, H.J., Anderson, B., Alley, R.B., Chamberlain, C, Dykes, R., Kehrl, L.M., and Townend, J., (2015) – 'Glacier Velocity variability due to rain-induced sliding and cavity formation', *Earth and Planetary Science Letters, July 17, 2015 [DRAFT]*

Houghton, J.T.,Y. Ding, D.J. Griggs, M. Noguer, P.J. van der Linden, X. Dai, K. Maskell, and C.A. Johnson (eds.)., (2001) – 'Climate Change 2001: The Scientific Basis. Contribution to Working Group I to the Third Assessment Report of the IPCC', Cambridge University Press, NY, USA, 881pp

Howard, I.P., and Rogers, B.J., (1995) – 'Binocular Vision and Stereopsis', *New York, Oxford University Press,* p.32 ISBN-0-19-50875-4

Howat, I.M., I. Joughin, S. Tulaczyk and S. Gogineni.., (2005) – 'Rapid retreat and acceleration of Helheim Glacier, east Greenland' *Geophys. Res. Lett.,* **32**(22), L22502. (10.1029/2005GL024737.)

Howat, I.M., Box, J.E., Ahn, Y., Herrington, A., and McFadden, E.M., (2010) – 'Seasonal variability in the dynamics of marine-terminating outlet glaciers in Greenland', *Journal of Glaciology,* Vol.56, No.198, 2010.

Huang, C.W., Chou, C.M., Lin, T.W., and Chang, C.Y., (2012) – 'Adaptive calibration method for camera distortion', *Journal of Vibration and Control,* 19(1), 86-93

Hugin., (2003a) – 'Control point detector parameters', *Accessed online at: http://hugin.sourceforge.net/docs/manual/Control_Point_Detector_Parameters.html*

Hugin., (2003b) – 'Align a stack of photos', *Accessed online at: http://hugin.sourceforge.net/docs/manual/Align_a_stack_of_photos.html*

I

IPCC AR5, (2012) – 'Chapter 9 – Evaluation of Climate Models', *IPCC WG1 Fifth Assessment Report*, [Draft], Accessed online at: http://www.climatechange2013.org/images/report/WG1AR5_SOD_Ch09_All_Final.pdf

IPCC AR5., (2013) – 'IPCC AR5 Working Group I: Climate Change 2013 – The Physical Science Basis', *Accessed online at: https://www.ipcc.ch/pdf/unfccc/cop19/3_gregory13sbsta.pdf*

IPCC AR5., (2014) – 'IPCC – Summary for Policy Makers. Synthesis Report - 2014', *IPCC, Fifth Assessment Report, Accessed online at: https://www.ipcc.ch/pdf/assessment-report/ar5/syr/SYR_AR5_FINAL_full_wcover.pdf*

IPCC, (2014) – 'Climate Change 2014, Synthesis report – Summary for Policy Makers', *IPCC,* Accessed online at: https://www.ipcc.ch/pdf/assessment-report/ar5/syr/AR5_SYR_FINAL_SPM.pdf

Iribarren Anacona, P., Norton, K.P., and Mackintosh, A., (2014) – 'Moraine-damned lake failures in Patagonia and assessment of outburst susceptibility in the Baker Basin', *Natural Hazards Earth System Sciences, 14,* 3243-3259

J

James, T.D., Murray, T., Selmes, N., Scharrer, K., and O'Leary, M., (2014) – 'Buoyant flexure and basal crevassing in dynamic mass loss at Helheim Glacier', *Nature Geoscience, 7,* 593-596 (2014).

Jeong, S., and Howat, I.M., (2015) – 'Performance of Landsat 8 Operational Land Imager for mapping ice sheet velocity', *Remote Sensing and Environment,* 170, 1 December 2015, pp 90-101

Jones, E.M.C., Silberstein, M.N., White, S.R., Sottos, N.R., (2014) –'In Situ Measurements of Strains in Composite Battery Electrodes during Electrochemical Cycling.', *Experimental Mechanics*, 54:971-985, basis of Jones E.M.C. Improved digital image correlation (2013).

Jones, E., (2015) – 'Improved Digital Image Correlation', *Mathworks File Exchange,* Accessed online at: https://www.mathworks.com/matlabcentral/fileexchange/43073-improved-digital-image-correlation--dic-

Joughin, I., S.B. Das, M.A. King, B.E. Smith, I.M. Howat and T. Moon., (2008) – 'Seasonal speedup along the western flank of the Greenland Ice Sheet.' *Science,* **320**(5877), 781–783.

Jouglin, I., Smith, B.E., Howat, I.M., Scambos, T., and Moon, T., (2010) – 'Greenland flow variability from ice-sheet-wide velocity mapping', *Journal of Glaciology,* 56 (197), 2010, pp. 415-430

K

Kääb, A. (2002). - 'Monitoring high-mountain terrain deformation from repeated air- and spaceborne optical data: examples using digital aerial imagery and ASTER data.' *ISPRS Journal of Photogrammetry and Remote Sensing*, 57(1–2), 39–52.

Kääb, A., Reynolds, J,M., Haeberli, W., (2005) 'Glacier and permafrost hazards in high mountains. In Global Change and Mountain Regions – a State of Knowledge Overview', *Huber UM, Bugmann HKM, Reasoner MA (eds)*. Springer: Dordrecht; 225–234.

Kääb, A., Frauenfelder, R., Roer, I., (2007) 'On the response of rockglacier creep to surface temperature increases', *Global and Planetary Change*, 56(1–2): 172–187.

Kayastha, R.B., Takeuchi, Y., Nakawo, M., and Ageta, Y., (2000) – 'Practical prediction of ice melting beneath various thickness of debris cover on Khumbu Glacier, Nepal using a positive degree-day factor'. *IAHS Publ. 264* (Symposium at Seattle 2000 – DebrisCovered Glaciers), 71–81

Kerr, T., and Owens, I., (2008) – 'Glaciers and climate change over the last century in Aoraki/Mt Cook region of New Zealand', *Glaciers of New Zealand*

Kirkbride, M.P., (1989) - 'The influence of sediment budget on the geomorphic activity of the Tasman Glacier, Mount Cook National Park, New Zealand'. PhD thesis, The University of Canterbury.

Kirkbride, M.P., (1993) - 'The temporal significance of transitions from melting to calving termini at glaciers in the Southern Alps of New Zealand.' *The Holocene* 3, 232–40.

Kirkbride, M., (1995a) - "Ice flow vectors on the Debris-mantled Tasman Glacier, 1957-1986" *Geografiska Annaler, Series A, Physical Geography, Vol. 77, No.3 (1995), pp. 147-157*

Kirkbride, M.P., (1995b). 'Relationships between temperature and ablation on the Tasman Glacier, Mount Cook National Park', New Zealand. N. Z. J. Geol. Geophys. 38, 17–27.

Kirkbride, M., Spedding, N., (1996) - 'The influence of englacial drainage on sediment-transport pathways and till texture of temperate valley glaciers.' *Annals of Glaciology* **22**, 160–6.

Kirkbride, M.P., Warren, C.R., (1997). 'Calving processes at a grounded ice cliff.' Ann. Glaciol. 24, 116–121

Kirkbride, M., and Warren, C.R., (1999) - "Tasman Glacier, New Zealand: 20th century thinning and predicted calving retreat" *Global and Planetary Change, Vol. 22 (1999), 11-28*

Kirkbride, M., (2010) - "Relationship between temperature and ablation on the Tasman Glacier, Mount Cook National Park, New Zealand" *New Zealand Journal of Geology and Geophysics, 38:1, 17-27*

Kirkbride, M.P., and Deline, P., (2013) – 'The formation of supraglacial debris covers by primary dispersal from transverse englacial debris bands', *Earth Surface Processes and Landforms,* Vol. 38, Issue 15, pp. 1779-1792, December 2013

Kjeldsen, K.K., Korsgaard, N.J., Bjork, A.A., Khan, S.A., Box, J.E., Funder, S., Larsen, N.K., Bamber, J.L., Colgan, W., Broeke, M.V.D., Siggard-Andersen, M.L., Nuth, C., Schomacker, A., Andresan, C.S., Willerslev, E., and Kjaer, K.H., (2015) - 'Spatial and temporal distribution of mass loss from the Greenland Ice Sheet since AD 1900',*Nature,* 526, 396-400, 2015

Knight, J. and Harrison, S. (eds), (2009) – "Periglacial and Paraglacial Processes and Environments." Geological Society, London, Special Publications, 320.

L

Lane, S.N., Richards, K.S and Chandler, J.H., (1993) – "Developments in photogrammetry: the geomorphological potential" *Progress in Physical Geography, 1993, 17:306*

Larson, C.F., Motyka, R.J., Arendt, A.A., Echelmeyer, K.A., and Geissler, P.E., (2007) – 'Glacier changes in southeast Alaska and northwest British Columbia and contribution to sea level rise', *Journal Geophysical Research,* 112(F1), F01007, doi: 10.1029/2006JF000586

LeBlanc, B., Niezrekcki, C., Avitabile, P., Chen, J., and Sherwood, J., (2013) – 'Damage detection and full-surface characterisation of a wind turbine blade using three-dimensional digital image correlation', *Structural Health Monitoring,* Sep-Nov 2013, vol. 12 (5-6), pp 430-439

Lepetit, V., Moreno-Noguer, F., and Fua, P., (2008) – 'EPnP: an Accurate O(n) Solution to the P*n*P Problem', *Int. J. Computer Vision,* DOI 10.1007/s11263-008-0152-6c

Liang, Z., Yin, B., Dai, X., Mo, J., and Wang, S., (2012) – 'Using camera calibration to apply digital image correlation outside the laboratory', *Optical Engineering,* 52 (12), 123102 (Dec 16, 2013).

Lorrey, A., Fauchereau, N., Stanton, C., Chappell, P., Phipps, S., Mackintosh, A., Renwick, J., Goodwin, I., Fowler, A., (2014) – "The Little Ice Age climate of New Zealand reconstructed from Southern Alps cirque glaciers: a synoptic type approach", *Clim. Dyn. (2014)*, *42:3039–3060, DOI 10.1007/s00382-013-1876-8*

Luckman, A., Murray, T., (2005) – 'Seasonal variation in velocity before retreat of Jakobshavn Isbrae, Greenland', *Geophysical Research Letters,* Vol.32., 2005

Luckman, A., Benn, D.I., Cottier, F., Bevan, S., Nilsen, F., and Inall, M., (2015) – 'Calving rates at tidewater glaciers vary strongly with ocean temperature', *Nature Communications,* 6, Article 8566, doi:10.1038/ncomms9566

Luthcke, S.B., Arendt, A.A., Rowlands, D.D., McCarthy, J.J., and Larsen, C.F., (2008) – 'Recent glacier mass changes in the Gulf of Alaska region from GRACE mascon solutions', *Journal of Glaciology,* Vol. 54, No. 188, 2008

Lyres, R.D., (2008) – "Field Techniques Manual- GIS, GPS and Remote Sensing" – Chapter 9: Geocorrection and Photogrammetry. *Accessed online at: http://www.rgs.org/NR/rdonlyres/C30C5A86-5364-49FE-9A58-58EE27315F9C/0/Chapter9GeocorrectionandPhotogrammetry.pdf*

N

Nakamura, K., Doi, K., and Shibuya, K., (2007) – 'Estimation of seasonal changes in the flow of Shirase Glacier using JERS-1/SAR image correlation', *Polar Science,* Vol.1, Issue 1-2

Naruse, R., and Skvarca, P., (2000) – 'Dynamic Features of Thinning and Retreating Glaciar Upsala, a Lacustrine Calving Glacier in Southern Patagonia', *Arctic, Antarctic and Alpine Research,* 32, No.4, 2000, 485-491

Neel, S.O., and Pfeffer, W.T., (2007) – 'Source Mechanics for monochromatic icequakes produced during iceberg calving at Columbia Glacier, AK', *Geophysical Research Letters,* 34, L22502, doi: 10.1029/2007GL031370, 2007

Nettles, M., Larsen, T.B., Elosegui, P., Hamilton, G.S., Stearns, L.A., Ahlstrom, A.P., Davis, J.L., Andersen, M.L., de Juan, J., Khan, S.A., Stenserg, L., Ekstrom, G., and Forsberg, R., (2008) – 'Step-wise changes in glacier flow speed coincide with calving and glacial earthquakes at Helheim Glacier, Greenland', *Geophysical Research Letters,* 35, L24503, doi:10.1029/2008Gl036127

Nichols, R.J., Marinova, N., Lowe, J.A., Brown, S., Vellinga, P., Gusmao, D.D. Hinkel, J., and Tol, R.S.J., (2010) – 'Sea-level rise and its possible impacts given a 'beyond 4 ° C world' in the twenty-first

Nick, F.M., and Oerlemans, J., (2006) – 'Dynamics of tidewater glaciers: comparison of three models', *Journal of Glaciology, 52, 183-190*

NIWA, (2011) –"Annual glacier volumes in New Zealand 1995-2010", NIWA, *Accessed online at: https://www.google.co.nz/url?sa=t&rct=j&q=&esrc=s&source=web&cd=4&cad=rja&uact=8&ved=0CDUQFjAD&url=http%3A%2F%2Fwww.stats.govt.nz%2F~%2Fmedia%2FStatistics%2Fbrowse-categories%2Fenvironment%2Fnatural-resources%2Fwater-physical-stock-account-1995-2010%2Fannual-glacier-ice-volumes-in-new-zealand-1995-*

2010.pdf&ei=SV34U9GaONajugSvgoKoBw&usg=AFQjCNF2bNurO721AtbDtbj9UYtPbHPzwQ&bvm=bv.73612305,d.c2E

century. *Philosophical Transactions of the Royal Society: Mathematical, Physical and Engineering Sciences,* 29 November 2010. DOI: 10.1098/rsta.2010.0291

NIWA., (2016) – 'Southern Oscillation Index', *Accessed online at:* https://www.niwa.co.nz/climate/information-and-resources/elnino/el-nino-and-southern-oscillation

NOAA., (2016) – 'Trends in Atmospheric Carbon Dioxide – Mauna Loa Observatory', *NOAA,* Earth System Laboratory*, Accessed online at: http://www.esrl.noaa.gov/gmd/ccgg/trends/*

NSIDC., (2016) – 'All about Glaciers – Facts about Glaciers', *National Snow and Ice Data Center, Accessed online at: https://nsidc.org/cryosphere/glaciers/quickfacts.html* Last updated, 2016

NZCCC, (2014) – 'Climate Change: IPCC Fifth Assessment Report New Zealand Findings', *New Zealand Climate Change Centre, Accessed online at: https://www.niwa.co.nz/sites/niwa.co.nz/files/NZCCC%20Summary_IPCC%20AR5%20NZ%20Findings_April%202014%20WEB.pdf*

NZ Topo Maps, *Data accessed from http://www.topomap.co.nz. Date accessed: 3/4/2016*

M

Ma, Y., Kosecka, J., Soatoo, S., and Sastry, S., (2001) – An Invitation to 3-d Vision – From Images to Models (book) Accessed here at: http://www.vision.caltech.edu/bouguetj/calib_doc/

Magd, A.E., and Hillman, P.F., (2009) – "Geomorphological monitoring of highly dynamic estuary using oblique aerial photographs" International Journal of Digital Earth, 2:2

Mann, M.E., Bradley, R.S., and Hughes, M.K., (1998) – "Global-scale temperature patterns and climate forcing over the past six centuries", *Nature, Vol. 430, 1 July 2004, 779-784*

Marggraf, A., (1746) cited by Britannica Encyclopaedia, -'Andreas Sigismund Marggraf', *Accessed online at: http://www.britannica.com/biography/Andreas-Sigismund-Marggraf*

Mattson, L.E., Gardner, J.S., Young, G.J., (1993) – 'Ablation on debris covered glaciers: an example from the Rakhiot Glacier, Punjab, Himalaya. In: Snow and Glacier Hydrology.' *Proceedings of the Kathmandu Symposium,* November 1992. IAHS Publ. No. 218, 1993.

Meier, M.F., (1984) – 'Contribution of small glaciers to global sea level', *Science,* 226(4681), 1418-1421

Meier, M.F., and A. Post., (1987) – 'Fast tidewater glaciers', *Journal of Geophysical Research,* 92 (B9), 9051-9058

Meier, M.F., and *7 others.,* (2007) – 'Glaciers dominate eustatic sea-level rise in the 21st century', *Science,* 317(5841), 1064-1067

MetService., (2016) – 'Aoraki/Mount Cook National Park', *Accessed online at:* http://www.metservice.com/mountain/aoraki-mount-cook-national-park, *Date accessed:* 11th April 2016

Mimura, N., (2013) – 'Sea-level rise caused by climate change and its implications for society', *Proc. Jpn. Acad. Ser. B. Phys. Biol. Sci,* 2013, 89 (7): 281-301

Motyka, R.J., Neel, S.O., Connor, C.L., and Echelmeyer, K.A., (2002) – 'Twentieth century thinning of Mendenhall Glacier, Alaska, and its relationship to climate, lake calving and glacier run off', *Global and Planetary Change,* 35, 93-112

Murray, T., Nettles, M., Selmes, N., Cathles, L.M., Burton, J.C., James, T.D., Edwards, S., Martin, L., Farrell, T.O., Aspey, R., Rutt, I., and Bauge, T., (2015) – 'Reverse glacier motion during iceberg calving and the cause of glacial earthquakes', *Science,* 349, 305-308

Murray, T., Selmes, N., James, T.D., Edwards, S., Martin, I., O-farell, T., Aspey, R., Rutt, I., Nettles, M., Bauge, T., (2015) – 'Dynamics of glacier calving at the ungrounded margin of Helheim Glacier, southeast Greenland', *Journal of Geophysical Research: Earth Sciences,* 120, 964-982, doi:10.1002/2015JF003531

O

Oerlemans, J., (2001) – "Glaciers and climate change", *Balkema Publishers, Rotterdam,* ISBN 90-265-1813-7, hardback

Oerlemans, J., (1997) – 'Climate sensitivity of Franz Josef Glacier, New Zealand, as revealed by numerical modelling', *Arct. Alp. Res.,* 29(2), 233–239, doi:10.2307/1552052.

Østrem, G., (1959) – 'Ice melting under a thin layer of moraine and the existence of ice cores in moraine ridges', *Geo. Ann.,* 41(4), 228-300

P

Paterson, W.S.B. (1994). 'The physics of glaciers.' Third edition. Oxford, etc., Elsevier

Pelliccioti, F., Stephan, C., Miles, E., Herreid, S., Immerzeel, W. and Bolch, T., (2015) – 'Maxx changes of the debris-covered glaciers in Langtang Himal 1974-2000 revealed by Hexagon and SRTM data', *Journal of Glaciology,* 61(225), doi: 10.3189/2015JoG13J237

Peltier, W.R., (2004) – 'Global glacial isostatic adjustment and the surface of the ice-age Earth: the ICE-5G(VM2) model and GRACE', *Annual Review of Earth Planetary Science,* 32, 111-149

Petit, J.R., Jouzel, J., Raynauld, D., Barkov, N.I., Barnola, J.M., Basile, I., Bender, M., Chappellaz, J., Davis, M., Delaygue, G., Delmotte, M., Kotlyakov, V.M., Legrand, M., Lipenkov, V.Y., Lorius, C., Pepin, L., Ritz, C., Saltzman, E., and Stievenard, M., (1999) – 'Climate and atmospheric history of the past 420,000 years from Vostok ice core, Antarctica', *Nature, 399,* 429-436

Pratap, B., Dobhal, D.P., Mehta, M., and Bhambri, R., (2015) – 'Influence of debris cover and altitude on glacier surface melting: a case study on Dokriani Glacier, central Himalaya, India', *Annals of Glaciology,* 56 (70), 2015

Purdie, J., and Fitzharris, B., (1999) - "Process and rates of ice loss at the terminus of Tasman Glacier: New Zealand"*, Global and Planetary Change 22 (1999) 79-91*

Purdie, H., (2011) – PhD Thesis – 'Controls on Spatial and Temporal Variation in Snow Accumulation on Glaciers in Southern Alps, New Zealand', *Victoria University of Wellington, 2011*

Purdie, H., Mackintosh, A., Lawson, W., Anderson, B., Morgenstern, U., Chinn, T., and Mayewski, P., (2011) – "Interannual variability in the net accumulation on Tasman Glacier and its relationship with climate", *Global and Planetary Change, Vol. 77, 142-152*

Purdie, H., (2013) – "Glacier retreat and tourism: Insights from New Zealand", *Mountain Research and Development, 33(4): 463- 472, 2013*

Purdie, H., Anderson, B., Chinn, T., Owens, I., Mackintosh, A., and Lawson, W., (2014) – 'Franz Josef and Fox Glaciers, New Zealand: Historic Length Changes', *Global and Planetary Change,* 121, 41-52

Purdie, H., Bealing, P., Tidey, E. & Gomez, C. (2015) - 'Bathymetric and terminus evolution as determined by remote-sensing techniques: Tasman Glacier, New Zealand',. *New Zealand Snow and Ice Research Group Annual Workshop.* Cass, Canterbury, 2-4 July.

Q

Quincey, D.J., and Glasser, N.F., (2009) – "Morphological and ice-dynamical changes on the Tasman Glacier, New Zealand, 1990-2007", *Global and Planetary Change, Vol. 68, 185-197*

R

Radic, V., and Hock, R., (2011) – 'Regionally differentiated contribution of mountain glaciers and ice caps to future sea-level rise', *Nature Geoscience,* Vol.4., February 2011

Redpath, T.A.N., Sirguey, P., Fitzsimmons, S.J., and Kääb,A., (2013) – 'Accuracy assessment for mapping glacier flow velocity and detecting flow dynamics from ASTER satellite imagery: Tasman Glacier, New Zealand.

Reznichenko, N., Davies, T., Shulmeister, J., and McSaveney, M.J., (2010) – 'Effects of debris on ice-surface melting rates: an experimental study.' *J. Glaciol.*, **56**(197), 384–394 (doi: 10.3180002214310792447725)

Richardson, J.P., Waite, G.P., FitzGerald, K.A. and Pennington, W.D., (2010) – 'Characteristics of seismic and acoustic signals produced by calving, Bering glacier, Alaska', 37, L03503, doi: 10.1029/2009Gl041113, 2010

Rignot, E., Rivera, A., and Cassasa, G., (2003) – 'Contribution of the Patagonian icefields of South America to sea level rise', *Science,* 302(5644), 434-437

Rignot, E. (2008) – 'Changes in west Antarctic ice stream dynamics observed from ALOS PALSAR data', *Geophysical Research Letters,* 35 (12), 2008

Rignot, E., Koppes, M., and Velicogna, I., (2010) – 'Rapid Submarine melting of the calving faces of West Greenland glaciers', *Nature Geoscience,* 3, 187-191, doi: 10.1038/NGEO765

Rignot, E., Mouginot, J., and Scheuchl, B., (2011) – 'Ice flow of the Antarctic Ice Sheet', *Science, 333 (6048),* 2011

Robertson, C.M., Brook, M.S., Holt, K.A., Fuller, I.C., and Benn, D.I., (2013) – 'Calving retreat and proglacial lake growth at Hooker Glacier, Southern Alps, New Zealand', *New Zealand Geographer,* 69, 14-25

Röhl, K., (2005) - 'Terminus disintegration of debris covered, lake-calving glaciers.' PhD thesis, The University of Otago, p. 434.

Röhl, K., (2006) – 'Thermo-erosional notch development at fresh-water calving Tasman Glacier, New Zealand.' *Journal of Glaciology* **52***, 203–13.*

Röhl, K., (2008) - 'Characteristics and evolution of supraglacial ponds on debris-covered Tasman Glacier, New Zealand.' *Journal of Glaciology* **54**, 867–80.

S

Sakakibara, D., and Sugiyama, S., (2014) – 'Ice-front variations and speed changes of calving glaciers in the Southern Patagonia Icefield from 1984 to 2011', *Journal of Geophysical Research: Earth Surface,* 119, 2541-2554, doi:10.1002/2014JF003148

Scambos, T.A., Haran, T.M., Fahnestock, M.A., Painter, T.H., Bohlander, J., (2007) – 'MODIS-based mosaic of Antarctica (MOA) data sets: continent-wide surface morphology and snow grain size', *Remote Sensing of Environment, 111 (2),* 2007

Schaefer, J.M., Denton, G.H., Kaplan, M., Putnam, A., Finkel, R.C., Barrell, D.J.A., Andersen, B.G., Schwartz, R., Mackintosh, A., Chinn, T., Schluchter, C., (2009) - 'High frequency Holocene glacier fluctuations in New Zealand differ from the northern signature.' *Science* 324, 622–5.

Scherler, D., Leprince, S., Strecker, M.R., (2008) – 'Glacier-surface velocities in alpine terrain from optical satellite imagery — accuracy improvement and quality assessment.', *Remote Sensing of Environment 112* (10), 3806–3819.

Schwartz, D., (2006) – 'Fast and robust curve intersections', *Mathworks Fileexchange,* Accessed online at: https://www.mathworks.com/matlabcentral/fileexchange/11837-fast-and-robust-curve-intersections/content/intersections.

Slabough, G.G., (2013) – 'Computing Euler angles from a rotation matrix', *Accessed online at: http://www.staff.city.ac.uk/~sbbh653/publications/euler.pdf ,* (verified: 2013-04-15)

Shumskiy, P.A., (1959) – 'Density of Glacier Ice', *International Geological Society,* Accessed online at: http://www.igsoc.org:8080/journal/3/27/igs_journal_vol03_issue027_pg568-573.pdf

Stewart, R.H., (1997) – 'Introduction to Physical Oceanography', *[TEXTBOOK], Accessed online at: http://oceanworld.tamu.edu/resources/ocng_textbook/contents.html*

Sugiyama, S., Skvarca, P., Naito, N., Enomoto, H., Tsutaki, S., Tone, K., Marinsek, S., and Aniya, M., (2011) – 'Ice Speed of a calving glacier modulated by small fluctuations in basal water pressure', *Nature Geoscience,* 4, 597-600, doi: 10.1038/NGEO1218

Sutton, M.A., Orteu, J-J., and Schreier, H.W., (2009) – 'Image Correlation for Shape, Motion and Deformation Measurements: Basic concepts, Theory and Applications', [Book], *Springer,* 2009, ISBN: 978-0-387-78746-6

T

Tang, Z.Z., Liang, J., Guo, C., and Wang, Y.X., (2012) **–** "Photogrammetry-based two dimensional digital images correlation with nonperpendicular camera alignment", *Optical Engineering, February 2012/Vol.51*

Truffer, M., Harrison, W.D., and March, R.S., (2005) – 'Record negative glacier balances and low velocities during 2004 heatwave in Alaska, USA: Implications for the interpretation of observations by Zwally and others in Greenland', *Journal of Glaciology,* 51(175), 663-664

Trussel, B.L., (2013)[PHD DISSERTATION] – 'Rapid Thinning and Collapse of Lake Calving Yakutat Glacier, Southeast Alaska', *Proquest Publishing,* University of Alaska Fairbanks, December 2013

U

UCSB., (2011) – "Geometry of Aerial Photography", Lecture notes. *Accessed online at: http://www.geog.ucsb.edu/~jeff/115a/lectures/geometry_of_aerial_photographs_notes.html*

UNEP., (2012) – 'Thematic Focus: Climate Change, Ecosystem Management', *Accessed online at: http://na.unep.net/geas/getuneppagewitharticleidscript.php?article_id=91*

V

Van der Veen, C.J., (1996) – 'Tidewater calving', *Journal of Glaciology,* 42: 375-385

Van der Veen, C.J., (2002) – 'Calving glaciers', *Progress in Physical Geography,* 26, 1, pp. 96-122

Van der Veen, C.J., (2010) – 'Fundamentals of Glacier Dynamics – Second Edition', *Taylor & Francis Group,* ISBN: 13:978-1-4398-3566-1

Venteries, E.R., (1999) – 'Rapid tidewater glacier retreat: a comparison between Columbia Glacier, Alaska and Patagonian calving glaciers', *Global and Planetary Change,* 22, 131-138

Vernier, F., Fallourd, R., Friedt, J.M., Yan, Y., Trouve, E., Nicolas, J.M., and Moreau, L., (2011) – "Fast correlation technique for glacier flow monitoring by digital camera and space-borne SAR images", *Journal on Image and Video Processing,*2011: 2011:11

W

Wagner, T.J.W., James, T.D., Murray, T., and Vella, D., (2016) – 'On the role of buoyant flexure in glacier calving', *Geophysical Research Letters,* Vol. 43, Issue 1, *16 January 2016*

Walter, F., Neel, S.O., McNamara, D., Pfeffer, W.T., Bassis, J.N., and Fricker, H.A., (2010) – 'Iceberg Calving during transition from grounded to floating ice: Columbia Glacier, Alaska', *Geophysical Research Letters,* 37, L15501, doi:10.1029/2010GL043201

Warren, C., and Aniya, M., (1999) – 'The Calving glaciers of southern South America', *Global and Planetary Change,* 22, 59-77

Warren, C.R., Kirkbride, M.P., (2003) – 'Calving speed and climatic sensitivity of New Zealand lake-

Winkler, S., (2004) – ' Lichenometric dating of the 'Little Ice Age' maximum in Mt Cook National Park, Southern Alps, New Zealand'. *The Holocene,* 14, 911-20

Wolf, P.R., Dewitt, B.A., and Wilkinson, B.E., (2000) – 'Elements of Photogrammetry: with Applications in GIS. Fourth Edition', *McGraw Hill, Accessed online at: https://accessengineeringlibrary.com/browse/elements-of-photogrammetry-with-applications-in-gis-fourth-edition#Preface01*

Y

Yang, Jiang-Ping., Ding, Yong-Jian., Liu, Shi-Yin., Tan, Chun-Ping., (2015) – 'Vulnerability of mountain glaciers in China to climate change', *Advances in Climate Change Research,* 6, 171-180

Z

Zemp, M., Frey, H., Gartner-Roer, I., Nussbaumer, S., Hoelzle, M., Paul, F., Haeberli, W., Denzinger, F., Ahlstrom, A.P., Anderson, B., Bajracharya, S., Baroni, C., Braun, L.N., Caceres, B.E., Cassasa, G., Cobos, G., Davila, L.R., Delgado, H., Demuth, M.N., Espizua, L., Fischer, A., Fujita, K., Gadek, B., Ghazanfar, A., Hagen, J.O., Holmund, P., Karimi, N., Li, Z., Pelto, M., Pitte, P., Popovnin, V.V., Portocarerro, C.A., Prinz, R., Sangewar, C., Seversky, I., Sigurdsson, O., Soruco, A., Usubaliev, R., and Vincent, C., (2015) – 'Historically unprecedented global glacier decline in the early 21st century', *Journal of Glaciology,* Vol.61, No. 228, 2015

Zhang, Z., (2000) – 'A Flexible New Technique for Camera Calibration'*, IEEE Transactions on Pattern Analysis and Machine Intelligence*, Vol. 22., No. 11, 2000, pp. 1330-133

Zhao, Haitao., Zhang, B., Wu, Changshan., Zuo, Zhengli., Chen, Z.C., and Bi, J., (2014) – "Direct georeferencing of oblique and vertical imagery in different coordinate systems", *ISPRS Journal of Photogrammetry and Remote Sensing, Vol. 95, (2014) 122-123*

Zhou, C., Zhou, Y., Deng, F., Ai, S., Wang, Z., and Dongchen, E., (2014) – 'Seasonal and interannual ice velocity changes of Polar Record Glacier, East Antarctica', *Annals of Glaciology,* 55(66), 2014

Matlab Scripts

Intersections of Curves (Used to calculate intersections with transects)

Code by:

Schwartz, D., (2006) – "Fast and Robust Curve Intersections", *Mathworks File Exchange,* Last updated – 27 Jan 2010. *Accessed online at: http://www.mathworks.com/matlabcentral/fileexchange/11837-fast-and-robust-curve-intersections*

Matlab Improved Digital Image Correlation

Code by:

Jones, E., (2015) – 'Improved Digital Image Correlation', *Mathworks File Exchange,* Accessed online at: https://www.mathworks.com/matlabcentral/fileexchange/43073-improved-digital-image-correlation--dic-